AD-A268 719

AGARD

ADVISORY GROUP FOR AEROSPACE RESEARCH & DEVELOPMENT

7 RUE ANCELLE 92200 NEUILLY SUR SEINE FRANCE

AGARD LECTURE SERIES 188

Rocket Motor Plume Technology

(L'Etude des Jets des Moteurs-Fusées)

DTIC
ELECTE
AUG 2 5 1993
S E D

NORTH ATLANTIC TREATY ORGANIZATION

DISCLAIMER NOTICE
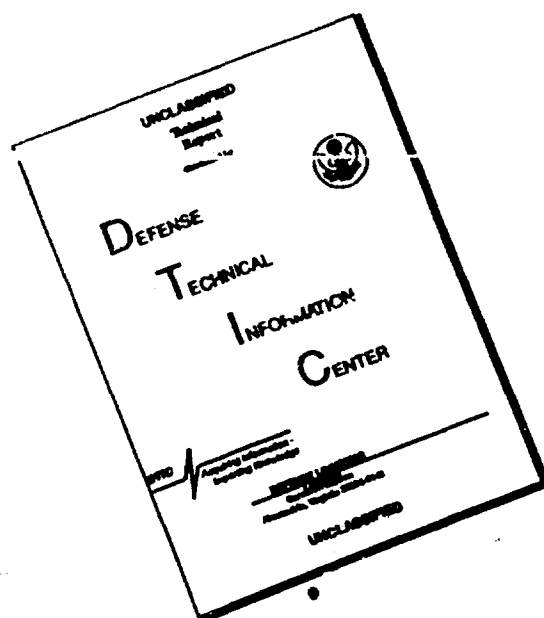
THIS DOCUMENT IS BEST QUALITY AVAILABLE. THE COPY FURNISHED TO DTIC CONTAINED A SIGNIFICANT NUMBER OF PAGES WHICH DO NOT REPRODUCE LEGIBLY.

AGARD-LS-188

AGARD

ADVISORY GROUP FOR AEROSPACE RESEARCH & DEVELOPMENT

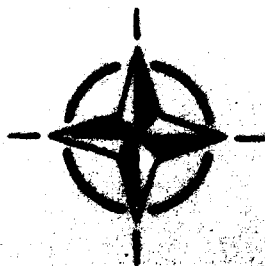7 RUE ANCELLE 92200 NEUILLY SUR SEINE FRANCE

AGARD LECTURE SERIES 188

Rocket Motor Plume Technology

(L'Etude des Jets des Moteurs-Fusées)

Accesion For		
NTIS CRA&I	☒	
DTIC TAB	☐	
Unannounced	☐	
Justification		
By		
Distribution /		
Availability Codes		
Dist	Avail and / or Special	
A-1		

DTIC QUALITY INSPECTED 3

The material in this publication was assembled to support a Lecture Series
under the sponsorship of the Propulsion and Energetics Panel
and the Consultant and Exchange Programme of AGARD presented on
7th—8th June 1993 in Neubiberg, Germany, 10th—11th June 1993 in
Ankara, Turkey.

North Atlantic Treaty Organization
Organisation du Traité de l'Atlantique Nord

93-19831

The Mission of AGARD

According to its Charter, the mission of AGARD is to bring together the leading personalities of the NATO nations in the fields of science and technology relating to aerospace for the following purposes:

— Recommending effective ways for the member nations to use their research and development capabilities for the common benefit of the NATO community;

— Providing scientific and technical advice and assistance to the Military Committee in the field of aerospace research and development (with particular regard to its military application);

— Continuously stimulating advances in the aerospace sciences relevant to strengthening the common defence posture;

— Improving the co-operation among member nations in aerospace research and development;

— Exchange of scientific and technical information;

— Providing assistance to member nations for the purpose of increasing their scientific and technical potential;

— Rendering scientific and technical assistance, as requested, to other NATO bodies and to member nations in connection with research and development problems in the aerospace field.

The highest authority within AGARD is the National Delegates Board consisting of officially appointed senior representatives from each member nation. The mission of AGARD is carried out through the Panels which are composed of experts appointed by the National Delegates, the Consultant and Exchange Programme and the Aerospace Applications Studies Programme. The results of AGARD work are reported to the member nations and the NATO Authorities through the AGARD series of publications of which this is one.

Participation in AGARD activities is by invitation only and is normally limited to citizens of the NATO nations.

Abstract

Requirements for missile guidance and stealth properties are changing and becoming more stringent. There is no up-to-date synthesis relating rocket motor plume properties to these new requirements. The work performed and recently finished within PEP WG 21 has formed the basis for this Lecture Series.

The scope of the Lecture Series will be rocket motor exhaust products and plumes in all their aspects. Plume properties will be addressed and methods of numerical simulation and experimental assessment described.

Specifically, plume structure, after-burning phenomena, primary and secondary smoke, plume radiation signatures and plume microwave interactions will be described in detail.

Operational aspects linked to these topics will discuss how rocket plumes influence missile detection, guidance and tracking. Ways in which plumes may be modified to reduce or eliminate this influence will be suggested.

Abrégé

Les spécifications en matière de guidage de missiles et de caractéristiques de furtivité évoluent et deviennent plus rigoureuses. Or, il n'existe aucune étude de synthèse récente qui permet de confronter les caractéristiques des jets des moteurs-fusées avec ces nouvelles exigences. Les travaux entrepris par le groupe de travail PEP WG 21, qui viennent de s'achever, ont servi de base à ce cycle de conférences.

Les conférences couvriront tous les aspects des jets des moteurs-fusées et des produits émis par ceux-ci. Les caractéristiques des jets de propulseur seront examinées et les méthodes de simulation numérique et d'évaluation expérimentale seront discutées.

En particulier, la structure des jets, les phénomènes de postcombustion, les fumées primaires et secondaires, les signatures par rayonnement des jets et les interactions/jets hyperfréquences seront décrits dans le détail.

Les conséquences opérationnelles liées à ces sujets montreront l'influence des jets des moteurs-fusées sur la détection, le guidage et la poursuite. Des propositions seront faites pour la modification des jets afin de réduire ou d'éliminer cette influence.

List of Authors/Speakers

Lecture Series Director

Mr R. Lawrence
DRA Office
c/o Royal Ordnance
Westcott
Aylesbury
Bucks HP18 0NZ
United Kingdom

Mr J.C. Chastenet
SNPE Centre de Recherches du Bouchet
Le Bouchet B.P. No.2
91710 Vert-le-Petit
France

Dr P. Kessel
8 Draco Drive
Edwards Air Force Base
CA 93524 7230
United States

Mr R. Dirscherl
Deutsche Aerospace AG
Dynamics Systems
Abt. VAR 331
P.O.B. 801149
D-8000 München 80
Germany

Mr P.K. Smith
Royal Ordnance
Rocket Motors Division
Summerfield
Kidderminster
Worcestershire DY11 7RZ
United Kingdom

Mr S. Dash
Science Applications Inc.
501 Office Center Drive
Fort Washington
Pennsylvania PA 19034
United States

Contents

INTRODUCTION

R LAWRENCE

DRA Office
c/o Royal Ordnance
Westcott
Aylesbury
Bucks HP18 ONZ

Rocket plume technology has been a subject of interest and study for many countries engaged in missile design and manufacture. For successful operational deployment of missile systems it is necessary to quantify the exhaust properties of the propulsion unit and its effects on missile guidance, tracking and signature. AGARD Lecture Series 188 addresses some major topics of this subject. The Series stems from the work of AGARD PEP Working Group 21 which investigated the question of terminology in the field of solid propellant rocket exhaust signatures with a view to agreeing and recommending a common terminology. Particular emphasis was placed on the classification of propellants in terms of Primary and Secondary smoke. The work resulted in the submission of a final report which became AGARD Advisory Report 287 entitled "Terminology and Assessment Methods of Solid Propellant Rocket Exhaust Signatures". Principal subjects were Primary and Secondary smokes, smoke classification, plume radiation and microwave properties. These were preceded by an introduction and comprehensive overview and supported by appendices.

The recommended "Smoke Classification" went forward to become a NATO standard.

With few exceptions the exhaust of a rocket motor is seen as an embarrassment to the missile user. The nature of the exhaust, characterised by the very rapid flow of chemically reacting, high temperature turbulent gases, presents a problem to the missile design team having concern for guidance, tracking and vulnerability to detection.

Where electromagnetic guidance and tracking signals pass through regions of the exhaust they undergo losses and distortion depending upon the local properties encountered along the path through the plume and the wavelength of the interacting incident wavefront.

In the context of detection, a rocket exhaust signature is regarded as that set of properties which may enable an observer to detect, locate and identify a missile. Millimetric, infra-red, visible and ultra-violet radiations from an exhaust afford opportunities for the passive detection and identification of a missile. Propellant chemical species contributing to a unique spectral pattern may well provide this identification. Equally, rocket exhausts often produce "Primary smoke" (originating in the motor) or "Secondary smoke" (plume condensates) which may also be detected by passive means. These form an observable contrast of exhaust smoke against background. Active detection is also possible where free electrons populating the turbulent flowfield act to present a radar cross section to an interrogating radar.

To reduce the risk of detection, the rocket exhaust signature must be minimised and some propel'ants offer distinct advantages over others in this respect. Double base propellants are often favoured where secondary smoke is likely to cause concern, without the formation of acid vapours in the plume, condensation occurs only in ambient conditions of extreme temperature and humidity. Impressive reductions in plume signature are witnessed when the exhaust is prevented from burning and, in certain cases, this can be achieved by using one of the double base range of propellants with a combustion suppressant added.

This suppression of burning, while reducing millimetric, infra-red, visible flame, and some ultra-violet radiations, must not be at the expense of increased smoke, itself part of the overall signature.

Over many years, measurements of plume emitted radiations, of microwave propagation and back scatter have been undertaken on ground level open sites and, where appropriate, in facilities simulating missile forward velocity and altitude. These facilities are expensive and cannot provide for an entire range of missiles or for every operational situation. Fully instrumented, carefully planned and executed flight measurements are the ideal answer, but again these are very expensive and can come only at the post design stage, well into the development programme. Problems found at this time are costly to remedy, with changes strongly resisted.

It is not difficult to see the attractions of reliable computational techniques for the prediction of flowfield properties where, early in system design studies, calculation of these properties and their effect on a proposed system can become available as input data to operational assessment. In addition, such plume modelling permits a rapid response to system problems and provides opportunities to make well informed predictions in situations where motors are not available, such as those of an adversary. Diagnostic value is also substantial when studying the effects of exhaust modifications, e.g. flame suppressants, signature reduction, etc.

Exhaust structures are complex. Working from computed combustion processes inside the motor and expansion of gases through the nozzle, an additional calculation develops the plume flowfield structure, a distribution in space of temperatures, velocities, pressures, chemical species concentrations and turbulence properties. The exhaust properties of interest, e.g. infra-red radiations, millimetric emissions, etc., are evaluated by selecting the appropriate application code to interface with the plume flowfield structure. This is simply stated, but is in reality a process posing a severe challenge to theoretical modelling skills as it attempts to describe the turbulent mixing of exhaust gases and surrounding ambient air streams, the many chemical reactions occurring in the exhaust and the gas dynamic features of shocks and recirculation.

A definitive description of the plume flowfield has yet to be established. Although modelling techniques continually improve, the stage has not been reached where they can be reliably used without experimental validation. The aims of a plume study group must be to perfect these techniques validated by experiments. Rocket exhaust technology is a field where research and project support can profitably proceed together in common programmes of prediction validation and ballistic trials.

The subjects of WG21 with strong emphasis on exhaust signatures were taken as a guide for the Lecture Series and in doing so it was recognised that two further subjects should be included: that of propulsion in the context of solid propellant rocket motors for tactical weapons, with low exhaust signatures as a major feature, and that of theoretical plume modelling which, from the foregoing, plays a prominent role in all aspects of rocket exhaust studies. Only in exhaust properties related to microwaves has propagation through the plume been considered. Traditionally and to this day, microwave radar systems have played an important role in missile guidance and tracking. With such prominence, propagation aspects merited inclusion. This is not to suggest that other propagation wavelengths from the electromagnetic spectrum are not used to good effect and instance as an example, infra-red laser beam guidance.

Launch site blast and contamination effects of the exhaust and aircraft engine ingestion of rocket exhaust products have not been included in the lecture programme.

PLUME PRIMARY SMOKE

J.C. Chastenet

S.N.P.E. Centre de Recherches du Bouchet
BP 2 . 91710 Vert-le-Petit . FRANCE

ABSTRACT

The exhaust from a solid propellant rocket motor usually contains condensed species. These particles, also called "Primary Smoke", are often prejudicial to missile detectability and to the guidance system . To avoid operational problems it is necessary to know and quantify the effects of particles on all aspects of missile deployment.

This paper first gives a brief description of the origin of the primary smoke. It continues with details of the interaction between particles and light as function of both particles and light properties (nature, size, wavelength, etc). The effects of particles on plume visibility , attenuation of an optical beam propagated through the plume and the contribution of particles on optical signatures of the plume are also described. Finally, various methods used in NATO countries to quantify the primary smoke effects are discussed.

1. INTRODUCTION

The exhaust from a solid propellant rocket motor are composed of gases and usually of particles or material that could condense during cooling of the combustion gases . This solid material creates, in the atmosphere, downstream from the nozzle a smoke cloud composed of small particles. This smoke is called Primary Smoke in opposition to smoke that could be generated, in particular climatic conditions, by the condensation of the water vapor contained in the exhaust and in the atmosphere.

Particles become important because they generally exist everywhere downstream of the nozzle and they remain a certain time. According to the quantity of particles created by the motor, this trail can be easily detected visually and can reveal the missile trajectory or the launch position from long distance. Also attenuation of laser guidance beams can occur during transmission through these considerable lengths of exhaust plume smoke.

Generally, primary smoke are prejudicial,but unavoidable, to missile detectability and to the guidance system . The objet of this paper is to give descriptions of (i) the origin of the primary smoke, (ii) their effects on plume visibility and transparency and (iii) various methods used in NATO countries to quantify the primary smoke effects.

This paper is a review of the chapter prepared by the french delegation of AGARD WG 21 [1].

2. ORIGIN OF PRIMARY SMOKE

Particles have a variety of origins. Propellant formulation is only one and among propellant ingredients, the main contributors to primary smoke are :

- Burning rate catalysts : Ferrocene compounds (catocene), lead oxides, lead salt (lead resorcinate), copper salts (copper chromate), iron oxides, etc

- Anti-instability additives : Zirconium carbide, zirconium oxide, silicon carbide, etc.

- Aluminium or other metals added to increase the thermodynamic performances

- Afterburning suppresant : Potassium salts (K_2SO_4)

This list is not exhaustive.

Thermodynamic computations have shown that these products, mostly metal compounds, are to be found in the exhaust as raw metal (Cu), hydroxides (KOH) or more often as oxides, chlorides or fluorides. Some refractory materials (mostly anti-instability additives) do not decompose in the combustion chamber and are discharged as particles through the nozzle.

Other than the propellant, all motor parts which are exposed to flame may pyrolise or ablate and generate smoke. The main contributors are :

- liner

- inhibitor

- thermal insulation

- nozzle

Their contribution can be significant, typically in the form of soot (carbon), silica and iron oxide, especially during and after burnout of the motor. Finally, the igniter may also play a significant role in the generation of primary smoke.

3. OPTICAL EFFECTS OF PRIMARY SMOKE

Particles or particle clouds interact with light in two ways, scattering and absorption. Scattering of the ambient light can make smoke highly visible and a major contribution to missile signature in the visible spectral range. Attenuation by smoke can interfere with a guidance system that should be used between the launching platform and the missile or its target.

These phenomena depend upon various factors :

- The size of the cloud or the optical path accros the cloud

- Particle concentration

- The optical wavelength

- The optical properties of particles defined by :

  - Their complex optical index

  - Their size and size distribution

  - Their shape, roughness, etc

The first two parameters are closely connected with motor performance and particularly the mass flow rate, thrust and combustion time.

Since it is difficult to describe arbitrary shaped particles, they are often considered to be spherical in calculations.

3.1 Interaction between light and particle

The interaction between light and a particle can be obtain by resolving Maxwell's equations with appropriate boundary conditions. The light scattering theory generally distinguishes three different cases over each of the following ranges :

- When the particle diameter is far smaller than the wavelength, the scattering is called Rayleigh scattering. Equal amounts of fluxes are scattered into the forward and backward hemisphere (fig. 1a) [2].

- When the particle diameter is greater than about one-tenth of the wavelength, the greater overall scattering and pattern complexity (fig. 1b and 1c) requires that the theory developped by Mie must be used. Although this theory is confined solely to isotropic spheres, it is customary to employ it even when the particles may be somewhat irregular in shape as those issuing from propellant.

- When the particle diameter is very large with respect to the wavelength, it is necessary to apply laws of geometrical optics.

The particles collected in rocket exhaust plumes with various mass flow rates show that equivalent diameters of non aggregate particles lay between 0.1 μm to 30.0 μm. A large number of small particles with diameters probably in the range 0.01 μm to 0.1 μm also exist, but they are difficult to quantify and their size precludes important scattering over the visible region of the electromagnetic spectrum (fig. 2).

Figures 3 and 4 show photographs of particles collected in plumes. The assumption of spherical particles can be well or less well verified.

In the visible, near or middle infrared, the important scattering is generally described by Mie's theory.

Following this theory, when a particle of complex index $m = n - ik$ is illuminated by unpolarized light, at the wavelength λ, represented by two electromagnetic vectors perpendicular and parrallel to the plane of observation (fig. 5) but having no coherent relationship, the scatterred light, in a direction making a angle θ with the direction of the incident light, consists of two incoherent components (indexed 1 and 2) such that the total angular intensity , at a distance d from the particle, is :

$$I(\theta) = I_0 \ \ (\frac{\lambda}{2\pi d})^2 \ \ \frac{i_1(\theta) + i_2(\theta)}{2}$$

where I_0 is the irradiance of the particle and i_1 and i_2 are the Mie functions, expressed by Riccati-Bessel functions and Legendre polynomials as functions of the dimensionless size parameter $\alpha = \frac{2\pi r}{\lambda}$ and $\beta = m\alpha$ where r is the radius of the particle (see [3] or [4] for more information).

Figure 6 gives typical relative variations of $\log i_1$ and $\log i_2$ versus θ for particles of Al_2O_3

and C (soot) when $\Psi = 45^o$ (defined in fig. 5).

Optical properties of particles are given in the form of dimensionless parameters. The intensity "intercepted" I_{ext} (e.g. not transmitted in the direction of the incident light) by the particle is proportional to i) the intensity of the incident light, ii) the section of the particle and is written :

$$I_{ext} = I_0 \pi r^2 Q_{ext}$$

The coefficient of proportionality Q_{ext} is called the extinction coefficient.
The total intensity scattered I_{sca} by the particle is also related to the same parameters :

$$I_{sca} = I_0 \pi r^2 Q_{sca}$$

and defines the scattering coefficient Q_{sca}. A part of the intensity of the incident light can be absorbed by the particle and is caracterised by the absorption coefficient Q_{abs} obtained from difference :

$$Q_{abs} = Q_{ext} - Q_{sca}$$

In the optical parameters of the particle, the absorption properties are charaterised by a complex refractive index ($k \neq 0$).

These coefficients can be calculated by Mie's theory, for exemple an expression of the scattering coefficient, for unpolarized light, is :

$$Q_{sca} = (\frac{\lambda}{2\pi r})^2 \int_0^\pi (i_1(\theta) + i_2(\theta)) \sin\theta d\theta$$

Typical variations of Q_{ext} are given in figure 7. An example of the influence of the imaginary part of the index on the scattering and extinction coefficient is given in figure 8.

3.2 Attenuation

The radiation intensity loss dI due to primary smoke is the consequence of the scattering and absorption by particles and can be expressed according to the Beer-Lambert-Bouguer law for monodispersion :

$$\frac{dI}{I} = -N\pi r^2 Q_{ext} dl$$

where r is radius of the particles, N the concentration of particles (number of particles/volume of mixture), Q_{ext} the extinction coefficient and dl optical path length.

With a constant exponent coefficient, the transmittance T_r can be written :

$$T_r = I/I_0 = e^{-\gamma_{ext} L}$$

where $\gamma_{ext} = N\pi r^2 Q_{ext}$ and L the total optical path length.

By replacing N by a function of Sauter mean diameter (Volume-to-surface) D_{32} and volume concentration of particles C_v (volume of particles /volume of mixture), this expression can by written :

$$T_r = \exp\left(-\frac{3Q_{ext}C_v L}{2D_{32}}\right)$$

Since the monochromatic beam crossing the plume scatters from particles of varying number density and size, the equation must be modified as :

$$\ln I/I_0 = -\int_0^L \int_0^\infty N(l,r)\pi r^2 Q_{ext}(r)drdl$$

where $N(l,r)dr$ represents the number of particles with radii between r and $r+dr$ per volume unit at the point l of the path.

The extinction coefficient can be predicted as shown in previous paragraph in the limit of single scattering.

Calculation of the plume flowfield permits the transmittance to interface with motor parameters such as mass flow rate or chamber pressure by substitution of the parameters C_v and l in the formula.

Figures 9 and 10 show the nature of particles in an original way. Two graphs, representing different wavelengths, show the particle mass fraction inducing a transmission factor of 95 % across a given particle cloud (optical path= 1 m, dilution = 5. 10^{-2}) as a function of particle size. The mass fraction of condensed materials in a given propellant plume at an equivalent dilution section must remain under these curves in order to obtain the specific transmission level.

Such representations show that :

- Carbone or soot are very absorbing, whatever the wavelength.

- When the particle radius is not too large, transmission is better in the infrared than in the visible region of the electromagnetic spectrum.

- Copper and lead have similar scattering features (but with respect to only the volumetric fraction, lead is more transparent than copper).

3.3 Particles emission

The scatterring properties of plume particles are at the origin of the signature in the visible range. Scattering can also produce a emission in the other part of the electromagnetic spectrum. It is true for both the U.V range and the I.R range where particles can scatter the radiation coming from the combustion chamber by the nozzle throat.

Furthermore, solid particles emit continuum radiation in approximate proportion to the particle concentration and the fourth power of their surface temperature obeying the Planck function. Specific details of size distribution and optical properties of the particles significantly affect this emission. So particles could product an emission in the UV, visible and I.R region of the electromagnetic spectrum especially in the hot part of the plume (afterburning region).

3.4 Smoke visibility

The term visibility is generally used to describe the possibility of detection by an observer without the aid of a auxiliary device. Quantitatively, visibility is expressed as a probability of detection for a given contrast between the objet (the plume) and its background, in this case the sky. Ignoring chromaticity factors as being less important than luminance contrast, the plume-background inherent contrast C_0 is defined by :

$$C_0 = \frac{L_p - L_b}{L_p}$$

where L_p and L_b are the luminances of the plume and the background with respect to a given observation point in a given wavelength band. The contrast tends to -1 for a ideal black objet and may have a large positive value if $L_p \gg L_b$.

Calculation of contrast involves a detailed knowledge of all radiation sources and transport functions (sunlight, diffuse skylight, diffuse light from ground, etc). The optical transmittance T_r appears in the contrast equation. For a given sunlight making a hypothetical angle of π with the direction of observation (setting sun in the back of observer, plume near the horizon), the transmittance appears for example in the plume luminance expression (assuming single scattering) :

$$L_{p,sun} = E_0 \frac{\gamma_{sc}(\pi)}{2\gamma_{ext}}(1 - T_r^2)$$

T_r being $exp(-\gamma_{ext}L)$, with L the plume dimension in the direction of observation and E_0 the irradiance.

Moreover transmission through the atmosphere affects the plume background contrast because of the angular scattering of environmental light towards the observer within his cone of vision.

The transmittance is so one of the more important parameters that permits to evaluate the visibility of the plume under specific environmental conditions.

A direct measurement is often preferred to numerical computation which depends upon a large number of ill defined parameters. This is particularly the case for optical indices found in the litterarure for pure compounds at room temperature. This is also the case for size distribution. These data applied to particles present in the rocket exhaust is highly questionable. Nevertheless, Mie's scattering calculations are useful for interpreting results of measurements and applying to the propellant optimization and other aspects of rocket motor design.

4. DESCRIPTION OF VARIOUS METHODS OF PRIMARY SMOKE ASSESSMENT USED IN NATO COUNTRIES

4.1 Opacity of primary smoke

Opacity is a physical parameter that can be directly measured and is independent of the optical environment.

Accurate and validated models for opacity prediction are still unavailable, but experimental techniques have been developed and used for years. From an engineer's viewpoint, transmission measurements is the only available way to assess primary smoke.

The U.S, the U.K., France , Germany and Italy are performing plume transmission measurements on static test, with the implicit assumption that the result of a comparison between two motors on a ground static test should be qualitatively unchanged in flight. An improvement in ground testing transparency results is interpreted as an improvement of transparency properties in flight. The methodology to translate transmission measurements from static tests into quantitative flight predictions is not yet available, but it could be developed with existing techniques.

Therefore, the practical application of plume transparency measurements on static firings is the comparison of propellants or motors, one with another. In some cases, the

purpose of these measurements is limited to a specific study - like the improvement of motor with respect to primary smokes, or the assessment of new ingredients in a propellant formulation; the experimental procedure can be defined on a case by case basis. For more general purposes, such as having a quantitative method for comparing the smoke properties of broad range of solid rocket propellant formulations, a widely accepted, standardised procedure is required.

In the following paragraphs more details will be given on the instrumentation, experimental procedures and interpretation of measurements used in the U.S.A [5], the U.K. [6] and in France [7] for the assessment of primary smoke transparency.

Three methods are curently used to determine the opacity of primary smoke during test firings :

- Firings in a closed chamber (U.S. Army Signature Characterization Facility (S.C.F.)) (fig. 11).

- Firings in a "smoke tunnel" (U.K. Royal Ordnance Smoke Tunnel (fig. 12), French SNPE "Fumimètre" (fig. 13)).

- Free jet firings (U.K Wyre Forest facility (fig. 14) and french SNPE "banc opacimétrique" (fig. 15, 16) for example). It seems to be the most widely used type of procedure in the NATO (excepted USA).

The three techniques do not share strictly common usage. Free jet transmission measurement is a technique adapted to evaluate the complete motor (propellant + inhibitor + etc). With some caution it can also be used to rank propellant and inhibitors formulations. The same use applies to smoke tunnel tests but with more restrictions on the maximum thrust of the rocket motor. On the other hand, the S.C.F. chamber is a facility which primarily assesses propellant formulation. Because of test duration and environmental control, this facility is better suited to carry more sophisticated experiments on primary smoke than those of transmission measurements : e.g. transmission spectrum, particle sizing and may be particle scattering characteristics.

4.1.1 Source and detector

The wavelengths of interest are in the $0.4 \mu m$ to $14. \mu m$ region, the most studied in the visible range (human eye response). The transmissometer source could be a wide spectrum lamp (France), a tungsten-halogen lamp (U.S.) or quartz halogen lamp (U.K.) with a suitable detector, silicon cell or radiometer equiped with a suitable filter (photopic or narrow band filter).

For specific studies, the source can be a optical laser ($1.06 \mu m$, $0.63 \mu m$, $10.6 \mu m$). In France, the transmisson at $0.63 \mu m$ (He-Ne laser) is considered as a good estimation of transmission in the visible range.

The system using the halogen lamp may be preferable because it avoids the necessity for precise alignment between source and detector, thereby being less succeptible to vibrational disturbances during the motor firing.

Current systems employ continuous sources but a chopped source is recommended to counteract interference from scattered ambient light falling on the receiver.

The detector should have a high frequency response (like a silicon photodiode) which can record the rapid fluctuations of the smoke transparency and a spectral response in the visible and near IR which spans the range of source wavelengths.

The energy recorded by the transmissometer involves both the direct flux and a small portion of the forward-scattered flux. The latter comes from a spatial volume, usually of double-conical shape, which surrounds the source to receiver axis and is defined by the angular divergence of the source beam, the angular field of view of the receiver and the source to receiver distance. These factors, and the receiver aperture area determine the total scattered flux received. Typically receivers with a small angular field of view ($< 10^o$) and

apertures of a few centimeters are employed in measuring the nominally direct transmittance [8].

Calibration is generally done by intercepting the beam with opaque material (Transmission=0%), various neutral density filters and no filter (100 %). The delay between calibration and the firing should be minimized.

4.1.2 Measurements paths

In general both transverse and axial measurements are performed, each of which has its associated advantages and disadvantages.

Transverse measurements are particularly well suited to propellant ranking, inhibitor assessment or the study of additive effects. They are indeed reproducible, constant with time, providing the burning surface area does not vary during the firing period and tests conducted near the nozzle exit not affected by secondary smoke. Furthermore, the limited volume of cloud viewed transversely gives an opportunity to undertake complementary optical measurements. These measurements are carried out at an angle of $\pi/2$ rad to the motor axis. The transmissometer axis must cross the motor axis at a position dowstream of the afterburning flame. This can be achieved using a constant distance for motors up to a certain thrust level or by maintaining a set distance downstream of the afterburning flame. The relatively short path length associated with transverse measurements will give transmissions of 90 % - 100 % with low thrust, low smoke, motors. At these smoke levels transmission measurements may not be sensitive enough to discriminate between motors. In such cases the path length can be increased by use of front silvered mirrors but great care must be taken to ensure that mirror surfaces remains clean and that vibration of the mirrors is prevented during firings.

Axial measurements are realistic for smoke assessment in a missile guidance context and allow discrimination between similar products

that produce near transparent smoke. These measurements are performed over a long path length with the transmissometer beam inclined at a shallow angle (typically 0.07 rad) to the motor axis and intercepting the plume axis at a set distance downstream of the motor again beyond any possible afterburning flame and usually at the position of the transverse beam.

4.1.3 Motor characteristics

In the U.S. Army MICOM S.C.F a 70 g $case$ bonded motor (50.8 mm diameter × 50.8 mm long, center perforated, 6.4 mm web) with a smokless igniter and no inhibitor is used. A typical smokeless pyrogen igniter contains one to three grains of N5 double base propellant. Tests have shown that this amount is undetectable in the S.C.F.

In U.K, low thrust motors (up to 400 N) can be fired in the Royal Ordnance (RO(S)) smoke tunnel. Higher thrust motor are fired in an open range facility. To compare propellants within a range of very different burning rates, 1500 N thrust motors of 8 s burn type with pyrogen (smokeless) igniters are normally employed. The thrust is adjusted by varying the diameter for end-burning grains. Adjustment in grain length can similarly produce a constant burning time. However, this is considered less important provided that reasonable burning time is exceeded (at least 5 s). For inhibition development and quality control, a standard test charge is used. This is a 150 mm cased SCB bi-propellant charge consisting of boost and sustain propellants having burning times of 6 s and 20 s respectively at thrust levels of order of 1000 N and 300 N. This charge can be produced in the required inhibitor system and, when fired in an insulated heavyweight test motor, provides information on inhibitor smoke, at boost and sustain burning rates and at those of transition from boost to sustain. For propellant ingredient trial the test charge is produced in a "smokeless" inhibitor system. Using the range of propellant burning rates available at RO(S)

this charge can have a burning time ranging from 4 s to 80 s at thrust level of 3 kN falling to some 150 N using the lowest burning rate propellants.

In France, transmission measurements are primary not used to identify propellants for classification, but are limited to the task of studying specific propulsion systems. The firing facilities "fumimètre" and "banc opacimétrique" function primarily for the assessment of smoke produced by inhibitors. For such work, motors with end burning grains (diameter 90 mm) of identical propellant formulation are fired.
They are now also used to compare different propellant formulations and to assess the effect of including additives. These firings employ motors with radial burning grains with a constant burning surface and a identical inhibitor; the motor thrust is typically between 2500 N and 5000 N.

4.1.4 Motor position

In free jet measurements, the height of the motor axis from the ground should be such that there is no interference between the smoke plume and the ground up to the position of the transverse transmissometer. Typical distances of 1.3 meters have been used.

4.1.5 Climatic conditions during firing

Firings should not be carried out in conditions of mist or rain. Conditions of temperatures and humidity should be such as to preclude the formation of secondary smoke.

The much longer path length involved in the axial measurements permits better discrimination between low smoke motors. However, as the path length increases so does the influence of atmospheric conditions.

Recommended maximum crosswind speed is 1. ms^{-1} for axial measurements and 3. ms^{-1} for transverse measurements..

The results of smoke measurement trials performed on open ranges will always be influenced by atmospheric conditions. It is therefore recommended that control rounds of a known smoke level are included wherever possible and that successive motors are fired as quickly as possible to minimise any changes which may take place during the duration of the trial.

4.1.6 Interpretation of the transmission measurements

For transmission in free jet (fig. 17 - 18), measurements are time average having before eliminated the unsteady part of the record at ignition and at the end of the firing. That remaining usually maintains a steady mean level making the average value representative of existing smoke conditions.

For transmission in closed chamber (fig. 19), the steady-state transmission measurements must be done after full mixing of the exhaust products and air. The plateau value is interpreted as a charateristic of the primary smoke generated by the formulation. To ensure a good estimation of this plateau value, transmission should be recorded over a period of time significally (typically 10 times) longer than the mixing time. In the SCF chamber, the mixing time is approximately 5 s to 30 s and measurements must be recorded over 300 s.

4.2 Smoke visibility

From an operational viewpoint, specifications for primary smoke visibility should be defined in terms of whether or not a missile will be visible to an enemy observer. Because this factor is sensitive to the operational environment, one of a limited number of "typical" or "worst-case" environnmental conditions should be defined for the missile, specifying the solar flux, the background, the atmospheric conditions or any parameter likely to affect the visibility.

Following the US Army Methodology, visibility can be defined in terms of the probability of missiles detection by unaided human eye. The major physical factors determining visibility are the size and the shape of the plume, its contrast with the background and transmissivity of the atmosphere; they can be derived from modelling plume flow and scattering of solar flux. Detection probability is related to natural variation in human eye response between individuals.

Many well, and less well supported assumptions have to be made in the process. The main weakness is thought to be the optical properties of particles.

The theory of interactions between light and particles is approached in the paragraph 3.1. It solves the Maxwell's equations for the interaction between a monochromatic plane wave and a spherical particle. It addresses both scattering and absorption by particles, but requires the knowledge of ill-known parameters such as the particles size and their optical index. Furthermore the assumption of spherical particle shape has to be made.

An experimental approach has been attempted in the U.K., with various methods of measurement. It included measuring the intensity of the reflected component from high intensity sources impinging on a smoke cloud and photographs of contrast scenes through the cloud, either at the time of firing or from cine or video records. All of these methods can provide useful information and differing smoke levels can be detected. However no system can provide all of the required information.

More complete information can be found elsewhere [9] [10].

Smoke visibility is an area where the development of measuring techniques is required. It may suffice here to emphasize that a complete and accurate assessment methodology is unfortunately not available but could be developed using present state of the art techniques.

4.3 Particles sizing measurement

Determining the size distribution of plume particles is difficult, complicated by the problem of never being certain that all particules have been measured or that the distribution contains those important particles of interest. In general the largest 10 % of particules represent 90 % of the mass.

In U.S Army Micom S.C.F, particles measurements are frequently obtained by using a particle analyser system in the range 0.3 μm to greater than 10. μm.

In France, collectings of particles are made using a particle collector. After the firing. the samples are analysed by electron microscop and X-rays diffraction system. But in fact, these measurements are only used qualitatively.

Caution is necessary when using calculated particle size distribution for an other purpose than which they were intended for. For example, in rocket motor performance calculations in which the effect of particles on delivered specific impulse is of interest, only the larger particles, with most of the mass and drag, are of interest. Models that gives this distribution are accurate enough [11] without regard to the many smaller particles that may be present. Such a distribution would be totally unsuited for calculating UV or visible light scattering [9], and might be inadequate for accurate determinations of infrared scattering as well since , for scattering radiation, the important particle sizes are comparable to the irradiating wavelength.

5. CONCLUSION

Primary smoke effects depend on motor characteristics (thrust, mass flow rate), motor conception (propellant, inhibitor, nozzle, etc) and a lot of ill-known particles parameters (quantity, nature, size, shape, optical properties, etc) but also on operational requirements and ambient properties (sunlight, background,etc). It is extremely difficult to define

standard conditions to characterise their effects. Each problem needs specific considerations.

Typically, the quantification of primary smoke effect is obtain by transmission measurements. Some theoretical considerations, generally based on Mie calculation, can help in the interpretations of results.

Standard tests have been described and chosen by AGARD WG 21 in order to provide a flexible and relatively inexpensive method which would allow to obtaining quantitative results characterizing primary smoke. It is hoped that similar procedures to those described above will form a base that may be adopted as standard among NATO countries.

Acknowledgements

The author thanks MM Ajdari and Souletis who actively participated in the AGARD-PEP WG 21 and permitted the elaboration of this chapter under the auspices of the French Ministry of Defence (STPE).

References

[1] AGARD Advisory Report No. 287,
Terminology and Assessment Method of Solid Propellant Rocket Exhaust Signature Report of the Propulsion and Energetics Panel Working Group 21,
AGARD-AR-287, to be publised

[2] McCartney, E.J,
Optics of the Atmosphere,
John Wiley & Sons, New York, 1976

[3] Kerker, M.,
The Scattering of Light and other Electromagnetic Radiation,
Ed Academic Press, New York 1963

[4] Van de Hulst,H.,
Light Scattering by Small Particles,
John Wiley and Sons, New York, 1957

[5] Thorn, L.B. and Pickley, L.W,
Propulsion Signature Characterization in the Army SCF,
Technical Report RD-PR-86-1, US Army MICOM, Dec. 1895

[6] Asthon, R.M and Taylor, F.L,
Instrument Techniques for Measurements of Rocket Motor Plume Characteristics,
Technical Report 88/58, Royal Ordnance plc, England

[7] Davenas, A.
Solid Rocket Propulsion Technology,
Pergamon Press, 1993

[8] Hodkinson, J.R.
The Optical Measurement of Aerosols,
Aerosol Science, C.N Davies, Ed Academic Press, New York, 1966

[9] Victor,A.C, and Breil,S.H.,
A Simple Method for Predicting Rocket Exhaust Plume Smoke Visibility,
J. Spacecraft and Rockets, Vol. 14, No. 9, pp 526-533, Sept. 1977

[10] Victor,A.C,
Effects of Multiple Scattering on Rocket Exhaust Plume Smoke Visibility,
J. Spacecraft and Rockets, Vol. 26, No. 4, pp 274-278, July-Aug 1989

[11] AGARD Advisory Report No. 230,
Propulsion and Energetics Panel Working Group 17 on Performance of rocket Motors with Metallized Propellants,
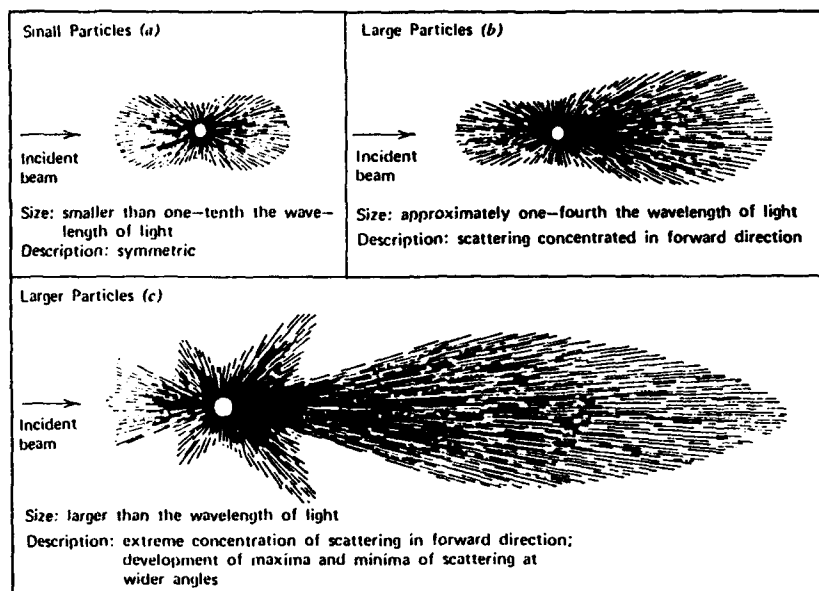AGARD-AR-230, September 1986

Figure 1: Angular pattern of scattered intensity from particules of three sizes : (a) Small particles, (b) large particles, c) larger particles [2]
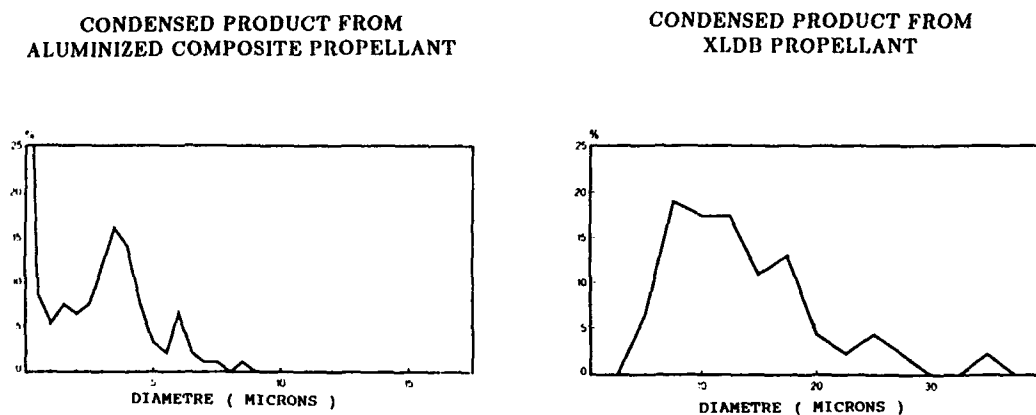

Figure 2: Particle Size Distribution of Condensed Products Collected in a Rocket Exhaust Plume. Analysed by Electro Microscope with X-rays Diffraction System. (SNPE)
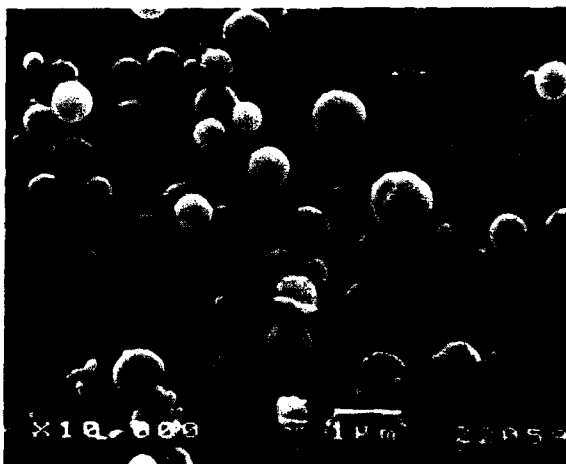
Figure 3: Particle Collected in a Rocket Exhaust Plume. (XLDB Propellant with zirconium carbide)

Figure 4: Particle Collected in a Rocket Exhaust Plume (XLDB Propellant with aluminium)
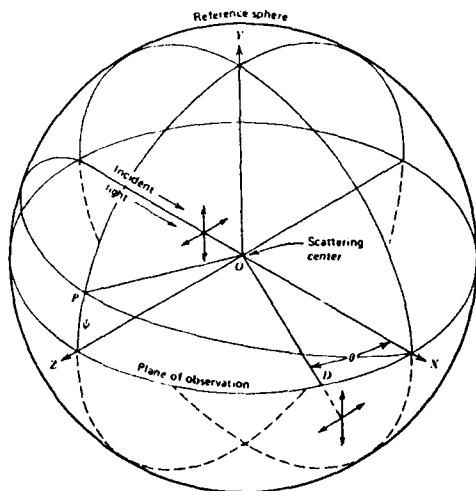
Figure 5: Geometry of Mie scattering. The two vectors correspond to incident unpolarized light. Line OD is the direction of observation and θ is the angle of observation. When the incident light is polarized, its electric vector is assumed to lie in plane POX, at angle Ψ to the plane of observation [2].
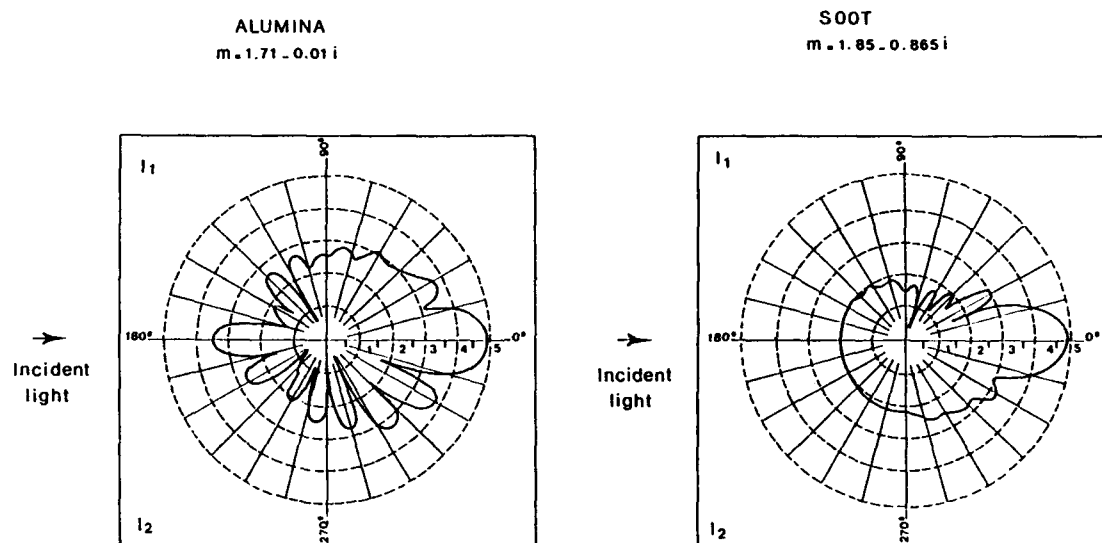
ALUMINA

m = 1.71 - 0.01 i

SOOT

m = 1.85 - 0.865 i

Figure 6: Variation of $\log i_1$ and $\log i_2$ versus θ for particles of Al_2O_3 and C (soot) when $\Psi = 45^0$, $r = 1\mu m$ and $\lambda = 0.7\mu m$.
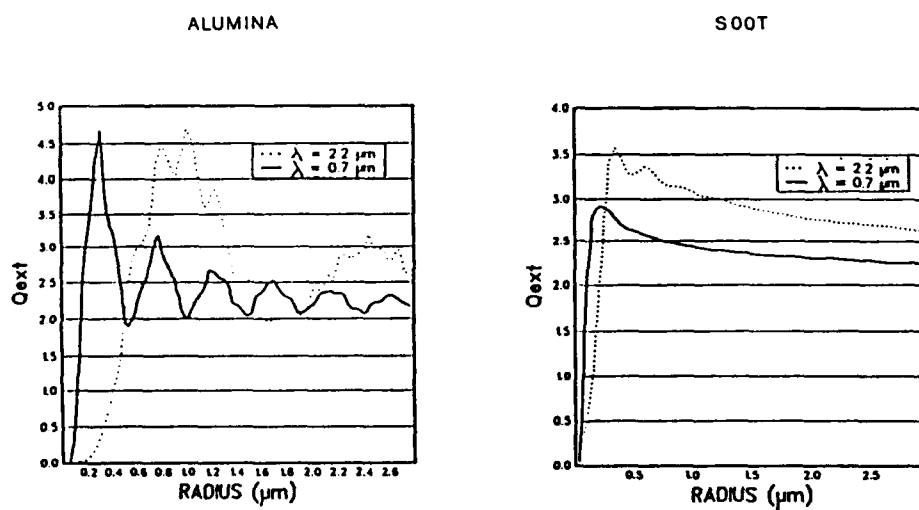
ALUMINA

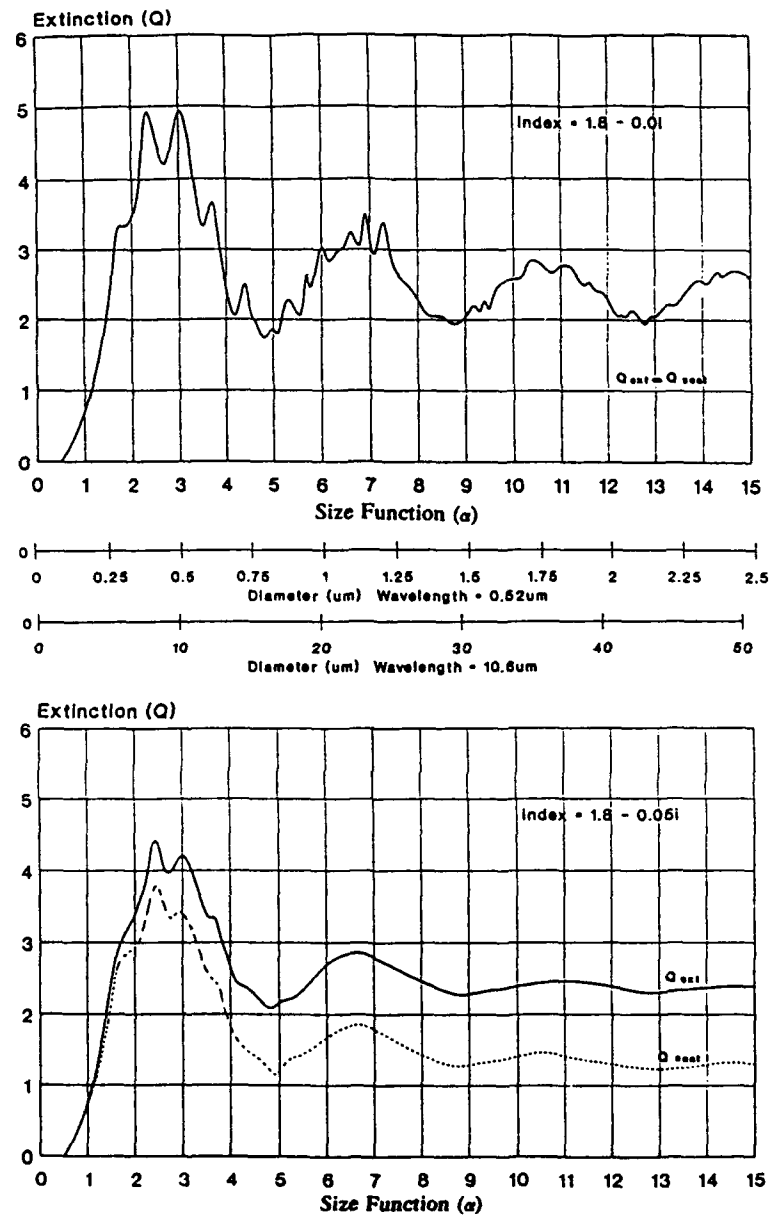SOOT

Figure 7: Typical variation of Q_{ext}

Figure 8: Example of the influence of the imaginary part of the index on the scattering and extinction coefficients. Size function $\alpha = \pi D/\lambda$ (UK Royal Ordnance).
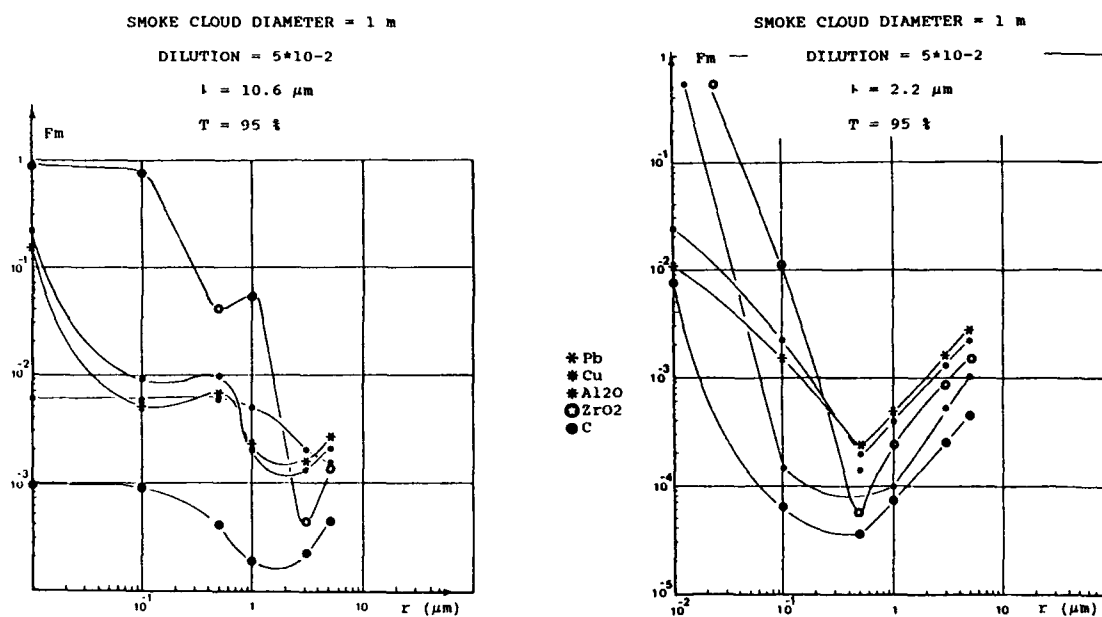
Figure 9: Mass fraction (Fm) of particles inducing a transmission factor of 95 % across a given particle cloud versus the particle size.
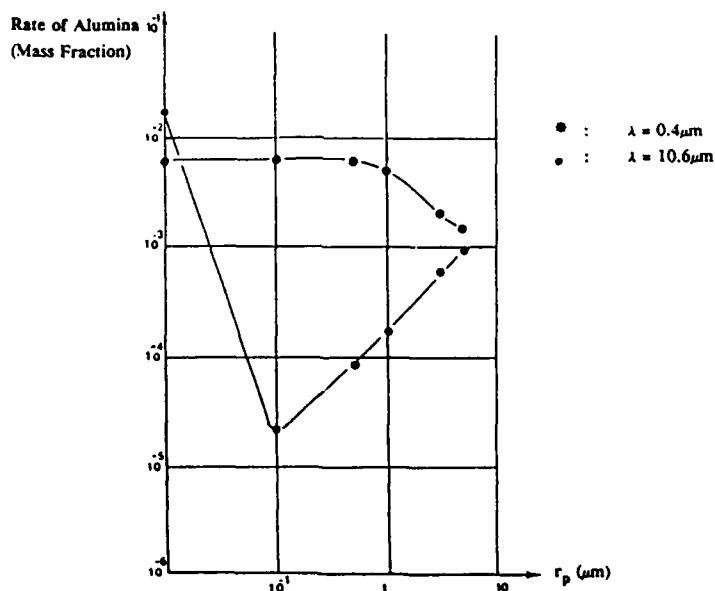

Figure 10: Maximum rate of alumina (mass fraction) in the combustion products for the following specifications : smoke cloud diameter : 1 m, dilution : 0.05, transmission : 95 %.
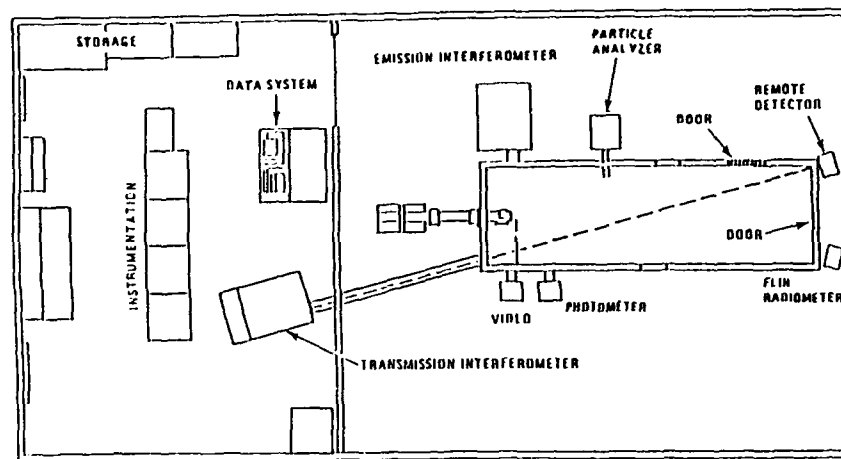
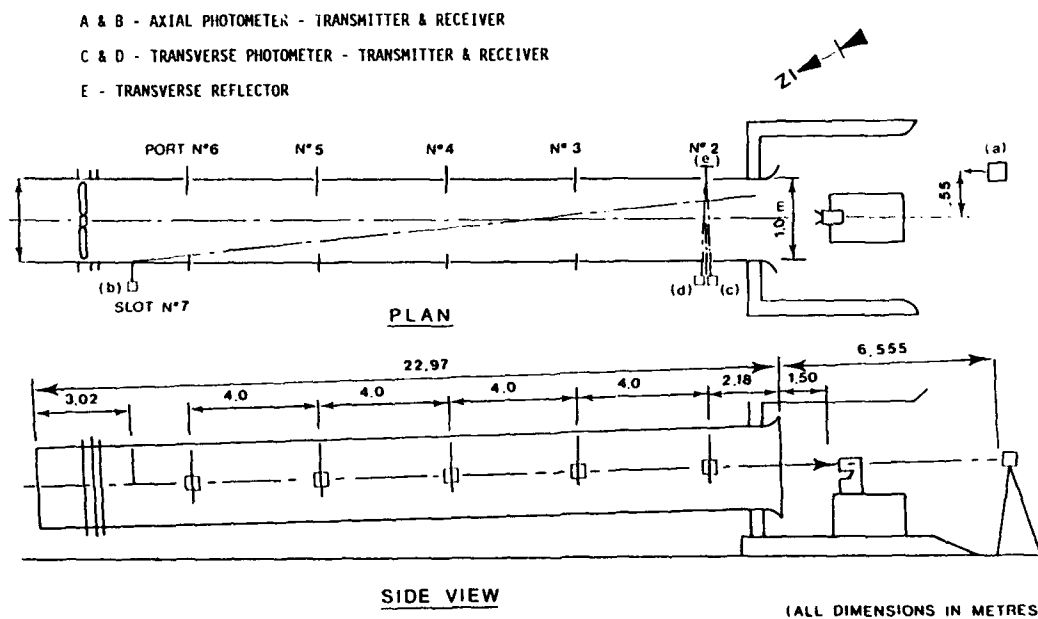Figure 11: US Army Signature Characterization Facility (S.C.F.)

A & B - AXIAL PHOTOMETER - TRANSMITTER & RECEIVER

C & D - TRANSVERSE PHOTOMETER - TRANSMITTER & RECEIVER

E - TRANSVERSE REFLECTOR

PLAN

SIDE VIEW

(ALL DIMENSIONS IN METRES)

Figure 12: UK (RO) R7 Smoke Tunnel

Figure 13: French SNPE "fumimètre"

A - CINE 50 PPS
B - AXIAL PHOTOMETER LAMP
C - IR-VISIBLE LIGHT-SOURCE
D - MOTOR
E - STILLS CAMERA
F - VIDEO
G - IR CAMERA
H - VISIBLE LIGHT EMISSION
I - TRANSVERSE PHOTOMETER
J - TRANSVERSE PHOTOMETER LAMP
K - AXIAL IR TRANSMISSION
  - AXIAL VISIBLE LIGHT
  - SMOKE REFLECTANCE
L - AXIAL PHOTOMETER
M - CINE 50 PPS
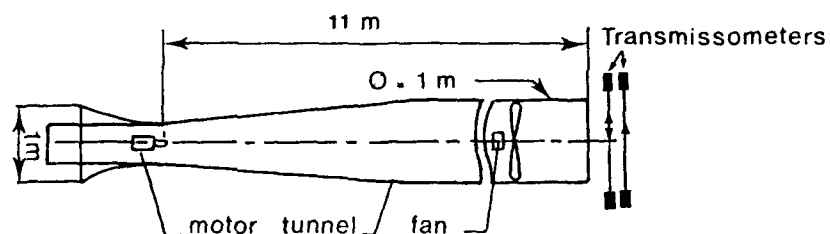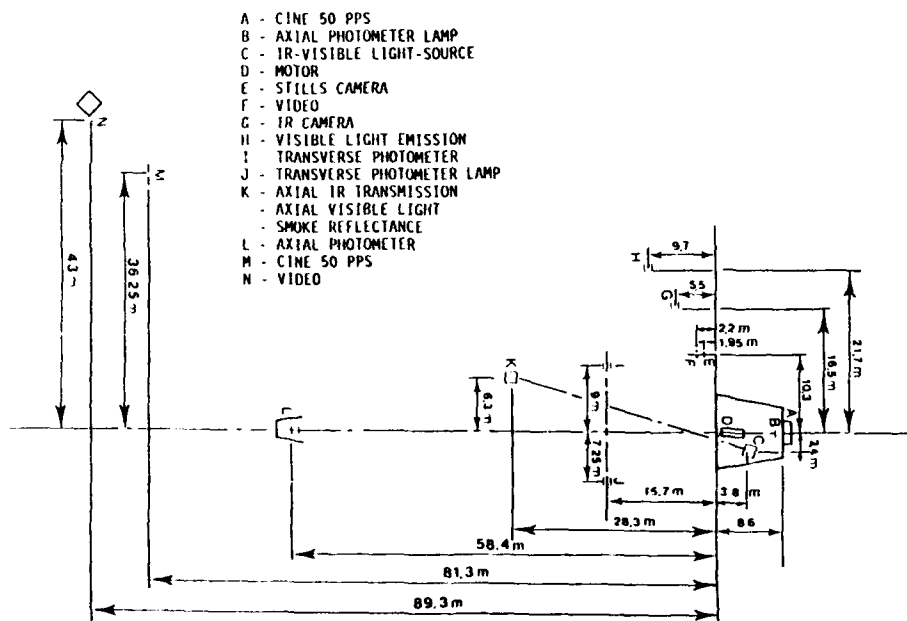N - VIDEO

Figure 14: Free Jet Firing. Plume Instrumentation Wyre Forest (UK)
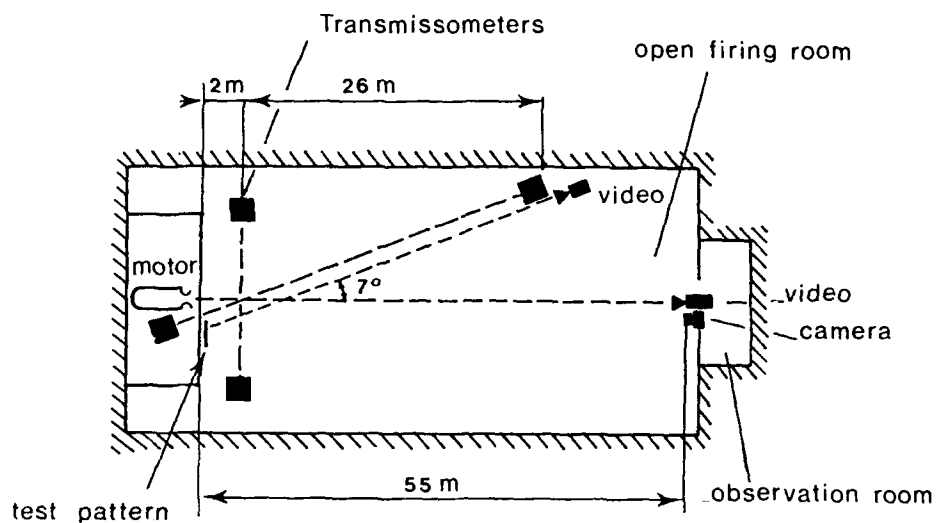
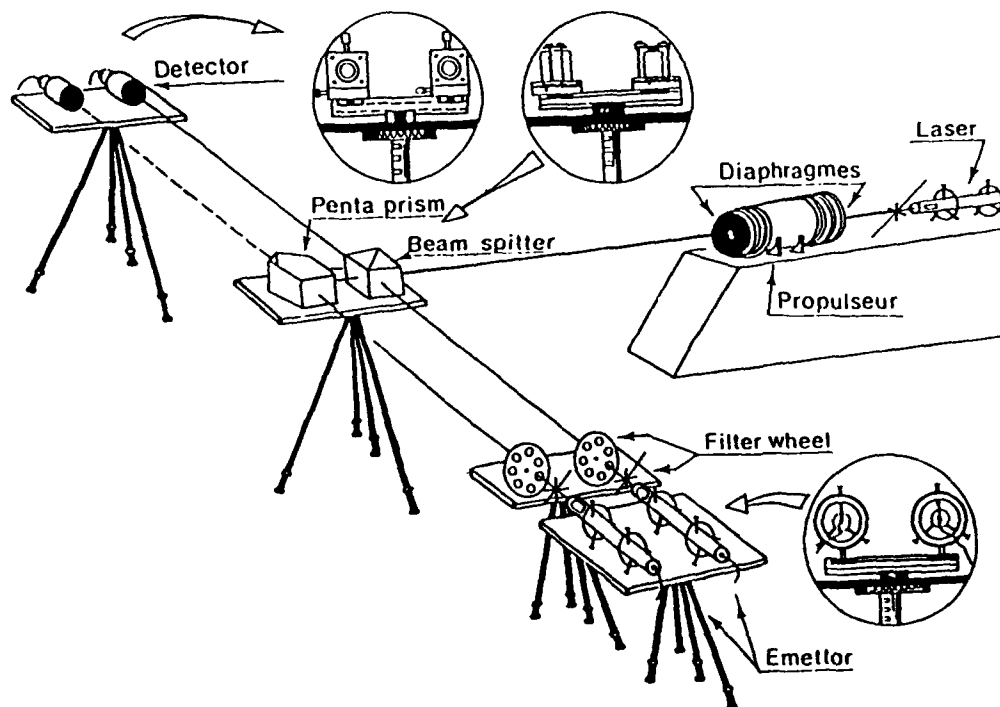**Figure 15: Free Jet Firing. French SNPE "Banc opacimétrique"**

Figure 16: Free Jet Firing. Transmission at 0.63 μm
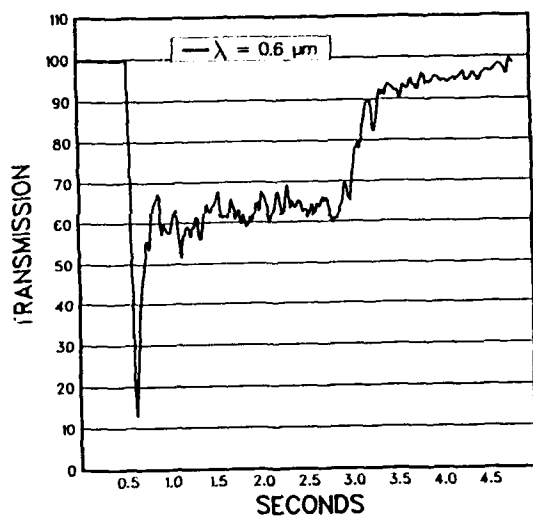
Figure 17: Example of transmission plot ($\lambda = 0.63\mu m$) Free Jet Friring, Transverse measurement (SNPE)
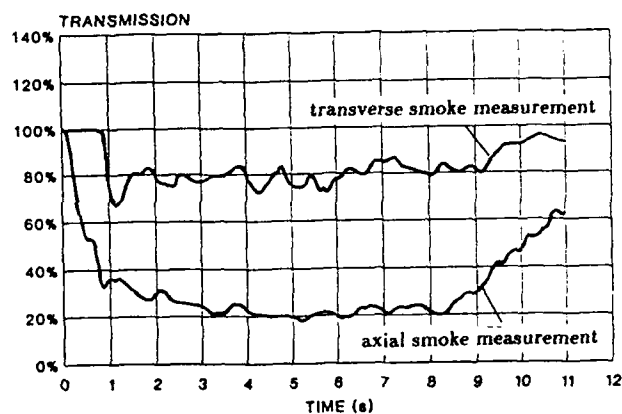

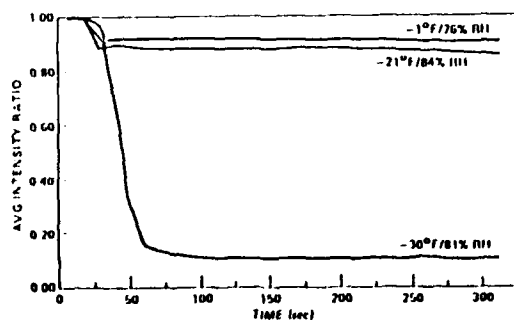Figure 19: FZZ Visible Transmittance (US SCF)

Figure 18: Typical results for transverse and axial transmission (UK (RO) Smoke tunnel)

LES FUMÉES PRIMAIRES

J.C. Chastenet

S.N.P.E. Centre de Recherches du Bouchet
BP 2 . 91710 Vert-le-Petit . FRANCE

RÉSUMÉ

Les produits éjectés par un moteur à propergol solide contiennent souvent des espèces condensées. Ces particules, aussi appelées "fumées primaires", sont souvent préjudiciables à la discrétion et au guidage du missile. Pour éviter des problèmes opérationnels, il est nécessaire de connaître et de quantifier les effets de ces particules dans toutes les conditions d'usage d'un missile.

Ce papier donne premièrement une rapide description de l'origine des fumées primaires. Il continue par le détail des intéractions entre les particules et la lumière en fonction des caractéristiques de la lumière et des particules (nature, taille, longueur d'onde, etc). Les effets des particules sur la visibilité du jet, l'atténuation d'un rayon optique à travers le jet et la contribution des particules aux différentes signatures optiques du jet sont aussi décrites. Finalement, différentes méthodes utilisées dans les pays de l'OTAN pour quantifier les effets des fumées primaires sont commentées.

1. INTRODUCTION

Les produits éjectés par un moteur à propergol solide sont composés de gaz et souvent de particules ou de produits susceptibles de se condenser lors de leur refroidissement. Ces matériaux solides créent, dans l'atmosphère à l'arrière de la tuyère, un nuage composé de petites particules. Ces fumées sont appelées fumées primaires en opposition aux fumées qui peuvent être générées, dans des conditions climatiques particulières, par la condensation de la vapeur d'eau contenue dans les produits de combustion et dans l'atmosphère.

Ces particules ont un rôle important parce qu'elles existent partout en aval de la tuyère et subsistent un certain temps. Selon la quantité de particules générées par le moteur, ce panache peut être facilement détecté visuellement et peut révéler la trajectoire du missile ou la position de la plate-forme de tir sur de longues distances. De plus l'atténuation d'un faisceau laser de guidage peut devenir importante sur de grands trajets à travers ces fumées.

Généralement, les fumées primaires sont préjudiciables à la discrétion et au guidage du missile cependant elles sont aussi inévitables. Le but de ce papier est de donner une description (i) des origines des fumées primaires, (ii) de leurs effets sur la visibilité et la transparence du jet et (iii) des différentes méthodes utilisées dans les pays de l'OTAN pour quantifier les effets de ces fumées.

Ce papier est une révision du chapitre préparé par la délégation française du WG 21 AGARD [1].

2. ORIGINE DES FUMÉES PRIMAIRES

Les particules ont de nombreuses origines. La composition du propergol n'est qu'une de ces origines et parmi les différents ingrédients du propergol les principales sources de fumées primaires sont :

- Les catalyseurs de combustion : composés ferrocéniques (catocène), oxydes de plomb, sels de plomb (résorcylate de plomb), sels de cuivre (chromite de cuivre), oxydes de fer, etc

- Les additifs anti-instabilités : carbure de zirconium , oxyde de zirconium, carbure de silicium, etc.

- L'aluminium ou autres métaux ajoutés pour accroître les performances thermodynamiques

- Les additifs anti-lueurs : sels de potassium (K_2SO_4)

Cette liste n'est pas exhaustive.

Des calculs thermodynamiques montrent que ces produits, principalement des composés métalliques, se retrouvent dans les produits de combustion sous la forme de métaux purs (Cu), d'hydroxydes (KOH) ou le plus souvent sous forme d'oxydes, chlorures ou fluorures. Quelques matériaux réfractaires (principalement des additifs anti-instabilités) ne se décomposent pas dans la chambre de combustion et restent sous forme de particules.

En dehors du propergol, toutes les parties du moteur exposées à la chaleur sont susceptibles de se pyrolyser ou de s'ablater et donc de générer des particules. Parmi les principales sources, on peut citer :

- les lieurs

- les inhibiteurs

- les protections thermiques

- les matériaux de tuyère

Leurs contributions peuvent être très significatives, typiquement sous forme de suie (carbone), de silice et d'oxyde de fer, particulièrement lors de l'allumage et de l'extinction du moteur. Enfin, l'allumeur peut jouer un rôle important dans la génération de fumées primaires.

3. LES EFFETS OPTIQUES DES FUMÉES PRIMAIRES

Une particule, ou un nuage de particules, intéragit avec la lumière de deux façons, par diffusion et par absorption. La diffusion de la lumière ambiante peut rendre le nuage très visible et devenir une contribution majeure de la signature du missile dans le domaine visible. L'atténuation par les fumées peut interférer avec le système de guidage pouvant être utilisé entre la plate-forme de tir et le missile ou sa cible.

Ces phénomènes dépendent de plusieurs facteurs :

- La taille du nuage ou la longueur du trajet optique à travers le nuage

- la concentration en particules sur ce trajet

- La longueur d'onde du rayonnement

- Les propriétés optiques des particules définies par :

  - Leur indice optique complexe

  - Leur taille et leur répartition granulométrique

  - Leur état (forme, rugosité, etc)

Le deux premiers facteurs sont intimement reliés aux caractéristiques du moteur et en particulier au débit, à la poussée et au temps de combustion.

Comme il est très difficile de décrire des formes quelconques, les particules sont souvent considérées sphériques dans les calculs.

3.1 Intéraction entre la lumière et une particule

Les intéractions entre un rayonnement et une particule peuvent être obtenues en résolvant les équations de Maxwell associées aux conditions aux limites appropriées. La théorie de la diffusion distingue généralement trois cas :

- Quand le diamètre de la particule est très petit devant la longueur d'onde, la diffusion est appelée diffusion Rayleigh. Des flux égaux sont diffusés dans les hémisphères avant et arrière (fig. 1a) [2].

- Quand le diamètre de la particule est plus grand qu'environ un dixième de la longueur d'onde, l'augmentation de la complexité de la polaire de diffusion (fig. 1b and 1c) nécessite l'utilisation de la théorie développée par Mie. Bien que cette théorie soit limitée à des sphères isotropiques, il est habituel de l'utiliser même pour des particules de forme irrégulière comme celles issues de la combustion des propergols solides.

- Quand le diamètre de la particule est très grand devant la longueur d'onde, on utilise les lois de l'optique géométrique.

Les particules récupérées dans les panaches de moteurs fusées de différents débits montrent que le diamètre équivalent des particules non aglomérées est compris entre $0.1\ \mu m$ et $30.0\ \mu m$. Un grand nombre de petites particules dont le diamètre est probablement compris entre $0.01\ \mu m$ et $0.1\ \mu m$ existe, mais elles sont difficilement quantifiables. Leur taille laisse présager un rôle diffusif important dans le domaine visible (fig. 2).

Les figures 3 et 4 montrent des photographies de particules récupérées dans des jets. On remarquera que l'hypothèse de particule sphérique est plus ou moins bien vérifiée.

Dans le domaine visible, le proche et le moyen infrarouge, les effets majeurs de la diffusion sont généralement décrits par la théorie de Mie.

D'après cette théorie, quand une particule d'indice complexe $m = n - ik$ est illuminée par un rayonnement non polarisé, de longueur d'onde λ, représenté par deux vecteurs électromagnétiques perpendiculaire et parallèle au plan d'observation (fig. 5) mais n'ayant pas de relation cohérente, le rayonnement diffusé, dans une direction faisant un angle θ avec la direction du rayonnement incident, est constitué de deux composantes incohérentes (d'indices 1 et 2) telle que l'intensité angulaire totale, à une distance d de la particule, est :

$$I(\theta) = I_0 \ \left(\frac{\lambda}{2\pi d}\right)^2 \ \frac{i_1(\theta) + i_2(\theta)}{2}$$

où I_0 est l'intensité du rayonnement éclairant la particule et i_1 et i_2 sont les fonctions de Mie, s'exprimant à l'aide des fonctions de Riccati-Bessel et des polynômes de Legendre en fonction du paramètre de taille sans dimension $\alpha = \frac{2\pi r}{\lambda}$ et de $\beta = m\alpha$ où r est le rayon de la particule (voir [3] ou [4] pour plus de détails).

La figure 6 donne des variations relatives typiques de $\log i_1$ and $\log i_2$ en fonction de θ pour des particules Al_2O_3 et C (suie) quand $\Psi = 45°$ (défini sur la fig. 5).

Les caractéristiques optiques des particules sont souvent données sous forme de paramètres sans dimensions. L'intensité du rayonnement "intercepté" I_{ext} (i.e non transmis dans la direction du rayonnement incident) par la particule est proportionnelle à i) l'intensité du rayonnement incident, ii) la section de la particule et s'écrit :

$$I_{ext} = I_0 \pi r^2 Q_{ext}$$

Le coefficient de proportionalité Q_{ext} est appelé coefficient d'extinction.
L'intensité totale diffusée I_{sca} par la particule s'exprime le la même façon :

$$I_{sca} = I_0 \pi r^2 Q_{sca}$$

et définit le coefficient de diffusion Q_{sca}. Une partie du rayonnement incident peut être absorbée par la particule et est alors caractérisée par le coefficient d'absorption Q_{abs} obtenu par différence :

$$Q_{abs} = Q_{ext} - Q_{sca}$$

Les propriétés d'absorption de la particule sont caractérisées par une partie imaginaire de l'indice complexe non nulle ($k \neq 0$).

Ces coefficients peuvent être calculés par la théorie de Mie, par exemple l'expression du coefficient de diffusion , pour un rayonnement non polarisé, est :

$$Q_{sca} = (\frac{\lambda}{2\pi r})^2 \int_0^\pi (i_1(\theta) + i_2(\theta) \sin\theta d\theta$$

Des variations typiques de Q_{ext} sont données sur la figure 7. Un exemple de l'influence de la partie imaginaire de l'indice optique de la particule sur les coefficients de diffusion et d'extinction est donné sur la figure 8.

3.2 Atténuation

La perte d'intensité du rayonnement incident dI due aux fumées primaires est une conséquence de la diffusion et de l'absorption du rayonnement par les particules. Il s'exprime, d'après la loi de Beer-Lambert-Bouguer, pour un nuage de particules sphériques identiques par :

$$\frac{dI}{I} = -N\pi r^2 Q_{ext} dl$$

où r est le rayon des particules, N la concentration en particules (nombre de particules/unité de volume de mélange), Q_{ext} le coefficient d'extinction et dl la longueur du trajet optique.

En considérant des coefficients constants le long du trajet optique, le coefficient de transmission T_r s'écrit :

$$T_r = I/I_0 = e^{-\gamma_{ext} L}$$

où $\gamma_{ext} = N\pi r^2 Q_{ext}$ et L la longueur totale du trajet optique.

En remplaçant N par son expression en fonction du diamètre moyen de Sauter (Volume à surface) D_{32} et la concentration volumique en particules C_v (volume de particules/volume de mélange), cette expression s'écrit :

$$T_r = \exp(-\frac{3Q_{ext}C_v L}{2D_{32}})$$

En fait, la concentration et la répartition des particules varient le long du trajet optique. L'expression doit donc être modifiée et prend la forme :

$$\ln I/I_0 = -\int_0^L \int_0^\infty N(l,r)\pi r^2 Q_{ext}(r) dr dl$$

où $N(l,r)dr$ représente le nombre de particules dont le rayon est compris entre r et $r + dr$ par unité de volume au point courant l du trajet optique.

Le coefficient d'extinction peut être prédit dans la limite de la diffusion simple par les méthodes explicitées dans le paragraphe précédent.

Le calcul de la structure aérodymanique du jet permet de déterminer la transmission en fonction des caractéristiques du moteur comme le débit ou la pression de chambre en substituant les valeurs de C_v et de l.

Les figures 9 and 10 montrent la nature des particules de façon originale. Deux graphes, relatifs à différentes longueurs d'onde, donnent la fraction massique de particules produisant une facteur de transmission de 95 % à travers une nuage donné de particules (longueur optique= 1 m, dilution massique = 5. 10^{-2}) en fonction de la taille des particules. La fraction massique de condensé pour un propergol donné et pour un facteur de dilution équivalent doit rester sous la courbe pour ne pas dépasser le niveau d'opacité spécifié.

Une telle représentation montrent que :

- Le carbone ou les suies sont très absorbantes, quelle que soit la longueur d'onde.

- Quand le rayon des particules n'est pas trop important, la transmission est meilleure dans le domaine infrarouge que dans le domaine visible.

- Le cuivre et le plomb ont des propriétés diffusives analogues (mais à même fraction volumique, le plomb est plus transparent).

3.3 Émission des particules

Les propriétés diffusives des particules sont à l'origine de la signature du panache dans le domaine visible. La diffusion peut aussi avoir un effet sur d'autres domaines du spectre électromagnétique. Cela est vrai dans le domaine ultraviolet et dans le domaine infrarouge où le rayonnement issu de la chambre de combustion à travers le col de la tuyère peut être diffusé et semble provenir du jet.

De plus, les particules émettent un rayonnement continu approximativement proportionnel à la concentration en particules et à la puissance quatre de leur température de surface selon la loi de Planck. Les répartitions granulométriques et les propriétés optiques particulières des particules peuvent cependant modifier cette émission. Les particules peuvent donc aussi générer un rayonnement propre dans le domaine U.V et I.R particulièrement dans les zones chaudes du jet (zone de postcombustion).

3.4 Visibilité des fumées

Le terme visibilité est généralement employé pour décrire la possibilité de détection d'un observateur sans l'aide de détecteur auxiliaire. Quantitativement, la visibilité s'exprime comme une probabilité de détection dans des conditions particulières de contraste entre l'objet (le jet du missile) et le fond, généralement le ciel dans ce cas. En considérant les facteurs chromatiques moins importants que le contraste en luminance, le contraste intrinsèque du jet sur le fond C_0 peut être défini par :

$$C_0 = \frac{L_j - L_f}{L_f}$$

où L_j and L_f sont les luminances du jet et du fond pour un point d'observation et un domaine spectral donnés. Le contraste tend vers -1 pour objet parfaitement transparent et peut prendre n'importe quelle valeur positive si $L_j \gg L_f$.

La détermination du contraste demande une connaisance détaillée de toutes les sources de rayonnement (lumière solaire, lumière diffusée par le ciel, lumière diffusée par le sol, etc). Le coefficient de transmission T_r apparaît dans l'expression du contraste. Pour un rayonnement solaire donné faisant un angle de π radians avec la direction d'observation (plaçant le ciel derrière l'observateur et le jet proche de l'horizon), la transmission apparaît dans l'expression de la luminance du jet (dans l'hypothèse de la diffusion simple) :

$$L_{j,soleil} = E_0 \frac{\gamma_{dif}(\pi)}{2\gamma_{ext}}(1 - T_r^2)$$

T_r étant $exp(-\gamma_{ext}L)$, avec L la dimension du jet dans la direction d'observation et E_0 l'éclairement.

De plus, la transmission à travers l'atmosphère peut modifier le contraste par diffusion de la lumière ambiante dans le cône de vision de l'observateur.

La transparence est donc l'un des paramètres les plus importants pour évaluer la visibilité d'un jet dans des conditions d'environnement spécifiques.

Une mesure directe est souvent préférable à des simulations numériques faisant appel à de nombreuses données mal connues. C'est particulièrement le cas des indices complexes donnés dans la littérature qui correspondent à des corps purs à température ambiante. C'est aussi le cas des répartitions granulométriques. Ces données appliquées aux particules présentent dans le jet de propulseur à propergol solide sont sujettes à caution. Quoiqu'il en soit, les calculs de diffusion selon la théorie de Mie sont très utiles pour interpréter les mesures et effectuer des optimisations de la composition du propergol et de tous les autres paramètres du moteur.

4. DESCRIPTION DE DIFFÉRENTES MÉTHODES DE CARACTÉRISATION DES FUMÉES PRIMAIRES UTILISÉES DANS LES PAYS DE L'OTAN

4.1 Opacité des fumées primaires

L'opacité est le paramètre physique qui peut être directement mesuré et est indépendant de l'environnement optique.

Des modèles viables et précis pour prédire l'opacité ne sont pas encore opérationnels, mais des techniques expérimentales ont été développées et sont utilisées depuis des années. Du point de vue de l'ingénieur, la mesure de transmission est la seule voie valable pour caractériser des fumées primaires.

Les U.S.A, le R.U., la France , l'Allemagne et l'Italie effectuent couramment des mesures de transmission au banc statique, en supposant implicitement que le résultats de la comparaison de deux moteurs au banc statique et aussi valable dans des conditions de vol. Une amélioration de la transparence au banc est interprétée comme une amélioration de la transparence en vol. Une méthodologie permettant de traduire les mesures de transparence en tirs statiques en des prédictions quantitatives en vol n'est pas encore disponible, mais peut être développée à partir des techniques existantes.

Pour ces raisons, l'application pratique des mesures de transparence en tir statique est limitée à la comparaison de propergols ou de moteurs entre eux. Dans certains cas, le but de ces mesures est limité à des études spécifiques - comme la réduction des fumées primaires générées par un moteur donné, ou l'évaluation des effets de nouveaux additifs dans un propergol- et la procédure expérimentale doit être définie au cas par cas. Pour des études plus générales, comme par exemple disposer d'une méthode quantitative de comparaison des propergols solides, en termes de fumées primaires, pour une large gamme de formulations,une procédure standardisée et

largement reconnue est nécessaire.

Dans les paragraphes suivants, des détails sont donnés quant à l'instrumentation, les procédures expérimentales et les méthodes d'interprétations des mesures utilisées aux U.S.A [5], au R.U [6] et en France [7] pour l'évaluation de la transparence des fumées primaires.

Trois méthodes sont couramment utilisées pour déterminer l'opacité des fumées primaires durant des tirs:

- Tir en chambre fermée (Dispositif de caractérisation de signature de l'U.S. Army - "U.S. Army Signature Characterization Facility (S.C.F.)") (fig. 11).

- Tir dans un "tunnel à fumées" (Tunnel à fumées du Royal Ordnance (R.U) (fig. 12), "Fumimètre" SNPE (France) (fig. 13)).

- Tir en jet libre (Dispositif de Wyre Forest (R.U) (fig. 14), "banc opacimétrique" SNPE (France) (fig. 15, 16)). Cette méthode est, a priori, la plus utilisée par les pays de l'OTAN (USA exceptés).

Ces trois techniques n'ont pas exactement le même usage. La mesure de transmission lors d'un tir en jet libre est une technique adaptée à l' évaluation d'un moteur complet (propergol + inhibiteur + etc). Avec quelques précautions elle peut être utilisée pour classifier les propergols et les inhibiteurs. Le même type d'application peut être traitée au tunnel à fumées avec tout de même des limitations quant au niveau maximal de poussée admissible. D'un autre coté les mesures en chambre fermée sont initialement prévues pour évaluer les formulations des propergols. La durée du test, le contrôle de l'environnement font que ce dispositif est propice à des caractérisations des fumées primaires plus sophistiquées que de simples mesures de transmission : i.e. mesure de spectre de transmission, mesure de taille de particules et éventuellement mesures directes des caractéristiques optiques des particules.

4.1.1 Source de rayonnement et détecteur

Les longueurs d'onde d'interêts vont de 0.4 μm à 14. μm, la plupart des études concernent le domaine visible (réponse de l'oeil humain). Le transmissomètre doit être constitué d'une source de rayonnement adaptée - une lampe à large spectre (France), une lampe halogène tungstène (U.S.A) ou une lampe halogène à quartz (R.U) - et d'un détecteur idoine - détecteur silicium ou radiomètre équipé de filtre (filtre photopique ou monochromatique).

Pour des études spécifiques, la source peut être un laser (1.06 μm, 0.63 μm, 10.6 μm). En France, la transmisson à 0.63 μm (Laser He-Ne) est considérée comme une bonne estimation de la transmission dans le domaine visible.

Un dispositif utilisant une lampe halogène est préférable car il ne nécessite pas d'effectuer un alignement rigoureux de la source et du détecteur.De plus il est moins sensible au vibration générées par le fonctionnement du moteur.

Les systèmes actuels emploient généralement des sources continues mais il est recommendé de chopper ce signal afin de corriger la mesure du rayonnement ambiant et du rayonnement propre du jet.

Le détecteur doit avoir un temps de réponse très court (diodes silicium) pour enregistrer les fluctuations rapides de la transparence des fumées et une réponse spectrale dans le visible et le proche infrarouge correspondant à la source.

L'énergie reçue par le détecteur du transmissomètre provient du flux direct et d'une partie du flux diffusé. Ce dernier provient d'un volume, généralement doublement cônique, qui entoure l'axe source-détecteur et est défini par la divergence angulaire du rayonnement issu de la source, par le champ angulaire du détecteur et la distance de la source au récepteur. Ces paramètres et l'ouverture du récepteur déterminent le flux reçu total. Typiquement, des récepteurs à faible champ angulaire ($< 10°$) et des ouvertures de quelques centimètres sont utilisés pour mesurer la transmission directe [8].

La calibration est généralement obtenue par interception du faisceau par un matériau opaque (Transmission=0%), différents filtres neutres et sans filtre (100 %). Le temps entre le tir et la calibration doit être minimisé.

4.1.2 Trajet optique de mesure

En général des mesures transverses et longitudinales sont effectuées, chacune a ses avantages et ses inconvénients.

Les mesures transverses sont particulièrement adaptées au classement des propergols, à l'évaluation des inhibiteurs et l'étude des additifs. Elles sont, entre autre, reproductibles, constantes au cours du tir pour peu que la surface en combustion ne varie pas et que la mesure de transmission soit effectuée à proximité de la tuyère pour ne pas être affectée par les éventuelles fumées secondaires. De plus, le faible volume du jet pris en compte laisse de la place sur le site pour effectuer des mesures complémentaires. Ces mesures sont effectuées perpendiculairement à l'axe du jet. L'axe du transmissomètre doit couper l'axe du jet derrière la zone de post-combustion. Ceci peut être respecté en effectuant la mesure à une distance fixe pour des moteurs dont la poussée est inférieure à un seuil donné ou en effectuant la mesure à un distance fixe de la zone de post-combustion. Le trajet optique relativement court lors des mesures transverses donne des transmissions de 90 % - 100 % pour des moteurs de faibles poussées et peu générateurs de fumée. Ces niveaux de transmission ne permettent pas toujours de discriminer les moteurs. Le trajet optique peut être augmenté en utilisant des miroirs cependant il faut s'assurer que les miroirs restent propres et ne sont pas sensibles aux vibrations durant le tir.

Les mesures longitudinales sont plus réalistes pour l'évaluation des fumées dans un contexte de guidage du missile et permettent une discrimination pour des moteurs générant des fumées de transparences analogues. Elles

sont, par contre, beaucoup plus sensibles aux conditions ambiantes (vent, humidité). Ces mesures sont réalisées avec un transmissomètre légèrement incliné par rapport à l'axe du moteur (typiquement 0.07 *rad*) et coupant cet axe derrière la flamme de post-combustion si possible à la même distance que la mesure transverse.

4.1.3 Caractéristiques du moteur

Les moteurs utilisés pour le dispositif U.S. Army MICOM S.C.F sont des chargements moulés-collés de 70 g (diamètre 50.8 mm , longueur 50.8 mm, canal central cylindrique, épaisseur 6.4 mm) allumés à l'aide d'un allumeur ne générant pas de fumée, aucun inhibiteur n'est utilisé. Un allumeur discret typique contient de un à trois grains de propergol double base N5. Des tests ont montré que cette quantité n'était pas détectable dans ce dispositif.

Au R.U, les moteurs de faibles poussées (jusqu'à 400 N) peuvent être tirés au tunnel à fumées du Royal Ordnance. Les moteurs de plus fortes poussées sont tirés dans un dispositif ouvert. Pour comparer les propergols sur une large gamme de vitesse de combustion, des moteurs de 1500 N de poussée et de 8 s de temps de combustion initiés à l'aide d'allumeur pyrogénique (discret) sont normalement utilisés. La poussée est ajustée en faisant varier le diamètre du bloc plein. L'ajustement de la longueur du bloc permet de régler le temps de combustion bien que cela soit moins important pourvu que la durée de combustion soit suffisante (au moins 5 s). Pour le développement d'inhibiteurs et le contrôle, un bloc test standard est utilisé. Il s'agit d'un bloc de 150 mm à deux régimes - accélération et croisière - de poussées respectives de 1000 N et 300 N et de temps de combustion respectifs de 6 s et 20 s. Ce bloc peut être produit avec l'inhibiteur voulu et permet d'obtenir une évaluation des fumées générées par l'inhibiteur pendant les phases d'accélération, de croisière et lors de la transition entre les deux phases. Pour la classifi-

cation des propergols, un système d'inhibage "discret" est utilisé. Ce dispositif permet de tester des propergols ayant des temps de combustion compris entre 4 s et 80 s et des poussées de 3 kN à 150 N.

En France, les mesures de transmission n'ont pas été développées pour la classification des propergols, mais dans le cadre d'études de systèmes propulsifs spécifiques. Les dispositifs "fumimètre" et "banc opacimétrique" ont été développés pour l'évaluation des fumées générées par les inhibiteurs. Les blocs utilisés sont des blocs pleins (90 mm de diamètre) d'une composition donnée.

Ils sont maintenant utilisés pour comparer les propergols et étudier les effets des additifs. Ces tirs emploient des blocs à canal central de surface de combustion constante et de même inhibiteur. La poussée est généralement comprise entre 2500 N et 5000 N.

4.1.4 Position du moteur

Pour les mesures en jet libre, la hauteur de l'axe du moteur au sol doit être telle qu'il n'y ait pas d'interférence entre le jet et le sol au point de mesure de la transmission transverse. Une hauteur de 1.3 m est généralement considérée.

4.1.5 Conditions climatiques lors du tir

Les tirs ne doivent pas être effectués par temps de pluie ou de brouillard. Les conditions de température et d'humidité doivent être telles qu'il n'y ait pas de formation de fumées secondaires.

Un grand trajet optique pour les mesures longitudinales permet une meilleure discrimination des moteurs peu générateurs de fumées. Cependant, un long trajet optique peut être facilement influencé par les conditions climatiques et rend les mesures moins reproductibles.

Un vent transversal de 1. ms^{-1} est une

valeur maximale pour les mesures longitudinales, 3. ms^{-1} pour les mesures transversales.

Les résultats des mesures en champ libre sont toujours influencés par les conditions climatiques. Il est recommandé d'effectuer un contrôle à un niveau de fumée connu à chaque fois que cela est possible et de tirer les différents moteurs aussi rapidement que possible pour éviter tout changement pouvant survenir pendant la durée de l'essai.

4.1.6 Interprétation des mesures de transmission

Pour la transmission en jet libre (fig. 17 - 18), les mesures sont moyennées en éliminant les parties transitoires correspondant à l'allumage et à l'extinction du bloc. La partie restante doit montrer un niveau pratiquement constant faisant de la valeur moyenne une quantité représentative des fumées existantes.

Pour les mesures en chambre fermée (fig. 19), le niveau de transmission doit être pris après un mélange complet des gaz de combustion et de l'air. La valeur plateau est interprétée comme une grandeur caractéristique des fumées primaires générées par la formulation. Pour assurer une bonne estimation de cette valeur plateau, la transmission est enregistrée pendant une durée significativement plus longue que le temps de mélange (typiquement 10 fois). Dans la chambre SCF, le temps de mélange est de l'ordre de 5 s à 30 s et les mesures sont acquises sur une durée de 300 s.

4.2 Visibilité des fumées

Du point de vue opérationnel, les spécifications de visibilité des fumées primaires sont définies en terme de détectabilité visuelle du missile par l'ennemi. Puisque cette caractéristique dépend des conditions opérationnelles, un nombre limité de conditions d'environnement "typiques" ou "extrèmes" doivent être définies pour le missile, précisant le rayonnement solaire, l'arrière plan, les conditions atmosphériques et tous les autres paramètres affectant la visibilité.

D'après la méthodologie américaine, la visibilité peut être définie en terme de probabilité de détection par un oeil humain. Les principaux facteurs déterminant la visibilité sont la taille et la forme du panache, son contraste sur l'arrière plan et la transmission de l'atmosphère. Ces grandeurs sont accessibles par la modélisation du panache et de la diffusion solaire. La probabilité de détection est aussi reliée à la disparité naturelle des réponses des yeux humains d'un individu à un autre.

Des hypothèses plus ou moins bien justifiées sont nécessaires à cette évaluation. Les plus hasardeuses concernent probablement les propriétés optiques des particules.

La théorie de l'intéraction du rayonnement et des particules est abordée dans le paragraphe 3.1. Elle concerne la résolution des équations de Maxwell pour les intéractions entre une onde plane monochromatique et une particule sphérique. Elle fournit à la fois les caractéristiques d'absorption et de diffusion du rayonnement par les particules mais nécessite la connaissance de paramètres mal connus tels que la taille et l'indice complexe de la particule. De plus, l'hypothèse d'une particule sphérique doit être faite.

Une approche expérimentale a été tentée au R.U à l'aide de différentes techniques de mesures. Elle incluait des mesures de la composante réfléchie de l'intensité d'une forte source éclairant le panache de fumées et des mesures de contraste à partir d'enregistrements photographiques ou vidéo. Toutes ces techniques fournissent des informations utiles et permettent de distinguer des niveaux de fumées détectables. Cependant aucun dispositif ne permet d'obtenir toutes les informations désirées.

De plus amples informations peuvent être trouvées dans les références [9] [10].

La visibilité des fumées est un domaine où le développement de techniques de mesure est encore nécessaire. Il suffit d'insiter ici sur le fait qu'aucune méthodologie n'est malheureusement disponible mais peut être développée à partir de l'état-de-l'art actuel.

4.3 Mesure de taille de particules

Déterminer la répartition granulométrique des particules présentes est très difficile, complexité accrue encore par le fait que l'on ne peut jamais être certain que toutes les particules intéressantes ont été analysées ou que la distribution obtenue englobe toutes les particules intéressantes. En général, 10 % des particules (les plus grosses) représentent 90 % de la masse totale.

Dans le dispositif "S.C.F" de l'U.S Army, les mesures sur les particules sont obtenues par un système d'analyse couvrant la gamme de 0.3 μm à plus de 10. μm.

En France, l'analyse de particules se fait en utilisant un récupérateur de particules dans le panache. Après le tir, les échantillons sont analysés par microscopie électronique et spectromérie X. Mais en fait ces mesures ne sont considérées que qualitativement.

Un avertissement est nécessaire quant à l'utilisation de distributions granulométriques dans un but différent de celui pour lequel l'analyse a été faite. Par exemple, pour le calcul des performances d'un moteur fusée dans lequel on s'intéresse aux effets des particules sur l'impulsion spécifique délivrée, seules les grosse particules, qui ont la plus grande trainée et la plus grande masse, sont intéressantes. Des modèles donnant de telles répartitions sont suffisamment précis pour ce propos [11] mais ne considérent pas les petites particules qui peuvent être présentes. De telles distributions sont totalement insuffisantes pour le calcul de la diffusion du rayonnement U.V et visible [9], et peuvent aussi être inadéquates pour la diffusion dans le domaine I.R. Pour ces phénomènes de diffu-

sion, la taille des particules importantes est de l'ordre grandeur de la longueur d'onde.

5. CONCLUSION

Les effets des fumées primaires dépendent des caractéristiques du moteur (poussée, débit massique), de la conception du moteur (propergol, inhibiteur, tuyère, etc), de beaucoup de paramètres mal connus relatifs aux particules (quantité, nature, taille, forme, propriétés optiques, etc) mais aussi des caractéristiques opérationnelles et des conditions ambiantes (soleil, arrière plan, etc). Il est extrêmement difficile de définir des conditions standards pour caractériser tous leurs effets. Chaque problème nécessite des considérations spécifiques.

En pratique, la quantification des effets des fumées primaires est obtenue par des mesures de transmission. Des considérations théoriques, généralement basées sur la théorie de Mie, peuvent aider à l'interprétation des résultats.

Des tests standards ont été décrits et choisis par le AGARD WG 21 dans le but de fournir des méthodes simples, relativement bon marché , permettant d'obtenir des résultats quantitatifs caractéristiques des fumées primaires. Il est souhaité que des procédures similaires à celles décrites ici forment une base qui puisse être adoptée comme un standard parmi les pays de l'OTAN.

Remerciements

Références

[1] AGARD Advisory Report No. 287,
Terminology and Assessment Method of

Solid Propellant Rocket Exhaust Signature Report of the Propulsion and Energetics Panel Working Group 21, AGARD-AR-287, à paraître

[2] McCartney, E.J,
Optics of the Atmosphere,
John Wiley & Sons, New York, 1976

[3] Kerker, M.,
The Scattering of Light and other Electromagnetic Radiation,
Ed Academic Press, New York 1963

[4] Van de Hulst,H.,
Light Scattering by Small Particles,
John Wiley and Sons, New York, 1957

[5] Thorn, L.B. and Pickley, L.W,
Propulsion Signature Characterization in the Army SCF,
Technical Report RD-PR-86-1, US Army MICOM, Dec. 1895

[6] Asthon, R.M and Taylor, F.L,
Instrument Techniques for Measurements of Rocket Motor Plume Characteristics,
Technical Report 88/58, Royal Ordnance plc, England

[7] Davenas, A.
Technologies des propergols solides,
Ed Masson, 1989

[8] Hodkinson, J.R.
The Optical Measurement of Aerosols,
Aerosol Science, C.N Davies, Ed Academic Press, New York, 1966

[9] Victor,A.C, and Breil,S.H.,
A Simple Method for Predicting Rocket Exhaust Plume Smoke Visibility,
J. Spacecraft and Rockets, Vol. 14, No. 9, pp 526-533, Sept. 1977

[10] Victor,A.C,
Effects of Multiple Scattering on Rocket Exhaust Plume Smoke Visibility,
J. Spacecraft and Rockets, Vol. 26, No. 4, pp 274-278, July-Aug 1989

[11] AGARD Advisory Report No. 230,
Propulsion and Energetics Panel Working Group 17 on Performance of rocket Motors with Metallized Propellants,
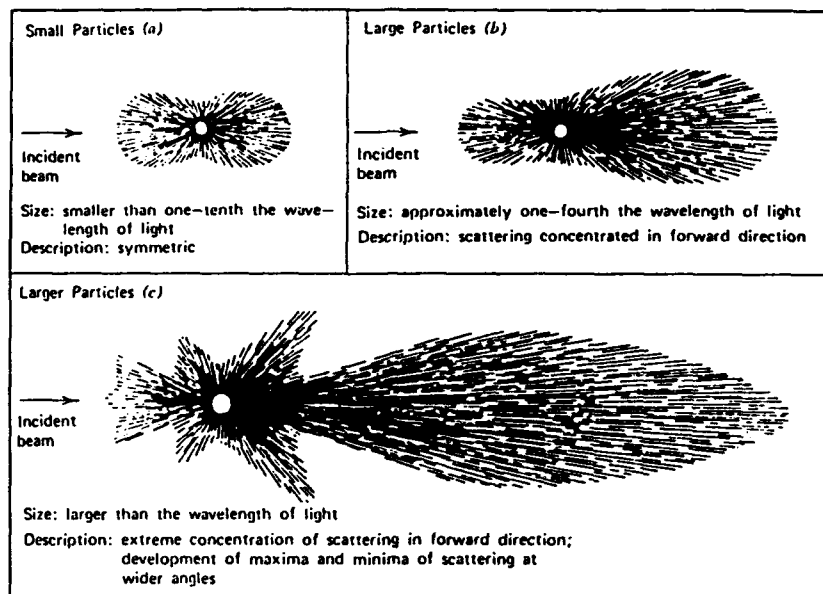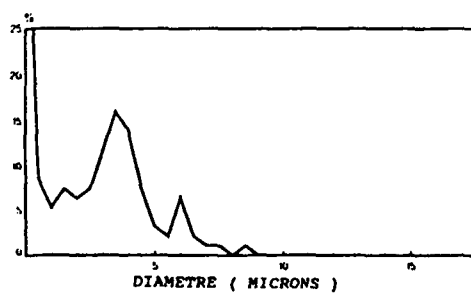AGARD-AR-230, September 1986

Figure 1 : Répartition angulaire de l'intensité diffusée par des particules de trois tailles :
(a) petites particules, (b) particules moyennes, (c) grosses particules [2]

Particules issues d'un propergol composite aluminisé

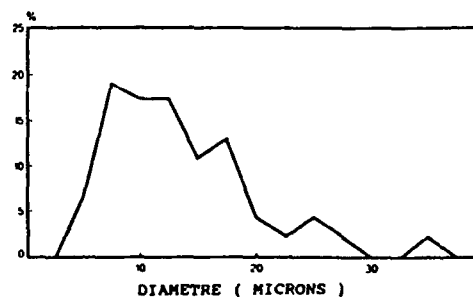Particules issues d'un propergol XLDB

Figure 2: Répartition granulométrique des produits condensés récupérés dans un jet de propulseur analysés par microscopie électronique et spectrométrie X. (SNPE-France)
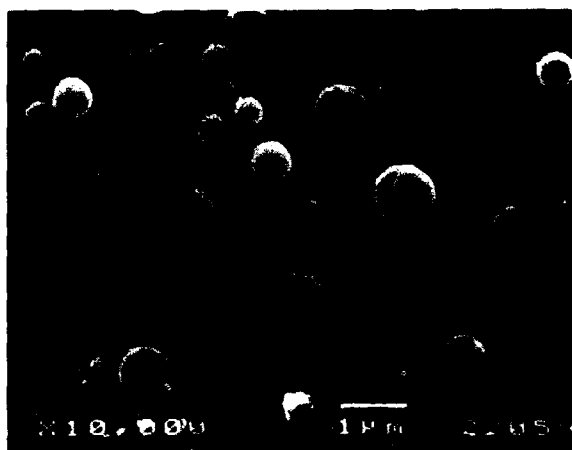
Figure 3: Particules récupérées dans un jet de propulseur. (Propergol XLDB au carbure de zirconium) SNPE

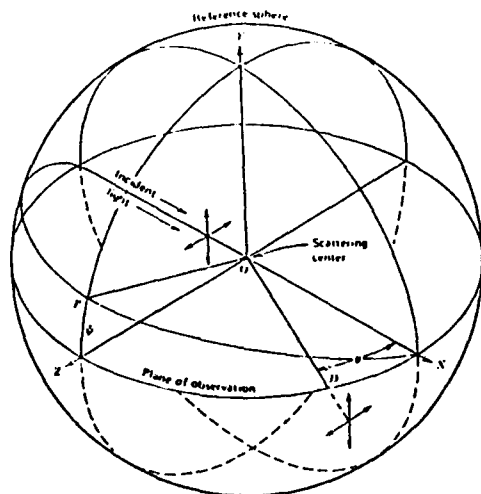Figure 4: Particules récupérées dans un jet de propulseur. (Propergol XLDB à l'aluminium) SNPE

Figure 5: Figure géométrique de la diffusion de Mie. Les deux vecteurs correspondent au rayonnement incident non-polarisé. La ligne OD est la direction d'observation et θ est l'angle d'observation. Pour un rayonnement polarisé, le vecteur électrique est supposé dans le plan POX, faisant un angle Ψ avec le plan d'observation [2].
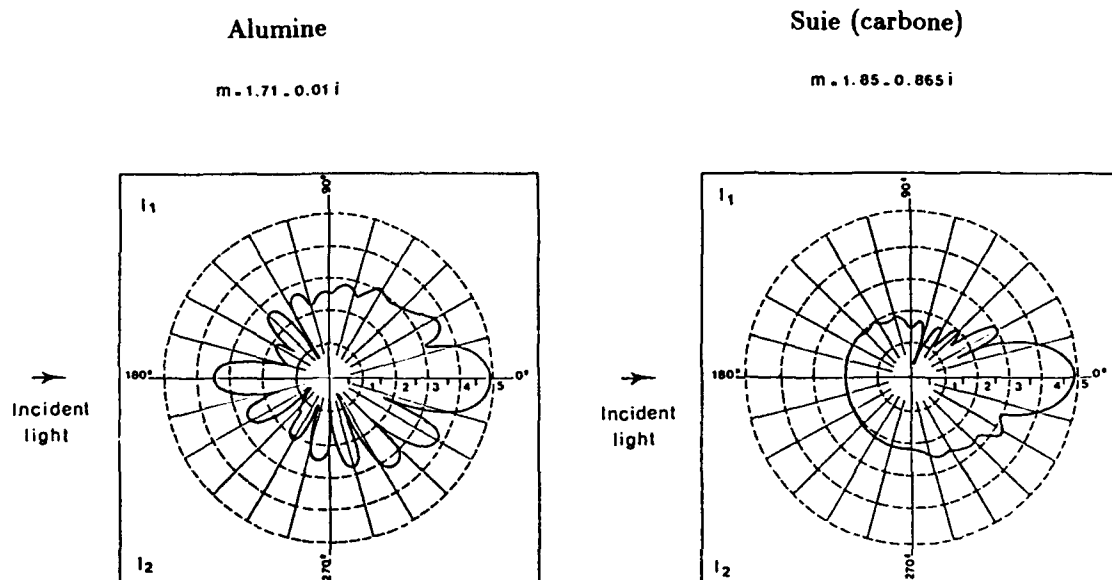
Alumine

m = 1.71 = 0.01 i

Suie (carbone)

m = 1.85 = 0.865 i

Figure 6: Variation de $\log i_1$ et de $\log i_2$ en fonction de θ pour des particules Al_2O_3 et C (suie) pour $\Psi = 45^0$, $r = 1\mu m$ et $\lambda = 0.7\mu m$.
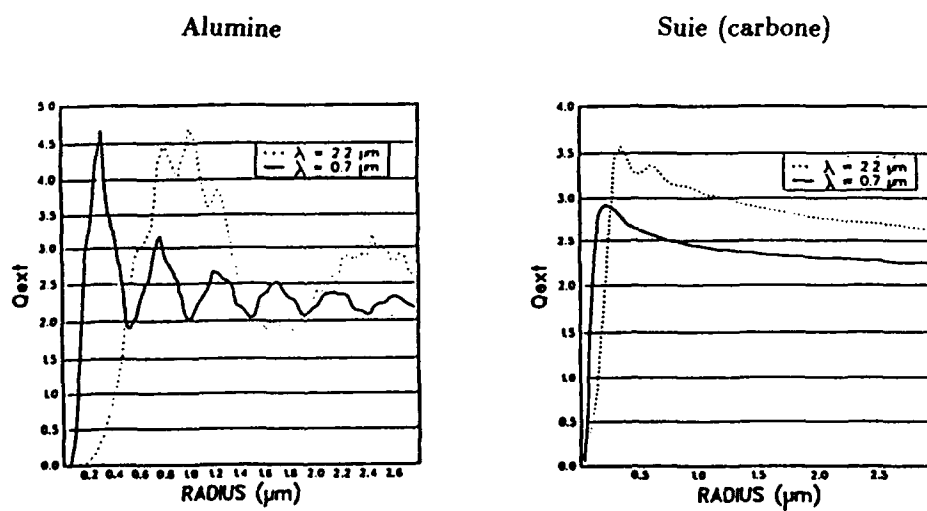
Alumine

Suie (carbone)

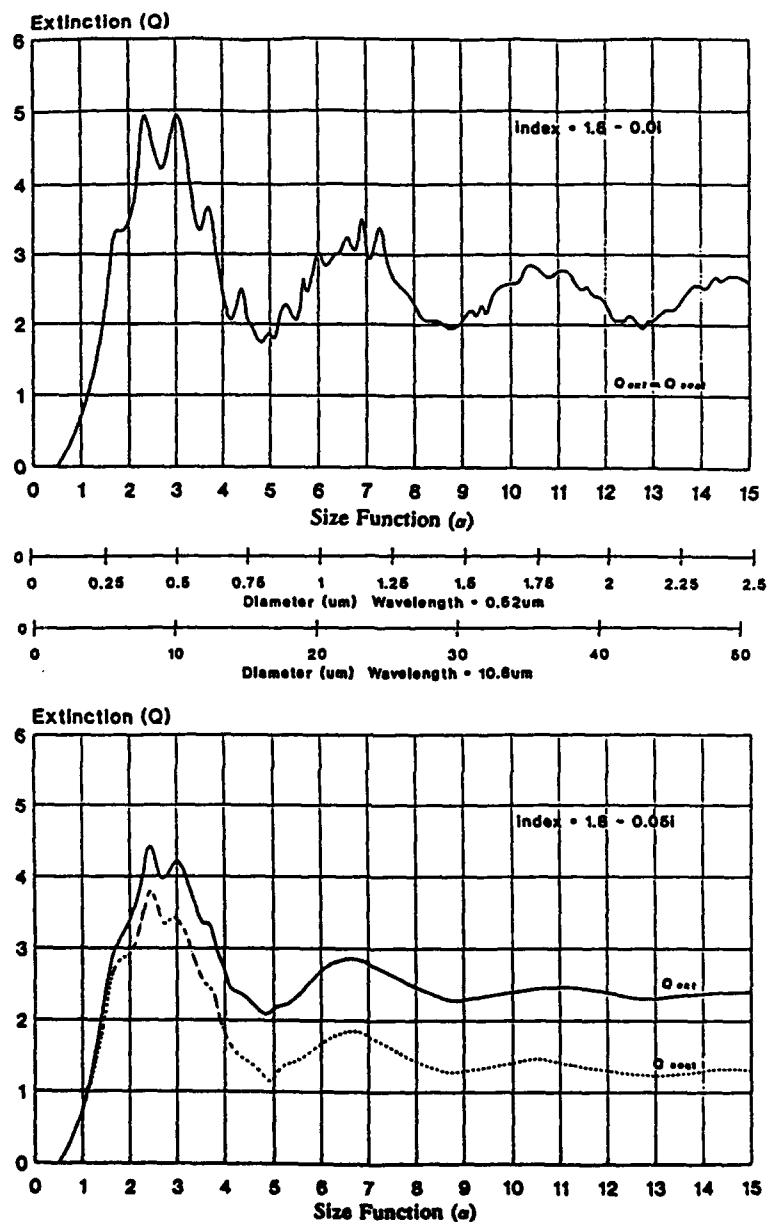Figure 7: Variation typique de Q_{ext}

Figure 8: Exemple de l'influence de la partie imaginaire de l'indice complexe sur les coefficients d'extinction et de diffusion. Paramètre de taille $\alpha = \pi D/\lambda$ (UK Royal Ordnance).
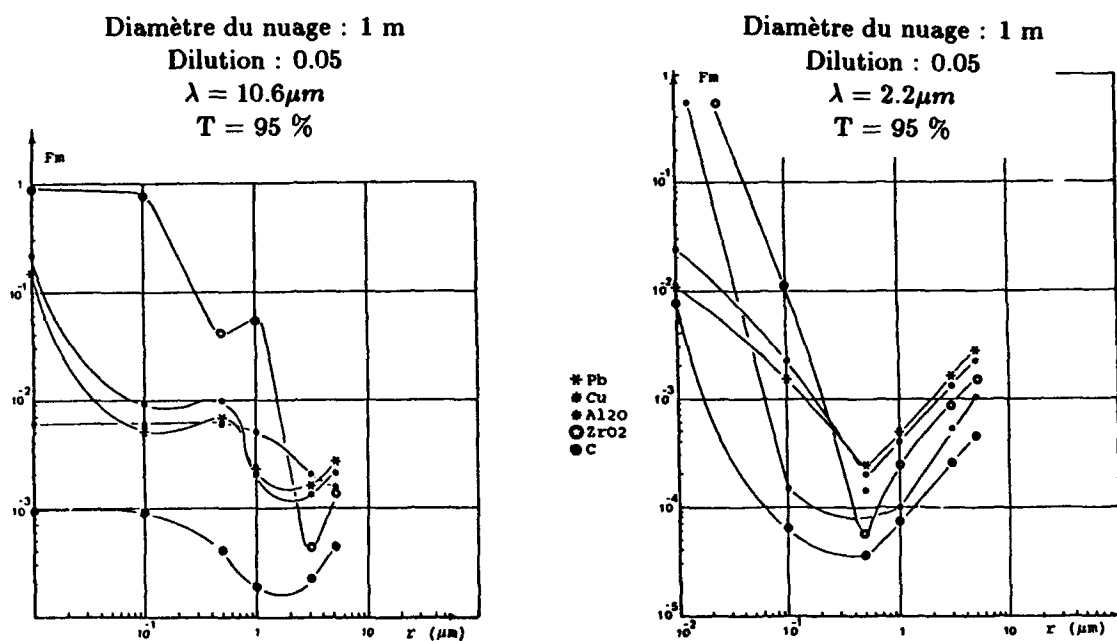
Diamètre du nuage : 1 m
Dilution : 0.05
$\lambda = 10.6\mu m$
T = 95 %

Diamètre du nuage : 1 m
Dilution : 0.05
$\lambda = 2.2\mu m$
T = 95 %

✳ Pb
✦ Cu
✦ Al2O
◯ ZrO2
● C

Figure 9: Fraction massique (Fm) de particules produisant une transmission de 95 % à travers un nuage donné en fonction de la taille des particules.

fraction massique
d'alumine

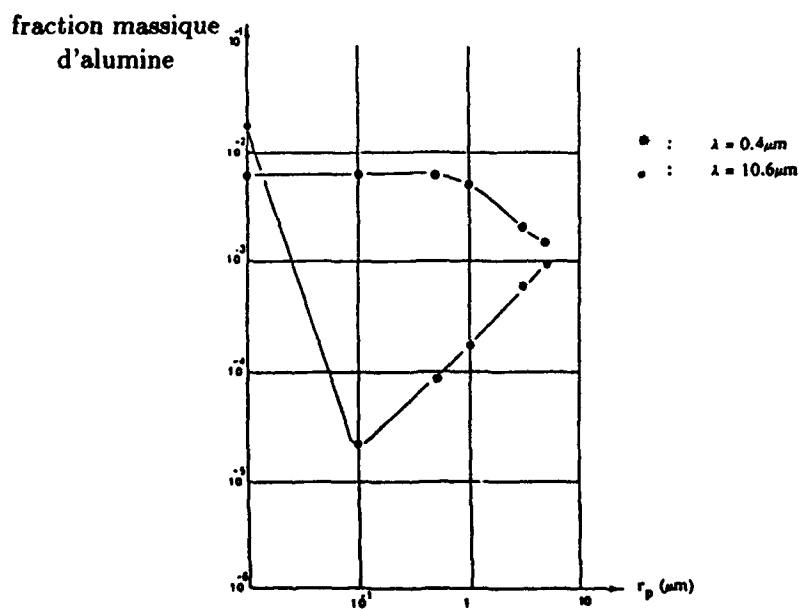● : $\lambda = 0.4\mu m$
● : $\lambda = 10.6\mu m$

Figure 10: Quantité maximale d'alumine (fraction massique) dans les produits de combustion pour les spécifications suivantes : diamètre du nuage : 1 m, dilution : 0.05, transmission : 95 %.
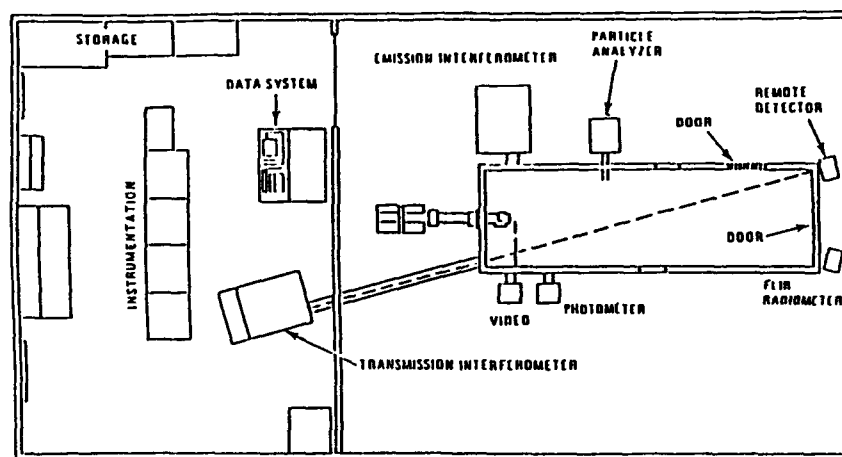
Figure 11: Dispositif de caractérisation des fumées de l'US Army (US Army S.C.F.)
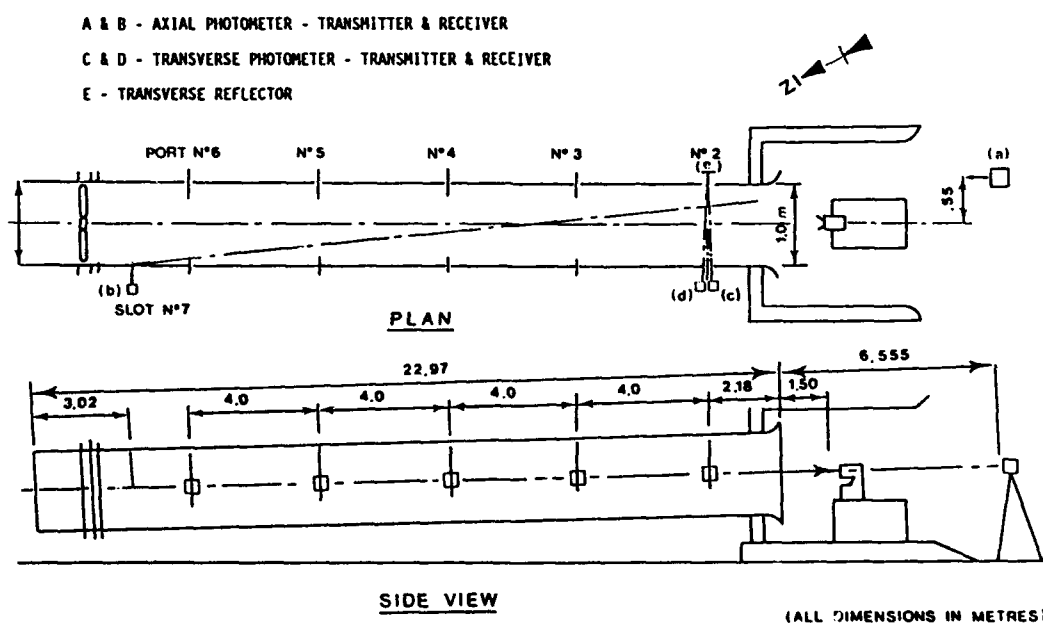

A & B - AXIAL PHOTOMETER - TRANSMITTER & RECEIVER

C & D - TRANSVERSE PHOTOMETER - TRANSMITTER & RECEIVER

E - TRANSVERSE REFLECTOR

PLAN

SIDE VIEW

(ALL DIMENSIONS IN METRES)

Figure 12: Tunnel à fumée R7 du Royaume Uni (RO)

Figure 13: "Fumimètre" SNPE (France)

A - CINE 50 PPS
B - AXIAL PHOTOMETER LAMP
C - IR-VISIBLE LIGHT-SOURCE
D - MOTOR
E - STILLS CAMERA
F - VIDEO
G - IR CAMERA
H - VISIBLE LIGHT EMISSION
I - TRANSVERSE PHOTOMETER
J - TRANSVERSE PHOTOMETER LAMP
K - AXIAL IR TRANSMISSION
  - AXIAL VISIBLE LIGHT
  - SMOKE REFLECTANCE
L - AXIAL PHOTOMETER
M - CINE 50 PPS
N - VIDEO
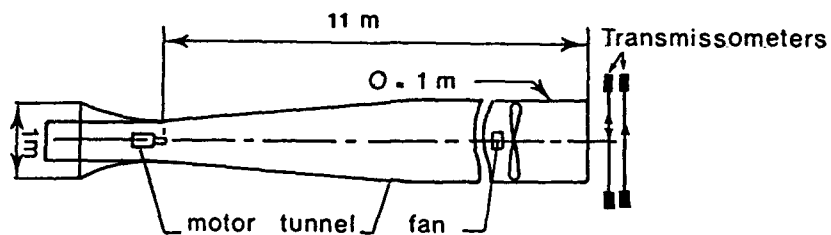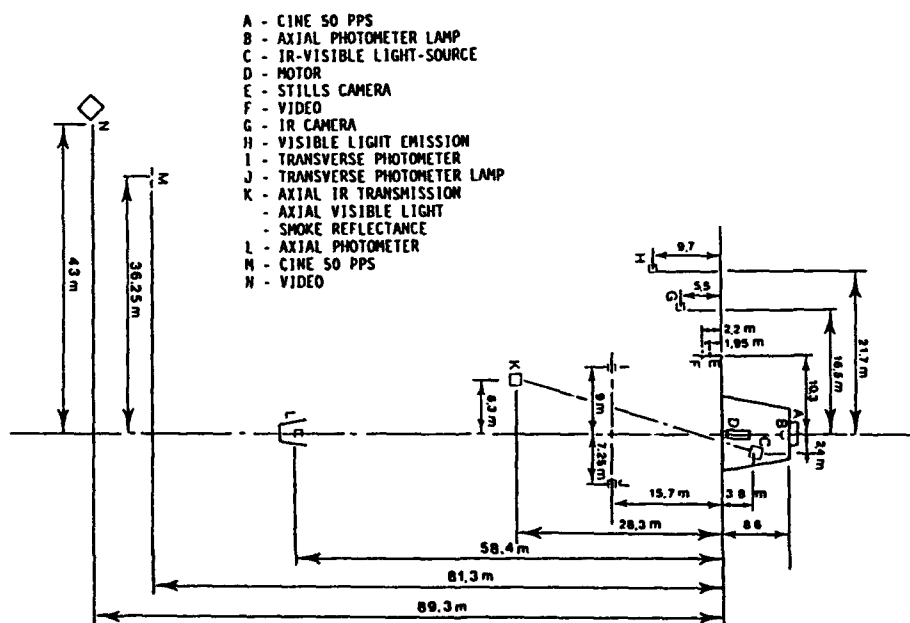
Figure 14: Tir en jet libre. Instrumentation du site de Wyre Forest (RU)
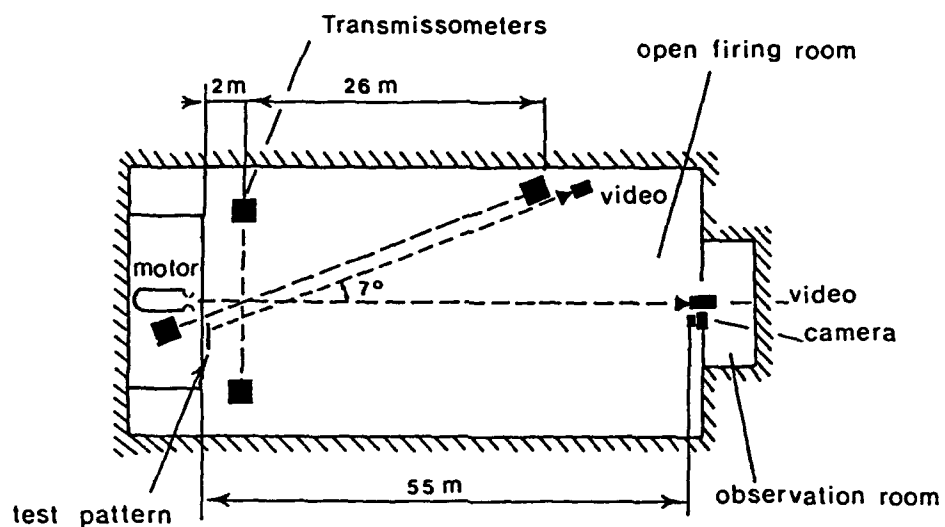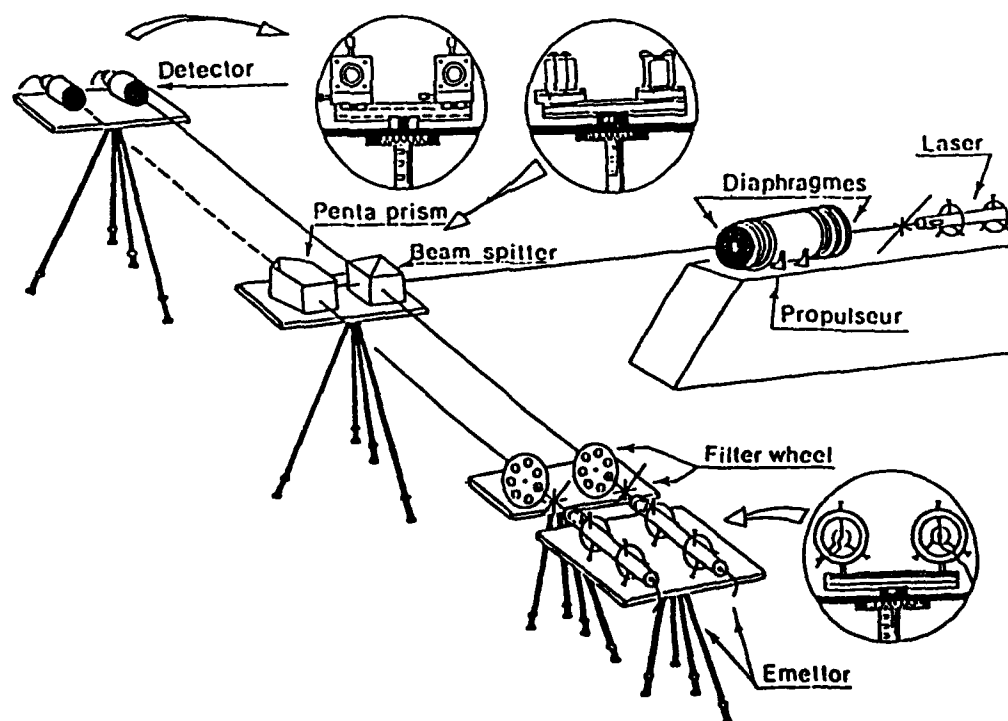
Figure 15: Tir en jet libre. "Banc opacimétrique" SNPE (France)
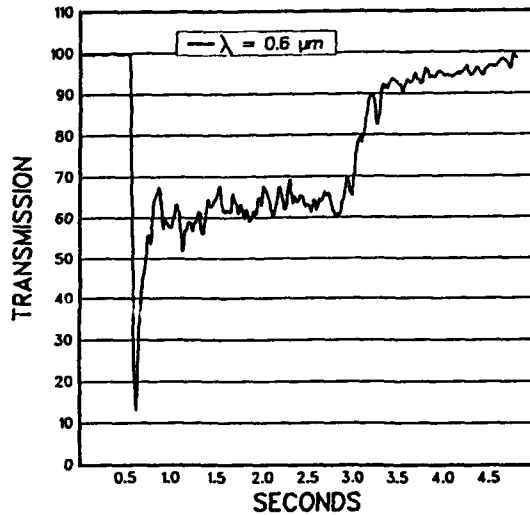

Figure 16: Tir en jet libre. Transmission à 0.63 μm

Figure 17: Exemple de courbe de transmission ($\lambda = 0.63\mu m$) Tir en jet libre, Mesure transverse (SNPE)
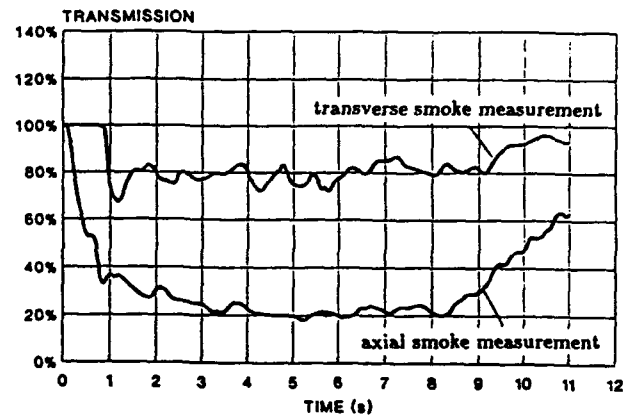

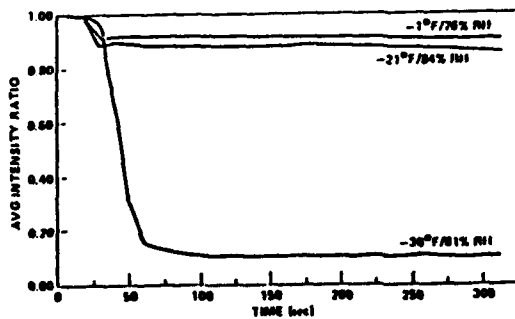Figure 18: Résultats typiques de mesure transverse et longitudinale (Tunnel à fumée de R.O (R.U))

Figure 19: Courbe de transmission visible (US SCF)

PROPULSION

P.K. SMITH

ROYAL ORDNANCE
Rocket Motors Division
Summerfield
Kidderminster
United Kingdom

1.0 SUMMARY

Current requirements for missile systems increasingly stress the need for stealth capability. For the majority of missile systems and missions the exhaust plume is likely to be the major contributor to overall missile signature, especially considering the recent developments in low emission and low Radar Cross Section coatings for motor bodies. This implies the need for the lowest possible rocket exhaust signature over a wide range of frequencies from the UV through visible and IR to microwave and radio frequencies.

The choice of propellant type, Double Base; Composite etc, plays a significant part in determining the exhaust signature of the rocket motor as does the selection of inert materials for liners, inhibitors and nozzles. It is also possible with certain propellants to incorporate additives which reduce exhaust signature either by modifying the chemistry of the afterburning plume or more significantly by suppressing secondary combustion and hence dramatically reducing plume temperature.

This lecture considers the feasibility of plume signature control on the various missions envisaged by the missile designer. The choice of propellant type and hardware components to give low signature is discussed together with performance implications. Signature reduction results obtained over a wide range of frequencies are also presented.

2.0 INTRODUCTION

Rocket motor plumes can exhibit dramatic differences in visual signature ranging from clean exhausts with secondary flame and little or no visible smoke, to plumes producing copious amounts of primary and secondary smoke to such an extent that the secondary flame becomes obscured or even invisible. In certain situations secondary combustion or afterburning can also be suppressed producing a rocket motor which burns without flame or smoke making it difficult to determine purely on visual grounds whether or not the motor is actually firing.

The visible signature is however only a very small part of the complete Electro-magnetic Spectrum. Guidance and detection of missiles is practicable at wavelengths ranging from the UV through visible and IR to microwaves and radio frequencies. Figure 1 shows atmospheric attenuation over infrared and millimetric wavelengths. Spectral regions of importance are those in which strong plume emissions occur in atmospheric windows where good long range transmissions are possible. Commonly used windows in the IR exist at 3-5 um and 8-12 um and in the millimetric region at 35 GHz and 94 GHz.

If signature control is required from a missile system then it is important that this is recognised at the design stage. The incorporation of, for example, flame suppression at a later stage is not necessarily an easy or satisfactory solution to guidance or tracking problems due to inference with other existing components of the missile. The objective of this lecture is to consider the various components of the rocket motor required for different types of tactical missile systems, explaining how stealth features can be adopted, illustrating the problems to be faced and the potential benefits to be gained.

3.0 FLAME SUPPRESSION

Throughout the lecture mention is made of flame suppression techniques because these are adjudged to be potentially the most attractive method of significantly reducing plume signature. When afterburning occurs the temperature of the exhaust plumes rises to a maximum approaching the chamber temperature at a distance of some 50 nozzle radii downstream of the exit plane. With flame suppression the nozzle exit plane becomes the hottest region with the temperature decreasing along the length of the plume.

With smokeless solid propellant rocket motors the fuel for secondary flame is Hydrogen and carbon monoxide. This mixes with atmospheric oxygen in the recirculation region at the nozzle exit plane resulting in a highly

flammable mixture. Shock waves in the plume result in regions of pressure concentration and temperature rise which lead to ignition. The temperature lag of any hot particles in the exhaust can also act as an ignition source. In all but low thrust low energy motors secondary combustion will take place unless inhibited by chemical means.

The reaction in the flame is propagated by free radicals such as H and OH. Combustion of hydrogen in air results in the formation of free radicals

$$H_2O_2 \rightarrow H_2O + H + OH$$
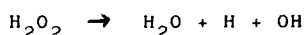
Removal of these radicals is the aim of combustion suppression. Potassium salts introduced into double base propellants as a small percentage of the propellant mass can stimulate the radical removing reaction processes.

$$K + OH + M \rightarrow KOH + M$$

$$KOH + H \rightarrow K + H_2O$$
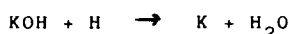
Extensive research work carried out at ROS has optimised the use of potassium salts for secondary flame suppression both in terms of the potassium salt used and the method of addition to the propellant. Both Sodium and Lithium salts have been shown to be possible but significantly less effective suppressants. Examples of the benefits of flame suppression are presented later in the lecture.

4.0 ROCKET PRINCIPLES

Solid propellant rocket motors are often referred to as being relatively simple devices requiring little or no servicing and having no moving parts. This is generally true although in a number of modern systems quite complicated actuation devices for thrust vector control are included in the basic design.

A definition of a rocket motor is a device for converting the thermo-chemical energy of a propellant into exhaust jet kinetic energy. The propellant for a solid rocket motor is contained and stored directly in the combustion chamber and can remain there for periods of time which can be as long as 20 years in some in service systems.

Figure 2 shows a typical solid propellant rocket motor with the various design features indicated. Selection of materials for the components can have a large influence on the plume signature obtained.

4.1 CASE AND END CLOSURES

The case and end closures are the components which form the pressure vessel for the propellant charge. The case also often acts as part of the missile structure. Requirements for the case include lowest possible mass together with high pressure capability. In many designs, such as where the missile experiences high 'g' loadings, high case stiffness is also necessary. Traditional case materials include steel and aluminium with various fabrication methods. Glass fibre constructions have also been extensively used but for applications which require high stiffness the case wall thickness and hence body weight become problematical. More recent case materials include, steel strip laminate, graphite fibres and Kevlar overwrapped aluminium. External case insulation is also used to protect certain motors against aerodynamic heating.

Case materials are not normally exposed during the motor burn and hence do not contribute towards plume signature.

4.2 IGNITER

The purpose of the igniter is to ignite the whole of the propellant grain as quickly and uniformly as possible enabling the motor to reach its operating pressure in a reproducibly short time. Over and under ignition across the motor operating temperature range are to be avoided, as is any igniter induced mechanical damage to the propellant grain.

Two main categories of igniter exist, pyrotechnic and pyrogen. Pyrotechnic devices contain ingredients such as Boron; Potassium Perchlorate and Aluminium. They have the advantage of being cheap to produce but have poor signature characteristics in particular high smoke levels. Pyrogen igniters are essentially small self contained rocket motors with only a very small amount of pyrotechnic material to initiate the burn. The propellant used in the igniter is usually the same or similar to the main propellant charge. The advantages of pyrogen igniters include more reproducible ignition across the temperature range and the ability to produce smoke free igniters using AA category propellants as described later. The main disadvantage of pyrogen igniters is involved with production costs and complexity. A propellant charge has normally to be manufactured for machining to produce the pellets necessary for inclusion into the pyrogen igniter. The pyrogen body has to act as a pressure vessel during the burn of the igniter and to achieve the correct operating conditions has to have some form of choke included in its construction. It is also possible to reduce ignition flash by the addition of flame suppressant materials to pyrogen igniter compositions.

4.3 CHARGE INSULATION/INHIBITION

Both charge insulation and inhibition materials are important in that they restrict the propellant from burning on unwanted surfaces and prevent combustion gases reaching and hence destroying the case insulating materials and even in the worst situation compromising the integrity

of the case materials.

Rocket motors normally fall into one of two categories either being cartridge loaded or case bonded. The advantages of cartridge load systems are that they in general present less formidable material problems. However in many cases these advantages are outweighed by energy considerations where the maximum possible propellant must be loaded into the available volume. This can usually only be achieved by case bonding, making this the only way of achieving the required performance from the available space envelope. In cartridge load applications the case is insulated by a suitable heat resistant/erosion resistant material such as Butyl; EPDM or chlorosulphonated polyethylene rubber. These are normally heavily filled with materials such as silica or refractory fibres to provide the necessary temperature and erosion resistance. The second part of the cartridge load system is the charge inhibition. This prevents the charge burning on surfaces other than those required and must bond adequately to the charge across the operating temperature range. The inhibition must also be resilient to any shock loading which the charge/motor may experience. Historically for double base propellants inhibitor materials such as ethyl cellulose of cellulose acetate were used to form charge inhibitors. However, these materials relied on nitroglycerine absorption to form a bond to the propellant. As the propellants aged, more and more nitroglycerine was absorbed by the inhibitor. This modified the burn rate of the propellant adjacent to the inhibitor and more importantly increased the amount of inhibitor consumed on firing. The smoke signature from such inhibitors therefore increased with age.

The two more recent types of materials used for charge inhibitors are either heavily filled plastic or rubbers designed to resist combustion, or polymeric materials such as acrylates or polyurethanes which are capable of burning but at a much slower rate than the propellant. It is possible with these materials to achieve virtually smoke free burning.

Some inhibitor formulations are self bonding to the propellant whilst others require the use of a bonding interface layer.

The second category of charge is the so called case bonded type where the charge insulation bonds the liner to the motor wall. In this case the inhibition, in addition to its heat resisting properties, needs to possess good mechanical properties over the operating temperature range of the rocket motor to accommodate the stresses produced by the mismatch in thermal expansion rates between the propellant and case materials. This normally limits the choice of material to filled rubbers. Because of the higher stresses bonding becomes more critical in case bond applications.

From the point of view of signature control any particulate matter liberated by the various insulation/inhibition materials will form smoke in the rocket motor exhaust. If refractory fillers are used the particle size should be chosen to minimise light attenuation and scattering. Figure 3 shows the scattering cross sections for a typical refractory and it can be seen that to achieve very low scattering coefficients sub micron particles should be used. The other chief source of smoke in charge inhibitor formulations is due to unburnt hydrocarbons where the oxygen/hydrocarbon ratio of the material is low. By the addition of oxygen rich fillers to these materials it is possible to achieve oxygen balanced systems which give virtually smoke free performance.

The presence of hot particles in the exhaust plume generally leads to significant levels of radiation throughout the Ultra Violet, visible and infrared spectral regions. These mechanisms are discussed more fully in the plume radiation lecture but the important parameters affecting plume signature are particle size distribution, temperature and concentration. Another important effect in flame suppressed plumes is particulate triggering of secondary combustion due to the thermal lag of the exhaust particles. This can have serious consequences in certain configurations where, for example, pressure changes inside the motor can lead to the release of relatively large pieces of inhibition/ insulation debris. This is especially apparent in boost sustain motors where the abrupt change in pressure between the two stages can lead to noticeable puffs of exhaust smoke. A similar effect is often seen at motor burnout. For these reasons it is preferable in cartridge load situations, where end burning charges are often used, to use the oxygen balanced inhibitors rather than erosion resistant materials. In case bond situations the charges are likely to be radial burning and therefore only small regions of insulation are exposed until cose to burnout, minimising the particulate matter released.

Rigid insulants are often used in the extreme aft ends of radial burning motors to provide better insulation and less particle release from these highly erosive areas.

4.4 END CLOSURES BLASTPIPE AND NOZZLES

Conditions in these regions which feature high temperatures and gas flows are highly erosive leading to the use of rigid insulants. The materials used may have fibrous inorganic materials added to

improve their insulating properties and leave a charred insulating layer after the organic material has been consumed. The most common of these materials has traditionally been asbestos. However, this is now being phased out because of carcinogenic effects and alternative materials such as silica phenolic and carbon-carbon materials are being developed. Graphite or even Molybdenum inserts which minimise erosion are being used specifically in the highly erosive choke area. The material require-ments for signature control are consistent with low erosion having the same constraints as for insulation materials.

Secondary flame suppression imposes particular restraints on nozzle design. The most favourable nozzle design for flame suppression is a fully expanded parallel flow nozzle which minimises exit plane temperature and pressure. Unfortunately this design of nozzle becomes excessively long for high pressure, boost motor applications. In these cases simple conical nozzles or Rao profiles are often used. Table 1 shows comparisons between conical, Rao and circular arc profile nozzles where the exit plane angle is progressively reduced from 15° through 7° to 0° whilst maintaining the same exit plane diameter and hence temperature and pressure.

Three motors with each standard of nozzle were fired. One of these contained no flame suppressing additive whereas the other two contained 0.5% and 0.75% respectively. In each case the size and condition of any secondary flame was assessed.

The results show the conical nozzles to be substantially worse than the other two types of nozzle in terms of flame suppression and, incidently, thrust losses. The differences between the Rao and circular arc nozzles are less pronounced but the zero degree exit angle, circular arc nozzles appear to be slightly superior.

4.5 MULTINOZZLES

At high thrust levels exhaust plumes become large producing high emissions. Flame suppression of these plumes becomes more and more difficult requiring high levels of additive to be used producing, in some cases, an unacceptably high smoke penalty. Figure 4 shows the amount of additive required to suppress typical CDB motors at various thrust levels. It can be seen that a level of approximately 1.0% is required for a thrust level of 24 KN. However if the single nozzle on the motor is replaced by four nozzles canted such that the plumes separate the thrust per nozzle drops to 6 KN

and the additive level reduces to approxi-mately 0.7% with a commensurate drop in exhaust smoke. It has been found that a cant angle of approximately 7.5° is required to ensure separation. The axial thrust losses vary as the cosine of the cant angle and therefore a thrust loss of only approximately 1% is incurred. Other penalties with multiple nozzles include higher production costs due to the increased complexity, and possibly lower nozzle expansion ratios if the maximum diameter at the exit plane is restricted to the missile body diameter If a requirement exists for a minimum signature motor having high energy and high thrust, then the use of multi-nozzles may be the only practical method available of obtaining flame suppression without having to incorporate excessive quantities of additive into the propellant These would in turn degrade performance and give an unacceptably higher smoke signature.

4.6 THRUST VECTOR CONTROL

A number of different types of TVC systems are commonly used on tactical missiles. These range from simple jetavator and spoiler blade devices to more complicated swivel nozzle systems. All such devices operate by deflecting the exhaust flow relative to the motor axis and by their nature are likely to modify exhaust size and plume properties. One such device is a spoiler blade system which deflects the plume by blade insertion at the nozzle exit plane. These types of device produce severe exhaust shocks and high recovery temperatures. They are therefore likely to produce high exhaust emissions and be extremely unfavourable for flame suppression except at very low thrust levels. A further device the gimballess swivel nozzle is typical of devices where the whole of the nozzle and choke assembly are moved. This type of TVC has little effect on the exhaust plume except in flight, where the angle of incidence of the exhaust gases to the air flow is changed. These devices are obviously the most favourable for minimising exhaust emissions and suppressing secondary combustion.

5.0 PROPELLANTS

The two main families of propellants, composite and double base, are shown in Table 2 and Table 3. The type of propellant chosen and ingredients involved have a profound influence on the rocket motor exhaust signature.

5.1 COMPOSITE PROPELLANTS

Composite propellants consist of a fuel and oxidiser held together in a rubbery binder. The binder which can be inert or energetic also acts sometimes as the fuel.

5.1.1 INGREDIENTS

The most widely used fuel is powdered aluminium which is normally incorporated into the propellants at levels of between 14-18%. Aluminium is cheap, readily

available and easily burns in combustion chambers. The combustion product, aluminium oxide, however produces dense primary smoke and also causes problems due to slag deposition on nozzles and end closures. A number of other metallic fuels have been considered. These include Boron: Beryllium and their Hydrides. Boron has been used in some applications such as solid propellant ramjets but its high melting point makes it a difficult material to burn efficiently. Beryllium is unlikely to be used due to toxicity and the hydrides present manufacturing and storage problems.

Ammonium perchlorate is normally used as the oxidiser in composite propellants being incorporated typically at levels of around 70%. The material is cheap; high energy and produces propellants with low pressure exponents. Ammonium perchlorate on burning liberates HCL which under certain conditions can cause secondary smoke. Certain other oxidisers can be used. These include Potassium Perchlorate and Ammonium Nitrate. Neither of these materials is as energetic as Ammonium Perchlorate. Potassium Perchlorate produces low burning rate propellants and Ammonium Nitrate, whilst smokeless and possibly attractive for insensitive munitions, presents manufacturing difficulties due to phase changes.

A number of different binder systems are in use. These include Polyurethanes; Carboxy-Terminated Polybutadiene (CTPB) and Hydroxy-Terminated Polybutadiene (HTPB). The most widely used binder system is HTPB which is easily processed and gives good mechanical properties across the temperature range.

5.1.2 PROPELLANTS
HTPB based composite propellants offer high energy coupled with excellent mechanical properties and are extremely cost effective to produce.

A range of composite propellant burning rates can be achieved by varying the particle size of the ammonium perchlorate and incorporating burning rate modifiers such as Ferrocene derivatives. The propellants produced are unplateaunised but can have low burning rate exponents and hence low temperature coefficients, typically 0.2-0.4%/°C.

Composite propellants containing aluminium fall into the AGARD recommended classification CC as shown in Figure 5. However, reduced smoke composite propellants can be produced by removing the aluminium from the propellant and replacing with energetic fillers such as RDX

and HMX. Here both the filler and HTPB binder act as the fuel. These propellants fall into the AGARD recommended AC class with small amounts of primary smoke but high levels of secondary smoke under certain conditions. Similarly minimum smoke propellants can be produced by removing aluminium and most or all of the Ammonium Perchlorate and replacing with an energetic binder and RDX or HMX fillers together with possibly Ammonium Nitrate. Problems however, arise with the burning rate of such propellants resulting in the use of small amounts of Ammonium Perchlorate to increase the range of available burning rates. These propellant fall into the AGARD recommended AA or AB classification.

The addition of Aluminium to propellants to increase energy also has the effect of reducing combustion instability in radial burning motors. In the absence of Aluminium, materials such as Zirconium Carbide are added to provide particulate damping. Careful choice of particle size is required to minimise primary smoke.

5.1.3 PROCESSING
Composite propellants are usually manufactured using a slurry cast, mould filling, process but are also capable of being extruded. The binder systems commonly used bond readily to the motor insulation or charge inhibition and so both case bond and cartridge load designs are easily produced.

5.1.4 PLUME SIGNATURE
The major problems with composite propellants are concerned with exhaust signature. Figure 6 presents the results of a firing trial carried out on two Double Base, low thrust (1.5 KN), motors, one without aluminium and one containing 2% aluminium. The results quoted are for the attenuation of a visible beam normal to the plume at a distance of some 16 metres from the nozzle. It can be seen that the transmission falls from 100% to approximately 50% for the aluminised round. Therefore even small proportions of aluminium will form dense clouds of primary smoke and for low signature exhausts all of the aluminium must be removed. This implies that other particles such as zirconium carbide must be added to prevent combustion instability in radial burning charges. The major source of smoke in composite propellants is however, secondary smoke formed due to the combustion of ammonium perchlorate releasing HCL into the exhaust. This will react with atmospheric water under certain temperature and humidity conditions forming dense clouds of secondary smoke. A full discussion of secondary smoke is presented in one of the following lectures and will not be included here. However, Figure 7 shows atmospheric condition predictions for secondary smoke formation for composite and double base propellants. It can be seen that in certain climatic regions, the conditions of low temperature and high relative humidity necessary to produce secondary

smoke in composites are likely *to be quite frequent occurrences.* Similarly Figure 8 shows that secondary smoke is likely to be produced by composite motors at high altitude. Secondary flame *suppression of composite propellants containing* Ammonium Perchlorate has been found to be ineffective due to chlorine present in the combustion gases spoiling the action of the afterburning suppression additives. Low emission levels at all wavelength from these motors are unlikely to be achieved, although certain plume properties such as Radar Attenuation can be improved by the addition of materials such as Molybdenum Trioxide.

5.2 DOUBLE BASE PROPELLANTS

The double base family of propellants generally use Nitrocellulose and Nitroglycerine as the two base materials but other nitroplasticisers may be used. Here the Nitrocellulose and Nitroglycerine function as fuel, oxidiser and binder with the Nitro-cellulose absorbing and gelatinising the Nitroglycerine to form an homogenous propellant grain.

5.2.1 INGREDIENTS

Double base propellants contain a number of ingredients in addition to Nitrocellulose and Nitroglycerine. Stabilisers are added to prevent the decomposition of the nitroglycerine and hence increase propellant storage lives. Ballistic modifiers are added to control the burning rate. Combustion instability can be controlled by the addition of particles such as zirconium carbide and flame suppressing potassium based materials can be used.

5.2.2 PROPELLANTS

A wide range of propellant burning rates can be achieved by the addition *of small amounts of ballistic modifiers* based usually on lead and copper salts. These modifiers produce super rate and so called plateau burning where the propellant burning rate becomes independent of pressure having a zero or even negative exponent over a certain pressure range. Operating on the plateau region of the curve enables very low, or even sometimes negative, temperature coefficients to be obtained, typically $<$ 0.2%/°C. This minimises variations in missile performance over the temperature range.

All but the very high NC containing double base propellants can be successfully case bonded allowing both cartridge load and case bond motors to be produced. Traditionally double base propellants gave very poor low temperature strain capability necessitating the use of mechanical stress relief devices in motors *designed to operate at low temperatures.* This has been overcome in the newer

classes of double base propellant such as Cross Linked Double Base (XLDB) and Elastomer Modified Cast Double Base (EMCDB). Figure 9 shows a comparison between CDB and EMCDB propellants with the latter showing a strain capability of 20% at -40°C.

The energy level of double base propellants is somewhat lower than composites but the more flexible types of propellants such as EMCDB contain much higher levels of nitroglycerine than conventional CDB and are therefore more energetic.

Aluminium and Ammonium Perchlorate can be incorporated into double base propellants if required resulting in the Composite Modified Double Base class of propellants. The use of these ingredients increases the energy of the propellant, but it does so at the expense of plateaunisation and hence low temperature coefficient. Perhaps even more importantly it increases energy at the expense of low exhaust signature.

Development has concentrated in recent years on the incorporation of high energy smokeless materials such as RDX : HMX into double base propellants. Propellants containing high levels of these materials have been produced in both XLDB and EMCDB. Up to 40% RDX has been successfully incorporated into EMCDB propellant without loss of plateaunisation and retaining good -40°C strain capability. At these levels of RDX, propellant energies approaching those of non aluminised composites are obtained. Combustion stabilising and flame suppressing additives can be incorporated into Double Base propellants without destroying plateaunisation.

5.2.3 PROCESSING

A number of manufacturing routes for double base propellant are in common use. These include:

a) A slurry cast process to produce XLDB propellant.

This process is similar to the slurry cast process for composite propellants where all of the ingredients are mixed together, a curing agent added and the mix dispensed into suitable moulds. Energetic fillers and other required materials such as instability suppressants are added at the mixing stage.

b) An extrusion process for Double Base propellants.

This is the well established hot rolling/extrusion process to produce EDB propellant. A variety of fillers such as RDX; HMX; instability suppressants and plateaunising agents can be incorporated at the compounding stage.

The extrusion process is most suited for the production of rigid, thin web, propellants used in short burn time applications.

c) A casting process for CDB and EMCDB propellants.

The casting process uses a powder grain normally based on a 1 mm cylinder containing Nitrocellulose and Nitroglycerine which is poured into a mould. The casting fluid composed of desensitised nitro-glycerine is passed through the powder bed and under the influence of heat and pressure the casting powder granules partially dissolve in the liquid by a process of gelatinisation of the nitrocellulose. As a result the granules swell and coalesce to form a monolithic block of propellant. Additives such as RDX; ballistic modifiers; and combustion stabilisers and flame suppressants can be incorporated into the powder grains. To achieve EMCDB properties elastomers are added to the casting liquid.

5.2.4 PLUME SIGNATURE

Double base propellants are generally much better than composite propellants for exhaust signature. NC/NG based propellants burn with extremely low levels of exhaust smoke. Even with the addition of Ballistic Modifiers and combustion instability and flame suppressants, propellant primary smoke is still low falling into the AGARD AA class of propellants. Nitramine fillers are also very low smoke producing and the net effect of nitramine filled propellants, because of ballistic modifier dilution, is usually lower smoke. Secondary smoke from double base propellants is absent except under very cold conditions (less than -40°C predicted).

The most significant advantage of double base propellants for plume signature control is the ability to incorporate flame suppressing additives. Low levels of certain potassium salts added to the propellant will suppress secondary combustion with only a small increase in exhaust smoke. Careful selection of the type of additive and its method of incorporation into the propellant minimise the effect of the additive on the mechanical and ballistic properties of the propellant.

6.0 MISSION PRINCIPLES

The fundamental requirement for a missile system is that it should have the highest possible probability of successfully completing its mission. This implies the missile either hitting its target or approaching sufficiently close to be within the lethality radius of a proximity fused warhead.

The plume signature from the rocket motor can reduce the mission capability of the missile both in terms of its interference with the missile guidance and tracking systems and by increasing the possibility of detection of the missile sufficiently early in its flight to allow effective countermeasures to be taken.

6.1 GUIDANCE AND TRACKING

The wavelengths involved in guidance and tracking vary from the Ultra Violet through visible and IR to millimetric wave radars. Favoured frequencies are those where atmospheric windows exist allowing long range communication at low powers. However, range limited frequencies are sometimes used to decrease the possibility of long range detection.

Various guidance and tracking systems are commonly used. These are more fully discussed in Ref 1 Chapter 6 but include Beam Riding : Command to Line of Sight (CLOS): Semi Active and Active Homing. In all cases, other than the autonomous stage of flight in Active Homing, the exhaust plume can have serious system implications if the guidance or tracking signal passes close to, or through, the exhaust plume. This is particularly so if the rocket motor is required to continue burning up to maximum range.

A further problem with guidance and tracking is in salvo operations. Here the exhaust plume of one missile may seriously interfere with target tracking or guidance of subsequent missiles.

A number of missile solutions to exhaust plume problems are possible. These include flight path offsets at critical periods to avoid excessive signal losses and the use of multiple antenae or reflectors attached to wings etc to remove propagation paths from highly attenuating regions of the plumes. Another possibility is to use a fully Active Homing System without mid-course guidance. All of these solutions add to increased missile complexity and hence cost. Reductions in plume signature, where these are possible, are much more desirable.

6.2 DETECTION

Exhaust emissions from rocket motor plumes can become a means of detection over a wide range of wavelengths varying from the UV to microwave frequencies. Again frequencies of interest are those where atmospheric windows occur making long range detection possible. Traditionally detection has concentrated on the IR regions of the spectrum where suitable detectors operating in the atmospheric windows make extremely long range detection possible. Because of problematical background behaviour in

the infrared, newly developed sensing devices in the UV are gaining in importance. In the mid UV, or solar blind region, atmospheric attenuation limits measurements to short ranges, but the availability of extremely sensitive detectors and the absence of natural sources make this region attractive. Long range detection is possible in the near UV but solar scatter is prominent.

The only solution available to the missile designer to delay or avoid detection is to minimise the rocket motor plume.

6.3 MOTOR CONSIDERATIONS

The most powerful tool available to the rocket motor designer requiring to reduce communication losses and minimise exhaust emissions is the ability with certain families of propellants to suppress secondary combustion. Experimental results presented later show dramatic reductions in plume emissions across the full range of frequencies from UV through visible and IR to millimetric wavelengths. Tne use of certain metallic compounds in none flame suppressed plumes can decrease microwave attenuation but is much less effective than flame suppression.

It is possible to use a number of different flight profiles for a missile system. Each of these has implications for exhaust control.

The simplest of these is the boost coast system where the missile is accelerated to a suitable velocity by a short burning rocket motor which then burns out allowing the motor to coast to target. This is taken to the extreme in shoulder launched systems where the motor is all burnt before the missile leaves the launcher tube. The major advantages of a boost coast system is the absence of plume during the coast phase removing any problems of plume interference with guidance and tracking, and making detection in the coast phase difficult. The disadvantages of such a system include decreased range due to high initial velocity and drag, low intercept velocity at target and the inability to use TVC systems during the coast phase. From plume signature consider-ations, suppression of afterburning in the higher thrust boost phase can present difficulties.

A number of the problems associated with boost coast can be overcome by using boost sustain motors. Figure 10 shows a typical boost sustain thrust profile. Such motors can have a significantly longer range for the same propellant mass and are often used in small antitank systems where the boost phase

accelerates the missile up to sonic velocities which are maintained during the sustain phase. As well as increased range these motors have the advantages of higher terminal velocity and higher manoeuvreability because TVC devices can be used throughout the flight. Flame suppression in the low thrust sustain phase is usually easily accomplished with only a small penalty. The boost phase presents the same problems as boost coast, but because of the much shorter boost burn time the boost phase can be all burnt, in certain situations, before the missile is acquired by the guidance/tracking system.

7.0 OPERATIONAL ASPECTS

A number of other problems exist which can be alleviated by exhaust signature control.

7.1 LAUNCHER DAMAGE

Hydrochloric acid mists liberated during the firing of composite propellants can cause significant damage to launchers. This necessitates the use of protective materials. Flame suppressed exhausts, being significantly cooler than afterburning plumes will in general cause less launcher damage. However, interactions between the launcher structure and the plume can initiate afterburning.

7.2 IDENTIFICATION OF LAUNCHER SITE

Exhaust trails formed from both primary and secondary smoke can reveal the position of the launch site. This is particularly significant in still air conditions where smoke clouds, especially secondary smoke clouds, can persist for relatively long times. Exhaust flash, especially under low light or night firing conditions, can illuminate and reveal the position of the launch site.

7.3 JET ENGINE FLAMEOUT

This has been a problem with air launched missile systems over the years and various measures such as relocating the missiles as far as possible from the engine air intakes have been taken to minimise the problem. However, if exhaust flame suppression can be accomplished this is a much more effective way of reducing the problem.

7.4 NIGHT BLINDNESS

A problem which occurs on night firings of missiles is that the intense exhaust flash during launch and the early phase of the flight can cause operator night blindness. This may impair the operators ability to carry out further tasks such as guidance and tracking for some seconds after launch. The visible emission results of two night firings are presented in Figure 11. The flame on motor gives a continuously high emission throughout the firing. However, on the flame suppressed round, only ignition flash and candling on burnout are detected.

The ignition flash is very short and is probably out of the field of view of the operator. The candling would be at extreme range and unlikely to occur in flight conditions. Night blindness will obviously be much less of a problem with suppressed plumes.

8.0 SIGNATURE REDUCTION IN SUPPRESSED PLUMES.

Throughout this lecture the potential benefits of exhaust signature control and in particular exhaust flame suppression have been discussed. The following figures present the results of a series of practical trials carried out on experimental CDB rocket motors to quantify the gains achieved at various wavelengths. Full details of the trials are discussed in reference 2 and the results presented here are a small selection of the total results obtained. The results show as far as possible a single pair of motors operating with a thrust level of approximately 7 KN. The propellant used was high energy nitramine filled double base, the first motor being flame on and the second motor flame suppressed.

Figure 12 shows the visual signature of the two motors. Just a trace of secondary combustion is visible on the suppressed round.

Figure 13 shows spectral radiant intensity over the wavelength band 300-360 nm the results quoted being the average of a number of scans throughout the firing. The results show a significant reduction in UV emission with flame suppression.

Figure 14 shows whole plume radiant intensity for the unsuppressed and suppressed round in the 3-5 um IR band. A reduction of roughly one order of magnitude is obtained.

Figure 15 shows similar results for the 8-13 um IR band. Again a significant but smaller reduction is obtained.

Figure 16 shows normalised long range IR emission spectra for a pair of similar thrust motors. Substantial reductions in peak Red Wing and Blue Spike emissions are obtained for the suppressed motor.

Figure 17 and 18 show millimetric attenuation of a pulsed radar beam traversing the plume in a two-way path via a dihedral reflector. The two pairs of plots are for the radar positioned with the beam first normal (Figure 17) and secondly (Figure 18) at an angle of 30° to the plume.

The results show that the attenuation of the beam in the flame suppressed

condition falls effectively to zero with only ignition flash and motor burnout detected. However in flame on conditions high attenuations are obtained which are proportional to the beam path length through the plume.

Rocket motor plumes also emit radio frequency radiation at millimetric wavelengths. Figure 19 shows plume emissions at 80 GHz for flame on and flame suppressed motors. The results are expressed as apparent blackbody temperature in degrees Kelvin. The flame on motor can be seen to be emitting radiation as if it were a blackbody raised to approximately 500°K whereas the suppressed motor shows very little increase in emission above background.

Figure 20 shows tranverse transmission measurements carried out on the smoke signatures produced. These show a small decrease in transmission 90% falling to approximately 85% with flame suppression.

9.0 CONCLUSIONS

The ability to control the exhaust signature of Solid Propellant Rocket Motors is of great benefit to the missile designer increasing the probability of mission success.

If stealth is of primary importance, it is possible to select motor components; propellant type and even missile flight profiles with the objective of minimising exhaust signature.

Dramatic reductions in plume emissions and guidance beam attenuations can be achieved by the suppression of secondary combustion. Designs where flame suppression techniques can be adopted provide the optimum route to minimum exhaust signature.

10.0 REFERENCES

1. AGARD Advisory report 287 Propulsion and Energetics Panel Working Group 21 Terminology and Assessment Methods of Solid Propellant Rocket Exhaust Signatures.

2. The Effects of Flame Suppression on the Exhaust Signature of Solid Propellant Rocket Motors
    P.K. Smith   AIAA paper 1991

3. Rocket Propulsion Elements
    G.P. Sutton

4. The Suppression of Secondary Combustion in Solid Propellant Rocket Motors.
    P.K. Smith : G.I. Evans
    SRS Technical Note 82/5

5. Spatial Resolved Radiometric
   Measurement in the 4-5 um and
   7.5-13 um Spectral Bands on
   Solid Propellant Rocket Motors
   with and without Secondary
   Combustion.
   J.M. Ridout : S. Cockle
   PERME Tech Report 237 (1982)

6. Radiometric and Spectrometric
   Investigation of the Effects of
   Flame Suppression on the Infra
   Red Radiation Emitted by a Series
   of Cast Double Base Propellant
   Rocket Motors.
   J.A. Donovan : J.M. Ridout
   PERME Tech Report 239 (1983)

7. Minimum Smoke Solid Propellant
   Rocket Motors.
   G.I. Evans
   A1AA/SAE Joint Propulsion
   Specialist Conference
   A1AA Paper No. 72-1192

8. Additives for the Chemical
   Modification of Rocket Exhaust
   Plumes. PERME (W) - IMI
   Collaboration Trial at Westcott
   16-17 May 1978.
   R.E. Lawrence : J.M. Ridout :
   B.C. Webb. PERME Memorandum 66

9. The Reduction of Exhaust Signature
   in Solid Propellant Rocket Motors.
   G.I. Evans : P.K. Smith
   AGARD PEP   CP 391 Paper 16

10. Elastomer Modified Cast Double
    Base Propellants.
    G.I. Evans : D. Facer
    AGARD PEP. CP 391 Paper 13

Table 1

Nozzle Profile Trials (Nitramine Loaded 7 KN Thrust Motor)

TRIAL NO	NOZZLE	SUPPRESSANT LEVEL %	FLAME
1	Conical	0	Continuous
2	Conical	0.5	Continuous - Detached
3	Conical	0.75	Continuous - Detached
4	RAO	0	Continuous
5	RAO	0.5	Flashes Only
6	RAO	0.75	Out
7	Cir Arc	0	Continuous
8	Cir Arc	0.5	Flashes Only
9	Cir Arc	0.75	Out

Both Rao and Circular Arc nozzles gave complete suppression at 0.75% additive. The circular arc nozzle gave a smaller visible flame at 0.5% additive.

Table 2   MAIN FAMILIES OF SOLID PROPELLANT

Propellant Family	Propellant Type	Main Ingredients	Additives (less than 5%)		
			Burning Rate Modifiers	Pressure Stabilizers	Signature Suppressants
Composite	Aluminized (some Zirconium or Beryllium envisaged)	Aluminium Ammonium perchlorate (AP) Inert binder (typically HTPB based)	Ferrocenic derivatives eg catocene		Molybdenum trioxide (MoO_3)
	Non or slightly aluminized	Some Aluminium Ammonium perchlorate(AP) Inert binder (typically HTBP based)	Ferric oxide Copper chromite	Aluminium Refractories eg Zirconium carbide Zirconium silicate Zirconium oxide	Molybdenum trioxide (MoO_3)
High Energy Composite	High Energy (NEPE type) Nitrate-ester Polyether or Polyester	Aluminium Ammonium perchlorate (RDX) or (HMX) Energetic binder based on inert polymer plasticized with liquid nitrate-ester			Molybdenum trioxide (MoO_3)

Table 3   MAIN FAMILIES OF SOLID PROPELLANT

Propellant Family	Propellant Type	Main Ingredients	Additives (less than 5%)		
			Burning Rate Modifiers	Pressure Stabilizers	Signature Suppressants
Double Base	Extruded Double Base / Cast Double Base	Nitrocellulose Nitroglycerine	Lead and Copper derivatives (mainly salts or oxides) (possibly Tin derivatives)	Refractories eg Zirconium carbide, Zirconium silicate, Zirconium oxide / Metals eg Aluminium	Potassium salts eg Potassium sulphate (K_2SO_4) Potassium cryolithe (K_3ALF_6) Other Alkali salts
Composite Double Base	Elastomeric Modified Cast Double Base (EMCDB) (or filled double base)	Nitrocellulose Nitroglycerin Inert Prepolymer curing agent (RDX) or (HMX) (Possibly some aluminium and ammonium perchlorate)	Lead and copper derivatives (possibly tin derivatives)	Aluminium / Refractories eg Zirconium carbide, Zirconium silicate, Zirconium oxide	Potassium salts eg Potassium sulphate (K_2SO_4) Potassium cryolithe (K_3ALF_6) Other Alkali salts
	Cross Linked Double Base (XLDB)	(RDX) or (HMX) Energetic binder based on inert polymer plasticized with liquid nitrate-ester. Some ammonium perchlorate may be added	Lead and copper derivatives	Aluminium / Refractories eg Zirconium carbide, Zirconium silicate, Zirconium oxide	Potassium salts eg Potassium sulphate (K_2SO_4) Potassium cryolithe (K_3ALF_6) Other Alkali salts
	Composite Modified Double Base (CMDB)	Nitrocellulose Nitroglycerin (RDX) or HMX) (Possibly some aluminium and ammonium perchlorate)	Lead and copper derivatives (possibly tin derivatives)	Aluminium / Refractories eg Zirconium carbide, Zirconium silicate, Zirconium oxide	Potassium salts eg Potassium sulphate (K_2SO_4) Potassium cryolithe (K_3ALF_6) Other Alkali salts
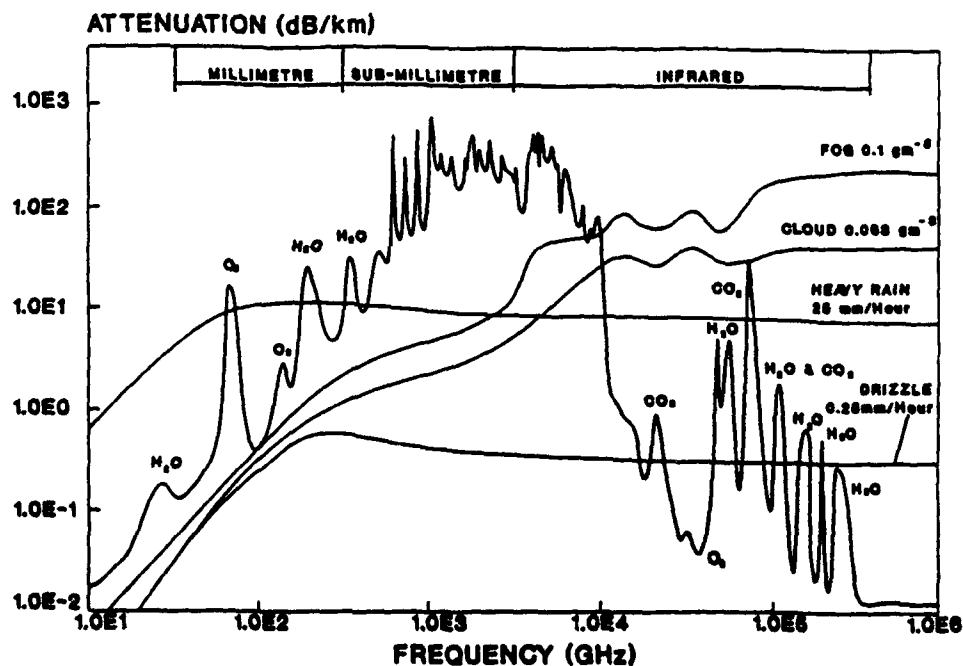
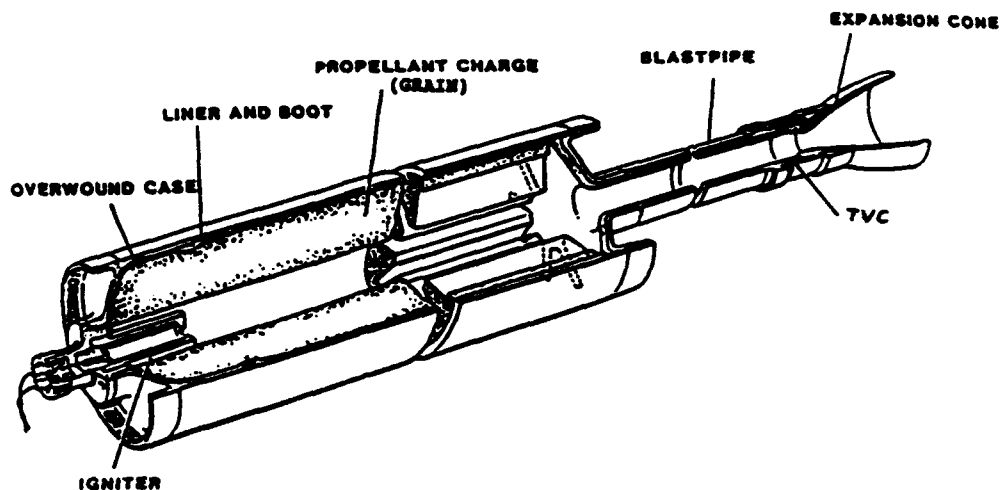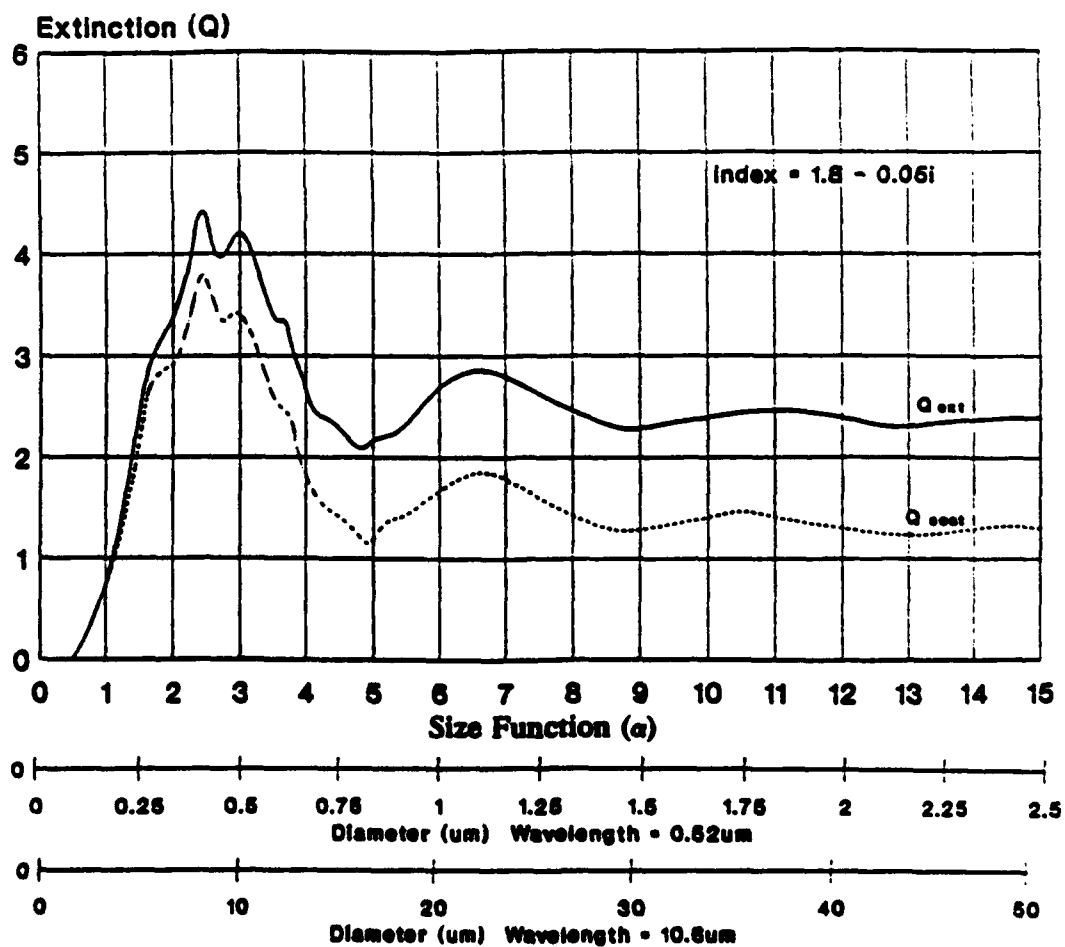Figure 1   Atmospheric Attenuation

Figure 2   Solid Propellant Rocket Motor

Figure 3   Extinction and Scattering Cross Sections for Typical Absorbing Solid
Particle (Size function $\alpha = \pi D/\lambda$).
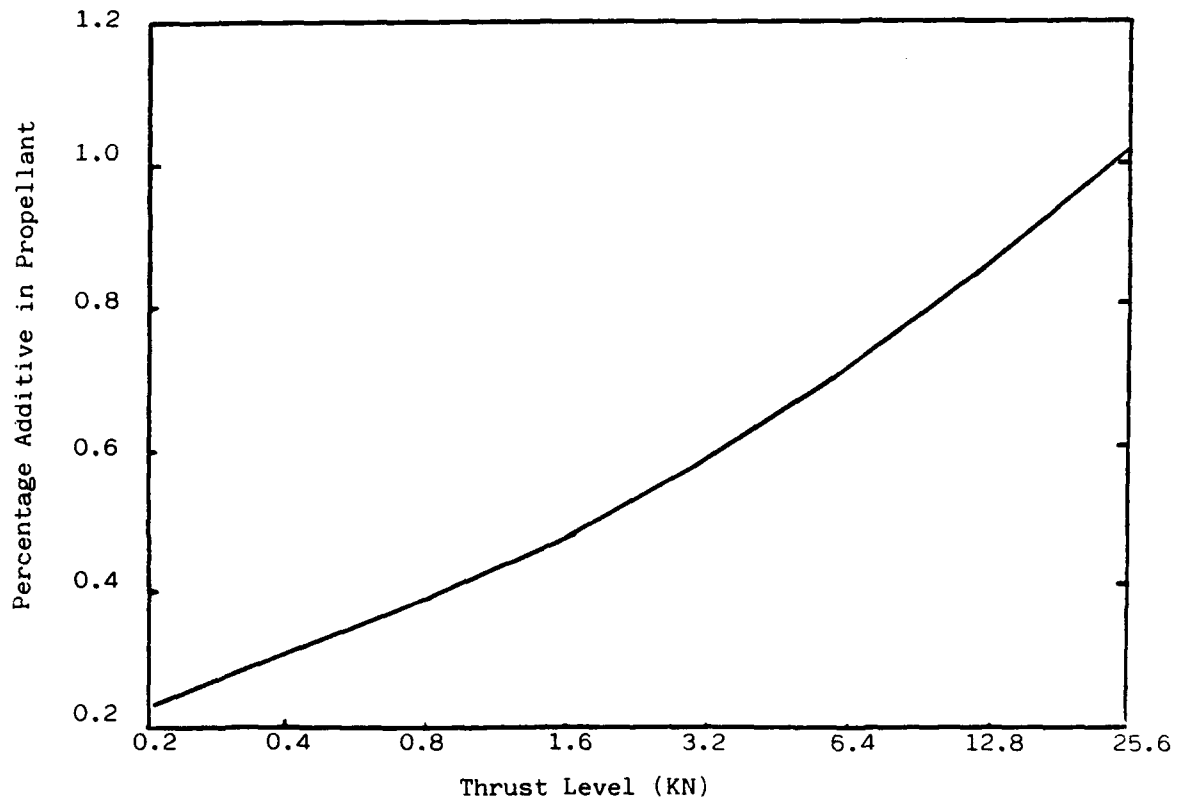
Figure 4   Additive Level to Suppress Secondary Combustion at Various Thrust
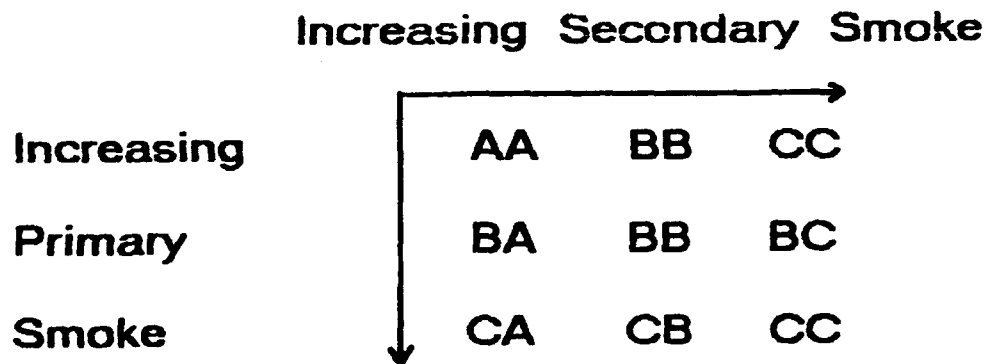   Levels.
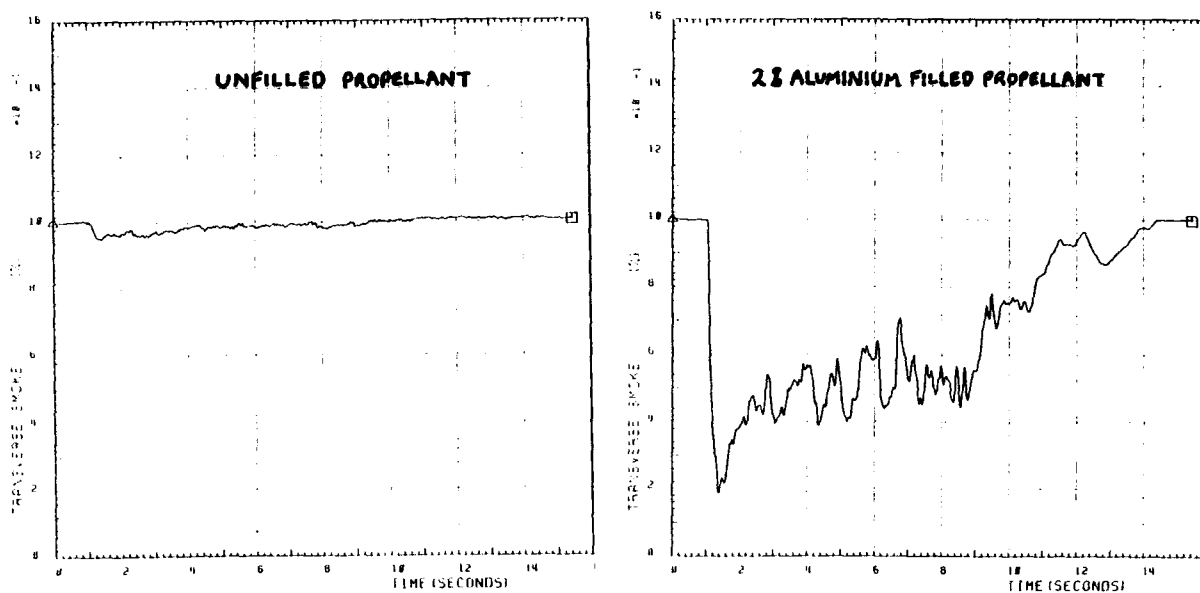

Figure 5   AGARD SMOKE CLASSIFICATION.

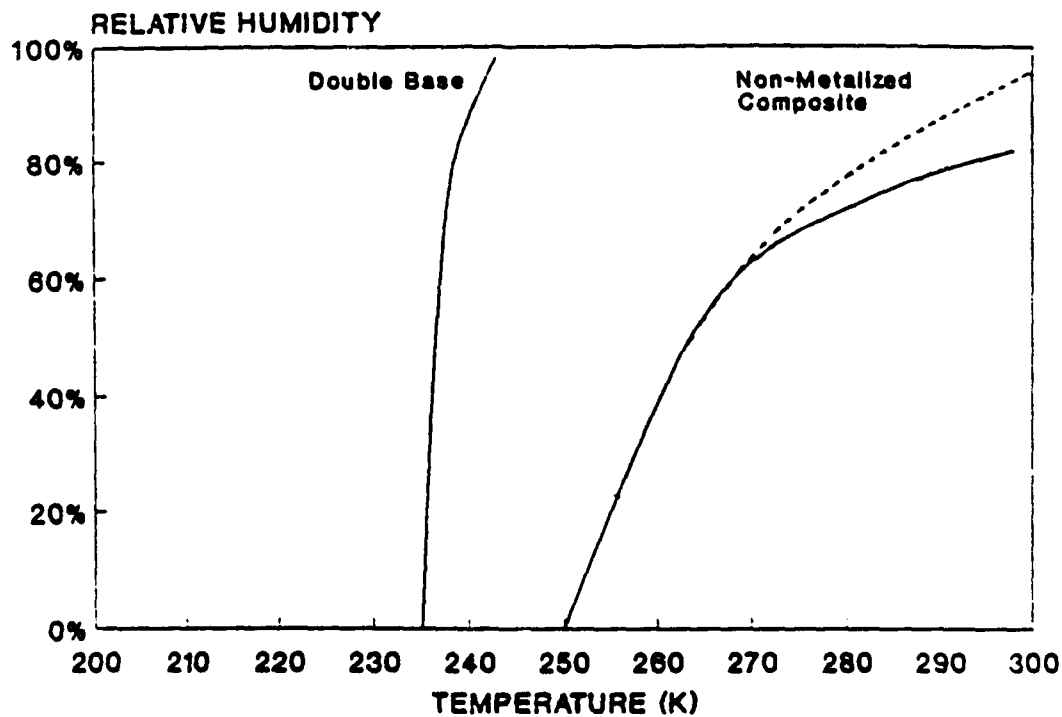Figure 6   Smoke Signature of 2% Aluminium Filled Propellant

Figure 7   Predicted Secondary Smoke Formation at Sea Level

RELATIVE HUMIDITY
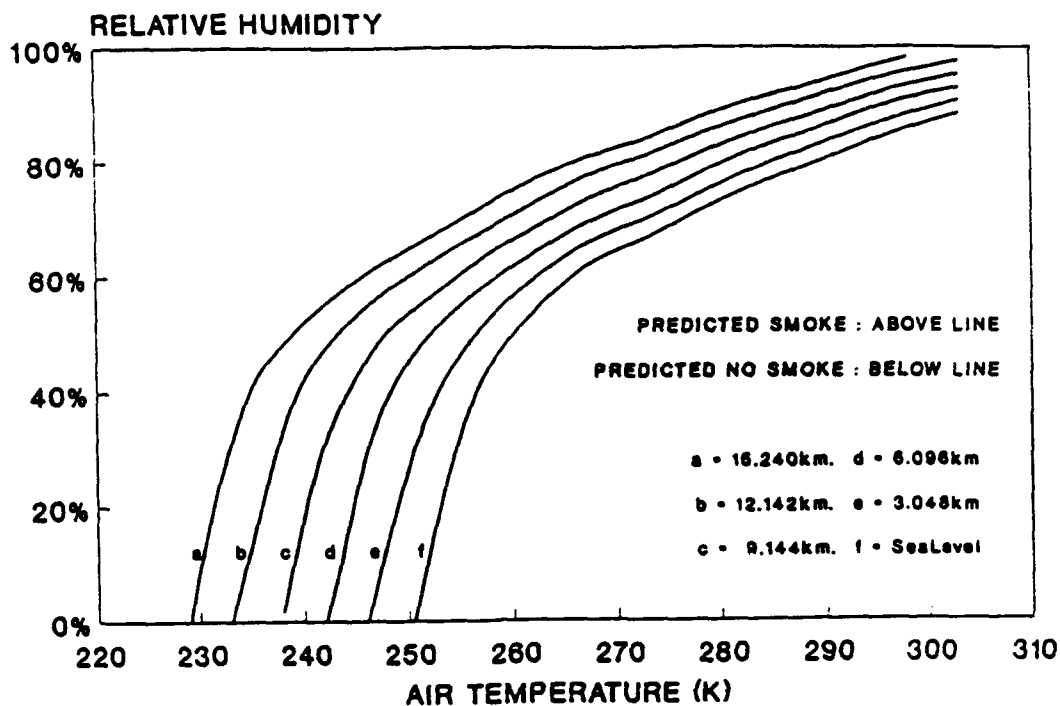
Figure 8   Predicted Secondary Smoke Formation as a Function at Altitude (Non Metallic Composite Propellant with Ammonium Perchlorate).
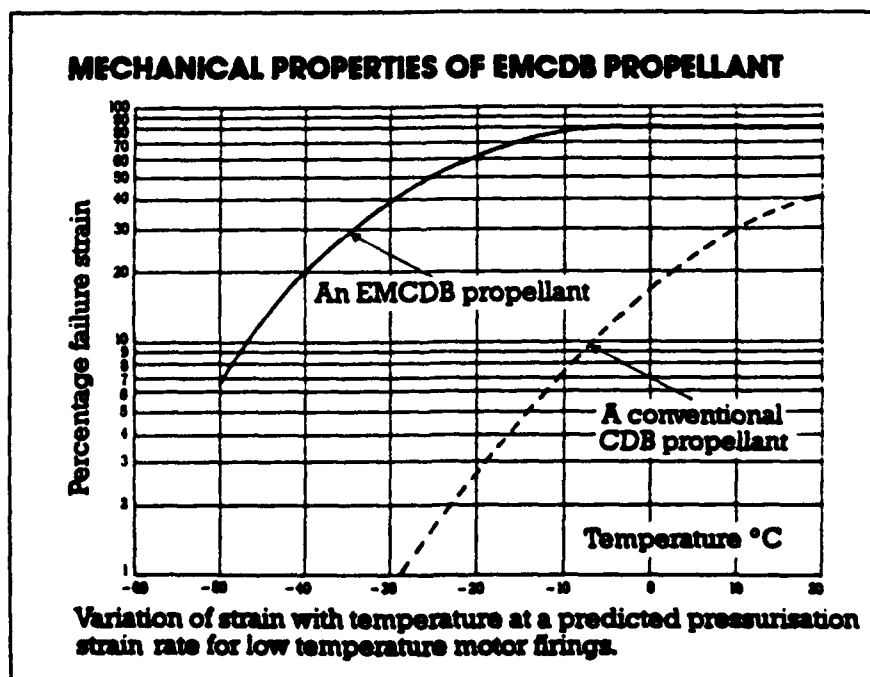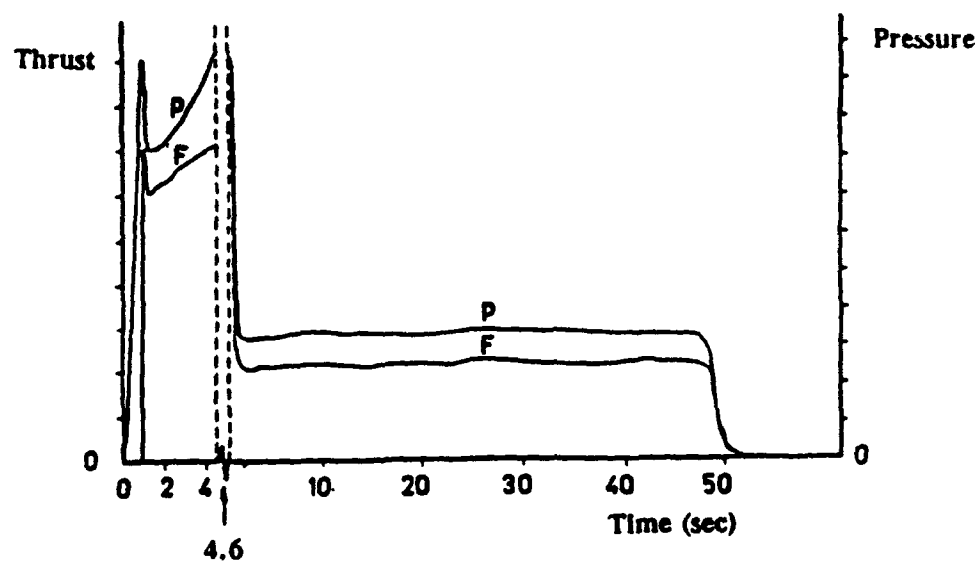

Figure 9   Comparison of Mechanical Properties CDB-EMCDB Propellants

Figure 10   Typical Thrust-Time, Pressure-Time Curves for a Boost Sustain Motor
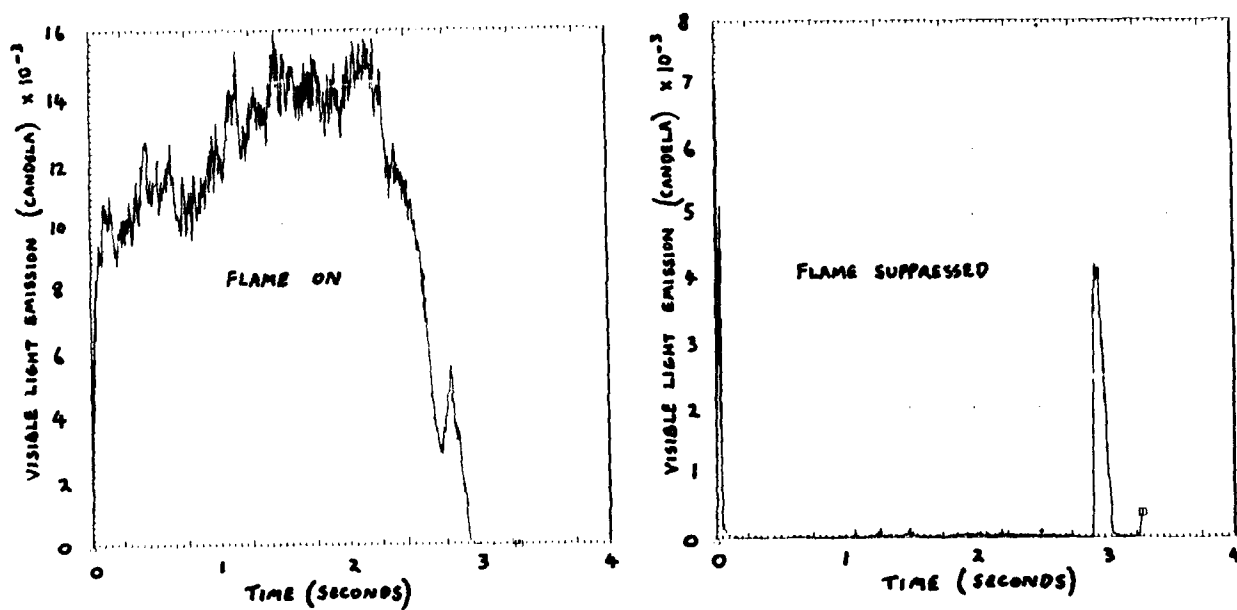

Figure 11   Plume Visible Emission (Night Firings)

Figure 12   Flame Suppression in Nitramine Filled 7 KN Thrust Motor
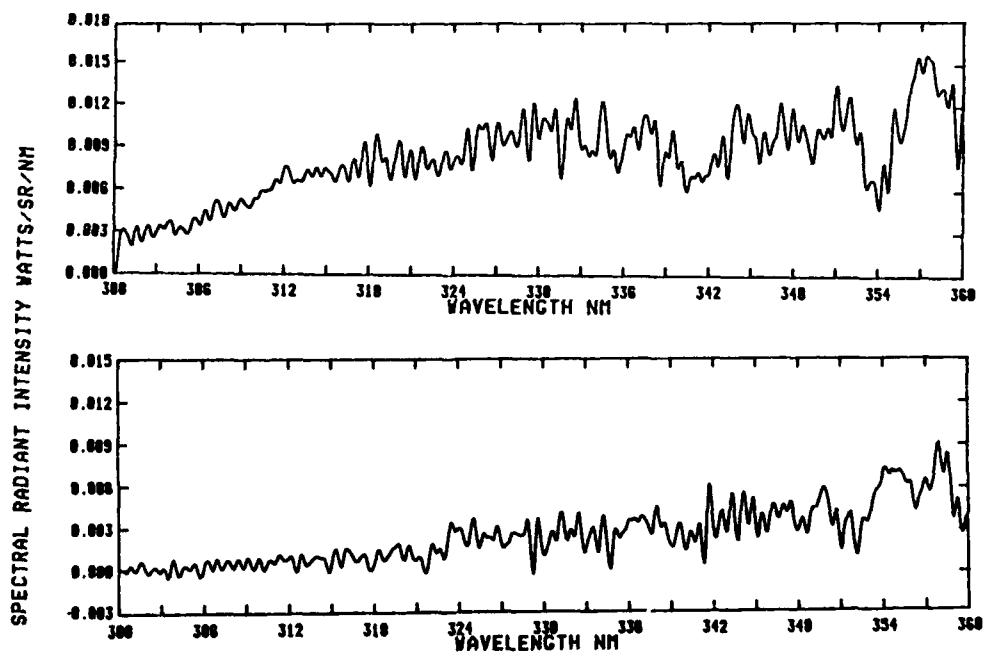

Figure 13   UV Radiometer Spectral Radiant Intensities

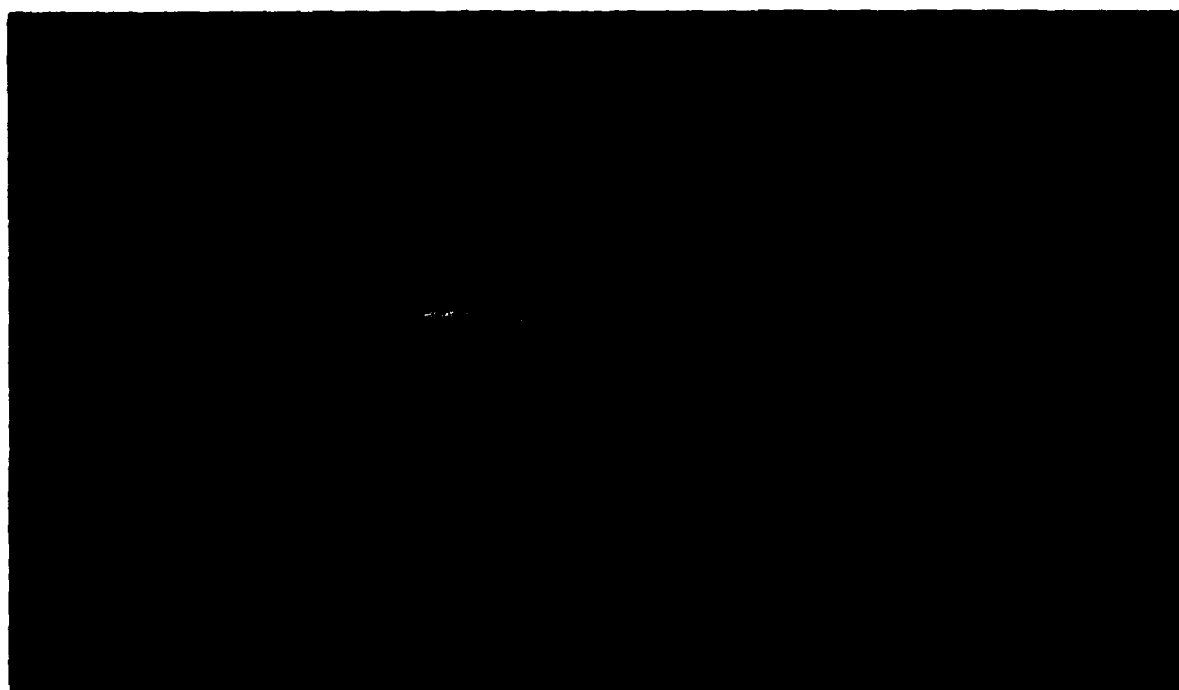Figure 14   Short Wave Infra Red (3-5 um) Radiant Intensities

Figure 15   Long Wave Infra Red (8-13 um) Radiant Intensities
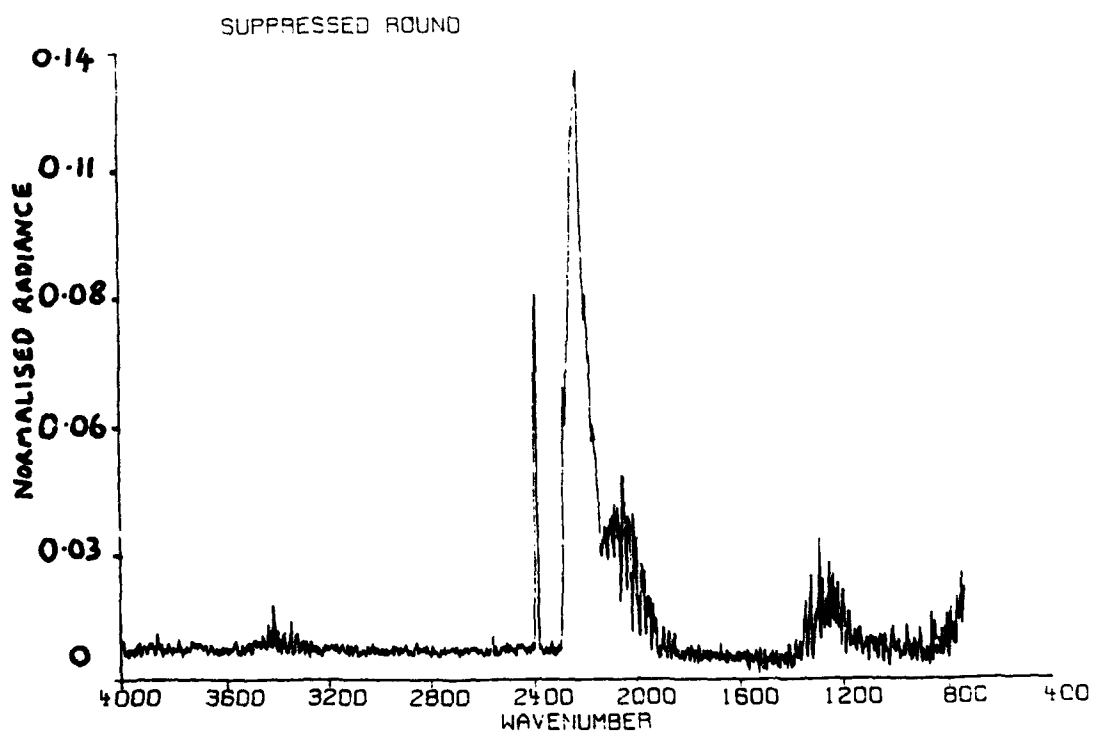
CONTROL ROUND
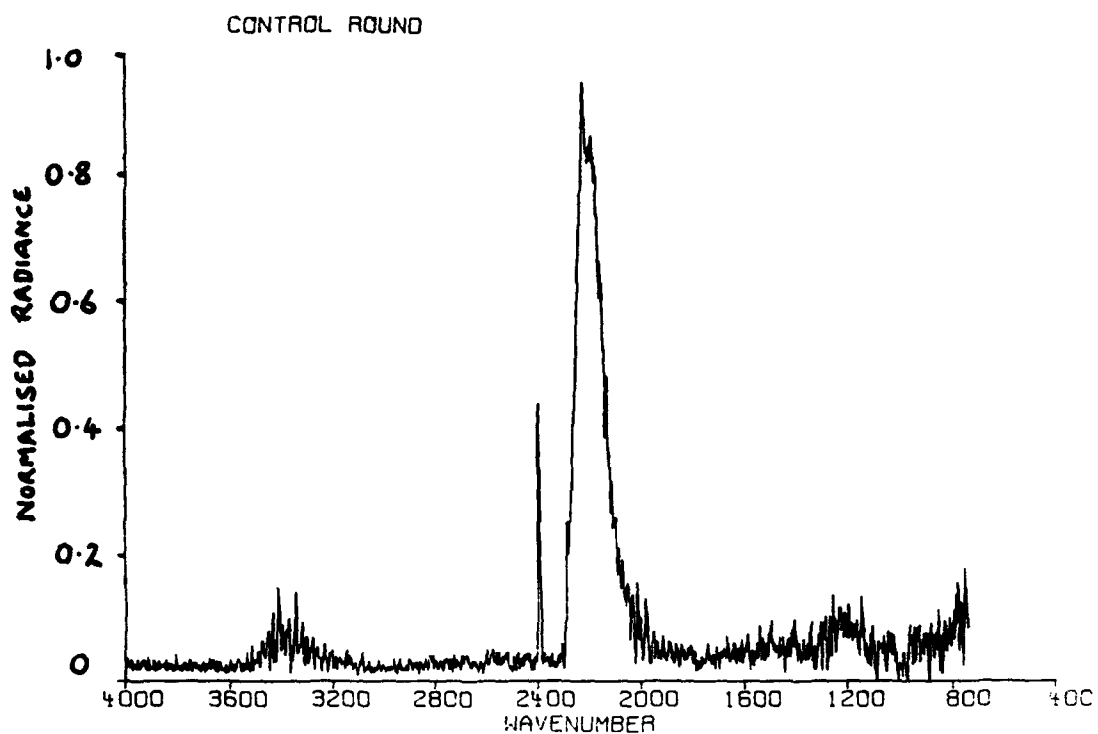

SUPPRESSED ROUND

Figure 16   Infra Red Normalised Spectral Radiant Intensities
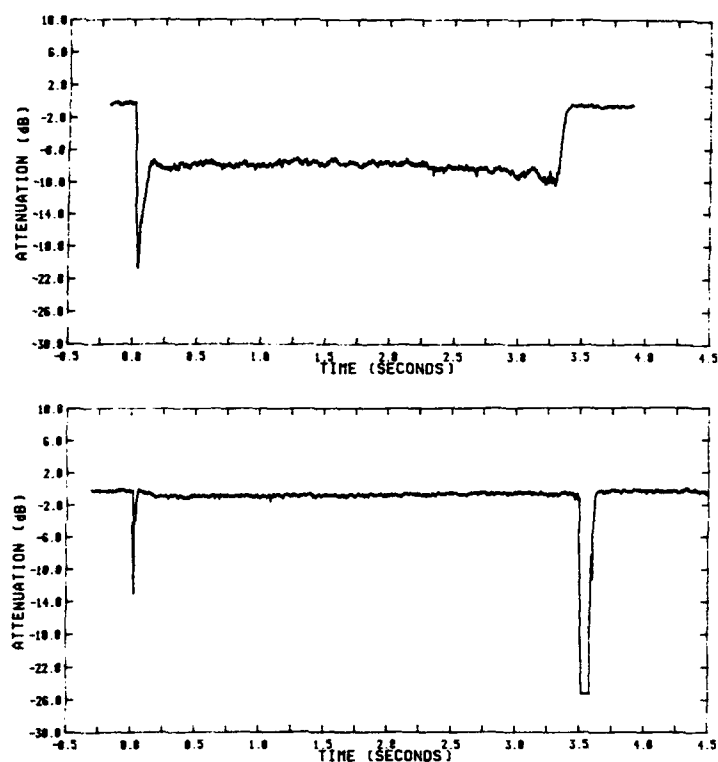
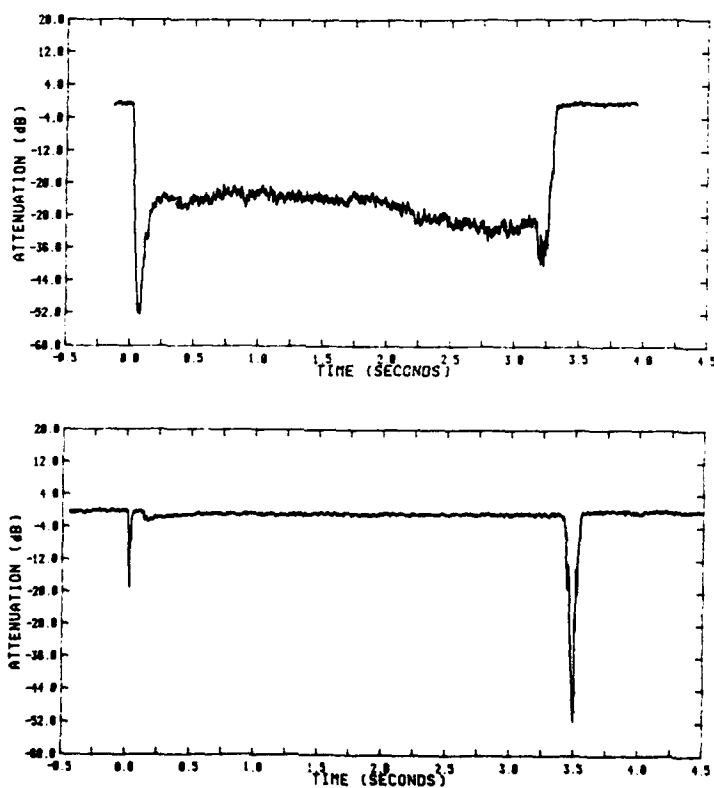Figure 17   Millimetric Wave Radar Attenuation (Normal to plume)

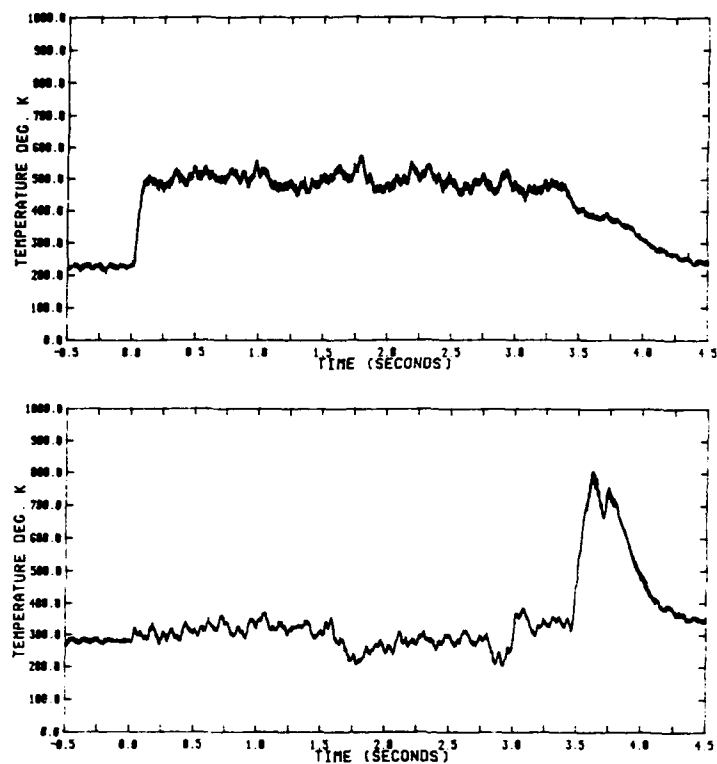Figure 18   Millimetric Wave Radar Attenuation (30° to plume)
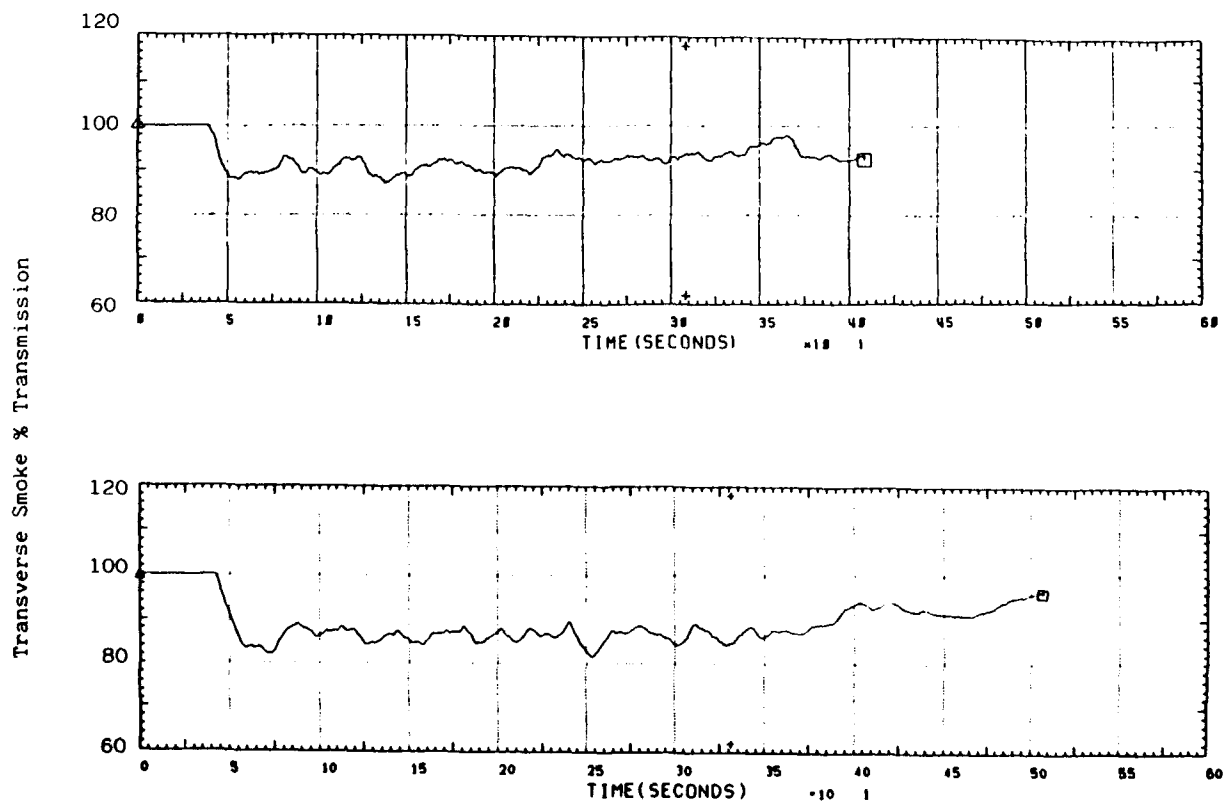
Figure 19   Millimetric Emissions (80 GHz)

Figure 20   Transverse Smoke Transmission

SECONDARY SMOKE

P. A. Kessel

Phillips Laboratory Propulsion Directorate
Edwards Air Force Base, California, U. S. A.

1. SUMMARY

The open literature on secondary smoke formation, prediction and classification is briefly reviewed. This review was limited to the open literature in order to promote the widest possible discussion within the AGARD engineering community. The recently completed PEP WG 21 proposal for smoke classification is presented. Secondary smoke is defined and the physics of condensation of vapor onto droplets is reviewed. The basis for the existing droplet condensation models is discussed and the existing methodology for predicting secondary smoke light attenuation and scattering is presented. Test data taken to establish the initial conditions for heterogeneous nucleation in rocket plumes is presented. Comparisons between secondary smoke predictions and flight data are presented. The state of the art of secondary smoke modeling is discussed and suggestions are made for improvements.

2. INTRODUCTION

Modern high performance solid rocket exhaust plumes are generally characterized by large volumes of flame and smoke that mark the location of the rocket powered device and its launch site and trajectory with unfailing accuracy and a high degree of persistence. A smoke laden plume may be either a hazard or a blessing depending upon the application. Tactical rocket designers go to great pains to eliminate smoke since it gives the enemy information about the location of the launch platform or launch site. Particle laden plumes may also interfere with microwave and laser beam signals used for range finding and communication purposes. On the other end of the spectrum, there are devices such as flares which are designed to have a very distinctive smoke laden plume for communication and countermeasures applications. This paper will attempt to summarize some of the large effort that has gone into developing methods to classify, understand, predict, measure and control the secondary smoke content of rocket plumes.

Smoke is a collection of fine liquid or solid particles that are suspended in the atmosphere such that their optical signature is in recognizable contrast to the background. The visible optical signature may arise because the particles absorb light, e.g., a carbon rich plume, which is a result of the high emissivity, or because the particles reflect or scatter light because of a low emissivity, e.g., contrails of high altitude ice crystals. In either case, the optical characteristics of the background can either obscure or highlight the plume. Attenuation of radiation along the optical path between the observer and the smoke plume also serves to obscure the plume.

Smoke in a rocket exhaust plume is classified as either secondary or primary smoke according to how it was formed. Secondary smoke is defined as the material that leaves the rocket as a vapor and subsequently condenses and solidifies as the plume cools due to expansion and mixing with the ambient atmosphere. Secondary smoke is mostly water and aqueous solutions of HCl, HF or soluble salts. At sufficiently high altitudes, secondary smoke may consist of highly reflective ice crystals that form long-lived contrails.

Primary smoke is defined as the liquid and solid particulate matter that is formed within the rocket more or less independent of any interaction with the atmosphere. Primary smoke is comprised of the oxides of the metal fuel such as aluminum, and in some cases, the soot created by the combustion process of carbon containing fuels. Primary smoke can be eliminated or at least greatly reduced by eliminating all materials from the propellant which would form a visible particulate cloud.

3. CONDENSATION CONSIDERATIONS

The condensation of the working fluid in an expansion is a problem that has concerned researchers and practical engineers for a long time (e.g., reference 1). The earliest works include those of C. T. R. Wilson in 1897 on the dynamics of cloud chamber expansions, and Stodola's work in the 1920's on steam nozzle expansions, reference 2. Hypersonic wind tunnel designers, such as Wagner, recognized that for high Mach numbers, the working fluid had to be kept at a sufficiently high total temperature to avoid condensation, reference 3.

The theory of condensation is well described in a number of thermodynamic texts. A simplified example is given here to bound the problem for further discussion. Figure 1 shows the temperature-entropy diagram of the saturation curve for water and the nozzle expansion path of water vapor to low (ambient) pressure from a range of nozzle stagnation conditions typical of solid rockets. The isentropic expansions are the envelope of vertical lines that intercept lines of constant pressure in the superheated region, i.e., no condensation occurs within the rocket nozzle. If the inevitable plume cooling process is assumed to be (for the moment) a constant pressure process, the resulting temperature at the intersection with the saturation curve would lie between 45°C and 100°C. This intersection, and the fact that the ambient temperature lies between -56°C and 55°C, indicates a high probability for the occurrence of condensation. Actually, the process is more complicated than this simple model since the water vapor is cooled by mixing with the ambient atmosphere, which may or may not be able to carry the water vapor in solution along with its burden of ambient humidity.
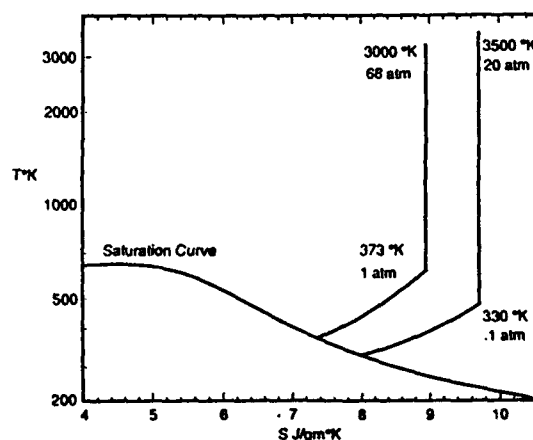
Fig. 1   Condensation Considerations on the T-S Plane.

Other variables that have been ignored in this simplified discussion, such as the role of dissolved gases and the role of droplet surface tension, are discussed in reference 5 which is summarized below. The effect of dissolved gases on the saturation vapor pressure of a solution over a plane surface, $\bar{p}$, can be approximated by:

$$\bar{p} = \frac{p^\circ}{(1 + in/n_s)} \qquad (1)$$

where p° is the saturation vapor pressure of the pure substance, i is the osmotic coefficient, n_s is the number of moles of solvent, and n is the number of moles of the solute, reference 4. Although the value of i is unity for an ideal solution, its value may be as high as 40 for concentrated solutions of HCl dissolved in water.

The correction on the effective vapor pressure due to droplet radius of curvature is:

$$\frac{p_r^\circ}{p^\circ} = exp\left(\frac{2\sigma v}{RTr}\right) \qquad (2)$$

where σ is the surface tension, v is the specific volume, R the gas constant, T is the temperature, and r is the droplet radius. This in effect increases the vapor pressure required to produce further condensation on the droplet. These two equations combine to give the vapor pressure for a solvent droplet, p_r:

$$p_r = p^\circ \frac{exp(2\sigma v/RTr)}{(1 + in/n_s)} \qquad (3)$$

This can be simplified to:

$$p_r = p_{sol}^\circ \, exp(2\sigma v/RTr) \qquad (4)$$

where p_{sol}° is an experimentally determined solution saturation partial pressure.

An example of how these effects determine where in the plume condensation occurs is illustrated in Figure 2, taken from reference 4. In this figure, the plume state conditions were modeled as a function of axial and radial distance. (That is, a consistent set of approximations were used to define the state properties and velocity of the expansion.) The gas temperature along the plume centerline corresponds to the intersection of the isentropic expansion and the constant pressure line in Figure 1. Condensation usually cannot occur here because the temperature is too high. As the mixing progresses, the gas temperature decreases due to the plume being diluted with ambient air. This process can be thought of as either cooling the hot moisture-laden plume or as increasing the moisture content of the ambient air. Two lines are shown in the figure. Line (a) is the locust of points at 21.1°C and 100% relative humidity. Line (b) is the locust of points at -40°C and 0% relative humidity. Lines (a) and (b) define the minimum point at which HCl and water will satisfy equation (1). Condensation of HCl can only occur outside of line (b), and condensation of water can only occur outside of line (a). Further limitations on condensation have not been addressed in this plot. The actual region of condensation will be less than indicated.
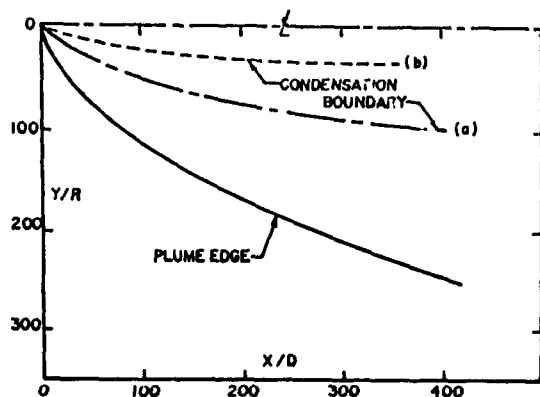

Fig. 2   Zones of Condensation in a Plume, ref 4.

Oliver has worked out the limiting cases for plane surface condensation. The first limiting case, labeled isothermal mixing, holds both the mixture temperature at the ambient air temperature and the ratio of air to plume gas constant. Thus the composition of the "air" is changed slightly to reflect mixing with the plume. The second limiting case, adiabatic mixing, conserves energy in the mixing process and sets the ratio of air to plume gas at the maximum which will permit condensation to occur at the specified temperature at sea level. Figure 3 shows the minimum relative humidity at which condensation will occur as a function of temperature for the two limiting cases for several propellants. That is, condensation may occur above these curves subject to the other limitations discussed above, but it cannot occur below these curves for the assumed mixing model. It is assumed that condensation will occur somewhere between the adiabatic and isothermal limits that are said to bound the problem.
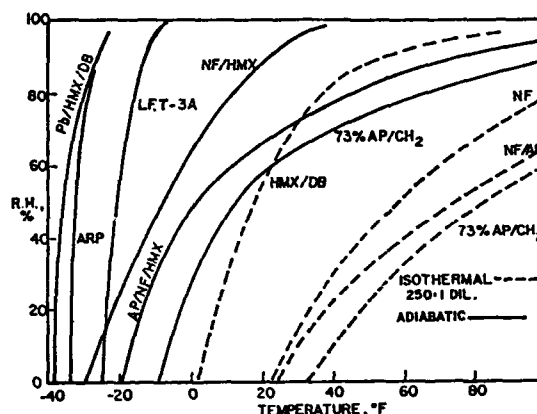

Fig. 3   Oliver Fog Predictions, ref 4.

The size of a drop in equilibrium with the condensing gas can be derived from equation (4):

$$r^* = 2\sigma v / \left(RTr \, ln(\frac{p}{p_{sol}^\circ})\right) \qquad (5)$$

This droplet is unstable. Rewriting equation (5):

$$p_{sol}^\circ = p \, exp\left(\frac{2\sigma v}{r^* RTr}\right) \qquad (6)$$

If the droplet grows by the addition of one molecule, the droplet radius increases but the vapor pressure at infinite extent does not increase, as discussed in reference 1. The slightly enlarged droplet has a lower equilibrium vapor pressure which allows additional molecules to be accepted. The process is continuous. Conversely, loss of a single molecule increases the vapor pressure and causes a continuous evaporation process. Since a droplet cannot grow if it is smaller than the critical radius, condensation requires a nucleation site whose radius is above the critical radius if condensation is to occur.

These nucleation sites can be formed by the spontaneous collision of molecules if the molecular density is high enough, or can exist as particles or droplets of a dissimilar material. Droplet growth by collision of similar molecules is call homogeneous nucleation. Droplet growth by collision with dissimilar molecules or particles is called heterogeneous nucleation.

The classical expression for nucleation rate is:

$$J = \sqrt{2/\pi} \left(N_A^{2/3}/R^2 \right) (p/T)^2 \left(\sqrt{\sigma \bar{M}}/\rho_r \right)$$
$$\times exp\left[-n^* \, ln(p/p_{sol}^\circ)/2 \right] \qquad (7)$$

where

$$n^* = (4\pi/3)\rho_r (N_A/\bar{M}) r^{*3} \qquad (8)$$

It can be seen that the rate of nucleation is a function of the ratio of p/p_{sol}°.

Unfortunately, the predictions of nucleation rate using equation (7) are orders of magnitude too low, strongly indicating that the nucleation process in solid rockets is heterogeneous. It is then necessary to rely on an empirical approach to accurately predict rocket plume droplet spatial distributions.

4. PREDICTION METHODOLOGY

4.1 Droplet Growth

From what we have discussed so far, it is obvious that the formation of secondary smoke is a dynamic process. This process is identical to the formation of clouds and rain. It is well known that this meteorological process can be influenced by seeding the clouds to create nucleation sites, and therefore obtain precipitation from the clouds. It should come as no surprise that the key to predicting the formation of secondary smoke is the prediction, albeit empirical, of the initial nucleation sites. Given the initial nuclei distributions, the differential equations describing droplet growth are integrated along Eulerian particle trajectories to predict the droplet distributions in the rest of the plume.

Several models exist in the open literature for the prediction of secondary smoke, notably the models of Miller, reference 4, Meyer, reference 5, Victor, reference 6, Wu, reference 7, and Shanks, reference 8. These models all share an approach in which the modeler uses a nozzle and plume flowfield which is computed ignoring the existence of droplets, then superimposes or overlays a highly empirical approach to predicting the further effects of heterogeneous condensation on droplet size. Alternatives to this approach exist in which the fully coupled flowfield and droplet field equations are solved simultaneously, such as the work of Courtney, reference 9, Kang, reference 10, McBride, reference 11 and Sugawara, reference 12. This approach is necessary for applications in which a large fraction of the working gas condenses and highly accurate predictions are desired. However, the cost in computational difficulty and computer time can be high. The approximate uncoupled approach used by the smoke community is consistent with the empirical basis for the initial conditions used in secondary smoke predictions.

The most comprehensive of these empirical models appears to be the model of Miller, reference 4, which will be described below. The rate of droplet growth is given by:

$$r\frac{dr}{dt} = \Phi_D (vD_f/RT_f) \left(\frac{p - p_r}{1 - p_r} \right) \qquad (9)$$

where the experimental correlation of mass transfer to the spheres is given as:

$$\Phi_D = 1.0 + 0.3Re_f^{1/2} Sc_f^{1/3} \qquad (10)$$

Several corrections are made to account for non-ideal factors. Since the droplet size is of the same order as the ambient mean free path, this classical equation for molecular diffusion is corrected by a factor derived from the work of Fuchs, as described in reference 4:

$$1/ \left[(2\pi \bar{M}/RT_r)(D/r\beta) + (r/(r + L)) \right] \qquad (11)$$

where β is a coefficient to correct for molecule rebound. The value of β is assumed to be unity for water, HCl and HF. Another correction factor is applied to the evaporation rate to compensate for the effect of condensation on the molecular velocity:

$$w = 2.0 \quad \text{for} \quad 0.000 < abs(s) < 0.001 \qquad (12)$$

where s is the ratio of the gas velocity normal to the surface of the droplet to the mean thermal speed of the gas molecules.

The resulting equation for the rate of change of drop radius is:

$$r\frac{dr}{dt} = \Phi_D^* (vD_f/RT_f) \left(\frac{p - p_r}{1 - p_r} \right) \qquad (13)$$

where:

$$\Phi_D^* = 2\Phi_D / \left[(2\pi \bar{M}/RT_r)^{1/2}(D/r) + 2r/(r + L) \right] \qquad (14)$$

The final result, equation (13), describes the droplet rate of growth for each condensing component.

Similarly the change in droplet temperature due to convective heat transfer is given by the basic equation:

$$mc_p \frac{dT_r}{dt} = \Phi_h^* k_f \cdot 4\pi r(T - T_r) + \dot{H}_c + \dot{H}_s \qquad (15)$$

where

$$\Phi_h^* = \frac{\Phi_h k (2\pi \bar{M} RT_r)^{1/2}}{C_p(\gamma + 1)/2\gamma)Pr\alpha + r/(r + L)} \qquad (16)$$

and

$$\Phi_h = 1.0 + 0.3Re_f^{1/2} Pr_f^{1/3} \qquad (17)$$

A correction for the effect of turbulent eddy size relative to the drop size is applied as appropriate:

$$u_r^2 = u'^2 \int_0^\infty (\Omega^{(1)}/\Omega^{(2)})\epsilon(k)dk \qquad (18)$$

where $\epsilon(k)$ is the turbulent eddy spectrum of the local gas stream, and is a function of the turbulence wave number, k:

$$k = 2\pi\omega/u_m \qquad (19)$$

where u_m is the average plume centerline gas velocity relative to the plume edge velocity. Also,

$$\Omega^{(1)} = [((1 - \beta)/\beta)(\omega/\alpha)]^2 \qquad (20)$$

$$\Omega^{(2)} = (1/\beta^2)(\omega/\alpha)^2 + (\sqrt{6}/\beta)(\omega/\alpha)^{3/2}$$
$$+ 3(\omega/\alpha) + 6(\omega/\alpha)^{1/2} + 1 \qquad (21)$$

$$\alpha = 3v/r^2 \quad , \quad \beta = 3\rho/(2\rho_r + \rho) \qquad (22)$$

Other details in Miller's paper give higher order corrections to the drag coefficient change due to high Reynolds number and turbulent velocity fluctuations. The droplet velocity is correlated to the freestream velocity and the statistical turbulent fluctuations. The droplet size distributions are then calculated starting with the initial nuclei distributions and the relations for droplet growth and droplet temperature. The effects of droplet coagulation and Brownian motion, turbulent diffusion and other higher order effects are neglected.

4.2 Signature Prediction

4.2.1 Mie Theory

The particles in the plume scatter light in three basically different ways according to the relationship between the wavelength of the light and the size of the particle. If the wave-

length of the light is small relative to the particle, the light behaves as is does in the macroscopic world, and the result is called geometric scattering or geometric optics. If the wavelength of light is much larger than the particle, the particle scatters the light in a more or less predictable and uniform way that is called Rayleigh scattering (molecules in the air scatter sunlight preferentially as a bright blue light). If the wavelength of light is on the same order as the particle size, the light is scattered in a more complex way that is called Mie scattering. The Mie parameter α is defined as the ratio of particle circumference to wavelength:

$$\alpha = 2\pi r/\lambda \qquad (23)$$

Unfortunately, the wavelength of visible light is of the same order as the circumference of the secondary smoke condensate particle, which forces us to resort to Mie theory for our scattering predictions.

Mie theory describes the scattering of light by single spherical particles, references 15 and 16. The assumption of sphericity is reasonable for small droplets in which surface tension dominates the deforming aerodynamic forces. (It is not a very good assumption for solid particles such as sand and ice whose crystalline structure dominates the particle shape). Mie theory is appropriate for particles that are widely spaced relative to one another. This minimum spacing is generally taken as ten particle diameters. Below that spacing, the particle optical effects interfere with each other and an additional correction factor must be applied to the results obtained using Mie theory.

An additional parameter to be considered is optical depth, τ, which is defined as:

$$I/I_o = exp(-\tau) \qquad (24)$$

where I/I_o is the fraction of light that passes through a cloud of particles (or anything else for that matter). If the optical depth is less than 0.1, then the cloud is said to be optically thin. If τ is greater than 0.3, the cloud is said to be optically thick, and the full corrections for multiple scattering must be applied. The intermediate range, $0.1 < \tau < 0.3$, is called the double scattering regime, which may require some correction. Note that the effects of multiple scattering and close particle spacing are different phenomena which can and should be treated differently. In a large diffuse plume we may get multiple scattering, that is the light interacts with many particles before it leave the plume, but still have a large enough particle spacing to apply uncorrected Mie theory on small areas of the plume.

The calculation of the Mie scattering function is complex. Full details are given in references 14 and 15. Hottel has collected these functions in reference 16:

$$Q(\theta) = \frac{1/2}{(2\pi/\lambda)^2} \left[i_\perp(\theta) + i_\parallel(\theta) \right] I \qquad (25a)$$

$$p(\theta) = 4 \left[i_\perp(\theta) + i_\parallel(\theta) \right] / (X_s x^2) \qquad (25b)$$

The expression of $i_\perp$ and $i_\parallel$ as functions of the size parameter x, the refractive index, n', and the angle θ and the definition of associated functions needed to evaluate extinction and scatter efficiency X_t and X_s are presented below:

$$i_\perp(\theta) = \left[\sum_{m=1}^{\infty} \frac{2m+1}{m(m+1)} \left(a_m \pi_m + b_m \tau_m \right) \right]^2$$

$$\qquad (25c)$$

$$i_\parallel(\theta) = \left[\sum_{m=1}^{\infty} \frac{2m+1}{m(m+1)} \left(a_m \tau_m + b_m \pi_m \right) \right]^2$$

where π_m and τ_m are angular functions derived from the Legendre polynomials

$$\pi_m(cos\theta) = \frac{dP_m(cos\theta)}{dcos\theta}$$

$$\tau_m(cos\theta) = cos\theta \, \pi_m(cos\theta) - sin^2\theta \, \frac{d\pi_m(cos\theta)}{dcos\theta} \qquad (25d)$$

P_m, the Legendre polynomials, are finite series defined by

$$P_m(x) = \frac{1}{2^m m!} \frac{d^m (x^2-1)^m}{dx^m} \qquad (25e)$$

a_m and b_m (the amplitude functions) are given by

$$a_m = \frac{S'_m(y)S_m(x) - n'S'_m(x)S_m(y)}{S'_m(y)\phi_m(x) - n'\phi'_m(x)S_m(y)}$$

$$\qquad (25f)$$

$$b_m = \frac{n'S'_m(y)S_m(x) - S'_m(\tau)S_m(y)}{n'S'_m(y)\phi_m(x) - \phi'_m(x)S_m(y)}$$

where $y = n'x$, and

$$S_m(z) = (\pi z/2)^{1/2} J_{m+1/2}(z)$$

$$\qquad (25g)$$

$$C_m(z) = (-1)^m (\pi z/2)^{1/2} J_{-m-1/2}(z)$$

Here $J_{m+1/2}$ and $J_{-m-1/2}$ are Bessel functions of the positive and negative half-orders, and

$$\phi_m(z) = S_m(z) + iC_m(z)$$

$$S'_m(z) = \partial S_m(z)/\partial z \qquad (25h)$$

$$\phi'_m(z) = \partial \phi_m(z)/\partial z$$

The efficiency factors for extinction and scatter can be derived from the values of a_m and b_m.

$$X_t = \frac{2}{x^2} \sum_{m=1}^{\infty} (2m+1)\Re(a_m + b_m)$$

$$\qquad (25i)$$

$$X_s = \frac{2}{x^2} \sum_{m=1}^{\infty} (2m+1)\Im \left(|a_m|^2 + |b_m|^2 \right)$$

X_a is obtained by difference. The above equations should give the reader some feeling for the complexity of evaluating the scatter properties.

The results of a typical Mie calculation are shown in Figure 4 for a range of aluminum oxide particle sizes for 0.55 μm wavelength light from reference 7. Since the particle radius varies from 0.01 to 5.20 μm, the Mie parameter varies from 0.114 to 59.4, which would cover the range from Rayleigh scattering to geometric optics. The plot shows that the light scattered forward preferentially, $0°$ scatter. The smaller particles show the trend toward Rayleigh scattering. The Mie theory is accurate, although cumbersome, in both the Rayleigh and geometric optics limits.

Complicated computer programs have been developed that accurately compute the optical behavior of optically dense two phase rocket plumes using Mie theory, reference 17. This is done by breaking the plume up into a large number of elements, each of which are optically thin. The mathematics of the solution are cumbersome. Suffice it to say that the bookkeeping allows each element to scatter and absorb radiation in the directions dictated by Mie theory in such a way that the multiple scattering limitation of Mie theory does not affect the accuracy of the result. These codes, in general, do not address the issue of extremely close particle spacing. The major problem with the finite difference approach to Mie scattering is the fact that, in theory, every element in the plume receives scattered radiation from every other element. This would lead to approximately $N \times N/2$ flux directions for a grid containing N elements. A number of limited flux direction models have been developed, the simplest effective model being the six flux model for three dimensional problems. These models work quite well for the areas in the plume where there are only weak radiative property gradients.
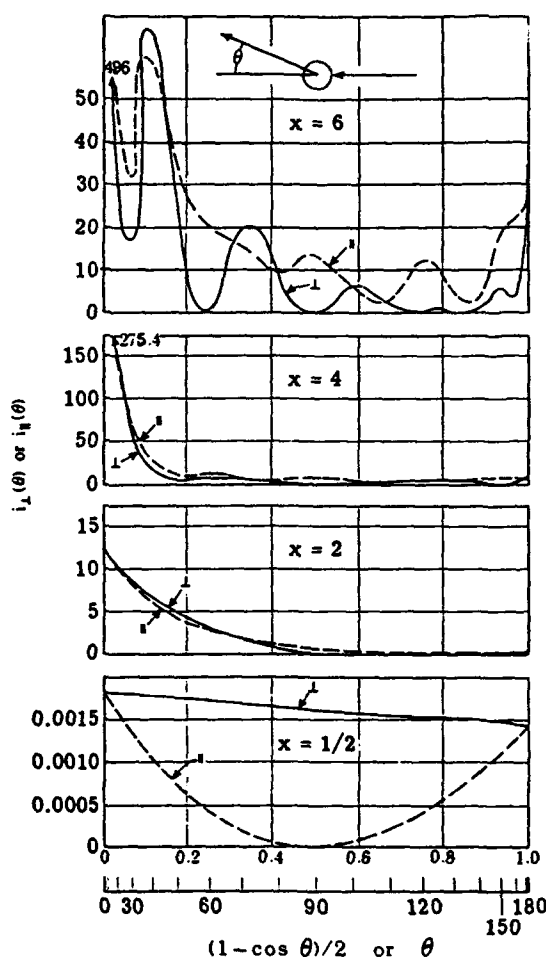
Fig. 4   Angular Distribution of Radiation Scattering
for Spherical Non-absorbing Particles, ref 16.

4.2.2 Approximate Methods

In contrast to the "correct" finite difference approach, a number of simplified signature models have been developed. Miller has simplified the Mie function by averaging the Mie function such that a particle extinction coefficient, K, can be calculated which satisfies the attenuation relation:

$$I/I_o = exp(-N\pi r^2 KL) \qquad (26)$$

Figure 4 shows how the extinction coefficient varies with particle index of refraction for $m=1.55$ as a function of the Mie parameter. Equation (26) must be integrated over the plume and may accommodate the variation in plume properties as a function of position:

$$ln(I/I_o) = -\int_0^L \int_0^\infty NKf(r)\pi r^2 dr dX \qquad (27)$$

The values of N and K can be computed from the known properties of the plume once the particle cloud is defined. Equation (27) is integrated over the plume and the attenuation of the light determined.

5. VISIBILITY CRITERIA

Reduced to its essence, the visibility evaluation consists of predicting the spatial signature of the plume in the desired

waveband, i.e., 0.40 to 0.78 μm, and comparing it to the signature of the background, and deciding if the resulting signature is discernible. Victor, reference 6, outlines a simple visibility model that he developed from the work of Jarman, reference 13. This method addresses all the elements necessary for a thorough visibility calculation and is summarized below.

He defined the contrast, C_o, between an object whose brightness is B, and the background whose brightness is B_o as:

$$C_o = (B - B_o)/B_o \qquad (28)$$

when observed close enough to the object so that there is no obscuration of the signal. If the observer is far away from the object, the signal from the object and from the background will be attenuated. The apparent contrast becomes:

$$C_R = C_o(B_o/B_r)exp(-\sigma R) \qquad (29)$$

The apparent brightness of the background will be:

$$B_r = B_o\, exp(-\sigma R) \qquad (30)$$

where R is the distance to the background, σ is the atmospheric attenuation coefficient (in units of km^{-1}), and B_r is the path luminance added due to the signal from the sun and the light scattered into the optical path. Therefore:

$$C_R = C_o(1 + B_R\, e^{\sigma R}/B_o)^{-1} \qquad (31)$$

and the path luminance is given by:

$$B_R = KB_o(1 - e^{-\sigma R}) \qquad (32)$$

where K is the ratio of horizon sky brightness to background brightness. Values of K vary:

0.2	Snow in sunlight
3.0	Zenith Sky in sunlight
1.0	Desert in sunlight
5.0	Forest in sunlight
1.0	Snow under overcast sky
1.0	Zenith overcast sky
7.0	Desert under overcast sky
25.	Forest under overcast sky
1 to 3	Rough seas
5+	Smooth seas under clear sky
1-	Smooth seas under overcast sky.

The threshold of visual contrast is defined as that value of contrast at which the object cannot be distinguished from the background. This is sometimes called the liminal contrast. The liminal contrast is an inverse function of size, or rather substended angle of the object. As the range to an object increases, its liminal contrast increases because the angle substended becomes smaller. Simultaneously, the apparent contrast between the object and its background, as described by equation (16), becomes smaller and the object fades from view. It should be noted that although this concept is based upon an assumed visual acuity of a human being, we can generate mathematical analogs that are related to the characteristics of optical sensors, background clutter, and random noise in the data gathering system. The signal from the plume to the observer is a function of the sunlight and skylight scattered by the plume into and the light transmitted through the plume along the optical path. Mathematically this is:

$$C_o = (B_p/B_o)-1 = B_{sun}/B_o + B_{sky}/B_o + B/B_o - 1 \qquad (33)$$

The criteria used to determine whether a plume is detectable by a human is subjective. Hoshikawa developed a model to do just that from data collected for a large variety of jet aircraft over a range of operating conditions, reference 17. Figure 5 shows experimental data which established the threshold of perception as a function of subtended angle. Figure 6 shows the probability of detection as a function of relative contrast as developed by Blackwell, described in reference 4.
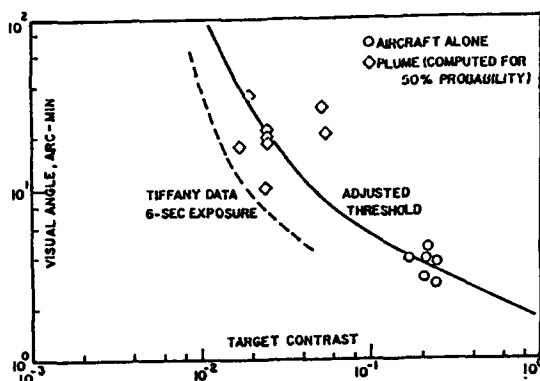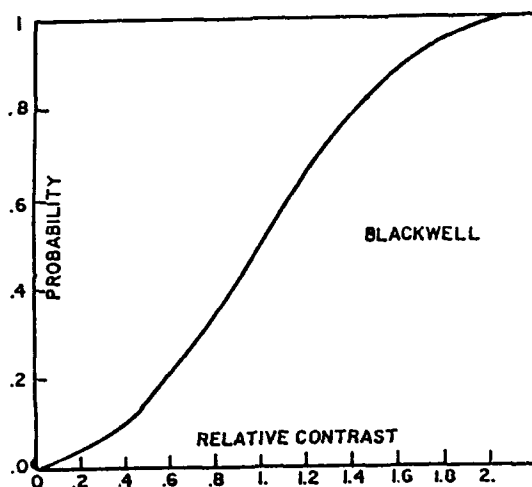
Fig. 5   Threshold of Perception, ref 4

Fig. 6   Probability of Detection as a Function of
Relative Humidity, ref 4.

6.0 NUCLEATION DATA BASE

It was mentioned above that secondary smoke is generated by heterogeneous nucleation, and that we cannot predict the nucleation sites from first principles. The obvious alternative is to perform tests to determine just what nucleation material exists at the exit plane of the nozzle.

6.1 Test Facilities

Data from two facilities has been available to determine the nucleation populations. The US Army Missile Command (MICOM) built a Smoke Characterization Facility (SCF) at Redstone Arsenal to facilitate testing of components of ground and airborne weapons systems to determine if they would function correctly in a smoky environment. The facility allows testing of small, i.e., 65-75 gram, solid rocket motors in a static environment into a humidity and temperature controlled atmosphere. The test procedure is to fire the motor into the controlled static environment and take data to characterize the smoke after the plume gases are mixed with the controlled ambient gases. A variety of data acquisition systems are in use at the facility. The USAF Arnold Engineering Development Center (AEDC) ballistic

range was modified to allow testing of a small scale rockets in their ballistic range. The ballistic range contains a 1000 ft long by 10 ft diameter tank downstream of the gun barrel in which flight conditions can be simulated. The chamber allows short flights in a controlled high altitude environment. External to the altitude chamber, a short environmentally controlled sea level chamber was built to catch the ballistic vehicle and obtain condensation data. Extensive instrumentation also exists in these facilities.

6.2 Data and Analysis

Data taken in the SCF, shown in Figure 7, was analyzed to determine the nuclei size and number. A number of assumptions are made in developing this data. It is assumed that the number of droplets present in the chamber are representative of the number of active nucleation sites throughout the firing. That is, there is no appreciable coalescence, breakup, homogeneous nucleation or deposition on the chamber surfaces. It is also assumed that all droplets in the chamber are the same size and that all the hydrogen is afterburned to form water. Light transmission measurements were made at 0.52, 0.63, 0.85, 0.95, and 1.06 μm wavelengths. The equilibrium temperature and partial pressures of condensable gases were recorded.

The values of the number density, N, the average radius, and the chemical composition of the droplets were calculated and are shown in Figure 7 for two types of propellants. Taken as a whole, the data indicate that the number density, N, is proportional to the particle size to the -0.5 to -1.0 power. Insufficient data exist to make any statement about how the exponent varies as a function of propellant. The data does support a statement that the maximum number density is proportional to the percentage of ammonium perchlorate (AP). There is insufficient data to support any general comment about the role of ammonium nitrate (AN). Miller draws the conclusion that the number of nuclei measured are about 3 to 6 orders of magnitude smaller than that observed for homogeneous nucleation of water, and that the reduced data are consistent with the results of other experiments.
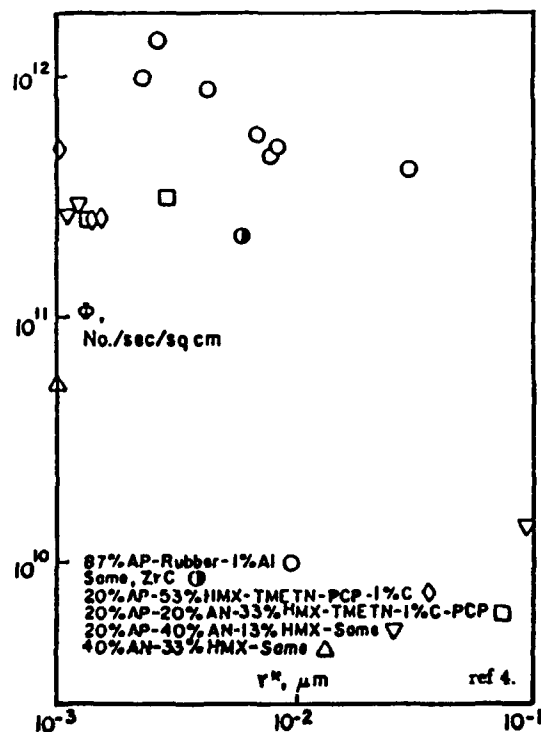

Fig. 7   Nucleation Data form MICOM Smoke Facility

7. COMPARISON WITH FLIGHT DATA

Miller reports the results of comparisons of predictions with flight data from two experiments in reference 4. One test was conducted by MICOM and another by the US Air Force.

In the flight experiment conducted by MICOM, a rocket using 87% AP, 1% Al, and 1% hydroxyl-terminated polybutadiene (HTPB) propellant was fired from an airborne aircraft and laser transmission measurements were made at 1.06 μm wavelength. The Low Altitude Plume Program (LAPP) was used to predict the plume flowfield, the DROP4 code was used to predict the secondary smoke formation, and the Optical Signature Analysis (OSA) code was used to predict the laser attenuation. All of the available adjustable parameters were varied to attempt to obtain agreement between the data and predictions. Table 1 lists the prediction and data. Some effort was made to establish the sensitivity of the calculation to the ambient conditions. No error bound was given for the experimental data.

Table 1: Comparison of Flight Test Data and Predictions, reference 4

	AMBIENT AIR TEMPERATURE/ HUMIDITY	I/I_o
PREDICTION:	80°F/ 90% RH	0.736
PREDICTION:	74°F/ 95% RH	0.775
TEST DATA:	80°F/ 78% RH	0.66

In the Air Force test, a missile launch from one aircraft was photographed from a second aircraft for various sun angles. The Lockheed Plume Visibility code was used to predict the visible signature, and comparisons were made with the photographic data. No details are available on the Lockheed computer program in the open literature. The resulting comparison between flight test data and predictions are shown in Figures 8-10. Comparison appears quite good in some respects. A variance of 25 m in range and 8° in aspect angle was reported, which Miller estimates would account for approximately a factor of two in plume contrast. It is significant that the comparison is best when the data set is well behaved, i.e., flight 3 vs. flights 1 and 2. The computer model appears to have been run with no adjustment to the prediction physics, although arbitrary values of nuclei were chosen to fit the flight data.

8. PROPELLANT CLASSIFICATION

8.1 Background

The general behavior of exhaust plumes of tactical, strategic and civilian launch system solid and liquid propellant rockets has been an issue of concern to propulsion system designers and military analysts for some period of time. Recently, the tactical rocket community has become increasingly sensitive to the effects of smoke laden plumes.

In the United States, this has led to a JANNAF classification system which is to a large degree a reflection of the measures that were taken to reduce primary and secondary smoke in the exhaust plume of tactical rockets. Propellants which use metals such as aluminum as an additive to basic fuels such as AP are called "smoky" propellants. Propellants which have the smoke content of the plume reduced by removing the aluminum component of the fuel are called "reduced smoke" propellants. Propellants which have everything removed that could contribute to the smoke problem (and still remain a viable propellant) are called "minimum smoke" propellants. This designation system is descriptive of how propellants are formulated, but does not address the issue of how well the propellants perform relative to the smoke issue.
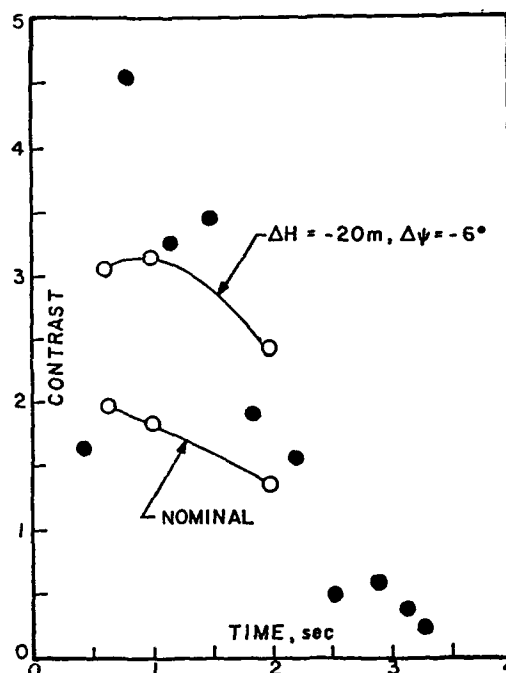

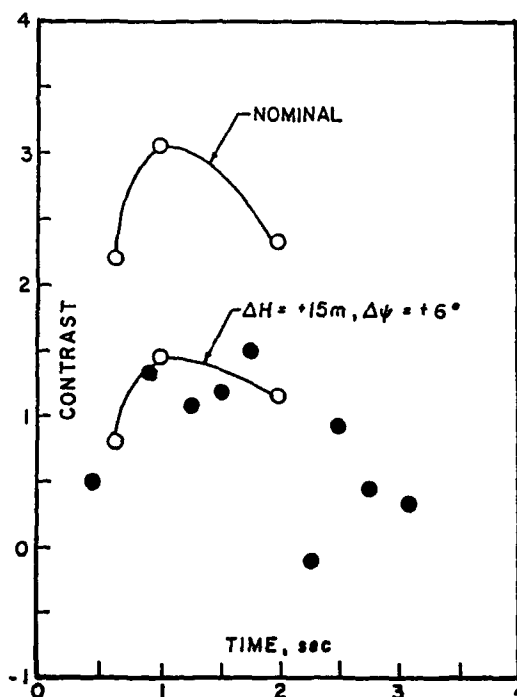Fig. 8 Comparison of Contrast Predictions for Flight Test 1, ref 4.

Fig. 9 Comparison of Contrast Predictions for Flight Test 2, ref 4.

The Propulsion and Energetics Panel (PEP) of the Advisory Group for Aeronautics Research and Development (AGARD) determined that the terminology which existed in the mid-1980's time period: smoky, reduced smoke, low smoke, minimum smoke, and smokeless, was too imprecise for quantitative engineering use. PEP Working Group 21
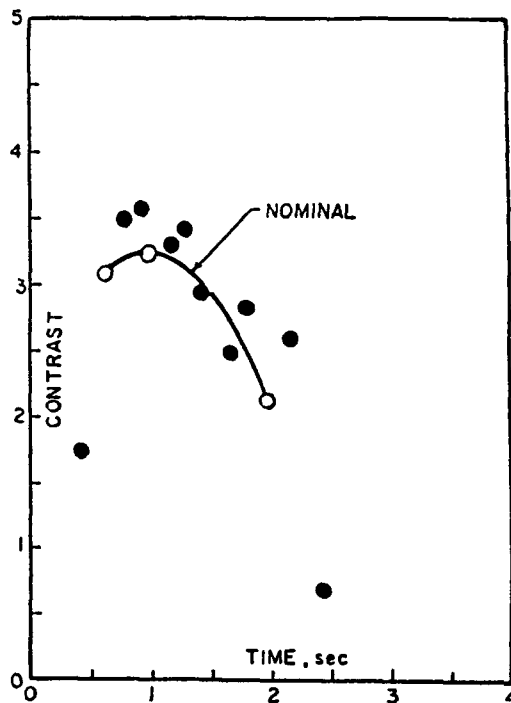
Fig. 10   Comparison of Contrast Predictions for Flight Test 3, ref 4.

(WG21) was established and tasked to develop a systematic way of classifying and measuring the smoke content of solid rocket exhaust plumes. The result of their efforts is reported in reference 18, and is summarized below.

The heart of the proposed system is the realization that the characterization problem would be greatly simplified if the primary and secondary smoke characteristics of a propellant are classified separately. The proposed classification system is comprised of two letters. The first letter indicates the propellants propensity to produce primary smoke: A being the least smoky through B to C being the most smoky. The second letter indicates the propellant propensity to produce secondary smoke: A being the least smoky through B to C being the most smoky. The resulting matrix is illustrated in Figure 11. Propellants classified as AA, AB, CC would correspond roughly to minsmoke, reduced smoke and smoky propellants, respectively.

Fig. 11   AGARD PEP WG-21 Proposed Primary and Secondary Smoke Classification Scheme, ref 18.

8.2 Primary Smoke

Characterizing primary smoke by its ability to transmit or a signal thru the plume has certain inherent advantages. The measurement is relatively easy to make and can be easily reproduced in the laboratory. Care must be taken in making the measurement that the test configuration does not bias the measurement and that secondary smoke formation is avoided. Some care should also be taken in selecting the wavelength of the laser used to make the measurement to avoid interaction with water vapor or carbon dioxide in the plume. Also, the index of refraction of the plume particulate matter may vary as a function of wavelength in an unknown manner so that characterizations made at two different wavelengths may not correlate very well.

Prediction of the transmission can be quite complicated. The equation for transmittance of a signal through a polydispersed particle cloud, taken from reference 18 is:

$$Tr = exp(-3\ \bar{Q}C_v L/2\ D_{32}) \tag{34}$$

where:

Tr = Transmittance = I/I_o

$\bar{Q}$ = Mean extinction coefficient

= a function of wavelength of incident

light, complex index of refracton,

and particle size distribution and shape.

D_{32} = Sauter mean surface to volume diameter

C_v = Particle volume loading,

volume of particles/volume of mixture

L = Length of path which contains particles

I = Intensity of transmitted light

I_o = Intensity of incident light

Some approximations are necessary to avoid having to solve the Mie equations:

$C_m = C_v \times$ particle material density

= mass of particles/mixture volume

$Tr = exp(-3\ \bar{Q}L/2\ D_{32}\ C_m/SG)$

= $exp(N\ C_m/SG)$

$N = -3/2\bar{Q}\ L\ D_{32} = 1.0$ assumed

Setting $N = 1.0$ eliminates all the terms that are unknown. Replace C_m with:

$$C_m = M_p\ M_{mix}\ P = \frac{M_p\ M_{mix}\ RT}{V_{gas}}$$

= Mass particles/Volume gas

where:

M_p = Mass of particles

R = Universal gas constant

T = mixture temperature

M_{mix} = Molecular weight of mixture

P = Pressure of mixture

so:

$$Tr = exp(-\sum_i \%M_{p,i}\ N_i/SG_i) \tag{35}$$

where $\%M_{p,i}$ = mass fraction of condensible species i. Redefining obscuration as $1 - Tr$:

$$AGARDP = 1 - exp\left[-\sum_i (\%M_{pi}N_i/SG_i)\right] \quad (36)$$

where

$$\%Mpi = \text{Mass percentage}$$
$$SG_i = \text{Specific Gravity}$$
$$N_i = \text{Optical property constant}$$
$$= 1.0 \text{ for rough calculations}$$
$$i = \text{species considered}$$

This expression is limited by the fact that the optical properties, laser wavelength and particle diameter distribution information was lost. The authors realized this and recommend that these parameters be included in any analysis when they are available. It should be pointed out that whatever the shortcomings of the predictive method suggested, that proper experimental procedure can still produce highly accurate, and therefore usable data.

8.3 Secondary Smoke

The secondary smoke numerical rating, AGARDS, is taken to be the ambient relative humidity necessary to induce condensation in the exhaust plume when the plume is expanded to 101,325 Pa pressure, and diluted by and in chemical and thermal equilibrium with 1000 parts of air at 275.13 K. The suggested procedure taken directly from reference 18 is:

(i) Determine the H_2O, HCl and HF content in mole fractions of the propellant exhaust products from a thermochemical prediction for a shifting equilibrium nozzle flow.

(ii) Referring to Figure 12, determine the curve which best corresponds to the total halogen exhaust gas mole fraction and select a point on the line whose abscissa corresponds to the H_2O mole fraction of the exhaust.

(iii) The ordinate of the selected point is the ambient humidity required for saturation, i.e., secondary smoke formation. The point also defines the AGARD "A", "B", or "C" secondary smoke classification for the propellant.
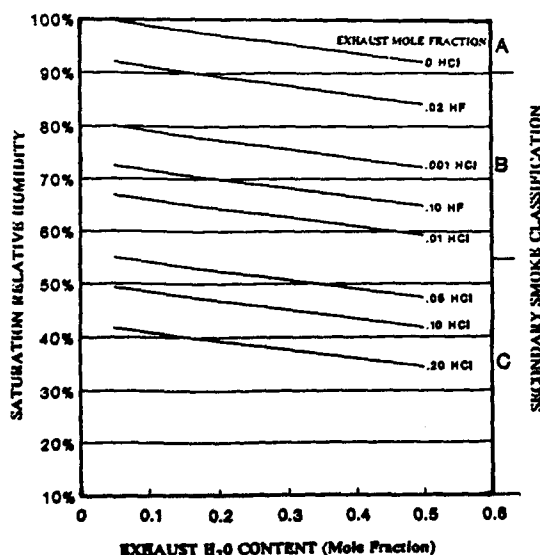
Fig. 12   Saturation Relative Humidity for AGARD Secondary Smoke Classification at 0°C, 1 atm., 1000 Dilution, ref 18.

8.4 Sample Calculations

The sample calculation given in reference 18 is repeated here. Given that the exhaust plane chemical composition is as in table 2.

Table 2: Example of Exhaust Chemical Composition

SPECIES	MASS FRACTION	MOLAR FRACTION
N_2	.1023	.0944
CO_2	.2368	.1391
CO	.1161	.1071
H_2O	.2488	.3569
H_2	.0088	.1130
HCl	.2577	.1826
$FeCl_2$	.0106	.0022
$Al_2O_3(s)$	.0189	.0048

The condensable species are $Al_2O_3(s)$ and $FeCl_2$. From equation (36):

$$AGARDP = 1 - exp(-[(1.89 \times 1.0/3.97)$$
$$+ (1.06 \times 1.0/3.16)])$$
$$= 0.56$$

which yields a primary smoke classification of B.

To calculate the secondary smoke classification, we take the mole fractions of H_2O and HCl from Table 2 as 0.3569 and 0.1826, respectively, for a total mole fraction of 0.5395. Since the partial pressure of the water vapor plus the partial pressure of exhaust condensibles must equal the saturation partial pressure for condensation to occur, and the partial pressure is equal to the total (atmospheric) pressure multiplied by the mole fraction, f, then:

$$P_{H_2O,amb} = P_{sat} - 1.10325[f_{H_2O} + f_{HCl} + f_{HF}] \quad (37)$$

The normal saturation pressure of water vapor is depressed by a factor, K, that depends upon the concentrations of HCl and/or HF. The saturation pressure of water at 273.15 K is 6.1078 mbar (610.78 Pa). Then:

$$P_{sat} = K \times 6.1078 \quad \text{mbar} \quad (38)$$

where K is the partial pressure of water over acid/normal saturation pressure of water. Substituting equation (38) into equation (37) yields:

$$P_{H_2O,amb} = 6.1078 \times K - 1.01325[f_{H_2} + f_{HCl} + f_{HF}] \quad (39)$$

or

$$RH_{amb} = 100 \times (K - 0.16589 f_{total}) \quad (40)$$

$$P_{HCl} = (1013.25/1000) \times 0.1826 = 0.185 \quad \text{mbar}$$

and the HCl depression factor, K, is read from Figure 13 as $K = 0.48$, which, when substituted into equation (40) gives:

$$RH_{amb} = 110 \times (0.48 - 0.16589 \times 0.5395) = 39\%$$

From Figure 12 with "Saturation RH" = 30 and "Exhaust H_2O Content" = 0.3569, the secondary smoke classification is C. The AGARD smoke classification for the propellant with exhaust products given in Table 2 is BC. More comprehensive examples are given in reference 18 from which this discussion was extracted.
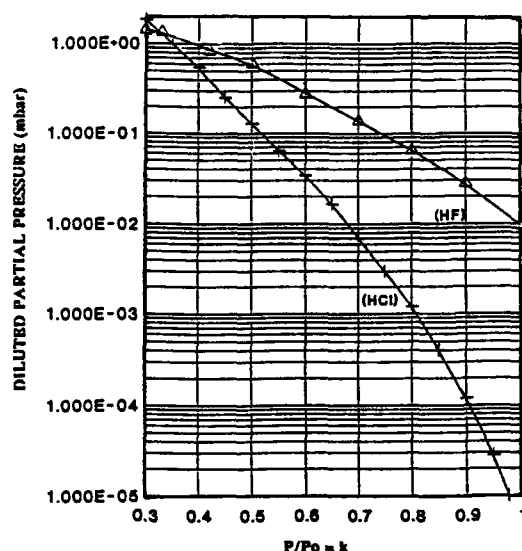
Fig. 13   Oliver Depression Factor for Acid/Water
Vapor Equilibria at 0°C, ref 18.

9. CONCLUDING REMARKS

The prediction of secondary smoke is perhaps the most difficult task the plume community has set for itself. In this context, the proposed PEP WG 21 smoke classification system for solid propellants is a tremendous improvement over the older methods, and should aid research in this area immensely.

The resulting particulate diameter and number density distributions which are a function of the radial position at the nozzle exit plane are strongly affected by the internal geometry of the burning surface of the grain, and the nozzle entrance, throat and exit contour. This well established fact should be taken into account in any serious comparison of propellants using different geometry test motors.

The data base reported in the open literature on heterogeneous nucleation sites in solid rocket exhaust plumes is sparse in terms of the number of tests and data points. There appears to be little or no data taken on the variation of heterogeneous nucleation sites as a function of nozzle radius and there is no discussion on the possibility that this effect could be significant.

There is no recorded attempt in the open literature to establish what the accuracy requirements are for prediction of secondary smoke effects. Without requirements it is impossible to evaluate the predictive methods and to justify the expenditures necessary to obtain the extensive data base of high quality data that is a necessary precursor to developing accurate predictive models.

The predictive methods described in the open literature are unvalidated. There has been no attempt reported to establish the range of application of the codes or the level of accuracy that can be expected. Research in this area is not as intensive as it has been in the past. Most of the papers available were old, or if recent applied technology developed some time ago.

It may be desirable to develop or adapt a suite of highly accurate research codes for the prediction of secondary smoke and its optical characteristics. These codes could be used to evaluate the simplifying assumptions made in developing the predictive codes currently in use in the field. Any new super code will not be a substitute for accurate and extensive flight data.

The existing numerical models of condensation effects and signature prediction are very conservative in the use of computer resources. The numerical models have too many free constants.

10. REFERENCES

1. Emmons, H. W., "Fundamentals of Gas Dynamics," in High Speed Aerodynamics and Jet Propulsion, Vol. III, Princeton University Press, Princeton, N.J., 1958.

2. Stodola, A., "Steam and Gas Turbines," translated from the sixth German edition, McGraw-Hill, New York, p. 117,(from reference 1).

3. Wagner, C., "Serechnungen uber die Moglichkeiten zur Erzielung hoher Machscher Zanlen in Windkanalversuchen," WVA Arch. A-385/1, 1942, (from reference 1).

4. Miller, E., "Smokeless Propellants in Fundamentals of Solid Rocket Combustion," Vol. 90, edited by Martin Summerfield, AIAA, New York, 1984, p. 841.

5. Myer, J. W., "Kinetic Model for Aerosol Formation in Rocket Plumes," AIAA Journal, Vol. 17, No. 2, February 1979, p. 135.

6. Victor, A. C. and Breil, S. H., "A Simple Method for Predicting Rocket Exhaust Smoke Visibility," AIAA Journal of Spacecraft, Vol. 14, No. 9, September 1977, p. 526.

7. Wu, B. J. C., "Possible Water Vapor Condensation in Rocket Exhaust Plumes," AIAA Journal, Vol. 13, No. 6, June 1975, p. 797.

8. Shanks, J., "Signature Enhancement Due to Particle Growth Within Liquid Fuels Rocket Plumes," 19th JANNAF Exhaust Plume Technology Subcommittee Meeting, US Army Missile Command, Redstone Arsenal, AL, 13-16 May 1991, (paper distribution unlimited).

9. Courtney, W. G., "Condensation in Nozzles," in Ninth Symposium on Combustion, The Combustion Institute, 1963, (quoted from reference 1).

10. Kang, S. W., "Analysis of Condensation Droplet Growth in Rarefied and Continuum Environments," AIAA Journal, Vol. 5, No. 7, 1967, p. 1288.

11. McBride, D. D. and Sherman, P. M., "A Solution for Equilibrium Condensation on Two Component Flow Through a Nozzle," Astronautica Acta, Vol. 16, 1971, p. 97, (quoted from reference 1).

12. Sugawara, M. and Oshima, N., "Analysis of Condensation in Supersonic Nozzles," in Twelfth Symposium (International) on Combustion, The Combustion Institute, 1969, p. 1193, (quoted from reference 1).

13. Jarman, R. T. and de Turville, C. M., "The Visibility and Length of Chimney Plumes," Atmospheric Environment, Vol. 3, 1969, p257, (quoted from reference 4).

14. Van de Hulst, H., "Light Scattering by Small Particles," John Wiley & Sons, New York, 1957.

15. Bohren, C. F. and Huffman, D. R., "Absorption and Scattering of Light by Small Particles," John Wiley & Sons, New York, 1983.

16. Hottel, H. C. and Sarofim, A. F., "Radiative Transfer," McGraw-Hill, New York, 1967, p. 399.

17. Hoshizaki, H., Chou, Y. S., Meyer, J., Wilson, K. H., and Thomas, P. D., "Plume Visability Detection Study," (quoted from reference 4).

18. AGARD Propulsion and Energetics Panel Working Group 21, "Advisory Report, Terminology and Assessment Method of Solid Propellant Rocket Exhaust Signature," Chapter 2: "Propellant Smoke Classification," 1993.

ROCKET MOTOR PLUME FLOWFIELDS: PHENOMENOLOGY AND SIMULATION

Dr. Sanford M. Dash
Science Applications International Corporation
Propulsive Sciences Division
501 Office Center Drive, Suite 420
Fort Washington, PA 19034-3211

SUMMARY
This article describes the varied processes occurring in rocket motor exhaust plumes and methodology for simulating these processes. Rocket motor plumes contain shock waves due to under/overexpansion; the exhaust mixes with the external stream in a highly compressible turbulent environment; unburnt products of combustion after-burn strongly at lower altitudes; and solid propellant plumes contain particulates which are generally out of equilibrium with the gas-phase exhaust. Earlier methodology simulated the varied processes using boundary layer type coupling. Current methods implement solutions of the full or reduced (parabolized) Navier-Stokes equations where all fluid dynamic and thermochemical processes are strongly coupled. Earlier methodology will be reviewed briefly while the status of current methods will be addressed in greater detail.

1. INTRODUCTION

The analysis of the complex flowfield generated by the interaction of an exhaust plume with the missile airframe external flow involves the consideration of flow regions with widely varying characteristic features and length scales. The supersonic exhaust plume issuing from the missile is imperfectly-expanded at typical flight conditions. It equilibrates to ambient pressure levels via a decaying sequence of expansion and shock waves which can be quite strong in the plume nearfield. The plume is additionally characterized by the turbulent mixing that occurs between the exhaust and external stream, and by the afterburning of the unburnt exhaust products with the entrained air. For solid-propellant missile exhausts, a multi-phase flow must be dealt with where the influence of gas/particle interactions on the plume structure can be quite pronounced at high particle loadings. The detailed analysis of a missile exhaust plume can entail the integration of over 100 partial differential equations which describe the complex interplay of wave/turbulent/chemical/ particle processes occurring in the plume. The analysis is complicated by the requirement to adequately resolve the varying length/non-equilibrium time scales over which these processes occur.

In this article, basic aspects of plume flowfield simulation will be reviewed. A very brief overview of earlier simple-component and zonal methods will be discussed. This article will emphasize the use of Reynolds-averaged Navier-Stokes (RNS) methodology and simplified variants which have now become viable tools for plume simulation. RNS based methods will see ever increasing usage as computers become more efficient and as our understanding of turbulence for complex 3D chemically reacting/multi-phase flows progresses.

2. CHARACTERISTIC FEATURES OF ROCKET MOTOR EXHAUST PLUMES

2.1 Plume Fluid Dynamics for Conventional Missile Exhausts

The axisymmetric plume flowfield associated with a conventional missile exhaust (single engine with rear/centered propulsive nozzle) can be subdivided into the three regions exhibited in Fig. 1, namely:

(1) the predominantly inviscid plume nearfield where wave strengths are strong and turbulent mixing processes are generally confined to thin layers;

(2) a transitional region where the mixing layers engulf the entire plume and wave strengths diminish due to turbulent dissipation; and,

(3) the fully viscous plume farfield where wave processes have totally diminished and a constant pressure, turbulent mixing environment prevails.
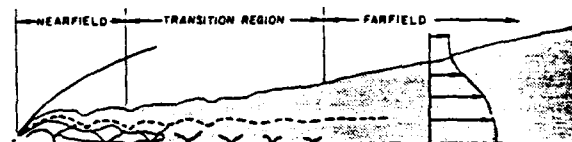

Figure 1. Structural features of plume nearfield, transition region, and farfield.

For engineering applications keyed to missile detection, guidance, etc., the overall plume structure is of interest with attention generally focused (e.g. in IR-related applications) upon the farfield solution (Ref. 1). For such applications, the nearfield solution serves to provide starting conditions for a farfield, constant pressure mixing/afterburning calculation and may be adequately represented by very simplistic techniques (Ref. 2). The plume structure beyond the nearfield region is simplistic and the discussion here will thus focus upon the details of the plume nearfield.

A schematic of a single inviscid shock cell of an underexpanded plume is exhibited in Fig. 2. The flowfield is initially characterized by an interaction at the nozzle lip to achieve a pressure balance between the exhaust gas and external flow. The ensuing plume interface (which separates the exhaust and external streams) has a monotonically decreasing slope, thus generating downward running compression

waves into the exhaust flow. These wave coalesce and form a barrel shock which progressively increases in strength, ultimately collapsing to form a Mach disc. The barrel shock divides the exhaust gas into two zones: (1) the core, which behaves independently of the external stream; and, (2) the barrel shock layer, which contains exhaust gas which has interacted with the external stream. Downstream of the Mach disc station, the reflected shock again divides the exhaust gas into two zones. In addition, a third zone exists comprising that portion of the exhaust flow which has traversed through the Mach disc. The inviscid shock cell terminates at the axial station at which the reflected shock intersects the plume interface. This shock cell pattern continues subject to an overall decay by turbulent diffusive processes.
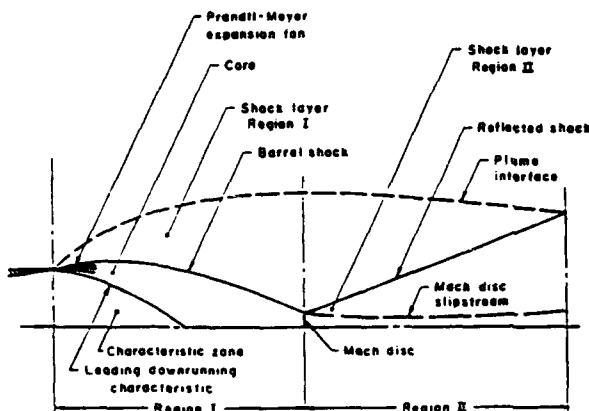

Figure 2. Wave structure in first shock cell of underexpanded jet in inviscid limit.

Now consider the nearfield viscous/inviscid structure of an underexpanded plume exhausting into a supersonic stream (Fig. 3). Turbulent mixing processes are initially confined to:

(1) the plume mixing layer, which comprises the curved shear layer growing along the plume slipstream (or interface, in the nomenclature of Fig. 2); and,

(2) the Mach disc mixing layer which grows along the slipstream separating the hot, initially subsonic flow which has traversed the Mach disc, with the colder/supersonic outer portion of the exhaust flow.
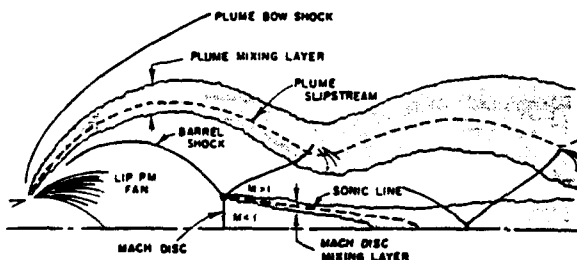

Figure 3. Structural features of plume nearfield at supersonic flight conditions.

The magnitude of viscous/inviscid interactions in the nearfield is highly problem-dependent as discussed and exemplified in earlier publications (Refs. 3-6). Significant viscous/inviscid interactions are associated with phenomena such as:

(1) shock/compression waves produced by the positive displacement effect of rapid chemistry and/or high Mach number viscous dissipation in the plume shear layer;

(2) expansion waves generated by the "washing away" of initial mass defect regions downstream of base/separated flow zones;

(3) the negative displacement of streamlines downstream of Mach discs due to the wake-like mixing that occurs; and,

(4) the shock/shear layer interactions occurring at the end of nearfield shock cells.

2.2 Plume Thermochemistry

Tactical missiles generally contain double-base or composite solid propellant rocket motors. The double-base propellants are typically referred to as low or minimal smoke propellants. Composites are high energy solid propellants containing metallic fuel additives (e.g. aluminum) and ammonium perchlorate as an oxidizer. Table I lists the chemical species typically comprising such systems (and also includes typical species for airbreathing ramjet/scramjet type missile systems employing hydrogen or conventional hydrocarbons as the fuel).

Table I. Chemical Species for Various Propellant Types

	1	2	3
Propellant Type	Liquid •Hydrogen •Oxygen	Liquid •Amines •Conventional Oxidizers (e.g., N₂O₄) Solid •Double Base (No AP)	Solid •Composite (AP and A1)
Elements (All systems contain N₂ as an inert species)	H/O	C/H/O	C/H/O/C1
Number of Species	7	9	13
Number of Reactions	8	10	16
Species	H H₂ H₂O N₂ O OH O₂	CO CO₂ H H₂ H₂O N₂ O OH O₂	A1₂O₃ CO CO₂ C1 C1₂ H H₂ H₂O HC1 N₂ O OH O₂

The chemical reaction mechanisms and reaction rates for these systems are given in Table II. These reaction mechanisms represent a "compromise" between the total number of reactions that could be selected and a practical set for

the afterburning environment of tactical missile exhausts. The reaction mechanisms listed were determined by Miller and Pergament;[7] the rates are based on a literature survey (the specific references for each reaction are given in Ref. 7) and generally concur with the rates listed in the earlier surveys of Slack and Ludwig,[8] Kolb et al.,[9] and Jensen and Jones,[10] all geared to the plume afterburning environment.

The prediction of the plume chemistry is initiated in the rocket combustion chamber (where an equilibrium assumption suffices), and must be continued through the throat and supersonic expansion region of the nozzle where the chemistry may be well out of equilibrium. The accurate determination of nozzle exit plane Mach numbers and pressures (which influence the plume expansion process) is somewhat contingent on the representation of the chemistry in the nozzle. For two-phase exhausts with significant particle loading, the nozzle flow is highly nonuniform and the coupled effects of chemical and gas/particle nonequilibrium must be accounted for, as will be discussed below.

problems, except, it now occurs in a complex, multi-phase environment with strong shock/expansion waves.

An exemplary solution for the complete exhaust plume structure of a typical tactical missile flying at sea level with a highly energetic propellant (system 3 of Table I) is exhibited in Figs. 4 and 5. Particulates (16 percent aluminum in the propellant) were equilibrated with the gas-phase in performing this calculation. Figure 4 depicts the variation of centerline temperature, and the mole fractions of CO_2, H_2O, CO and H_2. Departures in decay rate from that of the inert species are indicative of species production/depletion due to afterburning. The afterburning is quite rapid at sea level, with the significant amounts of unburnt CO and H_2 in the exhaust depleted within 100 exit radii. The temperature variations produced by the shock structure in the nearfield (< 10 exit radii) are shown in Fig. 4. The farfield temperature variations are shown in the contour plots of Fig. 5. Nonequilibrium gas/particle calculations for this system would produce substantial differences in the overall flow structure due to the relatively high particle loading.
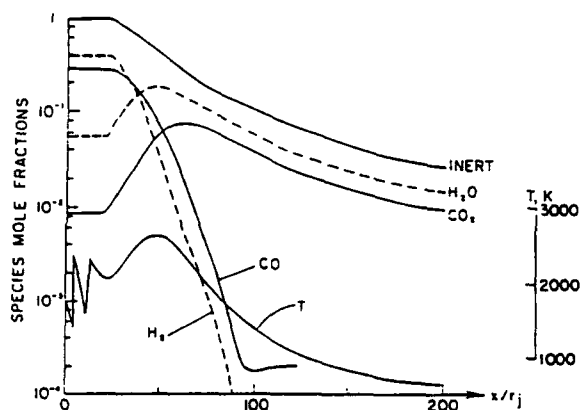
Table II. Reaction Mechanisms and Rate Data
for Tactical Missile Chemical Systems

$$k_f = AT^{-N} \exp(E/RT)$$

Reaction No.					A	N	E
System 1 - Hydrogen/Oxygen (H-O) Reactions 1-8							
1.	OH + O	$\rightleftharpoons$	H + O$_2$		3.0(-11)	-1.0	-960
2.	OH + H	$\rightleftharpoons$	H$_2$ + O		1.4(-14)	-1.0	-7000
3.	OH + OH	$\rightleftharpoons$	H$_2$O + O		1.0(-11)	0	-1100
4.	OH + H$_2$	$\rightleftharpoons$	H$_2$O + H		3.5(-11)	0	-5180
5.	H + H + M	$\rightleftharpoons$	H$_2$ + M		2.0(-30)	1.0	0
6.	H + O + M	$\rightleftharpoons$	OH + M		1.0(-29)	1.0	0
7.	O + O + M	$\rightleftharpoons$	O$_2$ + M		3.0(-34)	0	1800
8.	H + OH + M	$\rightleftharpoons$	H$_2$O + M		1.0(-25)	2.0	0
System 2 - Carbon/Hydrogen/Oxygen (C-H-O) Reactions 1-10							
9.	OH + CO	$\rightleftharpoons$	CO$_2$ + H		2.8(-17)	-1.3	660
10.	CO + O + M	$\rightleftharpoons$	CO$_2$ + M		6.5(-33)	0	-4360
System 3 - Carbon/Hydrogen/Oxygen/Chlorine Reactions 1-16 (C-H-O-Cl)							
11.	Cl + H$_2$	$\rightleftharpoons$	HCl + H		1.4(-11)	0	-4260
12.	Cl + H$_2$O	$\rightleftharpoons$	HCl + OH		5.0(-11)	0	-17600
13.	HCl + O	$\rightleftharpoons$	OH + Cl		6.0(-12)	0	-6000
14.	H + Cl$_2$	$\rightleftharpoons$	HCl + Cl		1.5(-10)	0	-1200
15.	Cl + Cl + M	$\rightleftharpoons$	Cl$_2$ + M		1.0(-33)	0	-1800
16.	H + Cl + M	$\rightleftharpoons$	MCl + M		4.0(-28)	2.0	0

Typical nozzle exit plane conditions of conventional tactical missile exhausts encompass: pressures ranging from 1 - 3 atm; Mach numbers ranging from 2 - 4; and, temperatures ranging from 800 -1200 °K for double base propellants, or, from 1500 - 2500 °K for the more energetic composite propellants. The nozzle exhaust can contain significant amounts of unburnt fuel and intermediate combustion products (e.g., OH, CO) which afterburn with the air entrained into the ensuing exhaust plume. The plume afterburning process for energetic propellants is very much akin to the combustion occurring in classical turbulent diffusion flame

Figure 4. Centerline variations of temperature and species for energetic tactical missile exhaust plume based on equilibrated gas/particle mixture solution.
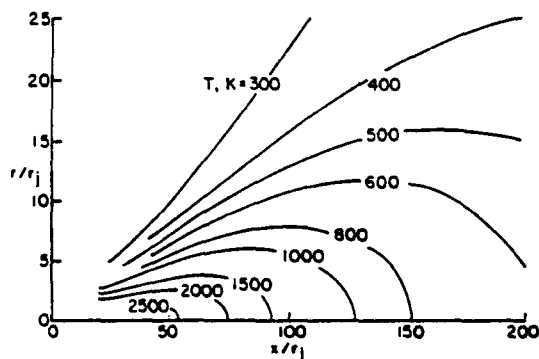

Figure 5. Temperature contours in farfield of energetic tactical missile exhaust plume.

For tactical missiles at higher altitudes, the rate of after-burning decreases due to the reduced pressure levels. Above 10 - 15 km and/or for "colder" double-base propellant systems (i.e. those with exhaust temperatures less than 1000°K), the ability to afterburn can sometimes be controlled by the conditions in the base region of the plume. The role of the base region as a flameholder has been noted and/or exhibited in a number of previous studies.[11,12] The combustion that occurs in the base can produce afterburning in the downstream plume shear layer that would not occur if base combustion were neglected. This is due to the increased initial temperatures in the plume shear layer and the increased concentration of free radicals. The influence of the base region is exhibited in the predictions of Jensen et al.[11] for a motor with a low temperature exhaust (T = 780°K) at sea level, with a flight Mach number of 0.9. Calculations made with the base included predicted afterburning to occur; those made neglecting the base exhibited no afterburning. The predicted centerline temperature variations and 500°K temperature contours with and without the base analysis included are exhibited in Fig. 6 showing the differences to be quite pronounced.
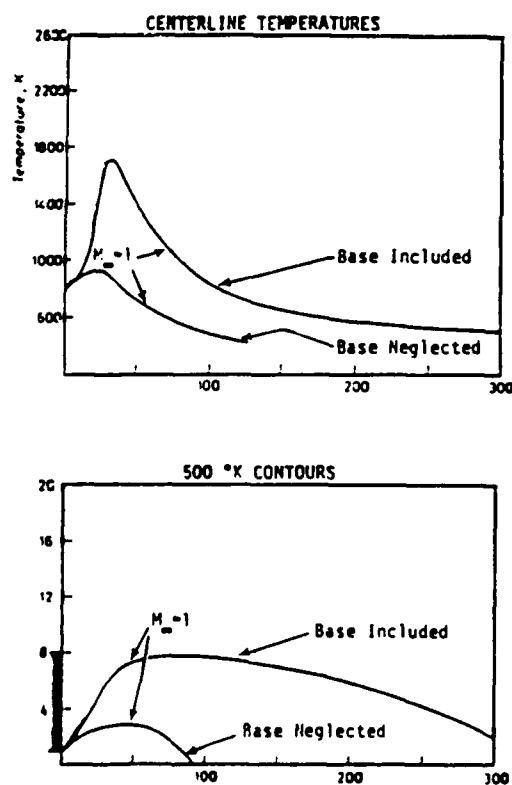

Figure 6. Base region flameholding effect: centerline temperatures and 500°K contours with and without base incorporated in plume solution.

2.3 Two-Phase Flow Processes

The particles in solid rocket motor exhausts are formed from condensed combustion products of metalized fuels (e.g. metal oxides such as Al_2O_3 in aluminized propellants).

For heavily metallized propellants, the particles can have mass loadings (mass flux particles/total mass flux) of 50 percent. Secondary sources of particles in the motor come from propellant stability additives and from ablation of the motor case. The particles are generally well out of equilibrium at the nozzle exit plane due to lag effects caused by the rapid nozzle expansion process. Particle velocities will be less than those of the gas, while the particle temperatures will be higher. The degree of gas/particle nonequilibrium is dependent upon the nozzle characteristics and particle sizes. The radial variation of particles at the nozzle exit plane is nonuniform; the larger particles, being relatively unresponsive to the gas expansion process, remain concentrated in the vicinity of the axis, while the smaller particles expand with the gas. This results in a highly nonuniform gas-phase exit plane distribution, with the higher temperature, slower gas concentrated near the centerline.

The particle lag processes occurring in the nozzle expansion continues in the nearfield plume expansion. Relaxation lengths for gas/particle equilibration (for a significant range of particle sizes) are, typically, comparable to inviscid plume length scales; but, nearfield wave processes are abrupt and quite strong. Thus, the path to equilibration is repetitively disrupted by passages through strong gas-phase discontinuities. For significant particle loadings, the nearfield inviscid flow pattern can be substantially altered by gas/particle interactions with wave processes being dampened due to the viscous dissipation associated with particle frictional drag.

To exhibit the influence of these lag processes on the inviscid plume expansion, consider the calculation of a two-phase underexpanded exhaust with the following uniform (and initially equilibrated) nozzle exit plane conditions: Mach number = 2.4 ; temperature = 1000°K; pressure = 1 atm; 12 percent loading (6 percent 2μm radius and 6 percent 4μm radius) of Al_2O_3 particles (distributed uniformly across the central half of the exit plane). The results of this calculation (taken from Ref. 13) are shown in Figure 7. The initially equilibrated particles are seen to geometrically lag behind the gas streamlines (emanating from the same point) in passing through the multiple cell wave systems. The lag effects are readily evidenced in the axis velocity (U) and temperature (T) variations where particle velocities are lower that the gas velocity in expansion regions and higher than the gas velocity in compression regions. Exactly the opposite lag effects occur for temperatures, and, as expected, the lags for the larger (4μm) particles are seen to be greater than those for the smaller (2μm) ones. There is a noticeable dissipative trend in both sets of axis curves showing a gradual decay in velocity levels and an increase in temperature.

The damping effect of particle drag on the axial pressure variation (carried out for 200 radii) is also exhibited in Fig. 7 by comparison of gas-only and gas-particle variations. In the single-phase (gas-only) calculation, significant damping is exhibited in the first three shock cells (peaks indicate the end of each cell) due to shock-induced viscous dissipation,

while beyond the third cell, wave processes are linear and no further damping occurs. In the two-phase (gas-particle) calculation, the damping is continual and much more pronounced and the position of the cells is modified (see the flowfield schematic also). It should be noted that while the averaged particle loading in this case is only 12 percent, the local loading in the axis region can be significantly higher since the particles expand non-uniformly.
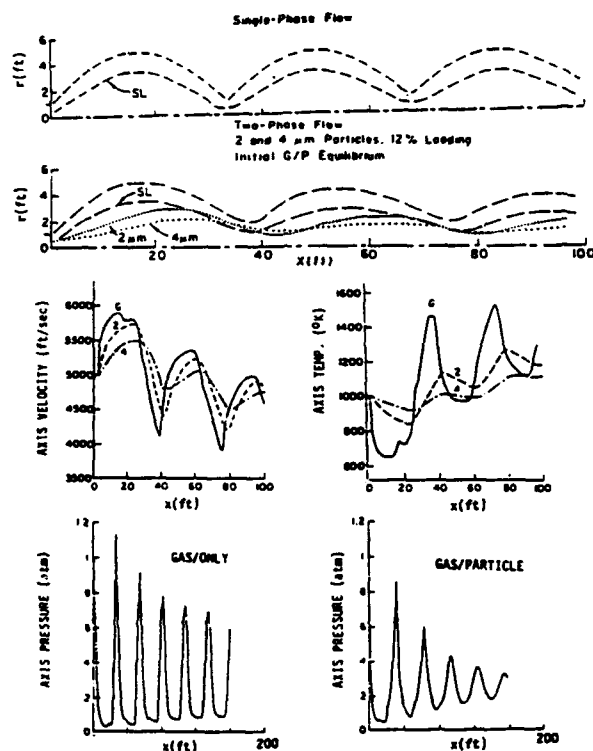

Figure 7. Influence of gas/particle nonequilibrium effects on inviscid plume structure.

A region of significant gas/particle nonequilibrium in the plume nearfield is the embedded subsonic zone behind the Mach disc. Gas-phase temperatures immediately downstream of the disc are quite high and the velocities quite low. *Temperature differences between gas and particle phases can exceed 3000°K, while velocity differences can be of the order of 10,000 ft/sec.* For single-phase flows, the acceleration of the subsonic flow in the Mach disc stream-tube to supersonic velocities is governed by the local pressure gradient and turbulent mixing processes. For two-phase flows, gas/particle interactions can initially *provide a significant accelerative mechanism and thus appreciably alter the flowfield characteristics in this region.* In addition, nonequilibrium phase change effects can occur and, possibly, combustion effects for non-inert particles (e.g. boron particles in rockets using boron-loaded solid propellants). Figure 8 exhibits the predicted centerline temperature variation in the plume nearfield of a heavily metallized (0.42 mass loading of Al_2O_3) solid propellant motor missile exhaust. The particle size distribution was

equally parcelled into 1, 3, and 10μm radius particulates. The significant degree of nonequilibrium just behind the Mach disc and the relative relaxation scales for each of the particle size groups is quite evident. These nonequilibrium predictions are compared with a calculation performed in the limit of full gas/particle equilibrium (particle properties equal those of the gas-phase). The equilibrium assumption is generally not a valid assumption in the nearfield of tactical missile exhausts, and the two-phase nonequilibrium equations to be discussed in the next subsection must be utilized.
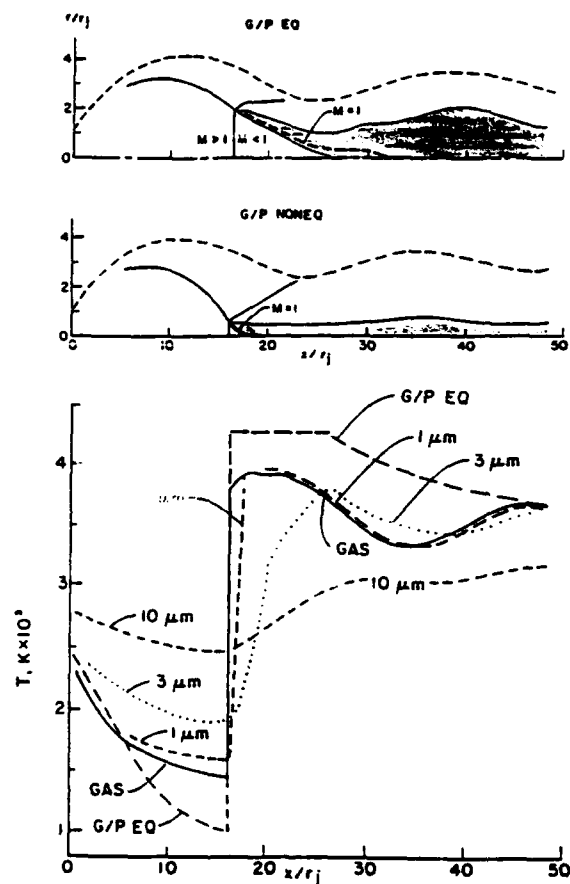

Figure 8. Influence of gas/particle nonequilibrium effects on Mach disc region structure.

2.4 Generalized Two-Phase Flow Equations

The equations governing the two-phase flow of a dilute gas/particle mixture in inviscid (non-turbulent) flow regions are well established.[14-16] The dilute assumption implies that the particulate phase occupies a negligible volume fraction of the flow, and, that the particles are collisionless. The dilute assumption is generally quite reasonable for the heavy particulates (e.g Al_2O_3) in tactical missile exhausts, but it can breakdown in localized regions of very high loading (e.g. nozzle wall, nozzle/plume centerline). Gas/particle coupling in inviscid flow regions is representable by

forcing function terms expressing the transfer of momentum and energy between the two phases. Since rocket exhausts contain particulates of varying types and sizes,[17,18] the particulates of each type (e.g. Al_2O_3) are divided into a number of characteristic size groups, j = 1, 2, ..., NP, each of fixed radius, r, and continuum-like particle cloud equations[14-16] are solved for each size group considered. The net contribution of all size groups considered is summed in evaluating the contribution of the particulates on gas-phase properties. The generalized two-phase flow equations describing the flow in solid propellant rocket exhausts are listed in Table III (from Ref. 17).

Table III. Generalized Two-Phase Flow Equations for Tactical Missile Exhausts

Global mixture continuity:

$$\frac{\partial}{\partial x}(r'\rho_M U) + \frac{\partial}{\partial r}(r'\rho_M V) = 0$$

Species continuity (i = 1, 2, ... NS):

$$\frac{\partial}{\partial x}(r'\rho_M U\alpha_i) + \frac{\partial}{\partial r}(r'\rho_M V\alpha_i) = \frac{\partial}{\partial r}\left(\frac{r'}{\sigma_\alpha}\rho_M \nu_M \frac{\partial\alpha_i}{\partial r}\right) + r'\omega_i$$

Particle continuity (j = 1, 2, ... NP):

$$\frac{\partial}{\partial x}(r'\rho_j u_j) + \frac{\partial}{\partial r}(r'\rho_j v_j) = \frac{\partial}{\partial r}\left(\frac{r'}{\sigma_r}\nu_r \frac{\partial\rho_j}{\partial r}\right)$$

Mixture streamwise momentum:

$$\frac{\partial}{\partial x}(r'[P + \rho_M U^2]) + \frac{\partial}{\partial r}(r'\rho_M UV) = \frac{\partial}{\partial r}\left(r'\rho_M \nu_M \frac{\partial U}{\partial r}\right) - r'\sum_j \rho_j\frac{(U - u_j)}{\tau_{v_j}}$$

Particle streamwise momentum (j = 1, 2, ... NP):

$$\frac{\partial}{\partial x}(r'\rho_j u_j^2) + \frac{\partial}{\partial r}(r'\rho_j u_j v_j) = \frac{\partial}{\partial r}\left[r'\nu_{p_j}\left(\rho_j\frac{\partial u_j}{\partial r} + \frac{u_j}{\sigma_r}\frac{\partial\rho_j}{\partial r}\right)\right] + r'\rho_j\frac{(U - u_j)}{\tau_{v_j}}$$

Mixture normal momentum:

$$\frac{\partial}{\partial x}(r'\rho_M UV) + \frac{\partial}{\partial r}(r'[P + \rho_M V^2]) = -r'\sum_j \rho_j\frac{(V - v_j)}{\tau_{v_j}}$$

Particle normal momentum:

$$\frac{\partial}{\partial x}(r'\rho_j u_j v_j) + \frac{\partial}{\partial r}(r'\rho_j v_j^2) = r'\rho_j\frac{(V - v_j)}{\tau_{v_j}}$$

Mixture energy:

$$\frac{\partial}{\partial x}(r'\rho_M U H_M) + \frac{\partial}{\partial r}(r'\rho_M V H_M) = \frac{\partial}{\partial r}\left(\frac{r'\rho_M \nu_M}{\sigma_H}\frac{\partial H_M}{\partial r}\right)$$

$$+ \frac{\partial}{\partial r}\left[\frac{r'\rho_M \nu_M}{\sigma_H}\left(\sigma_H - 1\right)\frac{\partial}{\partial r}\left(\frac{U^2}{2}\right)\right]$$

$$- r'\sum_j \rho_j\left[(Q - |Q - Q_j|)\frac{(Q - Q_j)}{\tau_{v_j}}\right]$$

$$+ r'\sum_j \rho_j\frac{(h - h_j)}{\tau_{v_j}}$$

Particle energy:

$$\frac{\partial}{\partial x}(r'\rho_j u_j h_j) + \frac{\partial}{\partial r}(r'\rho_j v_j h_j) = \frac{\partial}{\partial r}\left[\frac{r'\nu_{p_j}}{\sigma_p}\left(\rho_j\frac{\partial h_j}{\partial r} + h_j\frac{\partial\rho_j}{\partial r}\right)\right] + r'\rho_j\frac{(h - h_j)}{\tau_{v_j}}$$

The generalized formulation presented here includes a formal equilibrium limit and simplified expressions for turbulent particle diffusion. Via this formulation, the complete spectrum of particle-to-mean flow and particle-to-turbulent time scale ratios can be analyzed.[17] In a problem encompassing particle groups of diverse size, the formulation provides for concurrent equilibrium treatment of the smaller (submicron) radius particle groups and nonequilibrium treatment of the larger radius groups.

This hybrid formulation is desirable for analyzing plume exhausts, since the particle size distribution is a function of engine/propellant characteristics,[18] but is independent of the plume expansion ratio which characterizes the plume size and, hence, the mean flow length and time scales. The ratio of particle-to-mean flow length and time scales (which indicates the ability of particles to track the mean flow) decreases with increasing expansion ratio. Thus, at large expansion ratios, a significant portion of the particulates may be effectively equilibrated with the gas-phase. The reader is referred to Ref. 17 for further details of this hybrid formulation.

2.5 Turbulence Phenomena/Single-Phase Flows

A technology area posing great uncertainty in simulating rocket motor exhaust plumes is the representation of turbulence processes. Turbulence processes occur in a highly compressible environment with large pressure gradients, chemistry, and multi-phase non equilibrium. Past work in assessing the performance of algebraic and two-equation turbulence models to analyze axisymmetric single-phase rocket plume mixing has been performed by Pergament, et al. as reported in Refs. 19-21. The conclusions drawn from these assessments studies were as follows:

(1) two-equation turbulence models, which solve coupled partial differential equations for the variation of turbulent kinetic energy and a turbulent length scale parameter, are most appropriate for rocket plume simulation. Simpler, algebraic eddy-viscosity models are inadequate and cannot account for turbulence lag (nonequilibrium) effects associated with the passage of mixing layers through strong wave regions, nor for complex length scale variations as would be associated with the interaction of the plume and Mach disc mixing layers;

(2) "compressibility-corrected" versions of two-equation models are required to account for the observed decrease in turbulent mixing rates that occur at high Mach numbers. Standard "incompressible" models (e.g. the popular $k\epsilon$ series of models developed by Launder et al.[22] do not account for such effects); and,

(3) hybrid/zonal modeling is required whereby different turbulence model parameters and/or turbulence models are utilized to analyze the different mixing regions in the plume (i.e., thin nearfield shear layers, wake-like Mach disc mixing region, and fully-developed plume farfield).

Based on these earlier assessment studies, the compressibility-corrected $k\epsilon$ model formulation of Dash et al.,[23] whose "convective-velocity" like correction parameters were set by high Mach number free shear layer data,[24] and the kW turbulence model of Spalding,[25] whose parameters were set by matching farfield decay rates in rocket exhausts,[26] were recommended for rocket plume applications. The "fluid dynamic" data base used to assess the performance of these turbulence models has included: the balanced pressure jet and shear layer data used in the 1972 NASA Free Turbulent Shear Flow Conference;[27] the AEDC liquid rocket engine data;[28] the NASA underexpanded jet data of Seiner and Norum;[29] and, the CALSPAN balanced pressure jet data for Mach 2, 3, and 4 jets exhausting into still air and supersonic streams.[30,31]

Let us first consider the isoenergetic, "one-stream" planar shear layer data of Fig. 9 (one stream moving at M_1, one stationary) discussed by Birch and Eggers in Ref. 24. The spreading parameters, σ, is the inverse of the rate of spread (the larger the value of σ, the slower the shear layer spread and thus the mixing rate) and is seen to increase as the Mach number of the moving stream, M_1, exceeds unity. Note that at $M_1 = 5$, the rate of mixing is reduced by nearly a factor of 4, a dramatic effect of direct relevance to the rocket motor exhaust plume environment.

Studies of high speed, balanced pressure jet data have indicated that a hybrid/zonal turbulence modeling approach[21] which utilizes the $k\epsilon$,cc model in the nearfield shear layer region of the jet (where the shear layer width, δ, to the jet half width, $r_\frac{1}{2}$, is less than .5) and the kW model downstream works quite well. Figure 10 schematizes this model and shows its performance for the jet into still air data of Eggers[34] (Mach 2.2) and of Johannesen[35] (Mach 1.4) with the turbulence models matched where $F = \delta/r_\frac{1}{2} = .4$).
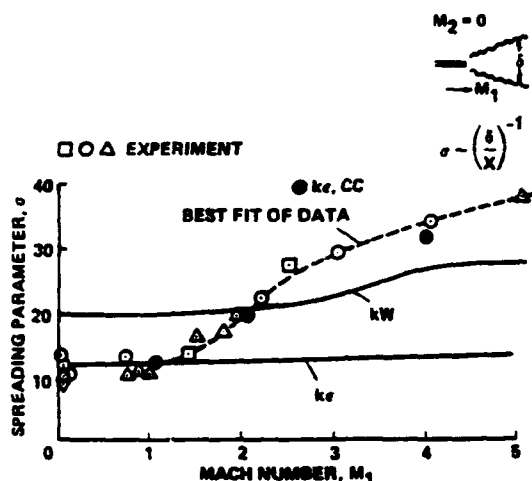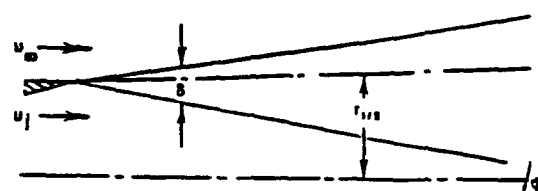

Figure 9. Observed spread rates for one-stream high-speed, isoenergetic shear layers and performance of several two-equation turbulence models.

The $k\epsilon$ turbulence model, which has been commonly used for free shear flows, shows no ability to reproduce the observed trends with Mach number and mixes at the incompressible spread parameter value of $\sigma = 11$ as noted in earlier assessment studies by its principal developers.[22] The kW turbulence model[25] duplicates the data at $M_1 = 2$, underestimates the mixing rate at lower M_1, and overestimates the mixing rate at higher M_1. The $k\epsilon$,cc model[23] duplicates the isoenergetic spread data as per its calibration.

As we move from simple planar free shear layers to axisymmetric jets, the turbulence issues become more complex since length scale issues arise (see the discussion by Pope in Ref. 32), and, since compressibility effects which dominate free shear layer behavior do not appear to be of significant influence in the fully-developed jet (downstream of the axial location where the shear layer reaches the jet axis). Numerical studies by Dash and coworkers[33] indicate that if the profile properties are known at an axial station of the jet where the flow is fully-developed, the downstream behavior is well-predicted without the inclusion of compressibility corrections (but with the inclusion of an axisymmetric correction[22,32] which has been calibrated by the low speed jet database).
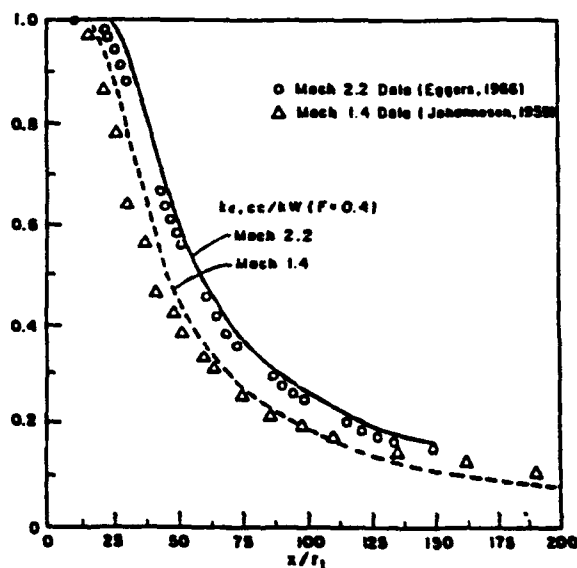

Figure 10. Hybrid/zonal $k\epsilon$, CC/kW turbulence model and analysis of high-speed jet data of Eggers and Johannesen (from Ref. 21).

For imperfectly expanded jets, the turbulence models that worked best for the balanced pressure data also work reasonably well. This has been demonstrated in comparisons with the Mach 2 jet data of Seiner described in Refs. 4-6 where predictions were made employing the SCIPVIS parabolized Navier-Stokes (PNS) code with the kW turbulence model (which works well at Mach 2 — the hybrid model predicts the same solution). A typical prediction of the multi-shock-cell jet structure is exhibited in Fig. 11, along with comparisons of predicted and measured pressure

decay along the jet centerline. More recent studies by Dash et al.[36] have indicated that PNS methodology for jets with shocks has deficiencies and that full RNS methodology is required to obtain the correct attenuation of wave intensities by turbulence. In this new light, the turbulence models for balanced-pressure jets that work well require some upgrades (e.g., pressure dilatation modeling terms).
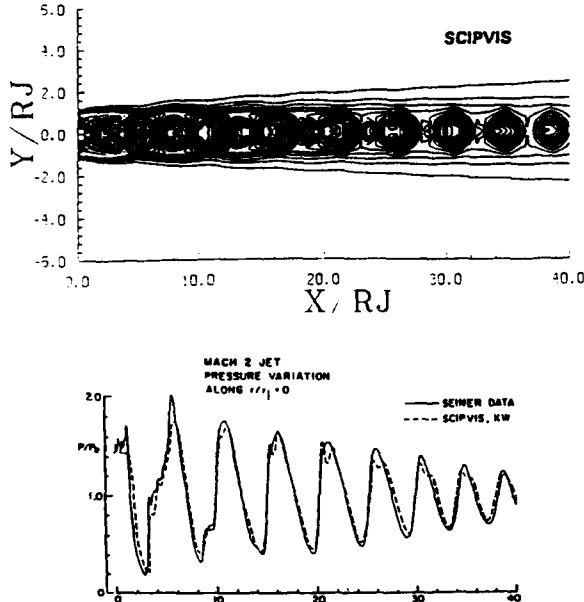

Figure 11. SCIPVIS PNS prediction of Mach 2 underexpanded jet calculated with kW turbulence model: a) density contours; b) pressure decay along jet centerline compared with data.

A very recent development in turbulence modeling for high-speed flows has been the formulation of compressible-dissipation models[37] to deal with high-speed compressibility effects. Specialization of such models to the $k\epsilon$ framework has recently been performed by Dash and coworkers for high-speed jets/shear layers as described in Refs. 33, 38 and 39. The new $k\epsilon$CD turbulence model has been found to reproduce a broad data base of fundamental building-block jet/shear layer data.[40] The most recent data contains turbulent information (e.g., Reynolds and normal stresses). The $k\epsilon$CD turbulence model is summarized below in Table IV. It provides the same comparison with the high-speed spread rate data of Figure 9 as the earlier $k\epsilon$CC model. However, it also correctly predicts the observed reduction in turbulent kinetic energy levels which the $k\epsilon$CC model does not. This is exhibited in Figure 12 using the recent data of Dutton and coworkers (Refs. 41 and 42). Similar observations have been made with a variety of data sets. For high-speed round jets, the Poper vortex-stretching correction[32] is additionally required and a heuristic means of "shutting-off" the compressibility effect (see Refs. 38 and 39). The round jet extension of $k\epsilon$CD (entiled $k\epsilon$CD/j) has been successfully applied to a variety of data sets including the very recent hot jet data of Seiner et al. (Ref. 43). Figure 13 compares $k\epsilon$ and $k\epsilon$CD velocity profile predictions (both with Pope vortex-stretching correction) with the Mach

2, 900°F round jet data of Seiner. The $k\epsilon$CD/j model reproduces the data while the $k\epsilon$ model predicts too fast a rate of mixing.

Table IV. $k\epsilon$CD Turbulence Model

The $k\epsilon$CD turbulence model utilizes a "compressible" turbulent viscosity, μ_t, given by:

$$\mu_t = C_\mu \rho k^2 / (\epsilon_s + \epsilon_o)$$

The incompressible value of turbulent dissipation, ϵ_s, is obtained from the equation:

$$\rho \frac{D\epsilon_s}{Dt} = \frac{\partial}{\partial X_i}\left[\frac{(\epsilon_s + \epsilon_c)}{\epsilon_s}\frac{\mu_t}{\sigma_\epsilon}\frac{\partial \epsilon_s}{\partial X_i}\right] + \frac{\epsilon_s}{k}(C_1 P - C_2 \rho \epsilon_s)$$

The compressible-dissipation, ϵ_c, is given by:

$$\epsilon_o = \epsilon_s\left[\alpha_1 \hat{M}_\tau^2 + \beta \hat{M}_\tau^4\right]$$

where $\hat{M}_\tau$ includes a Zeman lag

$$\hat{M}_\tau = M_\tau - \lambda \ ; \ M_\tau = \sqrt{2k}/a$$

and the coefficients utilized are as follows:
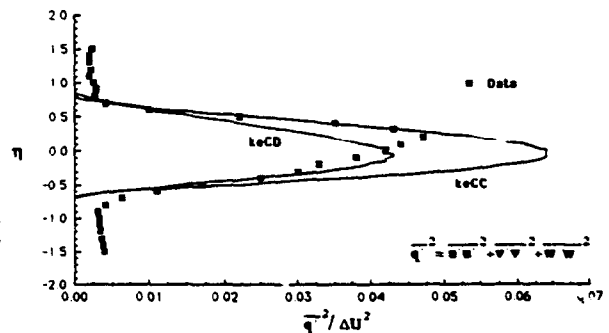
$$\alpha_1 = 1 \ \text{(same as Sarkar)}$$
$$\lambda = .1 \ \text{(same as Zeman)}$$
$$\beta = 60 \ \text{(fits LaRC data the best)}$$

The equation for turbulent kinetic energy, k, is given by:

$$\rho \frac{Dk}{Dt} = \frac{\partial}{\partial X_i}\left[\frac{\mu_t}{\sigma_k}\frac{\partial k}{\partial X_i}\right] + P - \rho(\epsilon_s + \epsilon_o) + \overline{p'd'}$$

where the turbulent production, P, in both the k and ϵ_s equations utilizes the compressible μ_t

Quantity	Primary Stream	Secondary Stream
Stagnation Pressures:	$P_{t1} = 552$ kPa	$P_{t2} = 43.4$ kPa
Stagnation Temperatures:	$T_{t1} = 279$ K	$T_{t2} = 289$ K
Static Pressures:	$P_1 = 40.3$ kPa	$P_2 = 40.3$ kPa
Freestream Velocities:	$U_1 = 543$ m/s	$U_2 = 91.2$ m/s
Static Temperatures:	$T_1 = 132$ K	$T_2 = 285$ K
Sonic Velocities:	$a_1 = 230$ m/s	$a_2 = 338$ m/s
Mach Numbers:	$M_1 = 2.36$	$M_2 = 0.27$
Freestream Densities:	$\rho_1 = P/RT_1 = 1.06$ kg/m³	$\rho_2 = P/RT_2 = 0.49$ kg/m³
Freestream Viscosities:	$\mu_1 = 9.10 \times 10^{-6}$ Pa-s	$\mu_2 = 1.77 \times 10^{-5}$ Pa-s

Figure 12. Comparison of asymptotic turbulence intensity profiles for the Gruber and Dutton high-speed shear layer data case.
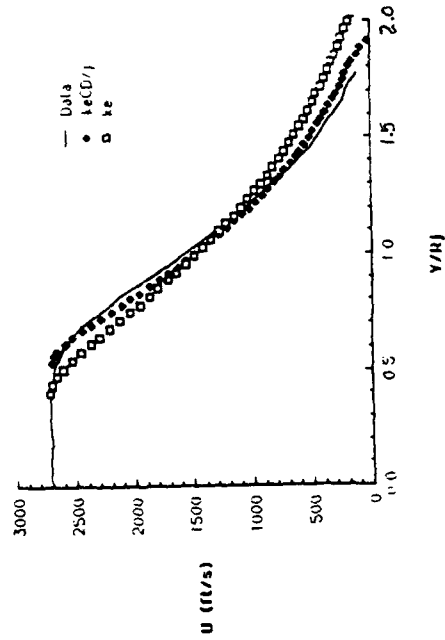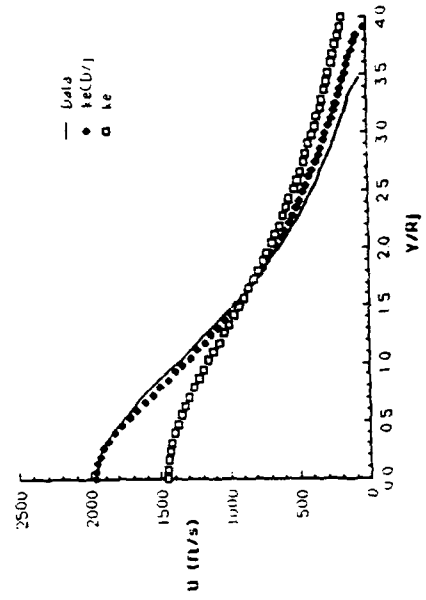
Figure 13. Comparison of kε and kεCD preditions with Seiner Mach 2, 900°F round jet data.

2.6 Turbulence Phenomena/Two-Phase Flows

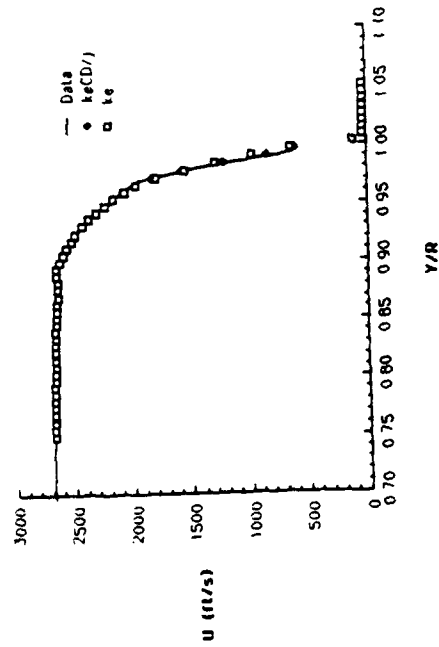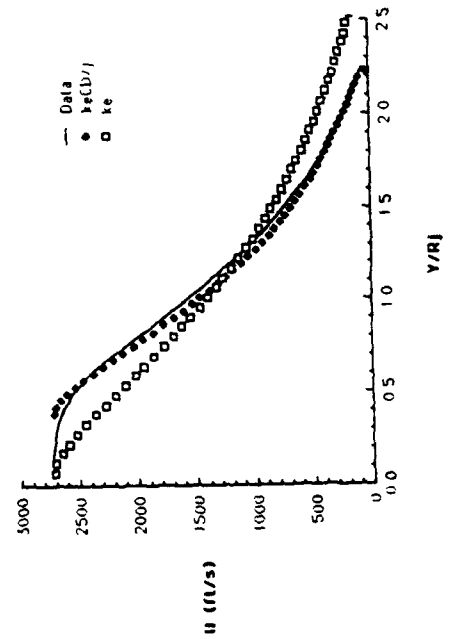For two-phase exhausts, the turbulence situation becomes quite more complicated. Earlier data for low speed particle-laden jets (see the survey of Melville and Bray[44]) had indicated the following:

(1) Particulates are dispersed by the turbulence in accordance with their ability to respond to the local turbulent fluctuations (which is a function of the particle size and material density, and the characteristics of the gas-phase turbulence structure). Thus, small/light particulates will be highly responsive and diffuse like gas-phase species while the large/heavy particulates will be non-responsive and will not diffuse. The Stokes number, $St = \sigma_P/\sigma_f$, which relates the particle relaxation time to the fluid/turbulence time scale is a measure of the particle's ability to undergo turbulent diffusion.

(2) The particulates can appreciably alter the gas-phase turbulent mixing rate via mean flow lag effects (as in nonturbulent flow regions) and via direct damping of the turbulent fluctuation levels. The net effect can result in a significantly altered flowfield in comparison to the analogous single-phase problem.

The inclusion of this phenomenology into a rocket plume turbulence model is quite complex since the single-phase turbulence characteristics discussed above must be maintained in the particle-free limit. Earlier work in this area had been confined to low speed particle-laden jets and includes: the two-phase eddy-viscosity formulation of Melville and Bray,[45] the several models investigated by Shuen et al.[46,47] and, the more complex second-order formulation of Elghobashi.[48] None of these formulations is directly applicable to a tactical missile plume environment. However, the Melville-Bray formulation employs particle-response concepts using an algebraic eddy-viscosity formulation which are readily extendable for use with two-equation turbulence models. The extension of the Melville-Bray approach was formulated by Dash,[49] made operational by Beddini and Dash[50,51] and applied to realistic tactile missile plume flowfields by Dash and coworkers.[17,52,53]

The particle relaxation time scale, σ_P, is given by:

$$\sigma_P = \frac{2}{9}\frac{\rho_s}{\mu}r_j^2\,\overline{C_D}(Re_j, M_j)^{-1} \tag{1}$$

where ρ_s is particle material density, μ is the laminar viscosity of the gas-phase mixture, r_j is the particle radius of the jth size group, and C_D is the drag coefficient (scaled to the Stokes flow value) which is a function of the lag Reynolds and Mach numbers (see Ref. 17 for the curve fits of Henderson, Hennsen and Crowe utilized for the wide range of conditions encounterable in rocket plumes). The characteristic fluid/turbulent time scale, τ_f, is given by:

$$\tau_f = \frac{\Lambda}{|U'^2|^{1/2}} \tag{2}$$

where Λ is the Eulerian macro length scale. If a $k\epsilon$ two-equation model formulation is employed, τ_f can be expressed by:

$$\tau_f = C_t\frac{k}{\epsilon} \tag{3}$$

where C_t is a time scale constant to be evaluated using appropriate data.

Recent numerical simulations[54-60] and experimental results[61-65] suggest that there are three ranges of particle response to fluid motion depending on the values of the Stokes number. For Stokes numbers much less than unity (category 1), the particles respond to changes in the flow and thus closely follow the fluid motion. For Stokes number much greater than one (category 3), the particles are nearly unaffected by changes in the flow and disperse much less than the fluid. In the broad classification of particle dispersion, characeized by Stokes numbers on the order of unity (category 2), the particles seem to become entrapped in the vortices (large scale structures) and flung outward by a centrifugal force. The centrifuging effect results in particles dispersing more than the carrier fluid. This phenomenon has been observed in both experiments and direct simulations but has yet to be modeled.

3. ZONAL/COMPONENT MODEL SIMULATION OF PLUMES AND MISSILE AIRFRAME INTERACTIONS

3.1 Zonal/Component Plume Models

During the period 1975-76, the first Zonal/Component missile plume model[66] was developed at General Applied Science Labs. (GASL) which solved the viscous/inviscid nearfield structure in detail using boundary layer type coupling concepts, contained generalized plume chemical kinetics, and contained a two-equation, compressibility-corrected turbulence model. Based on U. S. government-sponsored "plume olympics" held in 1977, the requirement for developing a new U. S. standardized plume model was made evident. A program was initiated in 1978 to develop a new standardized low altitude plume model which would involve upgrades and extensions to the features of the GASL model. This resulted in the Standardized Plume Flowfield model (SPF), a primary tool used for analyzing tactical missile exhaust plumes in the United States.

The JANNAF SPF is a computer code comprised of a unified series of "modules" which provide for the integration of the flow equations in various flow regions; the inclusion of generalized chemical kinetics, two-phase flow interactions, various turbulence models; and specialized procedures for interfacing with the external flow and for treating embedded subsonic zones behind Mach discs. The various modules contained in the SPF are exhibited in Fig. 14. There are presently three versions of the SPF that have been developed or are now under development. These versions are combinations of the numerical techniques summarized in Table V. The specific features of the three

versions are summarized in Table VI. A brief overview of each of these Zonal/Component Plume models is provided below.
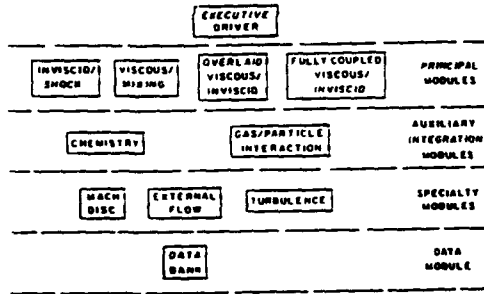

Figure 14. Modular structure of JANNAF standard plume flowfield model (SPF).

Table V. Computational Techniques Used in SPF

Procedure	Flow Regions	Features
Hyperbolic spatial marching technique	Supersonic inviscid flow regions, i.e., nearfield core and external bow shock layer	Conservative shock capturing approach utilizing mappped domains between fitted discontinuity surfaces
Parabolic spatial marching technique	Pressure equilibrated plume farfield	Mapped gas phase stream function coordinates. Implicit treatment of source terms
Overlaid spatial marching technique	Nearfield plume shear layer	Extended form of parabolic technique with equations "overlaid" on map of inviscid nearfield solution for variable pressure field and edge conditions
PNS spatial marching technique	Mach disc mixing region and transitional region	Extended form of hyperbolic shock capturing approach in supersonic regions; pressure-split/partially parabolic approach in subsonic flow regions

Table VI. Versions of SPF

Version	SPF/1	SPF/2	SPF/3
Nearfield	Mixing overlaid on inviscid map	Plume mixing layer overlaid on viscous/inviscid map containing Mach disc mixing solution	Same as SPF/2
Transition Region	Mixing with prescribed pressure decay	As earlier; plume and Mach disc mixing layers merged	Parabolized Navier-Stokes
Farfield	Constant pressure mixing	Constant pressure mixing	Constant pressure mixing
Features/ Limitations	Single-phase flow; No Mach disc mixing/chemistry; Uniform composition exhaust; Finite rate chemistry in mixing solution	Single- and two-phase flow: Mach disc mixing/chemistry; Nonuniform composition exhaust; Finite rate and equilibrium chemistry option	All the proceeding features plus finite rate chemistry thoughout the plume

SPF/1 Model

A description of SPF/1 methodology is available in articles published in the JANNAF 11th[87] and 12th[88] Plume Technology Meetings and in AIAA papers.[69,70] The SPF/1 model is

built upon two principal components: 1) a shock-capturing inviscid plume model[13] (entitled SCIPPY); and 2) a turbulent mixing/afterburning model[71,72] (entitled BOAT). In the plume nearfield, an overlaid procedure[72] is utilized to couple the viscous shear layer and inviscid plume solutions; in the farfield, a constant pressure mixing solution is utilized. The Mach disc problem is treated inviscidly using a sting-approximation for small discs and the Abbett procedure for larger discs (see Ref. 13 for details).

The overlaid concept is a direct extension of classical boundary layer methodology to the analysis of axisymmetric shear layers. In boundary layer theory, the inviscid flow pattern is first calculated followed by a boundary layer calculation with edge conditions and pressure gradients set by the inviscid flow pattern. In the direct extension of this approach to nearfield axisymmetric shear layers, the inviscid exhaust plume and external flow patterns are first determined and the shear layer calculation is then initiated along the inviscid plume interface (Fig. 15). Local edge conditions and pressure gradients are set in accordance with the calculated inviscid flow pattern and the rate of growth of the shear layer.
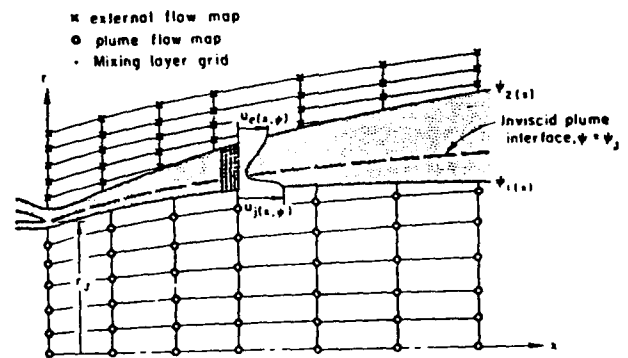
Figure 15. Overlaid grid network for coupling of turbulent shear layer with nonuniform jet/external flow inviscid solutions.

SPF/2 Model

SPF/2 uses the same methodology as SPF/1 but adds capabilities for treating two-phase flow and viscous processes downstream of Mach discs. A description of the procedures developed for dealing with these problems in SPF/2 is available in articles published in the JANNAF 12th[73], 13th[74], 14th[52], and 16th[53] Plume Technology Meeting Proceedings, and in Refs. 17 and 49. As in SPF/1, SCIPPY and BOAT serve as the principal components, extended to incorporate two-phase nonequilibrium effects as described in the above references.

In SPF/2, an approach to account for the strongly interactive viscous and two-phase flow processes behind Mach discs has been developed. This approach is implemented within the confines of the two-step overlaid methodology via extensions to only the shock-capturing SCIPPY model which permit spatial marching through this region (i.e., the

extended version of SCIPPY calculates the inviscid nearfield structure and the coupled Mach disc mixing region in a one pass mode of operation).

The SPF/2 analysis of a two-phase plume requires the stipulation of nozzle exit plane conditions to initialize the calculation, based on a comparable treatment of nonequilibrium processes in the nozzle. Until quite recently, such a code had not been available. A newly developed Navier-Stokes code, PARCH/RN, is now employed whose description will be deferred to a later section of this chapter. Earlier calculations with SPF/2 employed an extended version of SCIPPY for the nozzle analysis as described in Refs. 75 and 76.

The SCIPPY nozzle, and SPF/2 nearfield and farfield predictions depicted in Figs. 16-20 exemplify the characteristic features of a complete two-phase tactical missile exhaust flow calculation. Figure 16 exhibits the limiting particle streamlines in the supersonic portion of the nozzle for the five particle size groups analyzed. Figure 17 exhibits the nozzle centerline temperature variations for the various particle groups and for the gas-phase. Figure 18 exhibits limiting particle trajectories in the plume nearfield (two shock cells). Figure 19 exhibits plume nearfield centerline temperature variations (note the jumps across the strong shocks at $x/r_i = 7$ and 16). Figure 20 exhibits centerline temperature variations in the plume farfield.

Figure 18. Limiting particle streamlines in nearfield of tactical missile exhaust plume.

Figure 19. Gas and particle temperature variations along plume nearfield centerline.
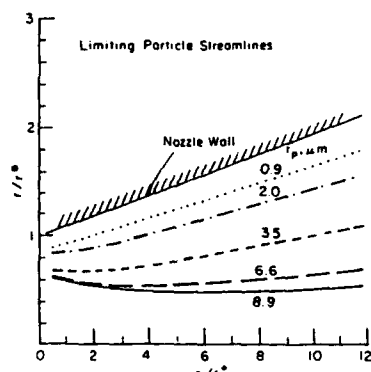

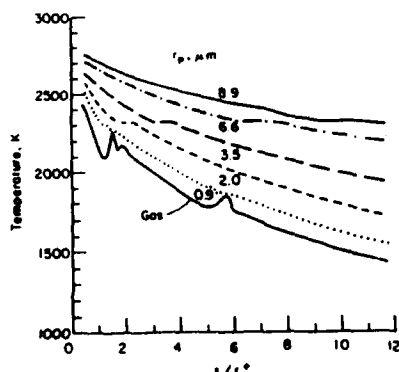Figure 16. Limiting particle streamlines in tactical missile nozzle, analyzed using five particle size groups.

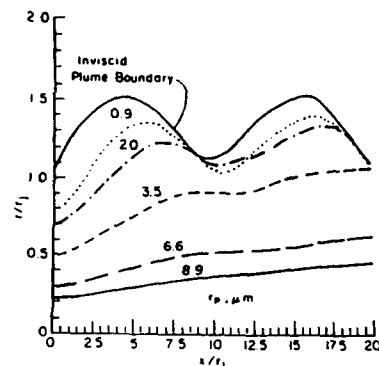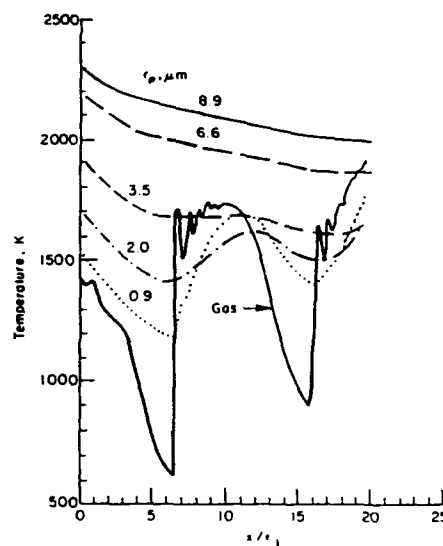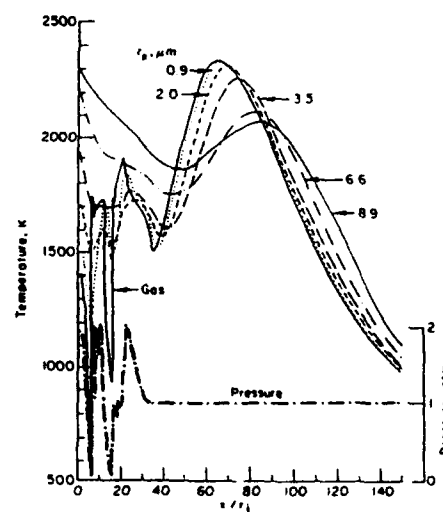Figure 17. Gas and particle temperature variations along nozzle centerline.

Figure 20. Gas and particle temperature and pressure variations along plume nearfield/farfield centerline.

SPF/3 Model

SPF/1 and 2 did not deal with the strongly interactive phenomena associated with plume/missile airframe interactions (e.g. base region phenomena and plume induced separation), and the fully-viscous transitional region of the plume. The SPF/3 model has been developed to provide these types of strongly interactive capabilities. The developmental work is based on the use of two principal components, SCIPVIS and SPLITP. SCIPVIS is a viscous extension of the SCIPPY shock-capturing model and is described in detail in Refs. 5 and 6. It has been applied (on a stand-alone basis) to the analysis of underexpanded jets into uniform supersonic and quiescent external streams as described earlier in the turbulence model discussions. SPLITP was initially formulated as a generalized implicit, parabolic solver for complex mixing problems. SPLITP was extended to encompass PNS-type capabilities for both subsonic regions (using the pressure-splitting methodology described in Ref. 77) and supersonic regions (using the characteristic-based wave solver methodology described in Ref. 78). It has also been used as a research tool to investigate jet/potential flow coupling techniques[79] to provide the technology base for treating jet interactions with a subsonic/transonic external stream.

SCIPVIS and SPLITP can be thought of as replacements for the SCIPPY and BOAT components of SPF/1 and 2. The SPF/3 version of SCIPVIS contains all earlier SCIPPY methodology including the PNS-based Mach disc mixing formulation. SPLITP has been demonstrated to perform the analysis of chemically-reacting plumes and curved shear layers yielding results equivalent to those of BOAT in a more efficient fashion (SPLITP is fully-implicit; BOAT has explicit fluid dynamics with coupled implicit chemistry). The use of SPLITP and SCIPVIS for analyzing the plume nearfield (including base/separated zones) is shematized in Figure 21. The "modernized" Chapman-Korst base region methodology is described in Refs. 79-82.
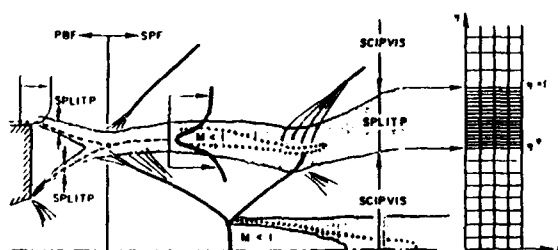
(RNS) computer codes for analyzing missile-related flowfield problems, it is only over the past several years that this methodology has been extended to encompass advanced thermochemical capabilities which permits the realistic simulation of exhaust plumes. In addition, significant advances have been made in the accuracy and robustness of the numerical algorithms utilized in the RNS solvers, and in the methodology for distributing the grid points using solution adaptive methodology. In discussing RNS numerical algorithms, the reader is referred to the text of Anderson et al.[83] for background - our discussion will be quite cursory. The reader is also referred to a recent AGARD article by the author and coworkers[84] for further details on the thermochemical coupling methodology which will be summarized in this chapter, and on numerical and validation studies.

The discussion of the RNS simulation of steady-state flows will distinguish between global time-asymptotic solvers and spatial-marching solvers. Global time-asymptotic solvers calculate all grid points in the flow domain of interest "concurrently", by advancing the solution in time until a steady-state is achieved (i.e., an elliptic mathematical problem in space is converted into a hyperbolic problem in time). Such solvers integrate the full RNS equations (or thin layer variants) and will be termed FNS solvers. They require the storage of all grid points in the flow domain of interest, and a solution can entail the use of very significant amounts of CPU time. FNS solvers "in principal" can handle all continuum flow regimes (subsonic/transonic/supersonic/hypersonic), and, can analyze recirculating flows as occur in base/separated flow regions. However, different classes of FNS solvers are best suited for different flow regimes (e.g., an FNS solver optimized for hypersonic flows with strong shock waves may not be well suited for analyzing very low speed, nearly incompressible flow problems) which can pose computational problems for simulating generalized tactical missile/plume interaction flowfields where varied flow regimes are encountered.

For supersonic/hypersonic flows with thin viscous regions, the RNS equations can be "parabolized" by omitting the stress/diffusive terms in the streamwise direction. The resulting parabolized Navier-Stokes (PNS) equations are spatially hyperbolic permitting a forward streamwise integration from one streamwise plane to the next. Here, only two streamwise planes need to be kept in storage at a time (or three, for 2nd order accuracy in the streamwise direction) and CPU requirements are rather modest even for complex 3D flows. However, even for supersonic flight velocities, all tactical missile/plume interaction problems contain regions of subsonic flow (e.g., surface boundary layers, behind Mach discs in plumes, etc.) and possibly, recirculating flow (e.g., base/separated flow regions). If subsonic regions are thin and elliptic/upstream influence effects negligible, numerical tricks can be employed to permit spatial marching through these regions (e.g., the use of sublayer approximations in the subsonic portion of wall boundary layers). The most recent PNS solvers employ time-iterative concepts in a spatial marching framework.

Figure 21. Use of SPLITP and SCIPVIS components in SPF/3 analysis of plume nearfield.

4. NAVIER-STOKES CODE SIMULATION OF ROCKET MOTOR PLUMES

4.1 Overview

While significant work has been performed over the past 10-15 years towards the development of Navier-Stokes

The solution at the unknown streamwise station is integrated in a time-asymptotic manner to steady-state, with the integration initiated utilizing the properties at the previous streamwise step. Adequate convergence is generally obtained in several time-integrations. This time-iterative procedure is capable of integrating through "thin" regions of recirculating flow (negative streamwise velocities would destabilize a conventional space-marching approach) and has provided significant improvements in overall accuracy and robustness over earlier direct spatial-marching procedures.

The inclusion of thermochemistry into "older" types of RNS solvers has been available for many years and will not be discussed in this chapter. The emphasis here will be on "modern" implicit/strongly conservative RNS solvers which first became available for perfect-gas missile aerodynamic flowfield problems about ten years ago. The inclusion of finite-rate chemistry into such solvers is a recent development and has followed two paths, namely:

1) the matrix-split method which loosely couples the time-iterative solution of the fluid dynamic and chemical species/kinetics equations but provides a strongly-coupled steady-state solution with "minimal" CPU expense for the costly kinetic calculations; and,

2) the large-matrix method which strongly couples the fluid and chemical species/kinetics equations providing a highly robust, but expensive procedure for including thermochemistry.

Each of these methods has inherent advantages for specific problems, and an overview of both approaches will be given based on the author's experience in the development and application of the PARCH (FNS) and SCRINT (PNS) matrix-split codes, and the CRAFT (FNS) and SCHAFT (PNS) large-matrix codes whose basic features are summarized in Table VII below. The remainder of this section will: provide a brief overview of recent developments in FNS and PNS methodology; describe methodology for the the inclusion of chemical and multi-phase nonequilibrium into modern RNS codes; and describe applications of such codes to plume related flowfield problems.

4.2 Recent Developments in FNS Methodology

The discussion will initiate with the work of Pulliam, Steger and coworkers at NASA/Ames[86] which led to the development of the Ames Research Code (ARC)[86] in the early 1980's. This code solved the thin layer FNS equations in a strongly-conservative manner using the implicit, approximately-factored scheme of Beam and Warming.[87] Beam-Warming implicit numerics provided significant improvements in run time to that of earlier explicit numerics (e.g., MacCormack scheme[88] and variants). Supplemented by upgrades such as a fast diagonalized matrix inversion procedure[89] and improved artificial dissipation models with pressure filters (to localize dissipation to strong wave regions),[90,91] the Beam-Warming based ARC code proved to be the most popular FNS code in the United States in the early to mid 1980's for solving steady subsonic, transonic and supersonic aerodynamic problems (.3 < M < 3).

**Table VII.** FNS and PNS Computer Codes with Advanced Thermochemistry

FNS CODES	PNS CODES
PARCH 2D/3D	**SCRINTX/3DT**
Finite difference discretization	Finite difference discretization
Beam-Warming algorithm	Beam-Warming algorithm
Matrix split chemistry	Matrix split chemistry
Multiphase flow (eq/non-eq)	Time-iterative framework (3DT)
Roe/TVD algorithm: air only	Roe/TVD algorithm: air only
Several two-eq. turb. models	$k\epsilon$ turbulence model
Generalized grid blanking	Specialized grid blanking
Generalized explicit BC	Implicit or explicit BC
CRAFT	**SCHAFT**
Extension of TUFF thin-layer NS code	Extension of STUFF PNS code
Finite volume discretization (2D or 3D)	Finite volume discretization
Roe/TVD algorithm	Roe/TVD algorithm: time-iterative
Stongly coupled/large matrix chemistry	Strongly coupled/large matrix chemistry
Fully implicit BC	Fully implicit BC
$k\epsilon$ turbulence model	$k\epsilon$ turbulence model
Research status: limited BC/ blanking	Research status: limited BC/ blanking

Recent ARC related methodology and applications were discussed by Pulliam and Steger in Refs. 92 and 93. ARC has formed the basis for numerous FNS projectile codes as typified by the work of personnel at the U.S. Army Ballistic Research Labs throughout the 1980's (see, e.g., Refs. 94-96). Recent upgrades to projectile aerodynamic versions of ARC have involved the utilization of 2nd-order upwind numerics as typified by the work of Shian and Hsu.[97,98]

A major extension of ARC methodology relevant to the nozzle/plume environment was performed by Cooper and coworkers at AEDC during the period 1985-1987, via development of a propulsive version entitled PARC.[99] Cooper incorporated the full stress terms, generalized boundary conditions, and added grid blanking (patched grid approach) as schematized in Fig. 22, which permits patching the overall flowfield to "blank out" grid points occupied by embedded obstacles (rather than contour the grid about such obstacles as would be required in conventional FNS codes). This facilitates the treatment of embedded boundaries such as steps, struts, cavities, etc., which would be difficult to deal with if blanking capabilities were not available. With blanking, the overall grid is broken down into a set of "patches' for each of the mapped coordinate directions (i.e., patching is done in mapped computational coordinates, not in physical coordinates). The patches are automatically constructed from boundary inputs. Figure 22 illustrates the patching concept for a simple 2D problem. Boundary conditions are applied along the outer computational boundaries as well as on the embedded boundaries, and are generalized to permit varied fluxes to cross the boundaries. The AEDC PARC code has been quite popular for propulsive flowfield simulation and test facility support as described in Refs. 100-106. However, all applications were for single-phase, perfect-gas flows and implemented simple algebraic turbulence models.
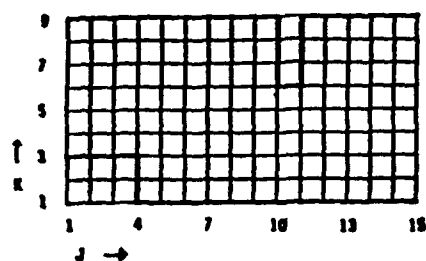
a. Computational grid
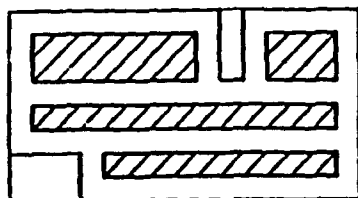
b. J-Patches
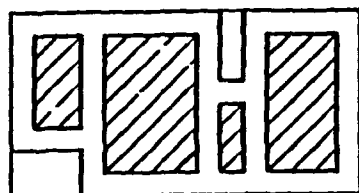
c. K-Patches

Figure 22. Patched grid methodology in PARC code for treating irregular geometries with simpled grids (from Ref. 99).

The work of the author and coworkers towards developing FNS plume/missile airframe steady flow predictive capabilities has focussed on the computer code, PARCH, for which 2D (planar/axisymmetric) and 3D versions have been developed. PARCH is an outgrowth of the NASA/Ames ARC aerodynamic code and the AEDC propulsive extension, PARC. The PARCH code developmental activities have taken place as follows:

1) The 2D and 3D versions of ARC and PARC were unified into a baseline PARCH2D Master Code and a baseline PARCH3D Master Code. The baseline PARCH2D/3D Master Codes contain all the desired capabilities available in the ARC and PARC codes. The coding was performed as an upgrade to PARC which had many propulsive-oriented features not available in ARC, particularly, grid blanking/patching.

2) As a prerequisite to incorporating extended thermochemical and turbulence modeling capabilities, implicit, approximately factored ADI based scalar solvers were developed to solve the chemical species and turbulence model convective/diffusive equations. These scalar solvers emulated the numerics of the PARCH fluid solver.

3) Matrix-split methodology was formulated to incorporate the chemical species equations and the finite-rate chemical kinetics into the PARCH codes.[107]

The sequential development of PARCH and related validation studies are described in Refs. 84 and 108-113. For tactical missile/exhaust plume interaction flowfields, two specialized versions have been developed, namely PARCH/TMP – a 3D missile/plume interaction model, and PARCH/RN – an axisymmetric rocket nozzle model. Both utilize diagonalized Beam-Warming numerics with matrix-split finite-rate chemistry. PARCH/TMP treats particulates using an equilibrated mixture approach; PARCH/RN provides for a full nonequilibrium treatment of particulates. Other specialized version of PARCH have been developed for varied applications.

PARCH is well suited to analyze steady, conventional and nonconventional, tactical missile/exhaust plume interactive flowfield problems. For problems with very strong shock waves (e.g., high velocity missiles, highly underexpanded jets, etc.) and/or unsteady flow problems (e.g., short duration lateral control jets), the shock capturing capabilities of the PARCH code may be deficient. Improvements to robustness and accuracy are obtained by moving from the finite-difference discretization/central difference numerics in PARCH, to finite-volume discretization/upwind numerics. Such a change is substantive particularly with the inclusion of chemical kinetics, since the matrix-splitting approximation in PARCH would not be consistent with the upwinding. The upwind matrix elements have to be carefully constructed using a strongly-coupled formulation to properly incorporate the real gas behavior (see, e.g., Refs. 114-116). Current activities by the author and coworkers have focussed on the development of the CRAFT code whose features are summarized in Table VII. CRAFT is an extension of the TUFF NS code developed by Molvik and Merkle[117] which utilizes Roe/TVD upwind numerics[118,119] with a finite-volume discretization of the equations, a fully-consistent Roe real-gas averaging, and a strongly-coupled, fully implicit treatment of the chemical kinetics. TUFF is an aerodynamic code; CRAFT has been extended to provide plume/propulsive capabilities. Plume/propulsive extensions to CRAFT have involved the inclusion of: the full stress terms; two-equation turbulence models; a dynamic grid for time-accurate applications of flows with moving boundaries; and a generalization of the clean air chemistry to that of generalized H/C/N/O systems. The recent development of a time-accurate particulate solver for CRAFT is described in Ref. 120, while generalized liquid/solid propellant thermochemical upgrades are summarized in Ref. 121.

4.3 Recent Developments in PNS Methodology

As per the FNS discussion above, for developments in the PNS arena, we will again start with "modern" codes which utilized finite-difference Beam-Warming numerics as typified by the Schiff and Steger PNS code[122] which evolved into the popular AFWAL 3D PNS code[123]—the most widely used PNS code in the United States in the early to mid 1980's for high speed aerodynamic simulation. Significant improvements to the AFWAL spatial marching PNS methodology were provided by the recent 2D and 3D UPS PNS codes of Lawrence et al.[124,125] which utilized Roe/TVD upwind numerics with a finite-volume discretization of the equa-

tions. Air chemistry was incorporated into such codes by Tannehill and coworkers as described in Refs. 126 and 127 using loosely-coupled methodology. The author and coworkers had developed extended versions of the AFWAL and UPS FNS codes for National AeroSpace Plane aerodynamic and propulsive applications. The internal flow code, SCRINT, was an AFWAL extension and the external flow code, SCRAMP, was a UPS extension (see Refs. 128 and 129).

The original versions of SCRAMP and SCRINT contained only equilibrium air thermochemistry. A research version, SCRINTX, was upgraded to include combustion-oriented finite-rate chemistry into the Beam-Warming numerical framework using a matrix-split approach.[107,130] SCRINTX was applied to a variety of combustor and nozzle related flowfield problems as well as to inlets. Its performance was compared with earlier PNS codes with chemistry as described in Ref. 131. It did quite well for problems where the central difference numerics were adequate to capture shock waves.

In 2D research with SCRINTX, first and second order (TVD) Roe upwind numerics were incorporated into the code after the matrix-splitting was performed. This simplified approach worked quite well for flows with air chemistry, but worked poorly for strongly combusting flow problems where the approximations entailed "broke down." Hence, the success obtained in this work (and the work of others, e.g., the work described in Refs. 126 and 127) for air chemistry, did not transfer to strongly combusting flows where chemistry strongly influences the wave field. For such flows, the Roe formulation requires use of strongly coupled fluid and chemical species equations. For space marching, such a Roe formulation depends upon an eigendecomposition whose derivation is quite difficult to perform.[132] The Roe (PNS) formulation with chemistry is much easier to develop if the approximate Riemann problem is posed in time rather than space. For time marching, the eigen-functions for a much simpler matrix are required, and in fact, this analysis has been completed by several researchers, such as Molvik and Merkle.[117] At the 3D level, the PNS work of the author and co-workers has concentrated on the inclusion of time-iterative methodology into existing finite-volume (SCRAMP3D) and finite-difference (SCRINT3D) spatial marching codes.[133] Significant improvements in robustness and accuracy, above that provided by the inclusion of upwind numerics, have been obtained by the use of time-iterative relaxation methodology as discussed in the recent PNS survey paper of Krawczyk et al.[134] Also, significant work was performed involving the use of advanced grid generation techniques in the cross-flow plane and grid blanking for the treatment of cavities and swept surfaces.

Preliminary 3D PNS work with chemistry had concentrated on the inclusion of chemistry into the SCRINT3DT code which was a 3D extension of the SCRINTX code with time-iterative PNS numerics. SCRINT3DT was made operational with matrix-split chemistry and operated with Beam-

Warming central difference numerics or simplified real gas Roe upwind numerics (the splitting was done before the Roe decomposition). As per the spatial marching experience with SCRINTX, its ability to analyze strongly combusting flow problems with simplified Roe real gas upwind numerics was found to be problematic - the obvious remedy was a reformulation of the Roe real gas methodology using a large matrix/fully-coupled framework. As this rather ambitious effort was to initiate, the STUFF 3D iterative PNS code of Molvik and Merkle[117] became available which had the large-matrix/fully coupled Roe formulation done properly for clean air chemistry. It was deemed more expeditious to use the STUFF code as a baseline code than to upgrade the SCRINT3DT code, and the added benefits of the finite-volume formulation of STUFF became available with this decision. The upgraded version of STUFF is called the SCHAFT code, and work to date has involved the generalization of the chemistry and the inclusion of two-equation turbulence models,[132,135-137] very much akin to the CRAFT code upgrades described above. The nearly identical structure of TUFF/STUFF (and thus CRAFT/SCHAFT), facilitates concurrent FNS/PNS upgrades.

In referring back to Table VII, there are thus 2 classes of codes for FNS and PNS solutions: finite-difference codes with central difference/Beam-Warming numerics and matrix-split/loosely-coupled chemistry (PARCH/SCRINT), and finite-volume codes with Roe/TVD upwind numerics and large-matrix/strongly-coupled chemistry (CRAFT/SCHAFT). PARCH is currently the utilized for steady-state tactical missile airframe/plume interactive flowfields, and there are distinct advantages to the matrix-split approach utilized for chemistry for dealing with large numbers of chemical species in a time-asymptotic simulation. CRAFT is currently used where shocks are very strong and more robust upwind/finite-volume numerics is required, and for time-accurate studies. PNS requirements are generally more stringent than FNS requirements, and SCRINT has not proven capable of dealing with the severe missile plume environment. The current code of choice is SCHAFT due to its enhanced robustness for such flows.

In the rest of this article, a brief description of PARCH code numerics and relevant applications to missile plume flowfields is provided. PARCH represents the current state-of-the-art for such methodology. PNS methodology is not applicable for subsonic/transonic flight, nor for recirculating regions such as the vehicle base region. However, for supersonic flight velocities, PNS methodology is applicable downstream of the plume first cell region. PNS methodology has been used in conjunction with FNS in a zonal manner as described in Refs. 138 and 139.

4.4 PARCH FNS Code/Gas-Phase Equations

PARCH solves the Reynolds averaged, compressible flow equations, cast in strong conservation form in generalized curvilinear coordinates:

$$\frac{\partial Q}{\partial t} + \frac{\partial E}{\partial \xi} + \frac{\partial F}{\partial \eta} + \frac{\partial G}{\partial \delta} - H = 0 \qquad (4)$$

A detailed description of the fluid dynamic elements in the above vector arrays and the transformation to generalized coordinates is provided in Refs. 86 and 99. The PARCH code contains options for solving thin layer equations and Euler equations in addition to the full NS equations.

With the addition of ns chemical species equations (i = 1,2,3, ..., ns) and the two $k\epsilon$ turbulence model equations to the continuity, momentum and energy equations, the [5 + ns + 2] vector array of dependent variables is given by:

$$Q = \frac{1}{J}\begin{bmatrix} \rho \\ \rho u \\ \rho v \\ \rho w \\ E_t \\ \rho \alpha_i \\ \rho k \\ \rho \epsilon \end{bmatrix} \tag{5}$$

The inviscid (E_i, F_i, G_i) and viscous (E_v, F_v, G_v) flux vectors take the form:

$$E_i = \frac{1}{J}\begin{bmatrix} \rho U \\ \rho uU + \xi_x P \\ \rho vU + \xi_y P \\ \rho wU + \xi_z P \\ (E_t + P)U \\ \rho U\alpha_i \\ \rho Uk \\ \rho U\epsilon \end{bmatrix} \tag{6a}$$

$$E_v = \frac{1}{J}\begin{bmatrix} 0 \\ \xi_x \tau_{xx} + \xi_y \tau_{xy} + \xi_z \tau_{xz} \\ \xi_y \tau_{yx} + \xi_y \tau_{yy} + \xi_z \tau_{yz} \\ \xi_z \tau_{zx} + \xi_y \tau_{zy} + \xi_z \tau_{zz} \\ \xi_x q_x + \xi_y q_y + \xi_z q_z \\ \mu(\xi_x \alpha_{ix} + \xi_y \alpha_{iy} + \xi_z \alpha_{iz}) \\ \mu(\xi_x k_x + \xi_y k_y + \xi_z k_z) \\ \mu(\xi_x \epsilon_x + \xi_y \epsilon_y + \xi_z \epsilon_z) \end{bmatrix} \tag{6b}$$

where $E = E_i - E_v$. Analogous expressions are obtained for the F and G arrays, and, the source term vector H takes the form:

$$H = \frac{1}{J}\begin{bmatrix} 0 \\ H_{P_u} \\ H_{P_v} \\ H_{P_w} \\ H_{P_h} \\ \dot{\omega}_i \\ P - \rho\epsilon \\ \frac{\epsilon}{k}(C_1 P - C_2 \rho\epsilon) \end{bmatrix} \tag{7}$$

In the above equations $\xi(x,y,z)$, $\eta(x,y,z)$ and $\delta(x,y,z)$ represent the curvilinear coordinates in the transformed computational domain: $\xi_x, \xi_y, \xi_z, \eta_x, \eta_y, \eta_z, \delta_x, \delta_y, \delta_z$, and J

represent the metrics and Jacobian of the transformation; ρ is the fluid density; P is the pressure; u, v, and w are the Cartesian velocity components in the x, y, and z directions; α_i represents the mass fraction of the ith chemical species, μ is the laminar viscosity; $q_{x,y,z}$ is the heat flux; k is the turbulent kinetic energy; and ϵ is the turbulence dissipation rate. U, V, and W are the contravariant velocity components.

For turbulent flow simulation, the laminar viscosity and thermal conductivity are replaced by their respective sums of laminar and turbulent values (i.e., $\mu + \mu_t$, k + k_t). Additionally, the source term H is comprised of the chemical production terms ω_i; the turbulent production $\underline{P}$, and the dissipation of turbulent kinetic energy, ϵ; and the gas/particle interaction terms $H_{P,u}$, $H_{P,v}$, $H_{P,w}$ and $H_{P,h}$ required for multi-phase flow simulation.

4.5 Matrix-Split Methodology

Applying conventional Beam-Warming algorithms to equation (4), utilizing Euler implicit time-differencing, yields the "delta" form finite-difference expression written below for the 2D system of equations:

$$[I + \Delta t(\delta_\xi A^N + \delta_\eta B^N - M^N)]\Delta Q^N$$
$$= -\Delta t(\delta_\xi E^N + \delta_\eta F^N - H^N)] = R^N \tag{8}$$

In equation (8), δ is a central difference operator, $\Delta Q^N = Q^{N+1} - Q^N$ where N denotes the time step level, and, the flux vectors E and F, (which are nonlinear functions of Q) have been linearized about Q^N, e.g., $E^{N+1} = E^N + A^N\Delta Q^N$ where $A = \partial E/\partial Q$. Equation (9) is the unfactored form of the block algorithm and represents a system of four fluid (five for 3D flows), n (= ns) species equations, and two turbulence model equations (which we will now dismiss to simplify our discussion of matrix splitting). We thus seek to decompose an n+4 system of coupled equations, to a system of four coupled fluid dynamic equations, and n scalar chemical species equations. Using the nomenclature

$$Q_f = (\rho, \rho u, \rho v, E_t)^T \tag{9a}$$

$$Q_o = (\alpha_1, \alpha_2, \alpha_3, \ldots, \alpha_n)^T \tag{9b}$$

the n+4 system is decomposed as:

$$\left[I + \Delta t\delta_\xi\left[\frac{A_{ff}}{A_{cf}} \frac{A_{fc}}{A_{cc}}\right] + \delta_\eta\left[\frac{B_{ff}}{B_{cf}} \frac{B_{fc}}{B_{cc}}\right] - \left[\frac{M_f}{M_c}\right]\right]$$
$$\times \left[\frac{\Delta Q_f}{\Delta Q_c}\right] = \left[\frac{R_f}{R_c}\right] \tag{10}$$

where $A_{ff} = \partial E_f/\partial Q_f$, $A_{cf} = \partial E_c/\partial Q_f$, etc.

The above system of matrices is split about the horizontal (indicated by the dashed lines) leading to the fluid dynamic system written as:

$$[I + \Delta t(\delta_\xi A_{ff}^N + \delta_\eta B_{ff}^N)] \Delta Q_f^N$$
$$= R_f^N - \Delta t(\delta_\xi A_{cf} + \delta_\eta B_{fc}) = \Delta Q_c^N \quad (11)$$

(where the source term M_f, having particulate contributions is treated explicitly, and has thus been incorporated into R_f.)

This exercise in matrix partitioning recovers the original 4 x 4 block structure of the perfect-gas fluid dynamic formulation, with addition of a forcing function on the explicit right hand side and revised elements of the A_{ff} and B_{ff} matrices on the implicit left hand side to account for generalized multi-component species and calorically imperfect behavior. The elements of the forcing function term, ΔQ_c, contain the net influence of the chemical species change (due to convection/diffusion/kinetics) on the fluid dynamic solution through pressure/species derivatives. The inclusion of this term on the right hand side is not essential to obtain a converged steady-state solution and it can be discarded. However, it cannot be discarded for time accurate computations. For the same reason, it cannot be discarded for a space marching PNS computation unless time-iterative methodology is incorporated.

4.6 Numerical Methodology in PARCH

All work with PARCH has focussed on the analysis of steady flow problems using non-time accurate procedures to expedite convergence to steady-state. The block unfactored, matrix-split, fluid dynamic equation (Eq. 11), with the explicit species term, ΔQ_c, removed, are approximately factored as follows:

$$\left[I + \Delta t \delta_\xi A_{ff}^N\right]\left[I + \Delta t \delta_\eta B_{ff}^N\right] \Delta Q_f^N = R_f^N \quad (12)$$

Equation (12) can be solved by block tridiagonal inversion, which is computationally expensive per time step, but generally permits taking large time steps (e.g., Courant numbers of 5 - 10) and obtaining converged solutions in a very reasonable number of iterations (e.g., 300 - 3,000, depending on the problem at hand, the grid, the initial and boundary conditions, etc.). Equation (12) can more efficiently be solved by using the diagonalized scheme of Chaussee and Pulliam[89] which uncouples the block system and reduces the work to the inversion of a scalar tridiagonal system. However, the implicit diagonalized solution is restricted to the Euler equations (the viscous terms do not diagonalize and must thus be treated explicitly), and the path to convergence for complex, viscous dominated flows can be slow and sometimes problematic.

The choice of the blocked tridiagonal inversion or diagonalized solution procedure for the fluid dynamic equations is available as a user option in PARCH and is problem dependent. With multi-zone versions, the diagonalized option can be used in some zones and the blocked option in others (e.g., for a missile/plume interactive problem, the zone of strongly interactive flow can be handled by the block procedure with all other flow zones analyzable by the generally more efficient diagonalized method). With central

difference numerics employed, artificial dissipation is required in nonviscous regions to ensure stability and diagonal dominance. The implicit/explicit second and fourth order dissipation model of Jameson et al.,[90] is employed in PARCH. Independent time steps are used to advance the equations based on a user-specified Courant number (locally applied at each grid point) with a flux change limiter (e.g., 20 percent change in $\Delta Q/Q$), which cuts back on the local time step in regions of severe change.

4.7 Chemical Species/Rate Kinetics Algorithm

Upon matrix splitting and decomposition of Eq. (10), the lower half contains the chemical species transport equations, written as:

$$\left[I + \Delta t(\delta_\xi A_{cc}^N + \delta_\eta B_{cc}^N) - M^N\right] \Delta Q_c$$
$$= R_f^N - \Delta t(\delta_\xi A_{cf} + \delta_\eta B_{cf}) = \Delta Q_f \quad (13)$$

The second term on the right hand side contains the forcing functions from the fluids upon the species, which is discarded for time-asymptotic steady-state solutions. Subsequent factorization leads to:

$$\left[(I - \Delta t M^N) + \Delta t \delta_\xi A_{cc}^N\right]$$
$$\left[(I - \Delta t M^N) + \Delta t \delta_\eta B_{cc}^N\right] \Delta Q_c = r_c^n \quad (14)$$

Equation (14) represents the numerically intensive task of inverting block NxN tridiagonal matrices. CPU costs and memory requirement can become prohibitive as the number of chemical species get large. An efficient alternative solution strategy has been devised, which breaks up the solution sequence into two steps:

    1) a point implicit solution of the chemical kinetic rate equations to yield ω_i; and.

    2) a globally implicit time integration of the species equations sequentially with the chemical source term specified from step 1.

Step 1 requires the inversion of an n x n matrix at each grid point. Recent numerical studies (Ref. 140) have indicated that this computation need not be performed at each time-integration. For rocket nozzle flows, performing step 1 once for every 50 fluid dynamic time steps, and holding the source term constant at the intermediate time steps has yielded the same converged solution obtained by performing step 1 for every integration step, with no convergence penalties. Hence, this splitting can be extremely cost effective for chemically reacting flows with a significant number of chemical species.

4.8 Multi-Phase Flow Capabilities

The PARCH code contains multi-phase flow capabilities for the simulation of solid propellant rocket nozzle/exhaust plume flowfields where the dilute particle assumption applies and eliminates particle volumetric effects. Gas/particle interactions can be treated in both the equilibrium limit (where particle velocities and temperatures are taken to be the same as that of the gas-phase) and the nonequilibrium limit (where particle velocities and temperatures differ from

those of the gas-phase). In the nonequilibrium limit, the analysis is presently restricted to flows with a primary stream wise direction where the particulate equations can be spatially integrated.

The particulate equations, cast in strong conservation form in generalized curvilinear coordinates, are listed below for two dimensions.

$$\frac{\partial E_P}{\partial \xi} + \frac{\partial F_P}{\partial \eta} - H_P = 0 \qquad (15)$$

The inviscid flux vectors (E_P, F_P) take the following form:

$$E_P = \frac{1}{J}\begin{bmatrix} \rho_P U_P \\ \rho_P u_P U_P \\ \rho_P v_P U_P \\ \rho_P h_P U_P \end{bmatrix} \qquad (16a)$$

$$F_P = \frac{1}{J}\begin{bmatrix} \rho_P V_P \\ \rho_P u_P V_P \\ \rho_P v_P V_P \\ \rho_P h_P V_P \end{bmatrix} \qquad (16b)$$

The source term vector H_P takes the form:

$$H_P = \begin{bmatrix} 0 \\ H_{P_u} \\ H_{P_v} \\ H_{P_h} \end{bmatrix} \qquad (17a)$$

$$= \frac{1}{J}\begin{bmatrix} 0 \\ -\rho_P(u_P - u)/\tau_u \\ -\rho_P(v_P - v)/\tau_v \\ -\rho_P(h_P - h)/\tau_h \end{bmatrix} \qquad (17b)$$

Particulate equations are solved for different particulate types (e.g., Al_2O_3) and for several representative sizes (e.g., 1 μm, 3 μm, 5μm, ...). The nomenclature to designate types and sizes has been eliminated for simplicity. In the above equations, u_P and v_P are the Cartesian particulate velocity components in the x and y directions and U_P and V_P are the contravariant velocity components. τ_u, τ_v, and τ_h represent characteristic particle times for velocity and thermal equilibration. Coupling between the gas and solid phase is provided through the gas/particle interaction source terms in both the gas-phase and particulate equations. This has recently been improved by a fully-implicit treatment of the source terms (which can be stiff for small radius particulates which are near equilibrium), including methodology for dealing with phase-change effects (i.e., solidification in the nozzle/plume expansion process). In nozzle/plume applications, the particle solution is typically updated (by marching down the length of the nozzle or the exhaust plume) every 50 iterations of the gas-phase solution (see Ref. 140).

The highly efficient particle spatial marching technique is, of course, limited to flows where there are no recirculating features. Applications include rocket nozzle flow and the farfield of the rocket exhaust plumes. The missile aftbody and plume nearfield is significantly more complex, being characterized by base regions, plume induced separation and thus, significant portions of recirculating flow. The analysis of particulates in such regions requires the usage of a time-asymptotic, elliptic solver. A new time-accurate 3D particle solver is (Ref. 120) now used in CRAFT utilizes implicit/upwind numerics and finite-volume discretization of the Eulerian particle-cloud equations. This new solver is to be implemented in PARCH for time-asymptotic, recirculating flow regions, via straightforward modifications.

5. NUMERICAL STUDIES

5.1 PARCH/RN Rocket Nozzle Studies

A complete missile calculation requires the analysis of the rocket nozzle/propulsive flowfield. For some problems, there can be strong coupling between the nozzle exhaust and the missile aerodynamic flowfields. A specialized version of PARCH (PARCH/RN) has been developed to analyze rocket nozzle flowfields, starting from equilibrium conditions in the combustion chamber. This version deals with multi-phase (gas/particle) nonequilibrium, as well as chemical nonequilibrium and is described in Refs. 110 and 113.

The Back and Cuffel perfect gas test case[141] is a popular one for validation of nozzle codes since both wall and profile data are available, and the large throat curvature poses a distinct numerical challenge to simulate the flow-field in this conical nozzle. The reservoir conditions were P_0 = 70 psia and T_0 = 540 R. The nozzle is a conical geometry with 45° converging and 15° diverging half angles. The throat radius is 0.8 inches with a small throat radius of curvature $(R_c/R_{th} = .625)$. Figure 23 shows the grid utilized and comparisons between the measured and the computed pressures on the wall and axis, for an Euler calculation. The agreement with data is seen to be good upstream of the nozzle throat; however, the comparison is poorer downstream of the throat. The cause of the discrepancy may be inadequate grid resolution in the throat region and failure to resolve the significant gradients produced by the small throat radius of curvature. The agreement with data is comparable to that achieved by most other investigators (see, the recent work of Marcum and Hoffman in Ref. 142).

To illustrate gas/particle nonequilibrium capabilities in PARCH, a solid propellant rocket motor nozzle calculation was performed with H/C/O chemistry (12 species, 16 reactions), and with Al_2O_3 particulates (30% mass loading). Preliminary calculations were performed assuming all the particles to have radii of 3 μm. Computations were performed with and without particles to illustrate the strong influence of particulates on the gas-phase flowfield. Figure 24 compares the Mach number contours from the gas only calculation with that of the multi-phase calculation. As shown by the Mach number contours, the presence of
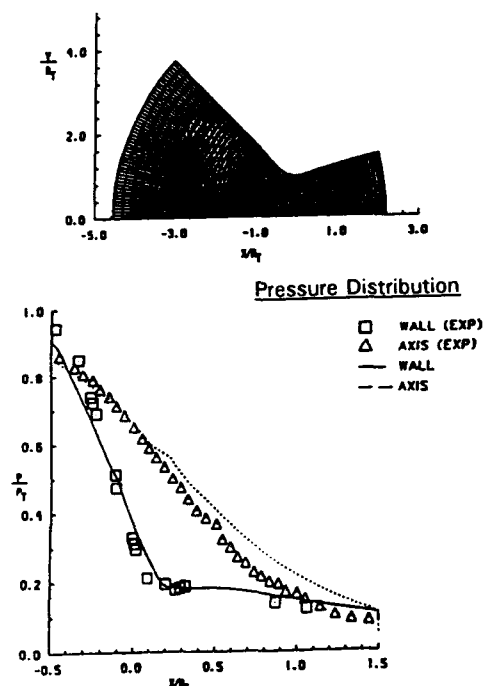
Pressure Distribution

Figure 23. PARCH simulation of Back and Cuffel nozzle test: grid utilized and comparison of predicted wall and centerline pressures with data.
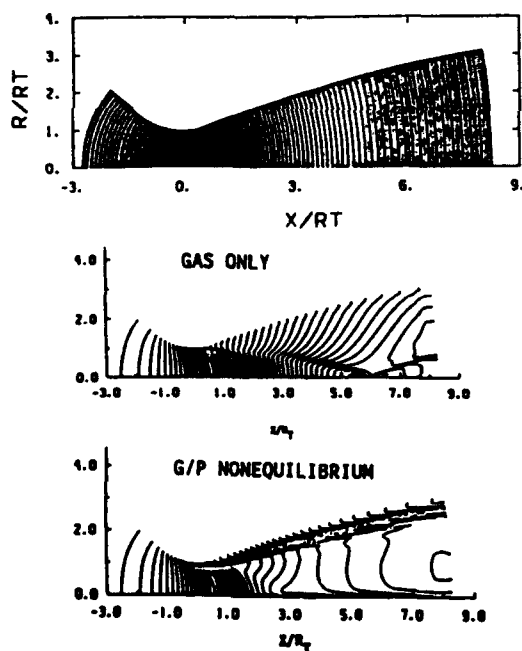

X/RT

Figure 24. PARCH analysis of solid propellant rocket nozzle flowfield: grid utilized and comparison of Mach number contours.

particles has a dramatic influence on the flowfield. The reflected shock disappears; the particles peel away from the nozzle at the throat and the limiting particle streamline effect is clearly seen. Figure 25 shows the temperature distributions along the nozzle centerline. Notice the

particulate temperatures lagging the gas temperature. At the nozzle exit plane, the thermal nonequilibrium between the gas and particles is almost 300°K. Also, the particles begin to solidify with the onset of phase changes indicated by the particle temperature remaining constant. Comparisons with an earlier spatial marching two-phase code[76] are also shown downstream of the throat.
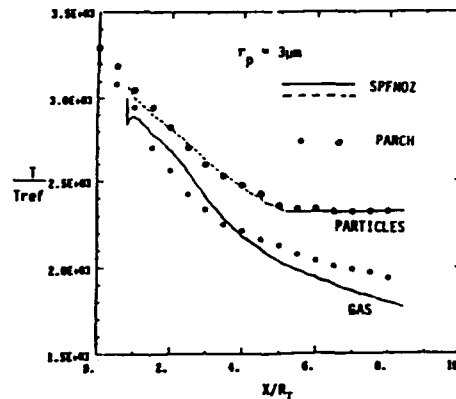
Figure 25. Comparison of PARCH predictions of nozzle centerline gas and particle temperatures with predictions using earlier SPF methodology.

This calculation was also performed with three particle size groups. The total mass loading of particulates remained the same however, it was distributed into particles of 3, 5, and 10 microns with relative mass fractions of .6, .3, and .1. Pressure, temperature, and Mach number contours are shown in Fig. 26. The striations evident in the contours of temperature and Mach number coincide with the limiting particle streamline locations of the three particle size groups (3μ is uppermost, 5μ is next, 10μ is lowest).

Figure 26. PARCH prediction of rocket nozzle pressure, Mach number and temperature contours with gas/particle nonequilibrium for 30% mass loading of Al_2O_3 distributed equally into three size groups.

5.2 Tactical Missile with Single Motor

The simulation of a complete, supersonic, generic missile airframe/nozzle/plume flowfield has been performed to establish the ability to analyze a multi-zone problem with detailed grid resolution. The calculation was performed using air treate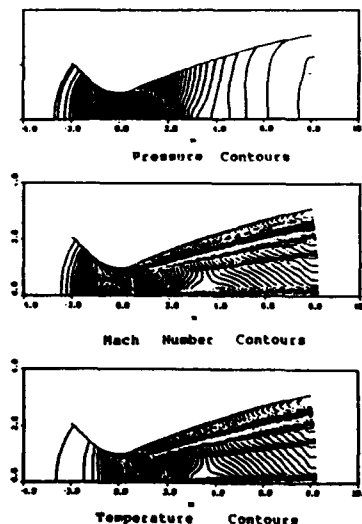d as a perfect gas throughout, and employed the kϵ turbulence model for treating near wall regions. Figure 27 shows the geometry considered and the overall domain of interest. To allow for detailed grid resolution and computational efficiency, the physical domain is divided into four zones which are analyzed separately as shown in Figure 27. These four zones include:

1) the missile body from nose to base;
2) the nozzle flowfield from chamber to exit plane;
3) the near field plume/base region; and,
4) the far field plume region.

The PARCH code was utilized in Zones 1-3; however, Zone 4, the far field plume, was analyzed using the spatial-marching SCHAFT PNS code which is more efficient for use in that extended region.
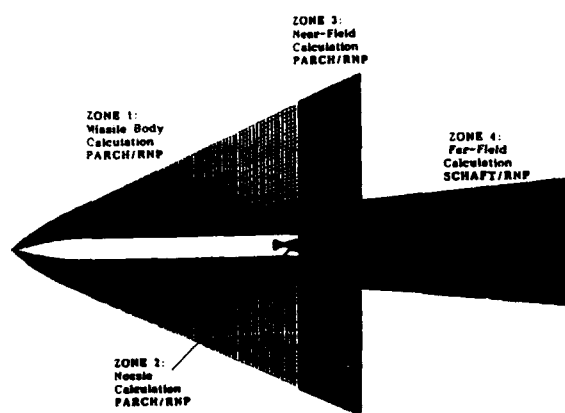

Figure 27. Composite grid of the four zones used for the complete missile/ plume flowfield calculation (grid for Zone 4 not completely shown).

The generic missile calculation simulated a missile travelling at Mach 3 at sea level (P = 1 atm, T = 540 °R). The generic missile had a 1 foot diameter and length of 13 feet and was represented by an ogive/cylinder. The outer boundary for the missile calculation conforms to the shape of the vehicle bow shock, and the grid is nearly uniform far from the body but is highly packed in the near-wall region to resolve the turbulent boundary layer. The boundary layer is assumed to be fully turbulent from the nose and an adiabatic wall boundary condition was applied. Contours of pressure, temperature, Mach number, and turbulent viscosity are shown in Figure 28. Note that by the end of the missile body, the strength of the bow shock has been diminished substantially, and a large turbulent boundary layer has developed (almost half the missile body radius). A 141 x 146 grid was used for the near-field plume region analysis. The upper boundary was a simple continuation of the straight line fixed freestream boundary from Zone 1. At

the inflow plane, the lower 41 grid points fixed the nozzle conditions at the exit plane; the next 59 grid points were used to resolve the base region above the nozzle exit; and the remaining points fixed the inflow conditions from the missile body calculation. The nozzle exit plane radius was 52.8% of the missile body radius. The flow exited the nozzle with an average Mach number of 3.5 with a nominal temperature and pressure of 2700 °R and 2 atm, respectively. Figure 29 exhibits the predicted Mach number contours for this nearfield plume zone. Note that no Mach disc is present. The overall scale of the complete problem is exhibited in Fig. 30, which shows the relative scales of the missile flow, the nearfield plume, and the farfield.

5.3 Tactical Missile with Four Motors

The simulation of the generic missile airframe/nozzle/plume flowfield described earlier has been extended to a four nozzle configuration. The missile body geometry, flowfield conditions, and computational zones are the same; however, the missile now contains four nozzles which contained the same total exhaust area as the above single nozzle. The missile body and nozzle flowfields are obtained as in the earlier single nozzle computation, and the near field plume/base is computed with the three-dimensional version of PARCH. Figure 31 shows the cross-flow grid in the base region. Figure 32 shows a magnified view of the first shock cell for comparison with the above single nozzle case. Note the dramatic differences in the solution produced by the four motors versus the single "equivalent" motor.

PARCH has been applied to the simulation of a four nozzle air-only laboratory experiment for which pressure data is available. It consists of four circular nozzles exhausting from a circular base region. The freestream is quiescent air at 533R and 1 atm. The nozzle exhaust is air at M = 2.6, P = 4.46 atm, and T = 224R. Figure 33 presents contours of density in the X-Z symmetry plane. Note the complex wave structure within the jets and the interactions between them. Figure 34 shows a comparison between the experimental and computed pitot pressure profiles at several axial locations in the X-Z symmetry plane. The results agree reasonably well, with the greatest discrepancy being on the centerline.

5.4 Missiles with Scarfed Nozzles

This unconventional propulsion configuration is sometimes used because the missile is guided by communications through a fiber optic cable attached to the missile base. Not only does this preclude use of conventional propulsion, but requires that the scarfed nozzle configuration be designed such that the base region does not entrain a significant amount of hot exhaust gas which could damage the cable. Figure 35 illustrates the scarfed nozzle geometry. In the calculation described, the missile airframe was analyzed without wings or fins and was performed for a flight Mach number .6 at sea level, at a 10° angle of attack. The conventional diagonalized Beam-Warming numerics in PARCH were employed. The chemistry was frozen and the flow was taken to be fully turbulent from the
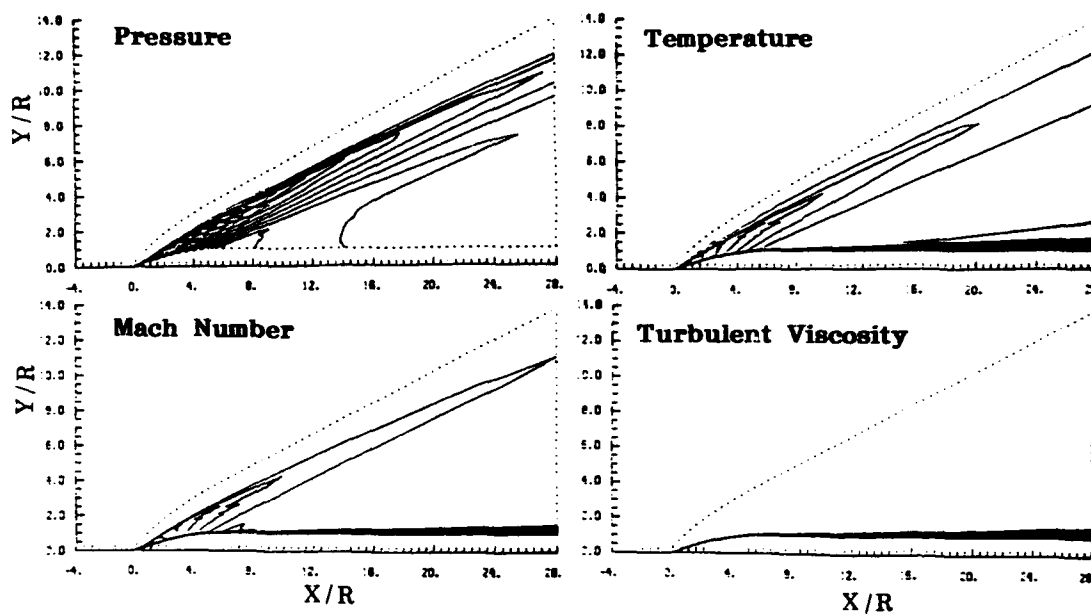
Figure 28. Computed pressure, temperature, Mach number and turbulenct viscosity contours for Zone 1.
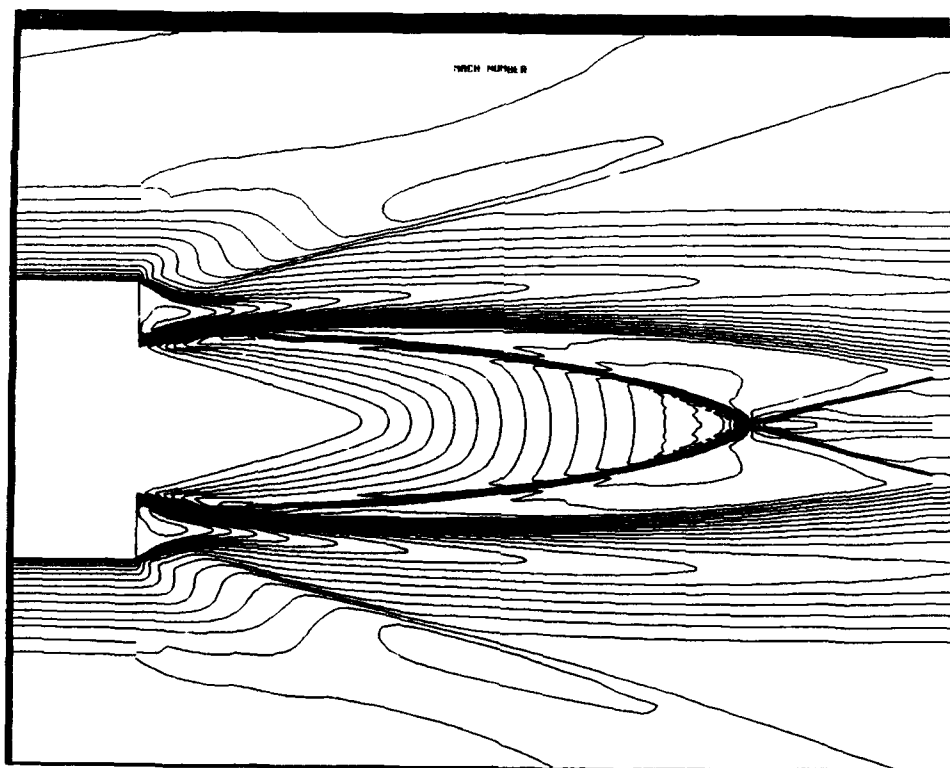
Figure 29. Predicted Mach number contours in nearfield plume zone for missile single nozzle.
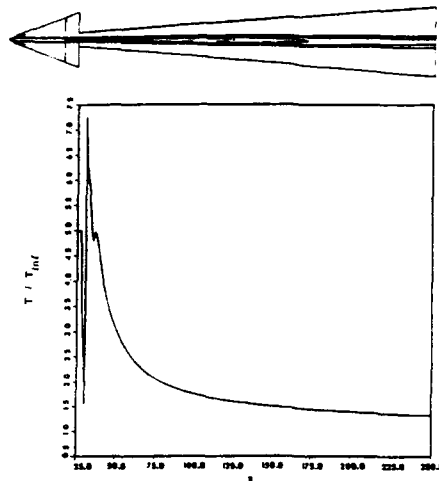
Figure 30. Computed temperature contours and centerline temperature for complete missile/plume flowfield.
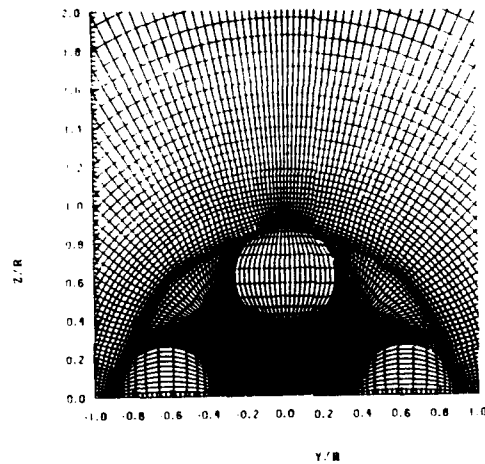
Figure 31. Base region grid utilized for generic missile with four motors.
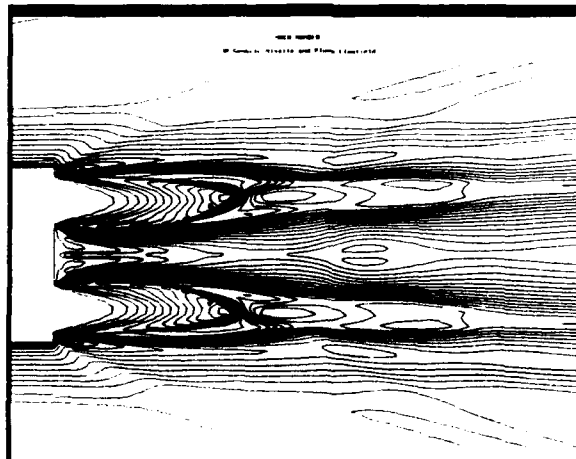
Figure 32. Predicted Mach number contours in nearfield plume zone for missile with four nozzles.
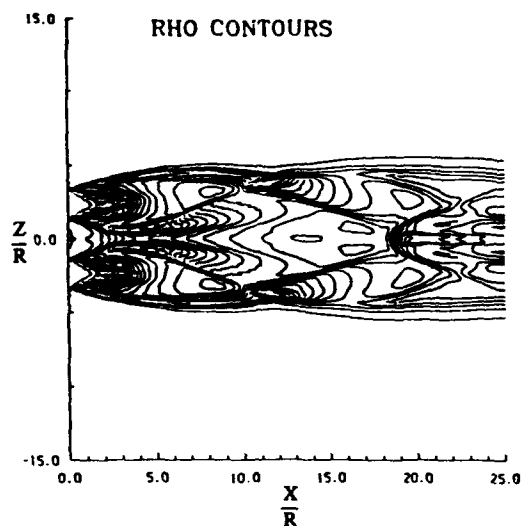
Figure 33. Computed density contours in X-Z symmetry plane.
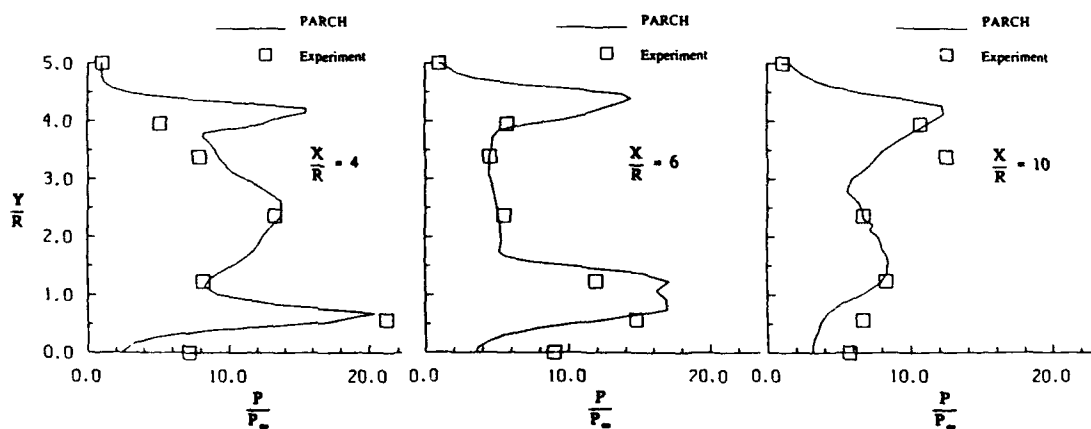
Figure 34. Pitot pressure profiles at several axial locations.
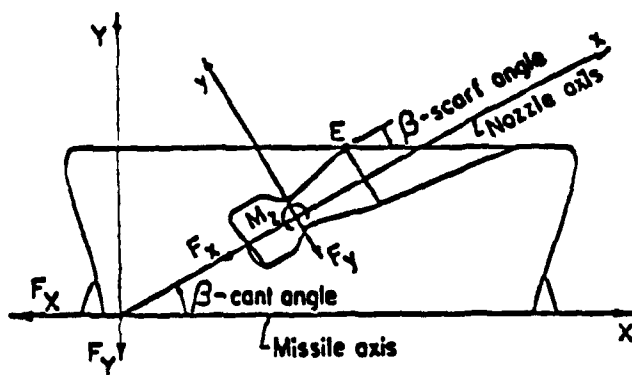
Figure 35. Scarfed nozzle geometry.

missile nose. The kε turbulence model was utilized for the surface boundary layer and the plume shear layers.

Mach number contours are exhibited in Fig. 36 in a plane containing the two nozzle axes (e.g., top view) and in a plane rotated 90° (e.g., side view). The side view contours show a thin turbulent boundary layer on the windward side of the missile, and indicate separated flow on the leeward side. The upstream influence of the propulsive jets is readily evident in the top view Mach number contours.
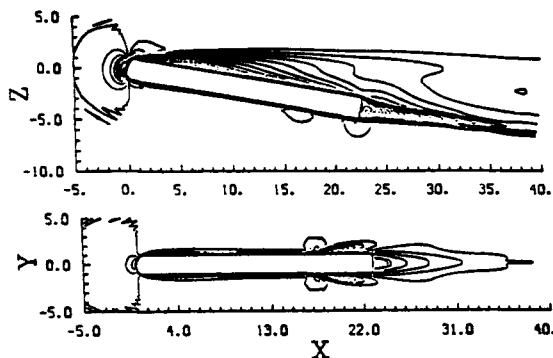
Figure 36. Mach number contours for tactical missile at 10° angle of attack.

To establish additional validation of the PARCH numerics, predictions have been made for the interaction of an inclined jet with an ogive/cylinder missile flowfield at zero angle-of-attack (Ref. 84) for which experimental data obtained at ONERA is available. The missile body is a cylinder with a parabolic ogive nose. The jet issues from a rectangular hole located 8.5 D downstream of the nose at an angle of 70° from the missile surface. The cylinder is considered infinite and base effects are neglected.

Figure 37 depicts Mach number contours in the X-Z symmetry plane for solutions obtained with PARCH with both central difference and Roe upwind algorithms. The jet interaction flowfield is predicted well by both algorithms with the upwind calculation exhibiting a substantially smoother, oscillation free solution. Figure 38 shows pressure contour comparisons in the Y-Z plane at a location of 6.5 D downstream of the nozzle. Comparison is made between the present calculations and the experimental data. Agreement is seen to be very good, with the predicted jet exhibiting somewhat more penetration than the data.

Figure 37. Computed Mach number contours in the X-Z symmetry plane.

Figure 38. Computed and experimental pressure contours in Y-Z plane at X = 6.5D downstream of the nozzle.

4-26

6. REFERENCES

[1]Dash, S.M., Pearce, B.E., Pergament, H.S. and Fishburne, E.S., "Prediction of Rocket Plume Flowfields for Infrared Signature Studies," Journal of Spacecraft and Rockets, Vol. 17, May-June 1980, pp. 190-199.

[2]Pearce, B.E. and Dash, S.M., "Use of Matched Initial Conditions for Predicting Low Altitude Rocket Plume Radiation," AIAA Journal, Vol. 17, June 1979, pp. 667-670.

[3]Dash, S.M. and Wolf, D.E., "Interactive Phenomena in Supersonic Jet Mixing Problems, Part I: Phenomenology and Numerical Modeling Techniques," AIAA Journal, Vol. 22, July 1984, pp. 905-913.

[4]Dash, S.M. and Wolf, D.E., "Interactive Phenomena in Supersonic Jet Mixing Problems, Part II: Numerical Studies," AIAA Journal, Vol. 22, October 1984, pp. 1395-1404.

[5]Dash, S.M. and Wolf, D.E., "Fully-Coupled Analysis of Jet Mixing Problems, Part I: Shock-Capturing Model, SCIPVIS," NASA CR-3761, January 1984.

[6]Dash, S.M., Wolf, D.E. and Seiner, J.M., "Analysis of Turbulent Under-Expanded Jets - Part I: Parabolized Navier-Stokes Model, SCIPVIS," AIAA Journal, Vol. 23, April 1985, pp. 505-514.
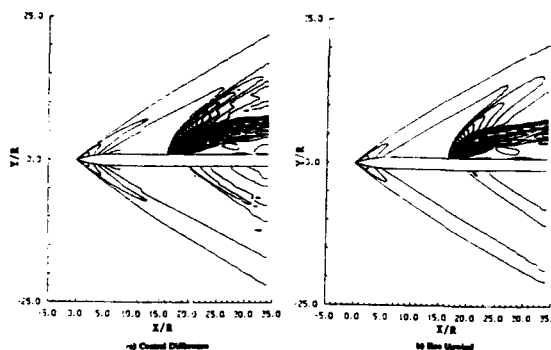
[7]Miller, W.J. and Pergament, H.S., "Chemical Reaction Mechanisms and Rate Coefficients for Use in the JANNAF Standard Plume Flowfield Model," proceedings of the 12th Plume Technology Meeting, CPIA Pub. 332, Nov. 1980, pp. 267-269.

[8]Slack, M. and Ludwig, C., "Plume Data Analysis of Advanced Propellants," AFRPL TR-78-4, September 1978.

[9]Kolb, C.E., et al., "Analysis of IR Radiation Signatures from Advanced and Conventional Propellant Rocket Exhausts," Vol. II, Aerodyne Research, Inc., Rept. No. 77-2471, Jan. 1977.

[10]Jensen, D.E. and Jones, G.A., "Reaction Rate Coefficients for Flame Calculations," Combustion and Flame, 1978, pp. 1-34.

[11]Jensen, D.E., Spalding, D.B., Tatchell, D.G. and Wilson, A.S., "Computation of Structures of Flames with Recirculating Flow and Radial Pressure Gradients," Combustion and Flame, Vol. 34, 1979, pp. 309-326.

[12]Victor, A.C., "Calculations of Rocket Plume Afterburning Coupled to Reacting Base Recirculation Regions," Journal of Spacecraft and Rockets, Sept. 1977, pp. 534-538.

[13]Dash, S.M. and Thorpe, R.D., "Shock-Capturing Model for One- and Two-Phase Supersonic Exhaust Flows," AIAA Journal, Vol. 19, July 1981, pp. 842-851.

[14]Soo, S.I., Fluid Dynamics of Multiphase Systems, Blaisdell Pub. Co., Waltham, MA, 1967.

[15]Marble, F.E. "Dynamics of Dusty Gases," Annual Review of Fluid Mechanics, Annual Reviews, Inc., Palo Alto, CA, 1970.

[16]Rudinger, G., "Relaxation in Gas-Particle Flow," Non-equilibrium Flows, Part 1, Marcel Dekker, Inc., New York, NY, 1969.

[17]Dash, S.M., Wolf, D.E., Beddini, R.A. and Pergament, H.S., "Analysis of Two-Phase Flow Processes in Rocket Exhaust Plumes," Journal of Spacecraft and Rockets, Vol. 22, No. 3, 1985, pp. 367-380.

[18]Hermsen, R.W., "Aluminum Oxide Particle Size for Solid Rocket Motor Performance Prediction," Journal of Spacecraft and Rockets, Vol. 18, November-December 1981, pp. 483-490.

[19]Pergament, H.S., Dash, S.M. and Varma, A.K., "Evaluation of Turbulent Models for Rocket and Aircraft Plume Flowfield Predictions," AIAA Paper 79-0359, January 1979.

[20]Pergament, H.S., "Assessment and Recommendation of Two-Equation Turbulence Models for Rocket and Aircraft Plume Flowfield Predictions," Naval Weapons Center, TP 6364, July 1982. (also JANNAF 13TH Plume Technology Meeting, CPIA Pub. 357, Vol. II, April 1982, pp. 73-126.)

[21]Pergament, H.S., Sinha, N. and Dash, S.M., "A Hybrid Two-Equation Turbulence Model for High Speed Propulsive Jets," AIAA Paper 86-1723, Huntsville, AL, June 1986.

[22]Launder, B.E., Morse, A., Rodi, W. and Spalding, D.B., "Prediction of Free Shear Flows: A Comparison of Six Turbulence Models," in Free Turbulent Shear Flows, NASA SP-321, Vol. I, July 1972, pp. 361-426.

[23]Dash, S.M., Weilerstein, G. and Vaglio-Laurin, R., "Compressibility Effects in Free Turbulent Shear Flows," Air Force Office of Scientific Research, TR-75-1436, August 1975.

[24]Birch, S.F. and Eggers, J.M., "A Critical Review of Experimental Data for Developed Free Turbulent Shear Layers," NASA SP-321, Vol. I, July 1972, pp. 11-40.

[25]Spalding, D.B., "Concentration Fluctuations in a Round Turbulent Free Jet," Chemical Engineering Science, Vol. 26, 1971, pp. 95-107.

[26]Jensen, D.E. and Wilson, A.S., "Prediction of Rocket Exhaust Flame Properties," Combustion and Flame, Vol. 25, 1975, pp. 43-55.

[27]Free Turbulent Shear Flows, NASA SP-321, Vols. I and II, July 1972.

[28]Nelius, M.A., Darlington, C.R. and Wasson, R.A., "Exhaust Plume Gas Dynamic and Radiation Measurements on a 500 lbf Thrust Liquid Rocket Engine at Simulated Flight Conditions," AEDC-TR-77-44, July 1977.

[29]Seiner, J.M. and Norum, T.B., "Aerodynamic Aspects of Shock Containing Jet Plumes," AIAA Paper 80-0965, 1980.

[30]Padova, C., Boyer, D.W. and Wurster, W.H., "Mach Number and Density Effects in the Mixing of Supersonics Jets," JANNAF 14th Plume Technology Meeting, CPIA Pub. 384, Vol. I, November 1983.

[31]Rhodes, R.P., "Analysis of Nonreactive Supersonic Turbulent Mixing Data," JANNAF 14th Plume Technology Meeting, CPIA Pub. 384, Vol. I, November 1983.

[32]Pope, S.B., "An Explanation of the Turbulent Round Jet/Plane Jet Anomaly," AIAA Journal, Vol. 16, 1978, pp. 279-281.

[33]Dash, S.M., "Observations on Practical Turbulence Modeling for High-Speed Jet/Plume Flowfields," AIAA 22nd Fluid and Plasmadynamics Conference, AIAA-91-1789, Honolulu, Hawaii, June 24-26, 1991.

[34]Eggers, J.M., "Velocity Profiles and Eddy Viscosity Distributions of a Mach 2.2 Nozzle Exhausting into Quiescent Air," NASA TN D-3601, 1966.

[35]Johannesen, N.H., "Further Results on the Mixing of Axially-Symmetrical Jets of Mach Number 1.4," Great Britain, Reports and Memoranda No. 3292, May 1959.

[36]Dash, S.M., Sinha, N., York, B.J. and Lee, R.A., "Progress in the Development of Advanced Computational Models for the Analysis of Generalized Supersonic Jet Flow-fields," AIAA 13th AeroAcoustics Conference, AIAA-90-3915, Tallahassee, FL, October 1990.

[37]Sarkar, S., "Applications of a Reynolds Stress Turbulence Model to the Compressible Shear Layer," AIAA Paper 90-1465, June 1990.

[38]Dash, S.M. and Kenzakowski, D.C., "A Compressible-Dissipation Extension to the $k\epsilon$ Turbulence Model and Building-Block Data for its Validation," AIAA-92-2766, 1992 AIAA SDIO Technology Conference, May 19-21, 1992.

[39]Dash, S.M., Sinha, N., and York, B.J., "The Critical Role of Turbulence Modeling in the Prediction of Supersonic Jet Shock Structure for Acoustic Applications," DGLR/AIAA 92-02-102, DGLR/AIAA 14th AeroAcoustic Conf., Aachen, Germany, May 11-14, 1992.

[40]Dash, S.M., Walker, B.J., and Seiner, J.M., "A Building-Block Approach for Turbulence Model Valida-tion/Upgrade Focussed on High-Speed Jet Flows," 19th JANNAF Propulsion Mtg., Feb. 24-27, 1992.

[41]Goebel, S. G. and Dutton, J.C., "Experimental Study of Compressible Turbulence Mixing Layers," AIAA Journal, Vol. 29, April 1991, pp. 538-546.

[42]Gruber, M.R. and Dutton, J.C., "Three-Dimensional Velocity Measurements in a Turbulent, Compressible Mixing Layer," UILU-ENG 92-4001, Univ. of Illinois, Urbana, January 1992.

[43]Seiner, J.M., Ponton, M.K., Jansen, B.J., and Lagen, N.T., "The Effects of Temperature on Supersonic Jet Noise Emission," DGLR/AIAA 14th Aeroacoustics Conf., Aachen, Germany, May 11-14, 1992.

[44]Melville, W.K. and Bray, K.N.C, "The Two-Phase Turbulent Jet," International Journal of Heat and Mass Transfer, Vol. 22, 1979, pp. 279-287.

[45]Melville, W. and Bray, K.N.C., "A Model of Two-Phase Turbulent Jet," International Journal of Heat and Mass Transfer, Vol. 22, 1979, pp. 647-655.

[46]Shuen, J.S., Solomon, A.S.P., Zhang, Q.F.,and Faeth, G.M., "The Structure of Particle-Laden Jets and Nonevapor-ating Sprays," NASA CR-168059, February 1983.

[47]Shuen, J.S., Solomon, A.S.P., Zhang, Q.F. and Faeth, G.M., "Structure of Particle-Laden Jets: Measurements and Predictions," AIAA Journal, Vol. 23, March 1984, pp. 396-404.

[48]Elghobashi, S.E. and Abou-Arab, T.W., "A Second-Order Turbulence Model for Two-Phase Flows," 7th Interna-tional Heat Transfer Conference, Munich, W. Germany, September 1982.

[49]Dash, S.M., "Gas-Particle Interactions in Rocket Exhaust Plumes," Multiphase Flows, Ed. D. Drew, Proceed-ings of Army Research Office International Workshop at BRL, Aberdeen, MD, February 1981, pp. 17-40.

[50]Beddini, R.A. and Dash, S.M., "Turbulent Mixing Analysis of Particle Laden Jets," JANNAF 13th Plume Technology Meeting, CPIA Pub. 357, Vol. II, April 1982, pp. 127-142.

[51]Beddini, R.A., Dash, S.M. and Pergament, H.S., "Numerical Investigation and Parametric Analysis of Gas/Particle Interaction in a High Speed Mixing Region," SAI/PR TM-16, Princeton, NJ, November 1983.

[52]Dash, S.M., Pergament, H.S. and Wolf, D.E., "Over-laid and Fully-Coupled Two-Phase Flow Versions of the JANNAF Standard Plume Flowfield Model (SPF/2 and SPF/3)," JANNAF 14th Plume Technology Meeting, CPIA Pub. 384, Vol. II, November 1983, pp. 169-225.

[53]Taylor, M.W., Sinha, N. and Dash, S.M., "Gas/Par-ticle Interactions in Turbulent Mixing Regions of Rocket Plumes with Applications to SPF/2 and SPF/3," JANNAF 16th Plume Technology Meeting, CPIA Pub. 451, Septem-ber 1986, pp. 25-48.

[54]Chein, R. and Chung, J.N., "Simulation of Particle Dispersion in a Two-Dimensional Mixing Layer," AIChE Journal, Vol. 36, No. 6., 1988, pp. 946-954.

[55]Chung, J.N. and Troutt, T.R., "Simulation of Particle Dispersion in an Axisymmetric Jet," J. of Fluid Mech., Vol. 186, 1988, pp. 199-222.

[56]Crowe, C.T., Chung, J.N., and Troutt, T.R., "Particle Mixing in Free Shear Flows," Progress in Energy and Combustion Science, Vol. 14, 1988, pp. 171-194.

[57]Crowe, C.T., Gore, R.A., and Troutt, T.R., "Particle Dispersion in Coherent Structures in Free Shear Flows," Particulate Science and Technology, Vol. 3, 1985, pp. 149-158.

[58]Samimy, M. and Lele, S.K., "Particle-Laden Com-pressible Free Shear Layers," AIAA/SAE/ASME/ASEE 26th Joint Propulsion Conf., AIAA-90-1077, Orlando, FL, July 1990.

[59]Samimy, M. and Lele, S.K., "Motion of Particles with Inertia in a Compressible Free Shear Layer," Physics of Fluids A, Vol. 3, No. 8, 1991, pp. 1915-1923.

[60]Uthuppan, J., Aggarwal, S.K., Grinstein, F.F., and Kailasnath, K., "Particle Dispersion in a Transitional Axisym-metric Jet: A Numerical Simulation," AIAA-93-0105, Reno, NV, January 1993.

[61]Kamalu, N., Wen, F., Troutt, T.R., Crowe, C.T., and Chung, J.N., "Particle Dispersion by Ordered Motion in Turbulent Mixing Layers," ASME Forum on Cavitation and Multiphase Flow, July 1988, pp. 150-154.

[62]Kamalu, N., Tang, L., Troutt, T.R., Chung, J.N., and Crowe, C.T., "Particle Dispersion in Developing Shear Layers," International Conf. on Mechanics of Two-Phase Flows, Taipei, Taiwan, June 1989, pp. 199-202.

[63]Lazaro, B.J. and Lasheras, J.C., "Particle Dispersion in a Turbulent, Plane, Free Shear Layer," Physics of Fluids A, Vol. 1, No. 6, 1989, pp. 1035-1044.

[64]Longmire, E.K., "Structure and Control of Particle-Laden Jet," Ph.D. Dissertation, Stanford Univ., Stanford, CA, 1990.

[65]Glawe, D.D. and Samimy, M., "Dispersion of Solid Particles in Compressible Mixing Layers," J. of Propulsion and Power, Vol. 9, Jan.-Feb. 1993, pp. 83-89.

4-28

[66]Dash, S.M., Boccio, J. and Weilerstein, G., "A Computational System for the Prediction of Low Altitude Rocket Plume Flowfields: Vol. I - Integrated Systems, Vol. II - Inviscid Flowfield Model (MAXIPLUM), Vol. III - Mixing/Afterburning Model (CHEMX), General Applied Sciences Labs., Inc., Westbury, NY, TR-239, December 1976.

[67]Dash, S.M., Pergament, H.S. and Thorpe, R.D. "The JANNAF Standard Plume Flowfield Model - Modular Approach and Preliminary Results," JANNAF 11th Plume Technology Meeting, CPIA Pub. 306, Vol. I, May 1979, pp. 345-442.

[68]Dash, S.M. and Pergament, H.S., "The JANNAF Standard Plume Flowfield Model: Operational Features and Preliminary Assessment," JANNAF 12th Plume Technology Meeting, CPIA Pub. 332, Vol. II, November 1980, pp. 225-288.

[69]Dash, S.M., Pergament, H.S. and Thorpe, R.D., "A Modular Approach for the Coupling of Viscous and Inviscid Processes in Rocket Exhaust Plumes," AIAA Paper 79-0150, January 1979.

[70]Dash, S.M. and Pergament, H.S., "A Computational System for the Analysis of Mixing/Chemical/Shock Processes in Supersonic Internal and Exhaust Plume Flowfields," AIAA Paper 80-1255, June-July 1980.

[71]Dash, S.M. and Pergament, H.S., "A Computational Model for the Prediction of Jet Entrainment in the Vicinity of Nozzle Boattails (The BOAT Code)," NASA CF 3075, December 1978.

[72]Dash, S.M., Wilmoth, R.G. and Pergament, H.S., "An Overlaid Viscous/Inviscid Model for the Prediction of Nearfield Jet Entrainment," AIAA Journal, Vol. 17, September 1979, pp. 950-958.

[73]Dash, S.M., "Computational Methodology for the Inclusion of Gas/Particle Nonequilibrium Effects in Exhaust Flowfields," JANNAF 12th Plume Technology Meeting, CPIA Pub. 332, Vol. II, November 1980, pp. 289-350.

[74]Dash, S.M. and Wolf, D.E., "Advances in Two-Phase Flow Modeling for the JANNAF Standard Plume Flowfield Model (SPF)," JANNAF 13th Plume Technology Meeting, CPIA Pub. 357, Vol. II, April 1982, pp. 41-72.

[75]Wolf, D.E., Dash, S.M., and Pergament, H.S., "A Shock-Capturing Model for Two-Phase Chemically Reacting Flow in Rocket Nozzles," AIAA Paper 85-0306, January 1985.

[76]Wolf, D.E., Dash, S.M. and Pergament, H.S., "Shock-Capturing Analysis of Multi-Phase Chemically Reacting Flow in Rocket/Scramjet Nozzles and Test Cell Diffusers," JANNAF 15th Plume Technology Meeting, CPIA Pub. 426, May 1985, pp. 197-232.

[77]Dash, S.M. and Sinha, N., "Noniterative Cross-Flow Integration for the Pressure-Split Analysis of Subsonic Mixing Layer Problems," AIAA Journal, Vol. 23, January, 1985, pp. 183-185.

[78]Dash, S.M., Sinha, N. and York, B.J., "Implicit/Explicit Analysis of Interactive Phenomena in Supersonic, Chemically Reacting, Mixing and Boundary Layer Problems," AIAA Paper 85-1717, July 1985.

[79]Dash, S.M., "Recent Developments in the Modeling of High Speed Jets, Plumes, and Wakes - Invited Survey Paper," AIAA Paper 85-1616, July 1985.

[80]Dash, S.M., Sinha, N., Wolf, D.E. and York, B.J., "Advances in Zonal PNS Modeling of Tactical Missile Plume/Afterbody Flowfields," JANNAF 15th Plume Technology Meeting, CPIA Pub. 426, May 1985, pp. 143-172.

[81]Dash, S.M., Taylor, M.W., Sinha, N., Wolf, D.E., Pergament, H.S., Coirier, W.J., Lee, S.H. and Lee, R.A., "Progress Towards the Development of the JANNAF SPF/3 Standardized Plume Model," JANNAF 16th Plume Technology Meeting, CPIA Pub. 451, September 1986, pp. 73-114.

[82]Dash, S.M., "Exhaust Plumes and Their Interaction With Missile Airframes," Tactical Missile Aerodynamics, Vol. 104, Progress in Aeronautics, ed. J.N. Nielson and M.J. Hemsch, AIAA, New York, 1986, Chapter XVII, pp 778-851.

[83]Anderson, D.A., Tannehill, J.C. and Pletcher, R.H., Computational Fluid Mechanics and Heat Transfer, Hemisphere Publishing Co., USA, 1984.

[84]Dash, S.M., Sinha, N. and York, B.J., "Computational Models with Advanced Thermochemistry for the Analysis of Missile/Plume Flowfield Interactions," AGARD Symposium on Missile Aerodynamics, Friedrichshafen, Germany, April 23-26, 1990.

[85]Pulliam, T.H. and Steger, J.L., "On Implicit Finite-Difference Simulations of Three-Dimensional Flow," AIAA Journal, February 1980, pp. 159-167.

[86]Pulliam, T.H., "Euler and Thin-Layer Navier-Stokes Codes: ARC2D, ARC3D," Notes for Computational Fluid Dynamics User's Workshop, The University of Tennessee Space Institute, Tullahoma, TN, UTSI Pub. E02-4005-023-84, March 1984, pp. 14.1 - 15.85.

[87]Beam, R. and Warming, R.F., "An Implicit Factored Scheme for the Compressible Navier-Stokes Equations," AIAA Journal, April 1978, pp. 393-401.

[88]MacCormack, R.W., "The Effect of Viscosity in Hypervelocity Impact Cratering," AIAA Paper 69-354, January 1969.

[89]Chaussee, D.S. and Pulliam, T.H., "Two-Dimensional Inlet Simulation Using a Diagonal Implicit Algorithm," AIAA Journal, February 1981, pp. 153-159.

[90]Jameson, A., Schmidt, W. and Turkel, E., "Numerical Solutions of Euler Equations by Finite-Volume Methods Using Runge-Kutta Time Stepping Schemes," AIAA Paper 81-1259, June 1981.

[91]Pulliam, T.H., "Artificial Dissipation Models for the Euler Equations," AIAA Paper 85-0438, January 1985.

[92]Pulliam, T.H., "Efficient Solution Methods for the Navier-Stokes Equations," Numerical Techniques for Viscous Flow Computations in Turbomachinery Bladings, Von Karman Institute Lecture Series, Brussels, Belgium, January 1986.

[93]Pulliam, T.H. and Steger, J.L., "Recent Improvements in Efficiency, Accuracy, and Convergence for Implicit, Approximate Factorization Algorithms," AIAA Paper 85-0360, January 1985.

[94]Neitubicz, C.J., Inger, G.R. and Danberg, J.E., "A Theoretical and Experimental Investigation of a Transonic Projectile Flowfield," AIAA Paper 82-0101, January 1982.

[95]Sahu, J. and Danberg, J.E., "Navier-Stokes Computations of Axisymmetric Transonic Flows with a Two-Equation Model of Turbulence," AIAA Paper 85-0373, January 1985.

[96]Weinacht, P. and Sturek, W.B., "Navier-Stokes Predictions of Static and Dynamic Aerodynamic Derivatives for High L/D Finned Projectile," AGARD Symposium on Missile Aerodynamics, Friedrichshafen, Germany, April 1990.

[97]Shian, N.H. and Hsu, C.C., "A Diagonalized TVD Scheme for Turbulent Transonic Projectile Aerodynamic Computation," AIAA Paper 88-0217, January 1988.

[98]Hsu, C.C., Shian, N.H. and Reed, C.W., "Numerical Simulation of Transonic Turbulent flow Past a Real Projectile," AIAA Paper 88-0128, January 1982.

[99]Cooper, G.K., "The PARC Code: Theory and Usage," AEDC-TR-87-24, October 1987.

[100]Cooper, G.K., Gerrard, G.D. and Phares. W.J., "PARC Code Validation for Propulsion Flows," AEDC TR-88-32, January 1989.

[101]Cooper, G.K., Jordan, J.L. and Phares, W.J., "Analysis Tools for Application to Ground Testing of Highly Underexpanded Nozzles," AIAA Paper 87-2015, June-July 1987

[102]Reddy, D.R. and Harloff, G.J., "Three-Dimensional Viscous Flow Computations of High Area Ratio Nozzles for Hypersonic Propulsion," AIAA Paper 88-0474, January 1988.

[103]Harloff, C.J., Lai, H.T. and Nelson, E.S., "2D Viscous Flow Computations of Hypersonic Scramjet Flowfields," NASP CR 1018, July 1988.

[104]Lai, H. and Nelson, E., "Comparison of 3D Computation and Experiment for Nonaxisymmetric Nozzles," NASP CR 1047, June 1989.

[105]Hsu, A.T., "Effect of Adaptive Grid on Hypersonic Nozzle Flow Calculation," NASP CP 1045, June 1989.

[106]Harloff, G.J. and Lytte, J.K., "Three-Dimensional Viscous Flow Computations of a Circular Jet in Subsonic and Supersonic Cross Flow," NASP CP 1021, August 1988.

[107]Dash, S.M., Sinha, N. and York, B.J., "Matrix-Split Approach for Inclusion of SPF Thermochemical Capabilities Into Beam-Warming Based PNS and NS Models," JANNAF 17th Plume Technology Meeting, CPIA Pub. 487, Vol. I, April 1988, pp. 91-110.

[108]York, B.J., Sinha, N. and Dash, S.M., "Computational Models for Chemically-Reacting Hypersonic Flows," AIAA Paper 88-0509, January 1988.

[109]Sinha, N., York, B.J. and Dash, S.M., "Applications of a Generalized Implicit Navier-Stokes Code, PARCH, to Supersonic and Hypersonic Propulsive Flowfields," AIAA Paper 88-3278, June 1989.

[110]York, B.J., Sinha, N., Ong, C.C. and Dash, S.M., "PARCH Navier-Stokes Reacting/Multi-Phase Analysis of Generalized Nozzle Flowfields," AIAA Paper 89-1765, June 1989.

[111]Sinha, N., York, B.J., Ong, C.C., Stowell, G.M. and Dash, S.M., "3D Navier-Stokes Analysis of High-Speed Propulsive Flowfields Using the PARCH Code," AIAA Paper 89-2796, July 1989.

[112]Dash, S.M., Sinha, N., York, B.J. and Ong, C.C., "3D Navier-Stokes Analysis of Tactical Missile External/Plume Interaction Flowfields," JANNAF 18th Plume Technology Meeting, Monterey, CA, November 1989.

[113]York, B.J., Sinha, N. and Dash, S.M., "PARCH Navier-Stokes Code Analysis of Rocket and Airbreathing Nozzle/Propulsive Flowfields," JANNAF 18th Plume Technology Meeting, Monterey, CA, November 19, 9.

[114]Liu, Y. and Vinokur, M., "Nonequilibrium Flow Computations: I - An Analysis of Numerical Formulations of Conservation Laws," NASA CR 177489, June 1988.

[115]Montagne, J.L., Yee, H.C. and Vinokur, M., "Comparative Study of High Resolution Shock Capturing Schemes for Real Gas," NASA TM 100004, 1987.

[116]Grossman, B., Cinnella, P. and Garrett, J., "A Survey of Upwind Methods for Flows with Equilibrium and Nonequilibrium Chemistry and Thermodynamics," AIAA Paper 89-1653, June 1989.

[117]Molvik, G.A. and Merkle, C.L., " A Set of Strongly Coupled Upwind Algorithms for Computing Flows in Chemical Nonequilibrium," AIAA Paper 89-0199, January 1989.

[118]Roe, P.L., "Approximate Reimann Solvers, Parameters, Vectors and Difference Schemes," J. Comp. Physics, Vol. 43, 1981, pp. 357-372.

[119]Chakravarthy, S. and Osher, S., "A New Class of High Accuracy TVD Schemes for Hyperbolic Conservation Laws," AIAA Paper 85-0363, January 1985.

[120]Hosangadi, A., Sinha, N., Dash, S.M., "Solution of Two-Phase Dilute Gas Particle Mixtures Using Upwind Finite-Volume Methodology," AIAA-92-0344, AIAA 30th Aerospace Sciences Meeting, Reno, NV, January 6-9, 1992.

[121]Hosangadi, A., Sinha, N., York, B.J., and Dash, S.M., "Progress Towards the Analysis of Transient Combusting, Multiphase Flows Using Upwind/Implicit Numerics," AIAA-93-0238, 31st AIAA Aerospace Sciences Meeting, January 11-14, 1993.

[122]Schiff, L.B. and Steger, J.L., "Numerical Simulation of Steady Supersonic Viscous Flow," AIAA Paper 79-0130, 1979.

[123]Kaul, U.K. and Chaussee, D.S., "AFWAL PNS Code: 1983 AFWAL/NASA Merged Baseline Version," AFWAL-TR-83-3118, May 1984.

[124]Lawrence, S.L., Tannehill, J.C. and Chaussee, D.S., "An Upwind Algorithm for the Parabolized Navier-Stokes Equations," AIAA Paper 86-1117, May 1986.

[125]Lawrence, S.L., Tannehill, J.C. and Chaussee, D.S., "Application of an Upwind Algorithm to the Three-Dimensional Parabolized Navier-Stokes Equations," AIAA Paper 87-1112, June 1987.

[126]Prabhu, D.K., Tannehill, J.C. and Marvin, J.G., "A New PNS Code for Chemical Nonequilibrium Flows," AIAA Journal, July 1988, pp. 808-815.

[127]Buelow, P., Tannehill, J.C., Levalt, J. and Lawrence, S.L., "A Three-Dimensional Upwind Parabolized Navier-Stokes Code for Chemically Reacting Flows," AIAA Paper 90-0394, January 1990.

[128]Krawczyk, W.J. and Harris, T.B., "Analysis of Aerospace Vehicle Scramjet Propulsive Flowfields: 2D Forebody/Inlet Code Development - Phase I," NASP CR 1003, August 1987.

[129]Krawczyk, W.J., Rajendran, N., Harris, T.B., York, B.J. and Dash, S.M., "Computational Models for the Analysis/Design of Hypersonic Scramjet Components, Part II: Inlet and Ramp/Forebody Models," AIAA Paper 86-1596, June 1986.

[130]Sinha, N., Krawczyk, W.J. and Dash, S.M., "Inclusion of Chemical Kinetics into Beam-Warming PNS Models for Hypersonic Propulsion Applications," AIAA Paper 87-1898, June-July 1987.

[131]Lee, R.A., Sinha, N. and Dash, S.M., "PNS Code Assessment Studies for Scramjet Combustor and Nozzle Flowfields," AIAA Paper 89-1827, June 1989.

[132]Dash, S.M., Sinha, N. and Lee, R.A., "Time-Iterative Upwind/Implicit 3D PNS Codes for the Analysis of Chemically-Reacting Plume/Propulsive Flowfields," JANNAF 18th Plume Technology Meeting, November 1989.

[133]Dash, S.M., Harris, T.B., Krawczyk, W.J., Rajendran, N., Sinha, N., York, B.J. and Carlson, D., "Three-Dimensional Upwind/Implicit PNS Computer Codes for Analysis of Scramjet Propulsive Flowfields," Sixth NASP Technology Symposium, NASP CP 6035, April 1989, pp. 129-172.

[134]Krawczyk, W.J., Harris, T.B., Rajendran, N. and Carlson, D., "Progress in the Development of Parabolized Navier-Stokes Methodology for External and Internal Supersonic Flows," AIAA Paper 89-1828, June 1989.

[135]Sinha, N. and Dash, S.M., "Implicit/Upwind 3D PNS Scramjet Propulsive Flowfield Code: SCHAFT3D," Seventh NASP Technology Symposium, NASP CP 7041, October 1989, pp. 151-180.

[136]Sinha, N., Dash, S.M. and Lee, R.A., "3D PNS Analysis of Scramjet Combustor/Nozzle and Exhaust Plume Flowfields," AIAA Paper 90-0094, January 1990.

[137]Dash, S.M., "Advanced Computational Models for Analyzing High Speed Propulsive Flowfields," 1990 JANNAF Propulsion Meeting, October 1990.

[138]Dash, S.M., York, B.J., and Kenzakowski, D.C., "Simulation of Complete Tactical Missile Nozzle/Plume/Hardbody Flowfields for Signature Predictions," 1st JANNAF SPIRITS Users Group Meeting, U.S. Army Missile Command, Huntsville, AL, 17-18 June, 1992.

[139]B.J. York, N. Sinha, S.M. Dash, A. Hosangadi, D.C. Kenzakowski, and R.A. Lee, "Complete Analysis of Steady and Transient Missile Aerodynamic/Propulsive/Plume Flowfield Interactions," AIAA-92-3603, AIAA/SAE/ASME/ASEE 28th Joint Propulsion Conf., July 6-8, 1992.

[140]Dash, S.M., Sinha, N., York, B.J., Lee, R.A., Hosangadi, A., and Kenzakowski, D.C., "Nozzle/Exhaust Plume Code Validation and Improvements in Numerics, Turbulence Modeling, and the Simulation of Nonequilibrium Processes," 19th JANNAF Exhaust Plume Technology Meeting, CPIA Pub. 568, May 1991, pp. 175-202.

[141]Cuffel, R.F., Back, L.H. and Massier, P.F., "Transonic Flowfield in a Supersonic Nozzle with a Small Throat Radius of Curvature," AIAA Journal, July 1969, pp. 1364-1366.

[142]Marcum, D.L. and Hoffman, J.D., "Calculation of Three-Dimensional Inviscid Flowfields in Propulsive Nozzles with Centerbodies," AIAA Paper 86-0449, January 1986.

MICROWAVE PROPERTIES
AND SYSTEMS OVERVIEW

by

Ronald Lawrence
DRA Office
c/o Royal Ordnance
Westcott
Aylesbury
Bucks, HP18 0NZ
United Kingdom

SUMMARY

Of particular significance to the operational success of a missile using microwave communications is the interference introduced by the rocket exhaust plume. As a hot and turbulent gas stream the exhaust has electrical properties that can seriously degrade guidance and tracking.

Also present is the potential for missile detection offered by energy scattered from microwave signals impinging upon the plume to present a radar cross section, and an exhaust signature from inherent emission sources within the plume.

This paper presented in AGARD Lecture Series 188, follows from AGARD Advisory Report 287 submitted by Propulsion and Energetics Panel Working Group 21 entitled "Terminology and Assessment Methods of Solid Propellant Rocket Exhaust Signatures". It provides a description of microwave propagation through a rocket exhaust, the cause of signal attenuation and the generation of phase and amplitude sideband noise. Consideration is given to the effects of missile flight velocity and altitude.

Diffraction and refraction processes are discussed, particularly in relation to plumes containing high density concentrations of free electrons. Radiation sources, mainly at millimetric wavelengths, are included together with signature implications.

The effects of exhaust interference with communications is examined from a system point of view and some methods of relief from this interference are considered.

1.0 INTRODUCTION

Microwave radar has long been an established means of missile location, tracking and guidance. It is capable of providing an all weather function in a variety of roles and for successful operation the guidance and tracking communication links must be free of serious interference.

In propulsion design for a missile it is important that the propulsion engineer is aware that guidance and tracking signals may pass through the exhaust plume. When these signals are conveyed by microwave carrier, attenuation and unwanted modulation of the carrier can occur because of interactions between the carrier wave and free electrons populating the hot, turbulent exhaust gases. This interference from the exhaust can seriously undermine communications with the missile and thereby reduce the overall operational efficiency of the system. Furthermore, scattering of energy from the incident wave and radiation from emission sources inherent in the plume may offer an adversary the opportunity to detect incoming missiles and take counter action.

The difficulties and expense of measuring exhaust properties for all missile configurations and operational conditions make reliable techniques for their prediction essential. Such prediction models can then be used to react quickly to demands for plume information, to identify interference problems in the very early stages of design, and to conduct research for the benifit of future systems.

Microwave" is a generic term used broadly to describe the centimetric range of wavelengths. Operating wavelengths used for tactical missile systems now include the millimetric range and frequencies fall typically between 3GHz and 120GHz. For the purpose of this report the term "microwave" will be extended to cover this range.

2.0 PLUME MICROWAVE PROPERTIES

2.1 Microwave Attenuation

Following normal combustion processes inside the rocket motor, fuel rich gases leave the nozzle to form a high velocity, turbulent gas stream which entrains oxygen from the surrounding atmosphere to promote conditions favouring the onset of further combustion in the exhaust. When this "secondary combustion" or "afterburning" as it is often called, occurs, the high temperatures attained permit ready ionisation

of metal impurities found as intrinsic impurities in the propellant. Sodium and potassium are common metal impurity species and, although present in small quantities (Say Na ≈ 100ppm and K ≈ 30ppm), the ionisation process populates the exhaust with a varying density distribution of free electrons.

The electric field of a wavefront incident on the exhaust from a distant transmitter accelerates the free electrons present and in so doing, extracts energy from the wave to be dissipated as heat in collisions with surrounding neutral molecules. This form of loss from the propagated wave integrated along its path to the on-board receiver is referred to as line-of-sight attenuation or absorption.[1]

Line-of-sight calculations [1,2] are based on computing the absorption of a single RF ray as it passes through the plume. Along the ray path, the plume is assumed to absorb as a series of homogeneous plasma volumes normal to the ray.

The attenuaticn α (or energy absorbed) per unit path length (dBm^{-1}) is given by :-

$$\alpha = 8.686 \left(\frac{\omega}{c}\right) \left[-\frac{(1-A)}{2} + \quad \cdots\cdots\cdots \right.$$

$$\left. \frac{1}{2} \left\{ (1-A)^2 + A^2 \left(\frac{v}{\omega}\right)^2 \right\}^{\frac{1}{2}} \right]^{\frac{1}{2}} \quad (1)$$

where $A = \omega_p^2 (v^2 + \omega^2)^{-1}$

The phase shift coefficient β is given by

$$\beta = \frac{1}{\sqrt{2}} \frac{\omega}{c} \left[(1-A) + \quad \cdots\cdots\cdots \right.$$

$$\left. \left\{ (1-A)^2 + A^2 \left(\frac{v}{\omega}\right)^2 \right\}^{\frac{1}{2}} \right]^{\frac{1}{2}} \quad (2)$$

Where ω is the angular frequency of the incident signal

v is the local electron-neutral body collision frequency

ω_p is the plasma frequency

The total phase shift θ through a length 'd' of homogeneous plasma is

$$\theta = (\beta - \beta_0)\,d$$

where $\beta_0 = \dfrac{\omega}{c}$ and

c = velocity of light in vacuo

The terms α and β are the real and imaginary parts respectively of the complex propagation constant γ which defines the electric field of the propagating ray :-

$$\overline{E} = \overline{E}_0\, e^{-\gamma x}\, e^{-i\omega t}$$

$$= \overline{E}_0\, e^{-x(\alpha + i\beta)}\, e^{-i\omega t}$$

where $\gamma = \alpha + i\beta$

Predictions of longitudinal (diagonal) attenuation using this line-of-sight method have shown reasonable agreement with measured attenuation from lightly ionised plumes, e.g. motors with composite propellants containing less than 5% aluminium and a predicted maximum electron density of less than 10^{16}m^{-3}.[2] Equally, focused-beam transverse attenuation predictions show similar agreement with measurements for conditions where, at the point of intersection between plume and beam axes, the half power radius of the beam does not exceed one fourth of the plume radius.

2.2 Forward Scatter (amplitude and phase modulation)

With the transmitter in the far field the incident plane wave illuminates the whole plume and energy additional to that from the line-of-sight path can reach the on-board receiver via a scattering mechanism. The geometry of the problem is illustrated in Figure 1a, which also defines some of the variables. Turbulence induced eddies of fluctuating electron density exist over large regions of the exhaust and become sources of incoherent scattering moving at local exhaust velocity. Each source volume (dV) contributes in some measure to the overall signal strength at the

receiver, but at a frequency removed from that of the incident wave by a "Doppler shift" imposed as a result of local eddy gas velocity with respect to the receiving and transmitting antenna.

Scattered energy produced in this manner is recorded as phase and amplitude sideband modulation spectra with a frequency range determined by incident wave frequency and local eddy velocities in the plume. It must be remembered that the propagated wave to the scattering source volume and from it to the receiver suffers attenuation in the way described in Section 2.1.

Calculations of forward scattering of microwave radiation by exhaust plumes have been performed since the mid 1960s. [3-6] Received scattered energy is related to the incident-received signal [3,7,8,9] by the equation :-

$$\frac{P_s}{P_i} = \frac{1}{4\pi G_{\beta_1}} \int_{Vol} \frac{G_{\beta_2} C_a}{r^2}\, \sigma\, dv \quad (3)$$

where P_s/P_i is the ratio of the noise power to the signal power, G_{β_1} the receiving antenna gain in the direction of the transmitter and G_{β_2} that in the direction of the element dv. The distance between the receiver and the scattering element is denoted by r and σ is the volume scattering cross-section. The volume of integration includes the whole plume. C_a is the attenuation loss factor along the path through the plume to and from the element dv.

The volume scattering cross-section (σ) is a local property of the exhaust plume and may be shown to be :-

$$\sigma = \frac{0.63 \times 32\pi^4 r_e^2}{(1 + v^2/\omega^2)^2} \cdot \frac{n'\, \sin^2 \psi\, a^3}{B} \quad (4)$$

where $n' = [n_e]^2 l^2$ the turbulent fluctuation of electron density [e'] and

$$B = (1 + 4a^2 k^2\, \mathrm{Sin}^2 \alpha/2)^{11/6}$$

the Kolmogorov turbulence function.

In this equation r_e is the classical electron radius, ψ the angle between the direction of scattering and the incident electric vector and α the scattering angle. I is the local intensity of electron concentration fluctuations, n_e is the local mean electron density and 'a' the turbulent length scale. ν is the local electron-neutral body collision frequency, ω the angular frequency of the incident signal and k the wave number ($k = 2\pi/\lambda$).

In Equations 3 and 4 the angles ψ and α and the distance r may be determined geometrically; ω, k and the receiving antenna gain function are known characteristics of the microwave system. If n_e, ω, I and a are defined throughout the plume flowfield the scattered power may be calculated.

Flowfield calculations can provide local gas velocity, mean electron density and electron-neutral body collision frequency but considerable uncertainty surrounds the turbulence characteristics. The turbulent length scale (a) is commonly taken to be the correlation length for turbulent velocity fluctuations which may differ from the required length scale for fluctuations in electron concentration. It can be calculated using a two-equation turbulence model in the plume structure program. The turbulent intensity (I) is often set to unity but can also be seen as a function of axial distance downstream of the nozzle exit and a corresponding radial distance. Both parameters are discussed in greater detail in Reference 10.

The "Doppler" frequency shift of the power entering the receiver from scattering elements dV is written :-

$$f_D = \frac{u}{\lambda}(\cos\beta_1 - \cos\beta_2) \qquad (5)$$

For a given element (dv), if the wavelength (λ) of the incident wave and the local gas velocity (u) are known the frequency of the scattered power for angles β_1 and β_2 of Figure 1 can be obtained from this equation. Summation of scattered energy from all parts of the plume generates the characteristic sideband noise associated with rocket exhaust interference. Plume properties, which will change with altitude and forward velocity, govern the total received power. Comparisons between prediction and experiment are shown in Figure 2.

2.3 Prediction Technique

Fundemental to the understanding of microwave propagation in rocket exhausts is a description of the plume structure. It is impracticable to measure all the parameters required and theoretical flowfield models have been developed to assist the understanding and to generate the required theoretical data for a range of applications. Microwave predictions are one such application and rely upon the construction of models in which the time averaged properties of combustion and flow are quantified.[2,11-15]. They are essentially the same as those for all other plume predictions but have additional properties particular to microwave interactions. These are :-

(i)   All ionisation chemistry, especially that for alkali metal impurities. Other minor species that may interact with and affect the ionisation processes.

(ii) Parameters that define the plume turbulent structure which, as a minimum, include turbulent intensity related to electron density fluctuations and turbulent length scale.

(iii) The electron collision frequency.

(iv) Free electron concentrations given by ionisation processes.[10]

Calculations start at the combustion chamber. From the propellant composition and enthalpy, steady-state temperature and combustion products are computed. This is followed by a calculation to determine conditions at the throat and the expansion of gases to the nozzle exit. The final stage, where high velocity gases leave the nozzle and react with the surrounding atmosphere, is a model to give the plume flowfield. This quantifies time averaged properties of the exhaust in an axisymmetric array, spatially identified by axial and radial point references with the origin on axis at the nozzle exit.

Parameters will have values determined by their spatial distribution throughout the plume as indicated by the contours of Figure 3. Turbulence quantities must be appended to the values shown in Figure 3, these can be derived from turbulence kinetic energy values used to determine the shear layer mixing for the time-averaged flow.

Missile flight must recognise altitude and forward velocity, both affect the plume shape. The

former because an increase in altitude means a decrease in ambient pressure and alteration in plume expansion, the latter because of free stream flow over the missile surfaces into the plume region.

It is important [2,16] to consider the recirculation region established at the base of the missile in flight when the base diameter substantially exceeds the nozzle exit diameter. Recirculation affects the development of the downstream plume and may be critical to the onset of afterburning. Calculations [17,18] of this region are commonly based on iterative solutions over a fixed grid domain and normally confined to structural information close to the nozzle exit where recirculation is significant.

2.4 Measurement Techniques

The greater number of plume measurements have been made under static, sea-level conditions with transverse and longitudinal propagation paths. To a lesser extent wind tunnels and altitude chambers have provided information mainly with transverse, focused beam studies. Dedicated flight trials have been rare and propagation data obtained is difficult to accurately match with missile flight attitudes.

2.4.1 Static, Sea-level

Of facilities, the most versatile is the open range, static firing site where short and long range microwave measurements can be conducted and where exhaust smoke and emissions can be examined.

2.4.1.1 Transverse measurements [19,20,21] of attenuation made with focused microwave beams over very short propagation paths through rocket exhausts offer the opportunity to spatially map the extent of the electrical plume by studying local properties at selected stations. Information gained in this way is especially valuable for the validation of theoretical models.

A system occasionally used in the UK operated with dual frequency channels, 14.5GHz and 35GHz. Separation between each transmitter and its receiver was 1.22m and matched conical horns with dielectric bi-convex lens formed the focused beams. The spatial resolution in the vicinity of the focus, midway between the horns, presented an Airy disc radius of 0.057m for 14.5GHz and 0.023m for 35GHz. Each microwave assembly was housed in a metal acoustic cabinet on anti-vibration mounts to minimise airborne and groundborne vibrations. These were then mounted on a frame which was raised and lowered by electrically driven jacks. System simplicity reduced the risk of false measurements, each transmitter consisted of a microwave generator, an isolator and a microwave feed to a lens corrected horn via calibration attenuators. Similarly, the receivers had lens corrected horns terminated by a crystal detector. Much the same equipment was used in the US through the early 1970s when measurements of this type were last made. A typical experimental facility is shown in Figure 4a with results from attenuation measurements using such a system compared with prediction in Figure 4b.

2.4.1.2 The concept of longitudinal measurements is one where propagation path geometries more nearly resemble those of a missile system. The receiving antenna is mounted on or near to the test motor, commonly in the nozzle exit plane, and the propagation path is to a transmitter in the far field at sufficient distance to allow illumination of the whole plume by a plane wave. The line of sight between the two antennae intercepts the plume axis at selected narrow aspect angles. Multipath interference by reflections from intruding objects in the propagation field should be avoided. A general geometry is shown in Figure 1. Rotation of a turntable mounted rocket during firing permits attenuation to be measured as a function of plume aspect (viewing) angle. Plume insertion loss and amplitude modulation have been measured for liquid and solid rocket motors at a variety of plume axis/wavefront interception angles in the frequency range 1.0GHz to 140GHz.

A measuring system [22] typical in plume studies consists of a microwave bridge in which one arm is an air path subjected to interference by the rocket exhaust and the second arm is a coaxial link providing an unmodulated reference (Fig 5). Propagation lies between two towers 31m apart and 9m high. A 1.4w, 9.5GHz source supplies power to an antenna on the transmitting tower and a lower power to the reference link between the towers. The receiving tower houses the rocket motor mounted on a rotating thrust stand with the receiving antenna attached to it adjacent to the nozzle. Both antennae are co-planar in the horizontal plane. Antenna polar patterns are shown in Figures 6 and 7 with the transmitter pattern, broad in the horizontal plane to illuminate the whole plume at any aspect angle and narrow in the vertical plane to prevent spurious ground reflections. Received and reference signals are mixed with those from a

local oscillator and the resulting intermediate frequencies (IF) are passed to the main processor housed in a control room 90m from the towers.

Attenuation is measured by mixing part of the received IF signal with that from a crystal controlled oscillator to provide a low frequency output for direct recording. It is seen as a signal loss over a linear dynamic range of 40dB. Diode detection is used to extract amplitude modulation, while received and reference IF signals are compared in a phase sensitive detector to obtain phase modulation.

Fourier analysis completes the process to obtain the frequency components of a spectral curve like those shown in Figure 8. Component signal magnitude is referred to the received carrier signal level (i.e. after attenuation) and quoted in a 1.0Hz bandwidth. The curves show amplitude and phase modulation spectra and are compared with the amplitude modulation spectrum (RPE) of an independent, similar equipment operating simultaneously at the same aspect angle. Phase modulation of a 9.5GHz incident wave has been recorded over a range of rocket motors and, for small amplitude modulation signals such as those generated in the plume, has yielded phase spectra that are in agreement with simultaneously recorded amplitude spectra.

Typical Performance

Attenuation

Dynamic range   -40 dB

System resolution (amplitude and phase modulation)

At 0 dB attenuation -100 dB to -120dB
At 30 dB attenuation - 99 dB to -103 dB

Cross talk

Signal AM to PM   -27 dB
PM to Signal AM   -30 dB
Ref AM to PM   -10 dB

Polarisation

Can be vertical or horizontal.
Occasional use of circular polarisation.

2.4.2 Flight Simulation

The exhaust structure of a missile in flight will vary under the effects of changes in altitude and forward velocity (say: sea-level - 30km, subsonic - Mach4). To simulate the range of conditions at ground level requires the construction of expensive facilities.

Wind tunnel dynamic plume tests, with a co-flowing free stream at altitude, provide the closest simulation of an in-flight missile, although there are often restrictions on antennae placement and undesirable shock reflection and wall effects to be avoided. Transverse attenuation measurements are best suited to these facilities and have been useful for analysing plume phenomena observed in flight.

It can be argued that because of the control available, the amount of information gained is more useful and cost effective than that of flight trials where interpretation is difficult. Such facilities have good value in research and prediction validation when studying plume expansion with altitude, nozzles, base flow effects, propellants and additives.

Similar remarks can be made about wind tunnel propagation measurements with velocity simulation only. However, wind tunnel exits can be fabricated to produce airflow over the missile body which, in some measure, simulates flight velocity. Given that the chamber exits to an open site area, a range of microwave measurements can be undertaken both transverse and longitudinal. It must be emphasised that for the latter case, spurious microwave reflections entering the receivers from any nearby objects or the ground must be made negligible, also any airflow interaction with the ground downstream of the tunnel exit may make conditions for longitudinal measurements unacceptable.

Sleds propelled by the rocket along high velocity tracks can simulate flight conditions but their use for longitudinal microwave measurements leave doubt about the results obtained. It must be kept in mind that although prefiring multipath reflections can be reduced, the dynamic case raises the possibility of plume refraction, diffraction or scattering causing unwanted returns from the track and nearby objects. This method of measurement should be approached with caution.

Altitude simulation without the dynamic aspects of flight are of limited use but have considerable research value where on small scale rocket firings, microwave probes can observe the effect of reduced ambient pressures on certain

chemical reactions, on the properties of additives, or other fundemental plume aspects.

2.5 Refraction

Variations of refractive index across the propagation path of a microwave beam will cause distortion of its wavefront and deviated rays can promote multipath effects in the farfield.

In a rocket exhaust plume two factors dominate in determining the spatial variation of local time averaged refractive index. One is the thermal inhomogeneity due to gradients of local plume static temperature, the other is the partially ionised nature of the plume gases caused by readily ionisable impurities in the propellant (e.g. sodium, potassium and calcium compounds). Local values of temperature, pressure and chemical composition, including concentrations of charged species (particularly free electrons) determine the plume refractive index field.

Calculations have estimated that for any given point in a plume, changes in refractivity due to ionisation are at least an order of magnitude greater than those due to temperature gradients.

The refractive index of a medium is given by $n = c/v$, where v is the velocity of electromagnetic radiation in the medium and c is its velocity in a vacuum. In an absorbing medium the index of refraction is complex: $\underline{n} = n(1 + ik)$. Solutions to Maxwell's equations for a monochromatic plane wave in free space provide the propagation constant $\gamma = \alpha + i\beta$ which can be related to the complex refractive index ($\underline{n}$) since $\alpha = \omega nk/c$ and $\beta = \omega n/c$ where ω is the angular velocity of the wave.

$$\therefore \underline{n} = \frac{\beta c}{\omega} + \frac{i\alpha c}{\omega}$$

The complex nature of the refractive index affects the path of the ray through an absorbing medium. Poynting's vector oscillates in such a medium, consequently the energy path cannot be obtained from this vector which leads to computations of considerable complexity. If absorption over one wavelength is not appreciable, then the complex law of diffraction deviates negligibly from Snell's law for absorbing media.

$$n_1 \sin \theta_1 = n_2 \sin \theta_2$$

where the subscripts refer to the media on either side of a boundary crossed by the radiation.

It is in the outer regions of the plume where refraction can occur with little attenuation of the propagated wave. This leads to refracted rays leaving the exhaust with considerable energy.

Calculation of refraction in these regions of low refractive index gradients can be achieved by the use of contours of constant refractive index. While recognising that the mean refractive index will gradually change through the outer plume, as an approximation the path of a ray can be stepped through small volumes of constant refractive index, changing direction at each interface. The step length can vary according to the local refractive index gradient and Snell's law can apply.

The fact that these rays emerge with little attenuation can result in multi-path effects in the field beyond the missile which may interfere with target tracking or with other missiles in salvo operation.

Multiple ray tracing as performed in References 23-26 will provide a more rigorous method of calculating refractive effects over a range of rocket exhausts.

2.6 Diffraction

Measured values of plume-microwave interference for highly-ionised plumes in longitudinal geometries show many of the characteristics of electromagnetic wave diffraction by solid objects. Simple diffraction models [2] have been used to good effect in describing signal behaviour. In more sophisticated models recently developed the diffraction evolves from the mathematical solution of the propagation equations and demonstrates that the effect is real. Current model development in this area incorporates the combined effects of refraction, absorption, scattering, and diffraction.

That diffraction may play a part in microwave propagation through highly ionised exhausts is indicated by Figure 9. It compares longitudinal attenuation measurements for a given double base motor with predictions from the line-of-sight code. At small plume interception angles from the axis, attenuations of 100dB or more are predicted. This is in marked contrast to the observed insertion loss which varies between -10dB and -30dB depending upon the location of the receiving antenna. Moreover, at these small angles, the variation of measured insertion loss

with frequency is not that to be expected should absorption be the dominant loss mechanism. Only at larger interception angles, where comparatively short path lengths close to the nozzle exist, is there reasonable agreement between prediction and measurement. This is further confirmed by Figure 4b, where transverse measurements at 35GHz, using a focused beam system, agree well with calculated values of attenuation for the same motor. It is clear however, that should attenuation measured over the relatively short diametric path at 3m be present over long paths through the length of the plume then attenuation in excess of 100dB would be expected.

More evidence of another propagation mechanism in operation is given by Figure 10a and b which presents plume attenuation at two wavelengths for a highly ionised exhaust plume. The measurements are compared with prediction at zero aspect angle and two plume axis intersecting aspect angles. The antenna displacement from the motor axis was changed for each firing.

Measured attenuation at 35GHz shows good agreement with predictions at zero aspect angle suggesting conformity with the line-of-sight theory of Equation 1 in Section 2.1 which was used for the calculation. However as the increase in aspect angle directed the propagation path into regions of higher electron density so that conformity lessened. Even at zero aspect angle it is the steepness of the curve at 15dB which gives the appearance of agreement. The bracketed point pair shows the difference in attenuation for the same displacement. Accepting uncertainties associated with predictions, experiment and theory are not in great disarray, particularly below the 10dB attenuation level.

Attenuation at 10GHz does not show the same degree of agreement and with the reduced slope of the experimental curves it is evident that they will cross those for 35GHz. Beyond the intersection, in increasing attenuation, there will be a reversal of exhaust penetrative powers between 35GHz and 10GHz, which is contrary to Equation 1. Slight differences in aspect angle do not invalidate these observations since the family of curves allows reasonable interpolation.

Clearly, for exhausts where high electron densities exist, the microwave propagation mechanism is not governed solely by absorption and other mechanisms such as diffraction should be sought.

A good theoretical description of plume diffraction has yet to evolve, it is a complex subject. [2,23,24] Recent investigations [25] have employed ray-tracing studies to estimate the temporal development of wavefront distortion and have indicated the existence of diffraction. From plume flowfield data of electron density contours, a three dimensional model of the spatial variation and gradients of the complex refractive index has been developed. It was based on the discovery that the contours of equal electron density, given by the theoretical plume flowfield, could quite accurately be approximated by finding a solution to the equation of intersection between a three dimensional "tear drop" function and an angled plane. Figure 11 shows the comparison between the axial variation of plume electron density (N_e) for a given plume as computed by (i) the plume flowfield model, (ii) a representation of the axial variation of N_e given by a simple exponential function and (iii) a 21st order least squares polynomial curve fit. The polynomial approximation is good, the complex stucture in the region close to the nozzle has been smoothed to minimise the order of polynomial. Ray tracing led to an investigation of the progressive wavefront distortion experienced by a plane wave propagated through the plume. The refracted wave front became compressed in a pronounced focal region shown in Figures 12 and 13 and crossed over itself prior to expansion and interaction with the undisturbed wave. A physical optics model confirmed that the diffraction was dominated by a highly localised, diffractive "stationary-phase" effect located in the region of maximum overall ray compression. An equivalent diffractor was established, having the form of an ideal absorbing disc, combining the diffracted field with the field from a direct ray. The equivalent diffractor was replaced by an effective diffracting surface, positioned in the same way. Three dimensional ray-tracing of a large number of rays and their truncation at a phase-time defined by the assumed location of this surface, was used to define secondary sources and represent the stationary phase region in a more natural way. The very high lateral spatial refractive index gradients in the region between the effective diffracting surface and the plane of the receiver were recognised by incorporating geometrical masking into the diffraction calculation. For small angles with respect to the plume axis, the effective diffractor approach was justified because the loss mechanism was dominated by the behaviour of the wavefront in a highly localised region. It was also strongly influenced by the masking effect of the intervening dense plasma and a non-abrupt

interaction of the direct ray between transmitter and receiver.

Ray tracing is illustrated in Figure 14 where the wave-front is seen to move through the plume. The contour shown is that of minimum electron density, given as $10^{10}m^{-3}$, and defines the theoretical plume boundary. Three microwave propagation frequencies are considered, 9.5GHz, 35GHz and 90GHz. The angle of incidence is 2° and the distance between rays set in this case to be 0.2m. The flowfield model was that of a double base propellant motor of 30kN thrust, where electron densities reached $10^{18}m^{-3}$. Figure 15 shows a sample comparison between calculated diffracted signal and measured attenuation for the same motor. The solid points are those of individual firings, the full line is that of the diffracted signal where E_0/E_i is the attenuation level in decibels. Work is still proceeding to evaluate this method for a range of rocket motors.

3.0 OPERATIONAL IMPLICATIONS

3.1 Guidance and Tracking [27]

From foregoing sections of the report it is clear that guidance and tracking difficulties may arise if the microwave link passes through, or close to, the missile exhaust. This is particularly so if the rocket motor is required to burn unabated to maintain closing velocity in the terminal stage of an engagement and approaching maximum range. Attenuation by the plume must be seen as an insertion loss within the microwave communication link. Furthermore, the sideband noise resulting from the scattering process can be at frequencies that may interfere with semi-active homing systems.

3.1.1 Beam Rider

Beam riding missile systems can suffer from plume effects because the missile lies in the target tracking beam. For a successful interception the centre of the tracking beam must be maintained on the target and this requires very precise angular measurement by the tracking radar. Beam attenuation or distortion due to the rocket exhaust could degrade the target definition that is so crucial in the closing moments before impact. Guidance signals to the rear aerial of the missile can pass through highly attenuating regions of the plume.

3.1.2 Radar Command to Line-of-Sight

The beam riding missile requires only a simple guidance receiver which minimises the cost, weight and complexity of the guidance payload. This advantage is carried into the Radar Command to Line-of-Sight (RCLOS) guidance system where the tracker locks on to the target and, when the missile is airborne, continuously measures the angle between the missile and the target. It is a technique that allows a relaxation of beam centre to target accuracy, seen as a problem in the beam rider, but to some extent this accuracy is now transferred to the measurement of the missile to target angle. A separate command link, usually operating at a wavelength different from that of the tracker, guides the missile to reduce the angle to zero thereby maintaining a line-of-sight interception course. Rocket exhaust interference problems associated with the beam rider system apply equally to the "RCLOS" system. Refraction of the outgoing target tracking signal in the outer regions of an exhaust plume can introduce multipath effects at the target which cause returns at the tracker receiver to produce false positional information. This results in erratic manoeuvres by the missile as guidance commands respond to this false information.

3.1.3 Semi-Active Homing

The principle of semi-active homing systems is one where the target is illuminated and tracked by radar and the missile is launched on an interception course ahead of the target, anticipating its future position. A target seeker in the nose of the missile receives reflections from the target and determines its direction in space. Reference signals from a direct link between missile and tracker combine with the seeker output to establish target range and speed (Doppler) providing continuous guidance update until impact. The integrity of the system is again threatened by rocket exhaust interference in the form of attenuation of the rear reference and corruption of its information by sideband noise or as "spillover" noise into the missile forward receiver or as a contribution to "clutter", a commonly used term to describe unwanted echo signals from objects other than the target such as ground, sea, counter radar chaff and precipitation. To counter the effect of "clutter", natural or intended, tracking and seeker radars often employ "rangegates" and "speedgates". They are similar in concept. The "rangegate" discriminates against radar returns other than those within a prescribed distance frame from the transmitter while the "speedgate" acts similarly in discriminating against those radar returns that fall outside a prescribed "Doppler" frequency band which can be related to

the velocity of the target. The signal to clutter ratio is significantly improved by their use.

In the context of semi-active homing, incoherent pulse radar systems, giving range information, would be sensitive to the amplitude of spurious signals that may appear as "clutter" in the rangegate. Continuous Wave Doppler and Coherent Pulse Doppler systems would be sensitive to signals having sideband frequencies that may affect the operation of the "speedgate" filter.

An indication of the "Doppler" frequencies encountered may be found in the simple relationship $f_D = 2V_t/\lambda$ where f_D is the "Doppler" frequency shift for a given radial target velocity (V_t) and stationary radar of wavelength "λ".

3.1.4 Active Radar Homing

In a semi-active homing missile the seeker is a tracking radar without the transmitter for target illumination. The active homing missile has the transmitter included making the missile fully autonomous when locked on to the target. The principle is that for semi-active homing but signal processing and computed course correction are done on board the missile. Only if the target falls outside the range of the illuminating radar is there a need for a remote signal link, this link gives mid-course guidance to the missile to maintain it on course and bring it into radar contact with the target. During the autonomous stage of flight the rocket plume is unlikely to cause problems, in mid-course guidance the rear facing link could suffer plume attenuation and sideband noise interference.

3.2 Salvo Operation

Where two or possibly more missiles are fired in a salvo the exhaust of one may seriously interfere with target tracking or with the guidance of another. This can be complicated still further when the salvo is intended to engage multiple targets. The problems recounted in Sections 3.1.2 and 3.1.3 are valid for salvo operations but with the addition of inter-link interference.

3.3 Discussion

In trying to outline the problems associated with exhaust/microwave system interference no attempt has been made to offer solutions. Those available to the engineer depend on the operational role, but few overcome exhaust interference without recourse to expediency and

some penalty.

Some solutions might be :-

(i) Flight path offset at critical periods of flight to avoid excessive signal losses.
Penalty : Loss of optimum path.

(ii) Provide electronic discrimination against interference.
Penalty: Increased electronic complexity, and cost.

(iii) Use of multiple antennae or reflectors attached to wing surfaces to remove propagation paths from highly attenuating regions of the plume.
Penalty: Lowered aerodynamic efficiency.

(iv) Boost-Coast propulsion such that the exhaust is absent in terminal stage of useful flight.
Penalty: Restricted terminal velocity (not always of importance).

(v) The reduction of free electron concentrations in the plume by chemical modification of propellant.
Penalty: None; costs are in original propellant formulations. However, should it be a remedial change of propellant from the original then costs could be extremely high.

(vi) The use of an Active Homing System without mid-course guidance.
Penalty: High cost, electronic complexity and weight.

While the broad principles of microwave homing, guidance, and tracking remain, sub-system technology has advanced to a remarkable degree. Reference 27 details some of these advances. Where past missile-borne systems have required large and heavy microwave and signal processing units, new generations of microwave equipment have become much smaller due to modern circuit design and fabrication. Signal processing, with the advent of monolithic integrated circuit technology, has led to miniaturization which has been carried into microwave technology with stripline techniques and microwave integrated circuits.

Millimetric waves offer the advantage of small, lightweight systems having very narrow beamwidths with good spatial resolution, essential

qualities for high accuracy and precise target definition. The physical size of microwave circuits are proportional to the inverse of the operating frequency and it is very noticeable in antenna design. Whereas at a frequency of 10GHz the antenna may have a diameter of 1.0m for a given beam width, at 95GHz, for the same beamwidth, the antenna diameter will be 0.1m.

This miniaturization process now makes it possible to have a complex homing system, such as that of active homing, within a missile of some 120mm diameter. One outcome of this reduction in size and payload is the opportunity to reduce the size and thrust required of a rocket motor for a given performance such that motors having combustion suppressed exhausts become the preferred option. This report will show that avoiding secondary combustion (afterburning) in the exhaust will prevent exhaust temperatures rising to cause ionisation and, without a large free electron population, exhaust emission will be dramatically reduced while attenuation and the generation of sideband noise will no longer be a problem.

4.0 BACK SCATTER
(Radar Cross Section)

Forward scattering from the source volume described in Section 2.2 has its counterpart in energy scattered rearwards, back along the path travelled by the incident wavefront. Again, a frequency spectrum from all contributions is created and such energy is referred to as back scatter and forms the plume radar cross section (RCS). Its echo potential is usually several orders of magnitude below that of the missile body but increasing use of radar absorbing materials in stealth body design is reducing the gap between body and plume radar return.

Back scatter of microwave radiation by a plume is calculated using the same scattering equations (3, 4 and 5) used for forward scatter. Some differences occur in the use of the equations for the two situations; for back-scatter the angle, α, is fixed at 180 degrees and the absorption function, C_a, is made of two parts that are generally the same on incidence and departure from a scattering element, dv. This contrasts with forward scattering where α assumes all values and C_a differs in value between that of incidence and departure.

To measure backscatter from the plume the transmitter and receiver are usually in the same location (mono-static radar). The scattered returns into the receiver can be expressed as an effective area compared with a known standard reflector and represent energy in the area under the spectral curve.

An important flight trial[28] was made in the U.S. dedicated to the measurement of backscatter. The results were compared with calculations. In general, Doppler frequency shift relates to plume flowfield velocity components along the radar line-of-sight through the plume and can be associated with specific regions of a flowfield prediction that calculates the spatial distribution of velocity. In the backscatter prediction code, specific RCS returns were associated with specific regions of the plume and hence, with specific velocities. These were then joined together to form the total theoretical radar cross section of the rocket plume. Figure 16a shows the total RCS Doppler spectrum measured in flight and was obtained by summing the Doppler spectra from nine individually resolved range "bins" in the RCS flight data. Doppler shift data from each of the range "bins" can also be plotted, each range "bin" corresponding to a 20.2m length of plume. This technique provided, in effect, a "diagnostic probe" with which to interpret data from the flight plume for comparison with spatially resolved plume calculations. Values from each of the nine "bins" are compared, calculation with experiment, in Figure 16b.

5.0 EXHAUST EMISSION

Microwave radiation from the exhausts of tactical missiles can be a means of detection. Interest centres largely on the millimetric region of the spectrum where propagation windows exist in the earth's atmosphere that allow the passage of millimetric waves over relatively short distances. Figure 17 shows the atmospheric spectral transmission range with windows at frequencies of approximately 35GHz, 94GHz and 140GHz.

The physical processes governing thermal emission from rocket exhaust plumes at millimetric wavelengths have been examined by Sume.[29] The mechanisms considered were free-free electron emission (bremsstrahlung), molecular band emission, free-bound electron emission, and the emission from aluminium oxide particles in the exhaust. The dominant mechanism was found to be the free-free continuum emission from electrons, and is the only mechanism considered in this treatment.

Losses during free electron-neutral body collisions occurring naturally in the ionised exhaust form the free-free emission, which is a continuum radiation. It is governed by the ionisation processes supported by high exhaust temperatures and alkali metal impurities in the propellant.

Electron concentrations of 10^{15}m^{-3} to 10^{18}m^{-3} and collision frequency of 10^{11}S^{-1} are typical at sea level.

5.1 Emission Theory

The monochromatic emission intensity along a line of sight path of length L through a non-isotropic, non-isothermal medium is given by :-

$$I(\lambda) = \int_0^L \exp\left[-\int_0^\ell K(\ell')\,d\ell'\right] K(\ell) I_B(\ell, \lambda)\, d\ell$$

(6)

where I_B (ℓ, λ) is the local black body emission and $K(\ell)$ is the absorption coefficient at wavelength λ. The absorption coefficient, at angular frequency $(\omega = 2\pi c/\lambda)$, of a plasma with no magnetic field present is given by Sume.

$$K = 2\omega\, n_2/c$$

where c is the velocity of light and n_2 is the imaginary part of the complex refractive index (n).

Following Sume

$$n^2 = (n_1 - i\, n_2)^2$$

$$= 1 - x(1 - i\,z)^{-1}$$

Assigning

$$x = \omega_p^2\, \omega^{-2} \quad \text{and} \quad z = \nu\omega^{-1}$$

with ν as the electron-neutral molecule collision frequency and ω_p as the plasma frequency given by

$$\omega_p^2 = N_e\, e^2/\epsilon_0 m$$

where N_e is the electron density, e and m are the electronic charge and mass respectively and ϵ_0 is the permittivity of free space, one now obtains :-

$$n_2 = \left[\frac{1}{2}\left\{-\left(1 - \frac{x}{1+z^2}\right) + \cdots\cdots\cdots\right.\right.$$

$$\left.\left.\sqrt{\left(1 - \frac{x}{1+z^2}\right)^2 + \left(\frac{xz}{1+z^2}\right)^2}\right\}\right]^{-\frac{1}{2}}$$

or if

$$\omega_p^2 \ll \nu^2 + \omega^2 \text{ and } \nu^2 \ll \omega^2, \text{ or if } \nu^2 \gg \omega^2$$

$$n_2 \cong \frac{x\,z}{2(1+z^2)}$$

Hence, if temperature, electron concentration and electron-neutral molecule collision frequency are known along the line of sight, the emission can be calculated. The quantities can all be predicted using standard rocket exhaust flow field calculations.

The black body emission is given by the Planck equation

$$I_B = C_1\, \lambda^{-5}\left\{\exp(C_2/\lambda T) - 1\right\}^{-1}$$

(7)

Since apparent brightness temperatures are required, the black body emission equation is simplified by ignoring the first term $(C_1\lambda^{-5})$, and the apparent brightness temperature is calculated. The engineering quantity, Apparent Brightness Temperature, is here defined as that temperature which is required in Equation 7 to give the same output emission as in Equation 6 at wavelength λ.

Three-dimensional geometry is used to define the lines of sight. The position of any point along these lines of sight may be transformed into the plume frame of reference, and, using linear interpolation, the values of temperature, electron density and collision frequency at any point can be calculated from the plume output.

Provision can also be made for the possible transmission of background radiation from sources on the far side of the plume to the detector. A uniform apparent brightness temperature, specified by the user, is assumed for the background radiation. This is added to the total calculated emissions at the end of each line of sight, and is taken as the total emission for lines of sight which do not intersect the plume.

5.2 Emission Measurements

To date emission data are sparse. One UK based experiment afforded the opportunity to undertake dual frequency measurements of emissions from double base and composite motors of 30kN and 10kN thrust, respectively. The frequencies of interest were nominally 35GHz and 90GHz and similarly constructed radiometers consisted of a dish antenna, radiometer head with a Dicke reference, a mixer with I.F. amplifier leading to a detector and band pass amplifier and finally coupled to a correlated detector. The antenna 3dB lobe widths were 1.3 degrees and 0.8 degrees for 35GHz and 90GHz, respectively. Data from the radiometer were analysed by a dedicated computer. Figure 18 shows the measured apparent brightness temperatures for the composite propellant motor and Figure 19 shows similar values for the double base motor.

5.3 Detection

Short range detection of exhaust millimetric radiation by passive sensors is possible and, with receivers having good spatial resolution, capable of providing accurate target bearings. The useful detection range of an incoming missile will be strongly influenced by the size and thermal ionisation characteristics of its exhaust. Much of the intense radiation may be obscured by the missile body when viewed at angles near to "head-on". Narrow angle reception would require rapid scan operation for surveillance purposes, the alternative of initial wide angle reception is likely to reduce detection sensitivity with increased background level, particularly at low elevations near the earth's surface. As a defence aid the detection of exhaust millimetric radiation may form part of a hybrid system to provide surveillance, detection and counter action.

6.0 REDUCTION OF EXHAUST INTERFERENCE AND SIGNATURE

It should be the aim in rocket design to produce a motor that yields no guidance or tracking problems and offers minimal signature.

Microwave attenuation, scattering and emission have been directly associated with the presence of free electrons in the exhaust brought about by ionisation of impurities at exhaust temperature.

6.1 Chemical Modification

Readily ionisable alkali metal impurities are a major source of free electrons in rocket exhausts. Of these, sodium, potassium and calcium are commonly encountered, forming a very small, but significant part of the propellant. Typical concentrations of these metals in solid rocket motors would be 30ppm by weight of potassium and 100ppm of sodium (and even higher levels of calcium) depending upon the type of propellant and its method of manufacture. Complete removal of these impurities from propellants is difficult and prohibitively expensive.

Composite propellants incorporate calcium in the phosphate form to reduce agglomeration in ammonium perchlorate, while the hydroxide is used to counter the acidity of nitro-cellulose in double base propellants.

The ionisation process very much depends upon exhaust temperatures, should they be lowered the electron population will then show a marked decline, thereby reducing the severity of microwave attenuation. Ultimately, if the plume is prevented from burning, very little or no attenuation is evident.

Exhaust combustion is supported by flame-propagation of free radicals like H and OH and rapid removal of these radicals is the aim of combustion suppression. Although paradoxical, potassium salts introduced into double base propellants as a small percentage of the propellant can stimulate the radical-removing reaction processes.

$$K + OH + M \rightarrow KOH + M$$

$$KOH + H \rightarrow K + H_2O$$
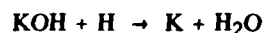
Sodium has similar reaction properties but, weight for weight, is unlikely to better potassium. An important aspect of flame suppression agents is that they should act in the gas phase rather than produce condensed products. Potassium compounds have been shown to be effective suppressants for double base propellants [30,31,32].

Some alkaline earths have been considered, notably molybdenum, iron, cobalt and tungsten.

[33,34]

Suppression additives can be introduced in a variety of ways, the most common being as a propellant ingredient but other methods such as annular spray rings, ablating rods or collars and charge or throat coatings are possible. While static rocket firings are used to assess the performance of additives it must be cautioned that in critical 'burn/no-burn' cases the turbulence of forward velocity or other perturbations in flight may influence the onset of exhaust combustion. Wind-tunnel tests or ultimately flight tests may be necessary to ensure complete confidence.

The case for composite propellants is one where total suppression is unlikely to be successful. Some relief from attenuation can be achieved by the introduction of certain metallic compounds into the exhaust which will lower the free electron concentration. Two chemical mechanisms are suggested. One involves the process of electron attachment where free electrons are replaced by heavy, slow moving, negative ions which contribute very little to microwave absorption [35]. Using molybdenum as an example, such mechanisms could be :-

$$e^- + H_2MoO_4 \rightarrow HMoO_4^- + H$$

$$e^- + H_2MoO_4 \rightarrow MoO_3^- + H_2O$$
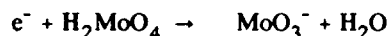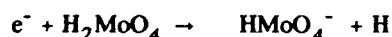
These reactions must over-ride the already acting reaction

$$e^- + HCl \rightarrow Cl^- + H$$
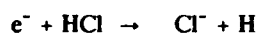
The other mechanism has the object of lowering the free radical concentrations in the exhaust but not to the point of flame extinction. If chlorine is present in the plume then in general the ionisation of alkali metals(A) takes the form

$$ACl^- + 3H \rightarrow A^+ + e^- + HCl + H_2$$
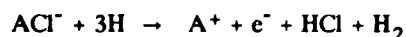
where concentrations of electrons $[e^-]$ can quickly fall if those of H (the hydrogen atom) drop [36]. It is important that the additive should remain in the gas phase in the exhaust, equally it should not form stable compounds with the chlorine.

With double base propellants any additive forming stable negative ions in the exhaust will, in some measure, reduce free electron concentrations, particularly since $[Cl^-]$ is not being generated.

7.0 CONCLUSIONS

It is argued that to fully evaluate the microwave properties of a rocket motor exhaust for a specific role, flight tests should be undertaken in the proposed operational environment. This is known to be very expensive when the full range of operating temperatures, altitudes and velocities are represented. Also missile manoeuvres and information on flight attitude at any instant can make the recording of accurate flight data a difficult task. Added to this is the fact that flight tests can only come at the post design stage when the programme is well advanced. Any fundamental changes at this point are often strongly resisted and a compromise enters the project. Confronted with these difficulties alternative plume studies were sought and have become an intrinsic part of missile system design. Theoretical studies offering reliable predictions at the time when design options are being considered would be the ideal way to optimise propulsion performance against plume effects. Application codes need to be improved with better models for diffraction and refraction, emission processes and radar cross section. But these codes are only as good as the theoretical plume flowfield model and it is here that we find the key and the challenge. It is largely recognised that further plume model development is essential; in shock treatment; in base flow; in condensed particle flow effects and the treatment of time dependant turbulence properties. In this, the advent of small, but ever more powerful, computers make possible the realisation of progress towards better models. For the present, plume technology has not yet reached the stage where modelling techniques preclude recourse to experiments. The aim of a plume study group must be to perfect these techniques supported by validation from well conceived experiments.

Exhaust technology is a field in which fundamental research and system applications can profitably proceed, hand in hand. System tests and model validation can be part of a common programme for research and project support. Facilities for measuring exhaust microwave properties should offer maximum flexibility to support the following typical objectives :-

(i)   To provide experimental data for new research concepts.

(ii)   To conduct experiments for the validation of prediction codes.

(iii)   To compare motors for specific

mission objectives.

(iv) To measure the microwave characteristics of propellants containing a range of additives for plume suppression and other interference relief.

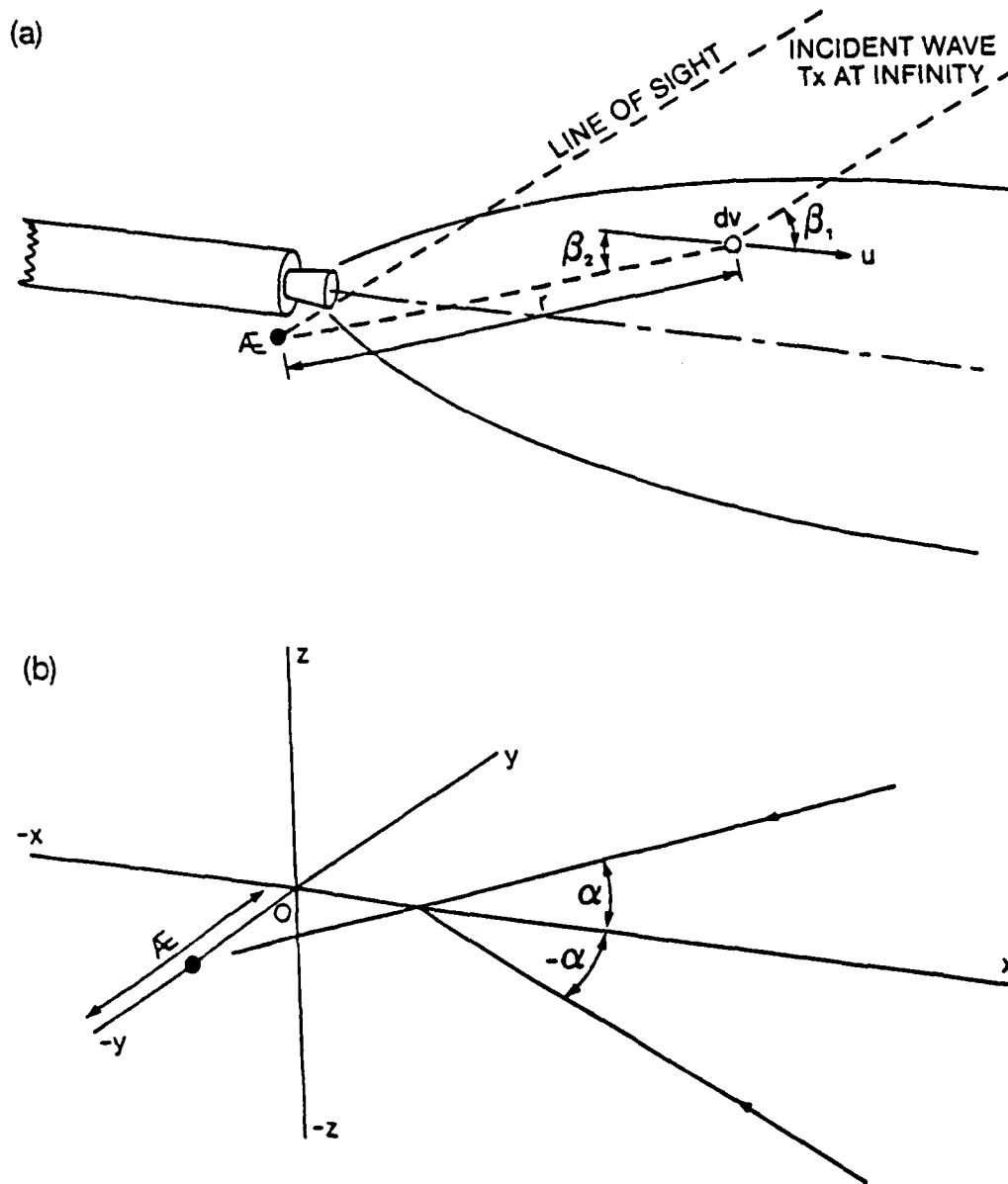(v) To evaluate rocket motors for service acceptance.

8.0 REFERENCES

1   Williams, H
    Radio Propagation through Rocket Exhaust
    Jets:
    Part 1.   Electromagnetic Wave
              Propagation in an Ionised
              Medium.
    RPE Report No 37, February 1959

2   Victor, A C
    JANNAF Handbook on Rocket Exhaust
    Plume Technology
    CPIA Publication 263, Chapter 4
    John Hopkins University, MD, 1977

3   Williams, H, Wilson, A S, Blake, C C
    Scattering from a Turbulent Rocket
    Exhaust Jet Illuminated by Plane
    Wave
    Electronics Letters Vol 7, No 189,
    Sept 1971

4   Smoot, L D, Underwood, D L
    Prediction of Microwave Attenuation
    Characteristics of Rocket Exhausts
    J Spacecraft and Rockets, Vol 3, No 3,
    March 1966

5   Smoot, L D, Seliga, T J
    Rocket Exhaust Plume Radar Attenuation
    and Amplitude/Phase Noise
    J Spacecraft and Rockets, Vol 4, No 6, June
    1967

6   Victor, A C
    Microwave Interference Characteristics of a
    Solid Rocket Motor Exhaust
    NWC China Lake, California,
    NWCTP4199, Oct 1968

7   Tartarski, V I
    Scattering from a Turbulent Medium
    NY McGraw-Hill 1961

8   Salpeter, E E, Treiman, S B
    Backscatter of Electromagnetic Radiation
    from a Turbulent Plasma
    J Geophys 69, No 4, 869, 1964

9   Granatstein, V L, Buchsbaum, S
    Proceedings of Symposium on Turbulence of
    Fluids and Plasmas
    Polytechnic Press NY, 1969

10 Cousins, J M, Jensen, D E
    On the Computation of Ionization Levels in
    Rocket Exhaust Flames
    Combustion and Flame 52, 111, 1983

11 Wilson, A S, Jensen D E
    Prediction of Rocket Exhaust Flame
    Properties
    Combustion and Flame 25, 43, 1975

12 Dash, S M, Pergamont, H S, Thorpe, R D
    The JANNAF Standard Plume Flowfield
    Model. Modular Approach and Preliminary
    Results
    CPIA Publication 306, Vol 1, May
    1979

13 Jensen, D E, Jones G A
    Theoretical   Aspects   of   Secondary
    Combustion in Rocket Exhausts
    Combustion and Flame 41, 71, 1981

14 Pergamont, H S, Dash, S M, Verma, A K
    Evaluation of Turbulent Models for
    Rocket and Aircraft Plume
    Flowfield Predictions
    AIAA Paper 79-0359, Jan 1979

15 Dash, S M
    Recent Developments in the Modelling of
    High Speed Jets, Plumes and Wakes
    AIAA Paper 83-1616, July 1985

16 Victor, A C
    Calculations of Rocket Plume Afterburning
    Coupled to Reacting Base Recirculation
    Regions
    J Spacecraft and Rockets Vol 14, No 9, 534,
    Sept 1977

17 Jensen, D E, Spalding, D B,
    Tatchell, D G, Wilson, A S
    Computation of Structures of Flames with
    Recirculating Flow and Radial Pressure
    Gradients Combustion and Flame 34, 309,
    1979

18 Mace, A C H, Markatos, N C,
    Spalding, D B, Tatchell, D G
    Analysis of Combustion in Recirculating

Flow for Rocket Exhausts in Supersonic Streams
J Spacecraft and Rockets 19, 557, 1982

19 Cummings, G A McD, Lawrence, R E, Travers, B E L
Radio Interference due to Rocket Exhaust Jets. A Detailed Study of the Interference Characteristics of a Selected Propellant
RPE Tech Report 71/73, 1971

20 Cummings, G A McD, Travers, B E L, Wilson, A S
Radio Interference due to Rocket Exhaust Jets. The Study of Jet Structure Using Focused Microwave Beams
RPE Tech Report 71/72, 1971

21 Victor, A C, Mantz, J C
Interaction of Focused Microwave Beams with a Rocket Exhaust
NWC China Lake, California
NWCTP5119, Feb 1972

22 Lawrence, R E
Radio Interference Caused by Rocket Exhaust Jets. The Measurement of Phase Modulation
RPE Tech Report No 70/9, Oct 1970

23 Golden, K E, Taylor, E C, Vincentie, F A
Diffraction by Rocket Exhausts
IEEE Trans AP 16, No 5, 614, 1968

24 Senol, A J, Romine, G L
Three-dimensional Refraction/Diffraction of Electromagnetic Waves Through Rocket Exhaust Plumes
J Spacecraft and Rockets 23, No 1, 39, 1986

25 Hall, C M, Strangeways, H J
Representation of Microwave Propagation Through High Electron-Density Rocket Exhaust Plumes by an Equivalent Diffracting Disc
Proc Int Conf on Electromagnetics in Aerospace Applications. Torino, Italy, 1989, pp 95-98

26 Molmud, P
RAYBEND - A Ray Tracing Program for Microwaves Propagating Through Rocket Plumes
JANNAF 12th Plume Technology Meeting, Oct 1980, pp 273-312

27 Ramsey, D A
The Evaluation of Radar Guidance GEC Journal of Research, Vol 3, No 2, 1985

28 Victor, A C
Private Communication

29 Sume, A
Millimetric Wavelengths Emissions from Solid Propellant Rocket Motor Plumes
Försvarets Forskingsanstalt Report C30291-E1, E3, Sept 1982

30 Smith, P K, Evans, G I
The Suppression of Secondary Combustion in Solid Propellant Motors
Imperial Metal Industries, Tech Note 82/5, 1982

31 McHale, E T
Flame Inhibition by Potassium Compounds
Combustion and Flame 24, 2377, 1975

32 Jones, G A
Comparison of Predicted and Experimental Microwave Attenuation for a Flame-Suppressed Rocket Exhaust Plume
DRA Fort Halstead, RARDE Tech Report 13/85, Nov 1985

33 Jensen, D E, Jones, G A
Theoretical Aspects of Secondary Combustion in Rocket Exhausts
Combustion and Flame, 41, pp 71-85, 1981

34 Jensen, D E, Webb, B C
Afterburning Predictions for Metal Modified Propellant Motor Exhausts
AIAA Journal Vol 14, No 7, 947, July 1976

35 Jensen, D E, Miller, W J
Electron Attachment and Compound Formation in Flames IV. Negative Ion and Compound Formation in Flames Containing Potassium and Molybdenum
Thirteenth Symp (Int) on Combustion (The Combustion Institute, Pittsburgh, 1971) p 363

36 Jensen, D E, Jones, G A
Mass-Spectrometric Tracer and Photometric Studies of Catalysed Radical Recombination in Flames
J Chem Soc Faraday Trans 1, 71, 1975

(a)

(b)

Fig. 1   Diagram Showing   (a)   Propagation Geometry

(b)   Co-ordinate System
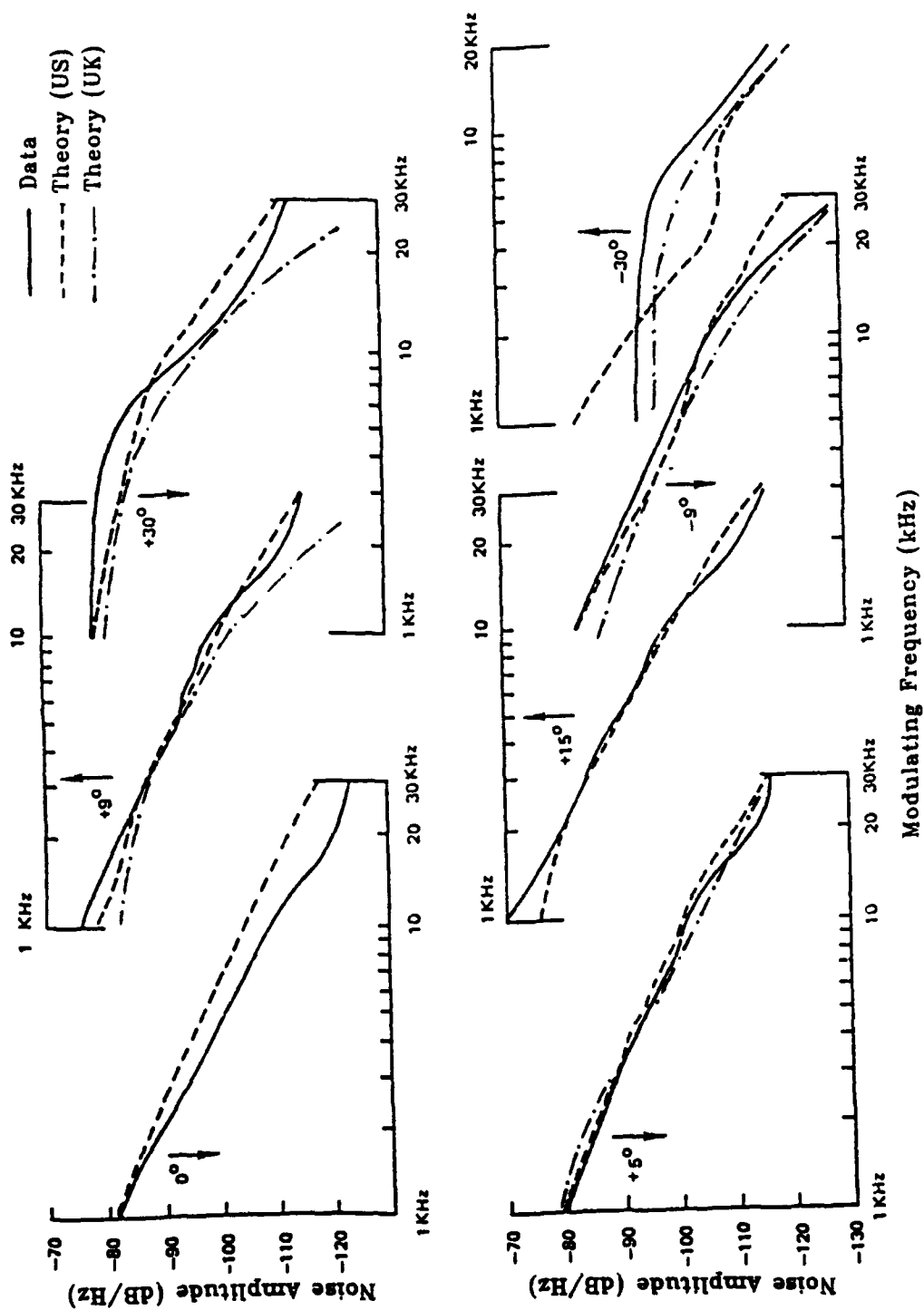
Fig. 2 Forward Scatter. Comparison between Measured Amplitude
Modulated Noise and Prediction

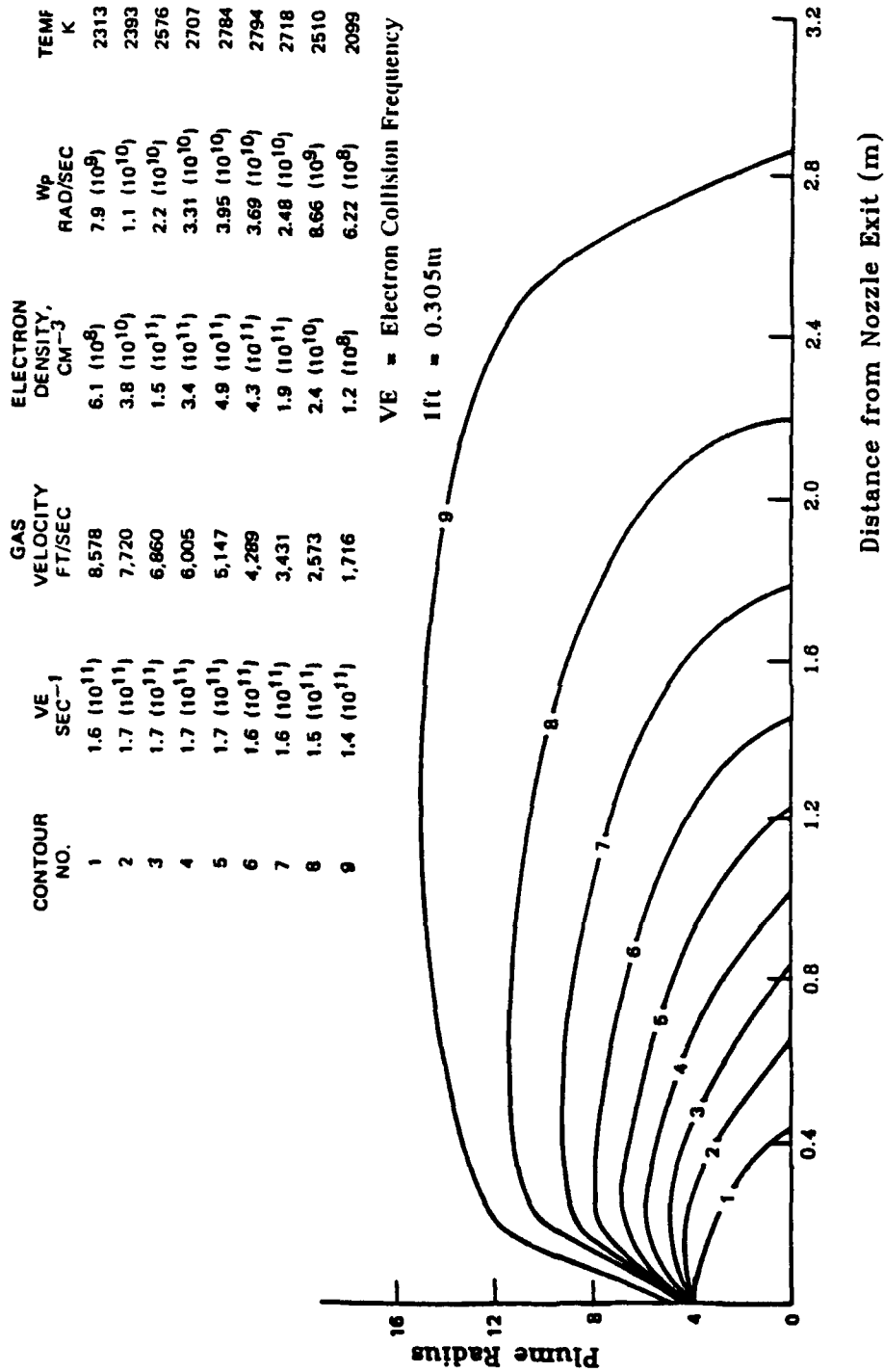| CONTOUR NO.	V_E SEC^{-1}	GAS VELOCITY FT/SEC	ELECTRON DENSITY, CM^{-3}	W_p RAD/SEC	TEMP K
1	$1.6 (10^{11})$	8,578	$6.1 (10^8)$	$7.9 (10^9)$	2313
2	$1.7 (10^{11})$	7,720	$3.8 (10^{10})$	$1.1 (10^{10})$	2393
3	$1.7 (10^{11})$	6,860	$1.5 (10^{11})$	$2.2 (10^{10})$	2576
4	$1.7 (10^{11})$	6,005	$3.4 (10^{11})$	$3.31 (10^{10})$	2707
5	$1.7 (10^{11})$	5,147	$4.9 (10^{11})$	$3.95 (10^{10})$	2784
6	$1.6 (10^{11})$	4,289	$4.3 (10^{11})$	$3.69 (10^{10})$	2794
7	$1.6 (10^{11})$	3,431	$1.9 (10^{11})$	$2.48 (10^{10})$	2718
8	$1.5 (10^{11})$	2,573	$2.4 (10^{10})$	$8.66 (10^9)$	2510
9	$1.4 (10^{11})$	1,716	$1.2 (10^8)$	$6.22 (10^8)$	2099

V_E = Electron Collision Frequency

1 ft = 0.305 m

Fig. 3 Calculated Plume Properties for Motor Filled with Aluminised Composite Propellant. Static, Sea-level.
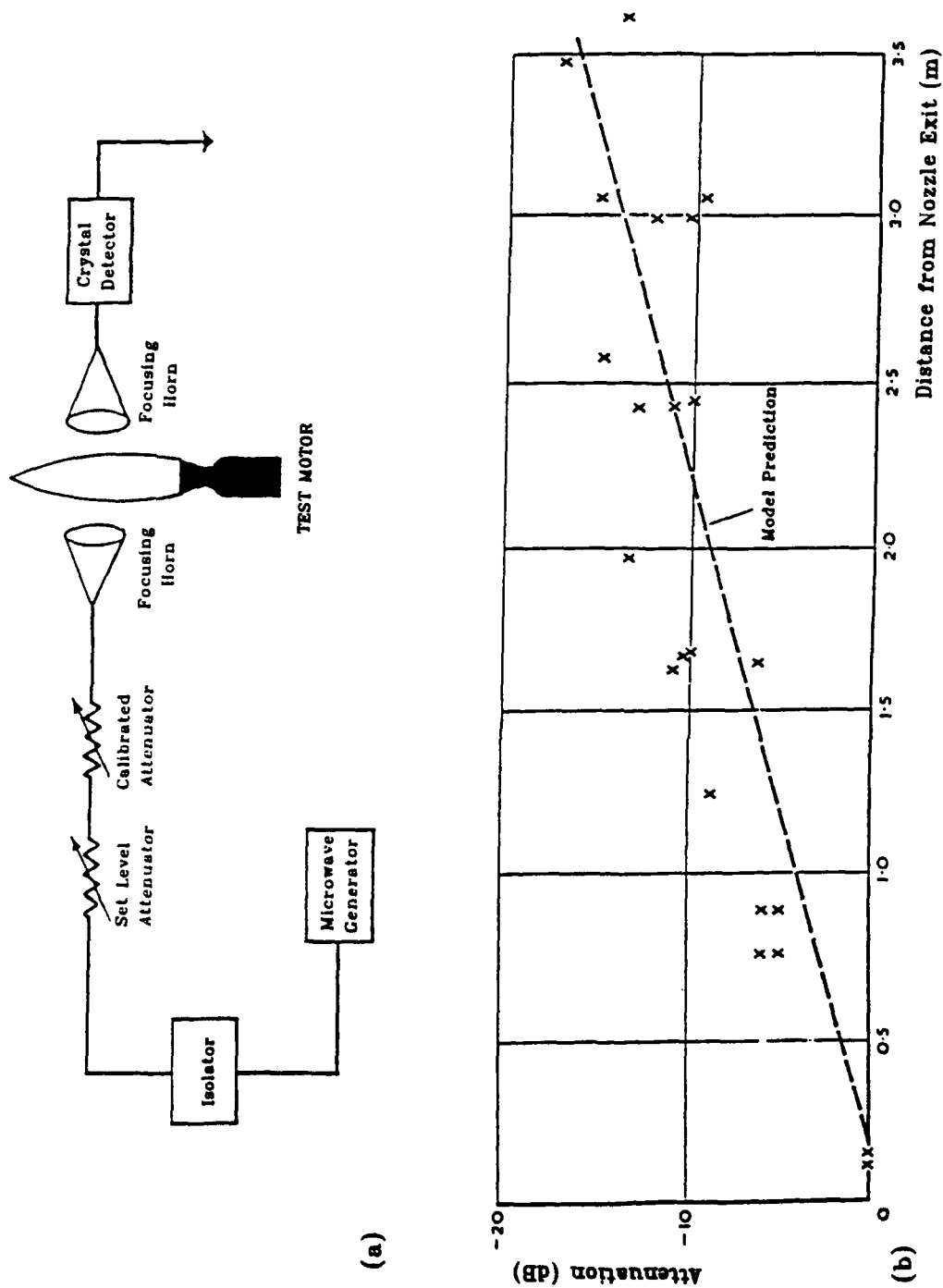
Fig. 4 (a) Transmitter and Receiver Assembly
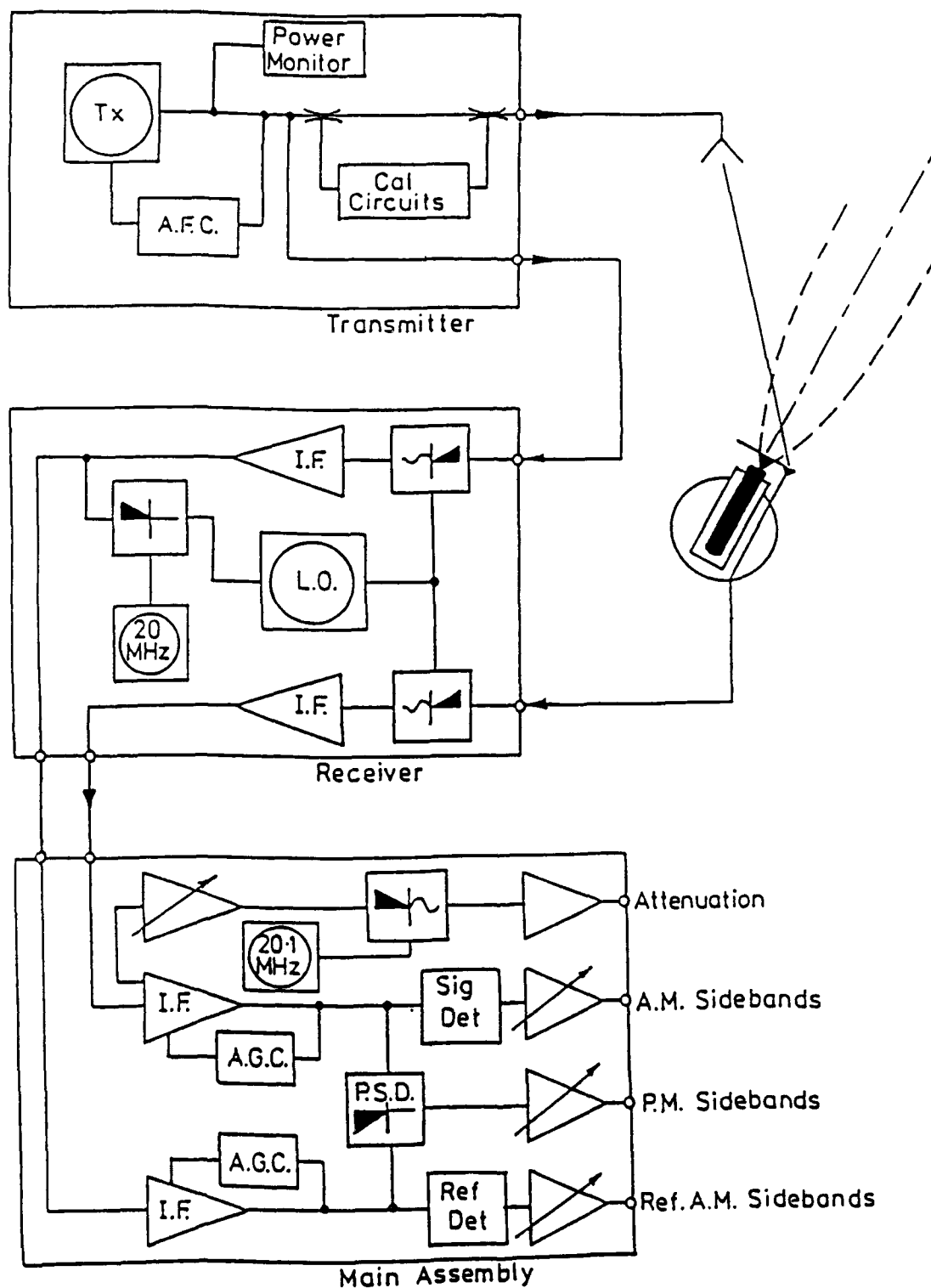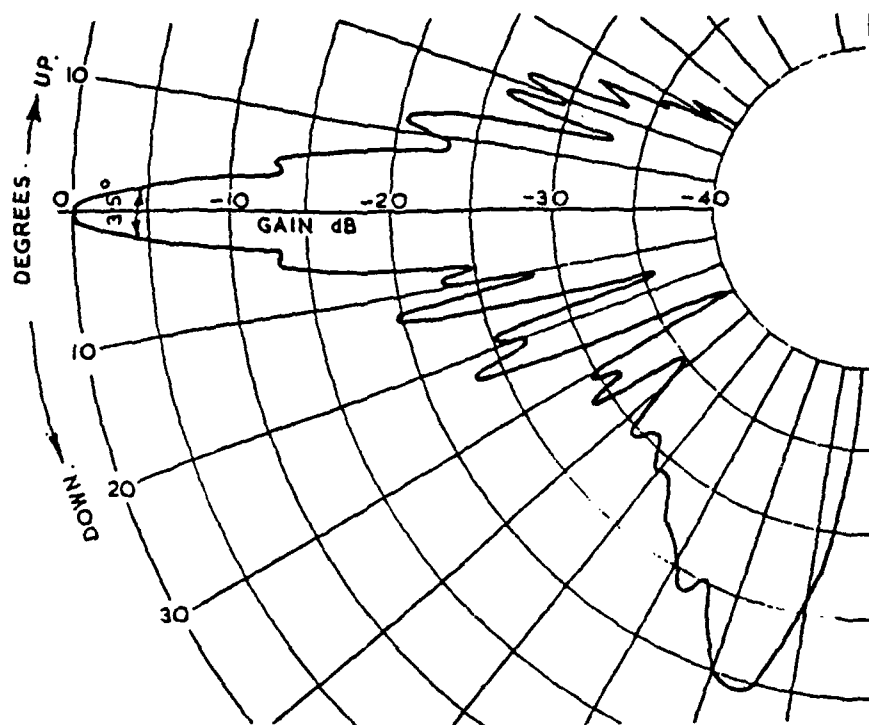(b) On axis Transverse Attenuation with Distance from
Nozzle Exit

Fig. 5   Attenuation Measuring Equipment. Schematic Diagram

Vertical Plane
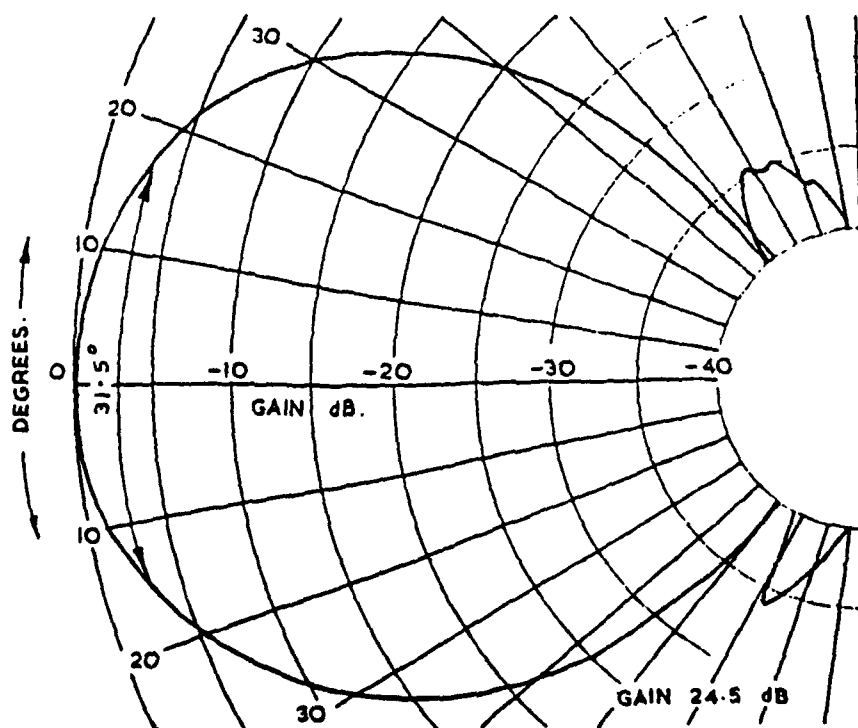
Horizontal Plane

Fig. 6   Tx.Antenna Polar Diagram. Vertical Polarization

Vertical Plane

Horizontal Plane
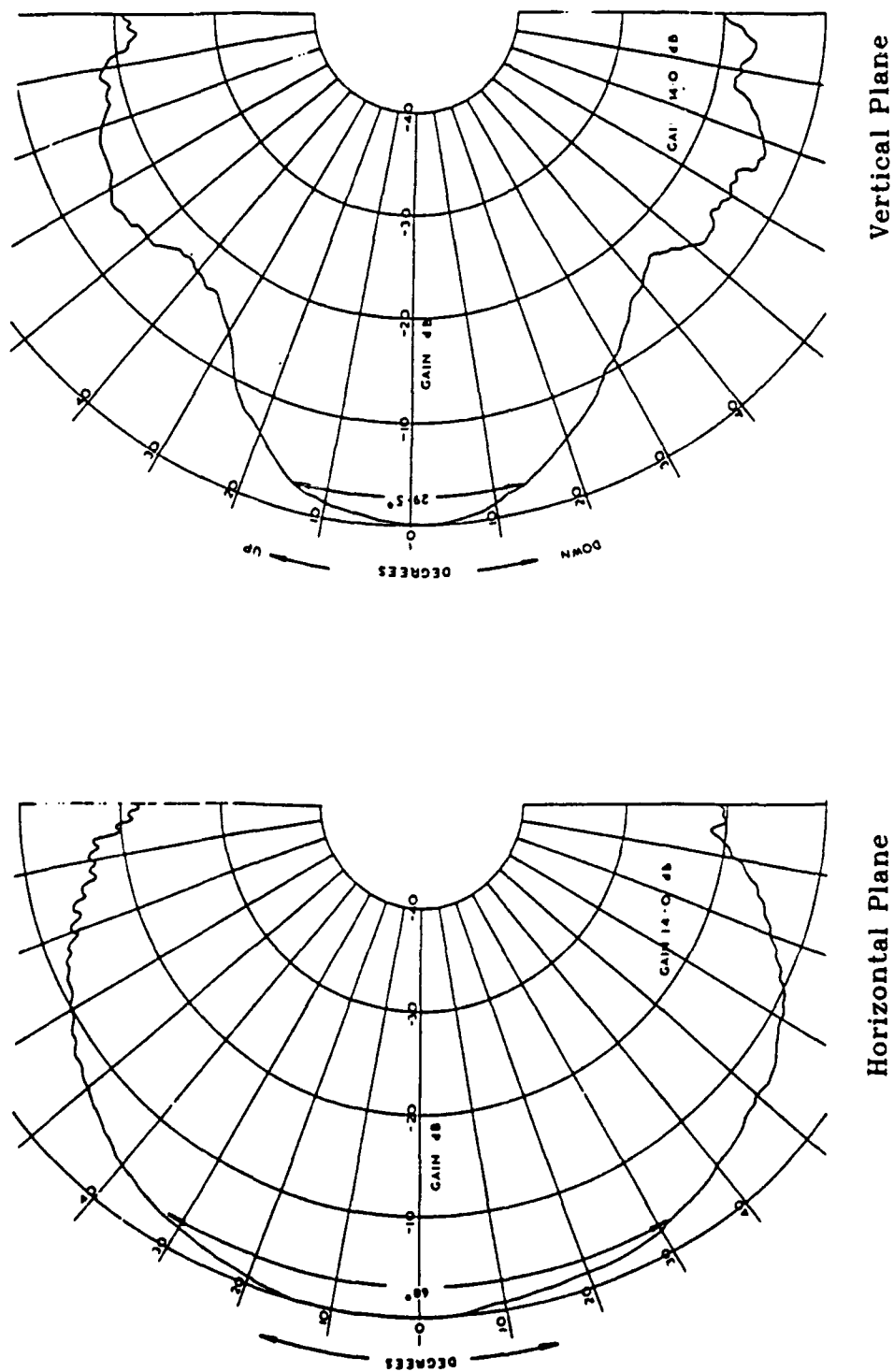
Fig. 7   Rx.Antenna Polar Diagram. Vertical Polarization
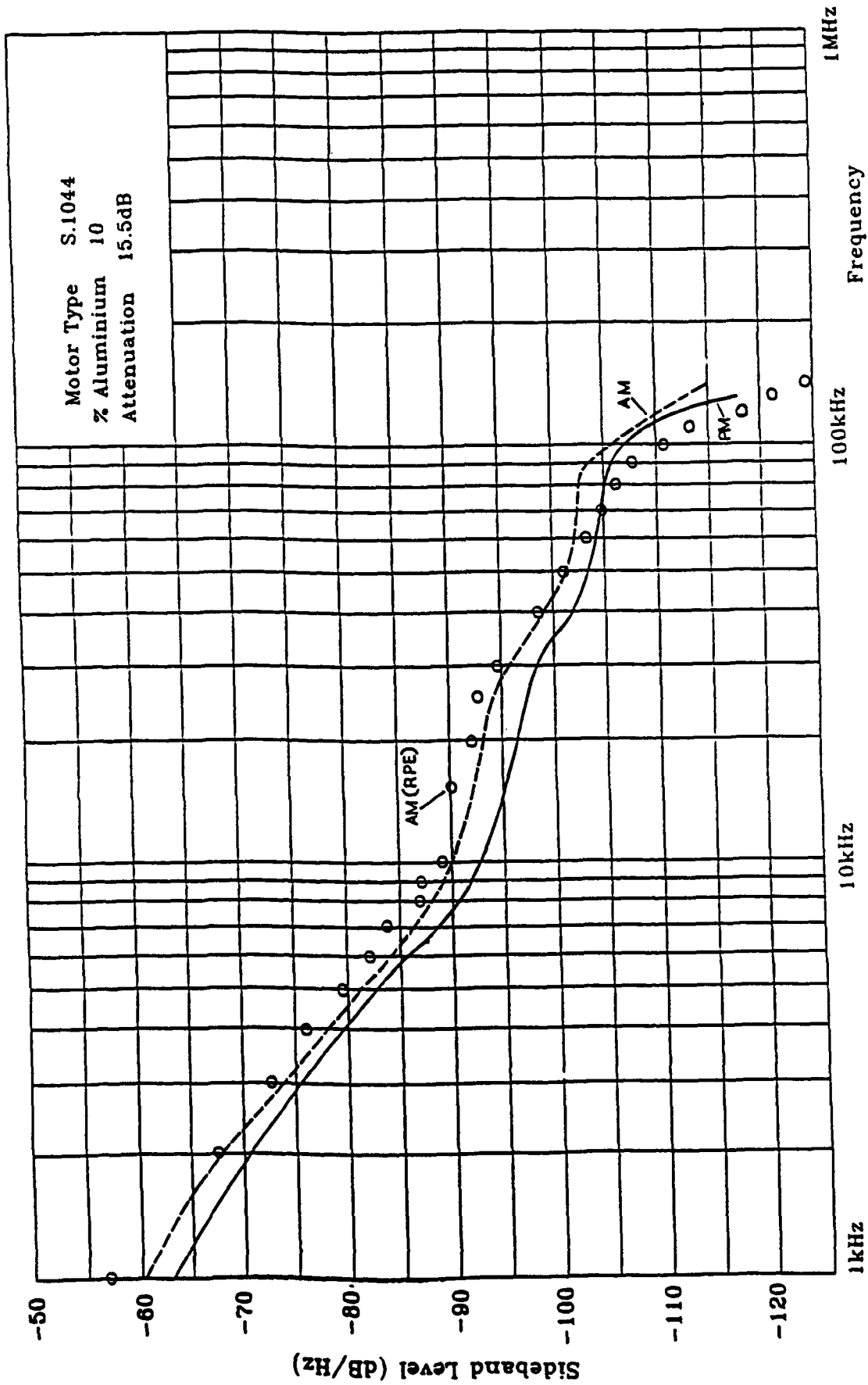
Fig. 8 Forward Scatter Spectra. AM and PM Noise Modulation

Interception angle, °	X-Band		J-Band		Q-Band	
	A dB	I dB	A dB	I dB	A dB	I dB
+ 3	-234	-15.0	-235	-18.0	-158	-19.0
+ 5	-185		-178	-22.0	-125	
+10	- 61	-22.0	- 58	-23.0	- 41	-30.0
+20	- 15.7	-13.5	- 15.1	-12.5	- 10.6	-

Nominal Frequencies: X(10GHz), J(16GHz), K(35GHz)

Fig. 9   Comparison of Calculated Absorption Loss (A) with Experimental Insertion Loss (I)
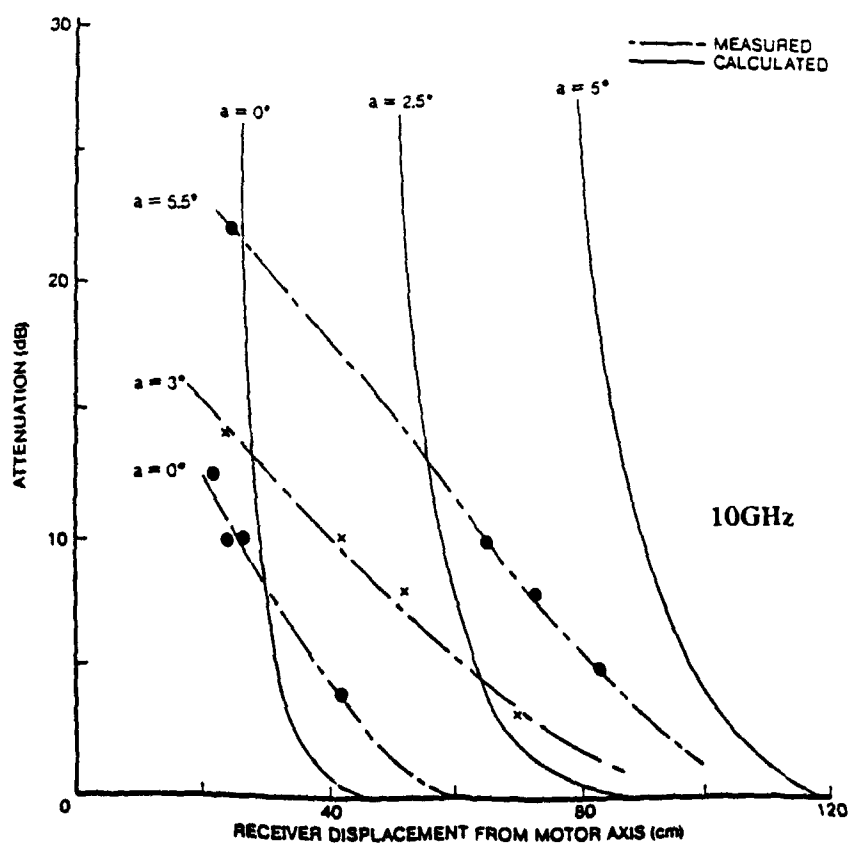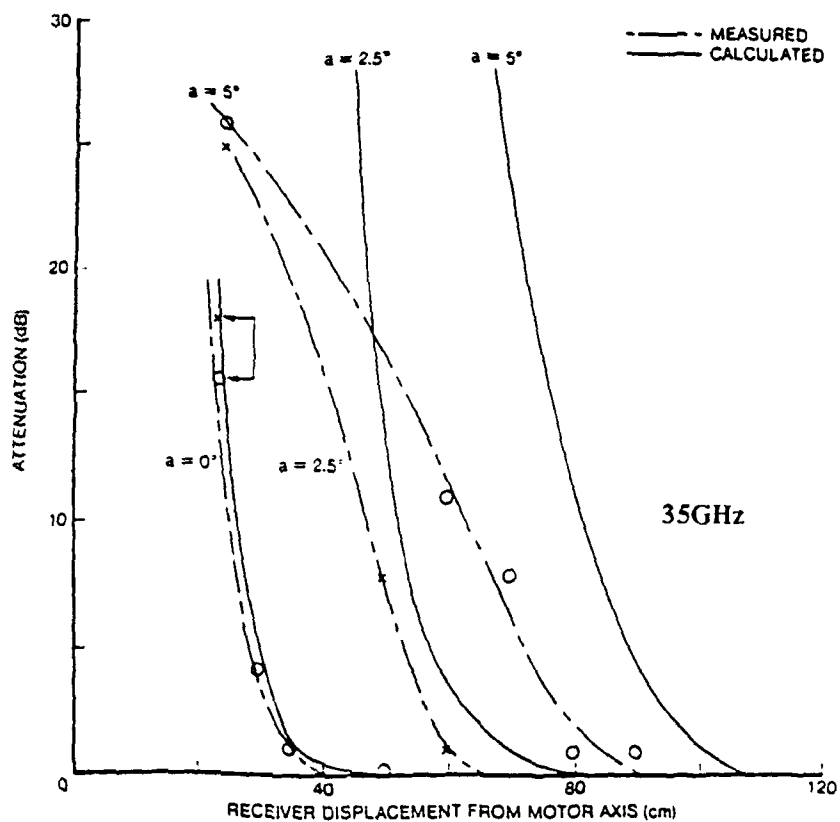
Fig. 10 Comparison of Predicted and Measured Attenuation Against Receiver Displacement for Three Aspect Angles
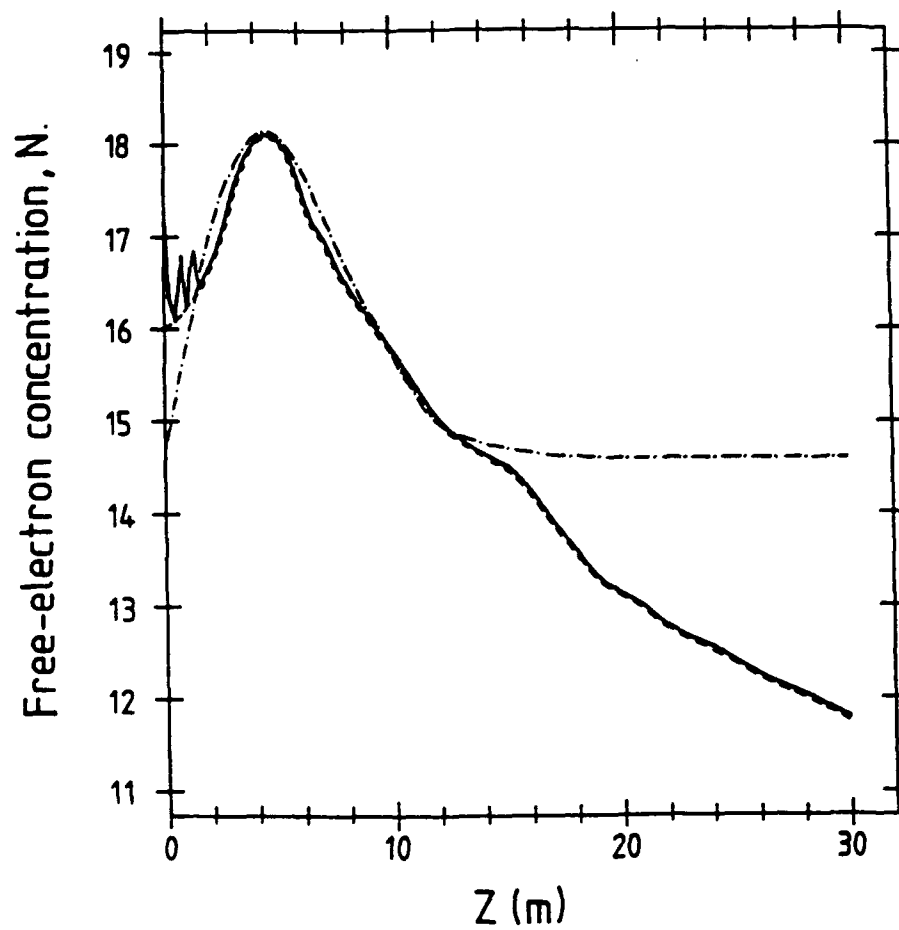
Fig. 11 Axial Ionisation Contours: Comparison between Plume Model and Approximations

Plume Flowfield Model ——————

Simple Exponential —·—·—·—·—·—·—

Least-squares Polynominal — — — — — — — —
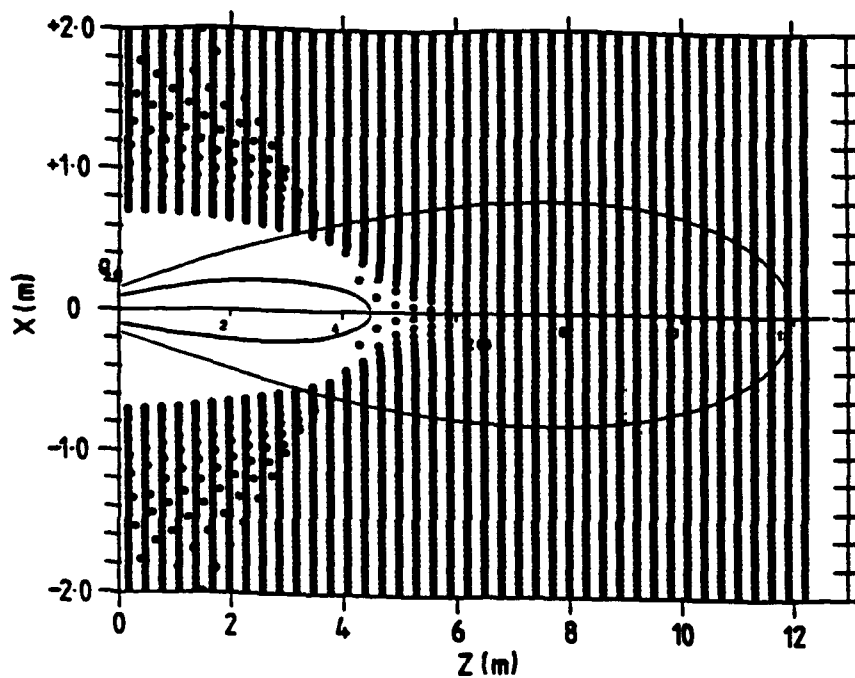
Fig. 12   Progressive Wavefront Distortion.
Freq. = 10GHz, Aspect Angle = 0°
Z = Plume Axis
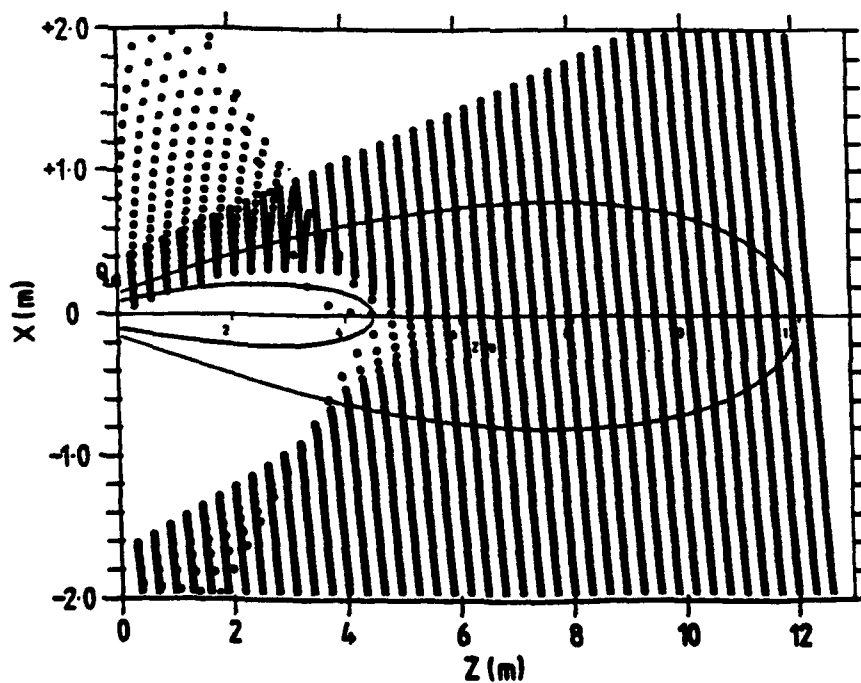
Fig. 13   Progressive Wavefront Distortion.
Freq. = 10GHz, Aspect Angle = 10°
Z = Plume Axis
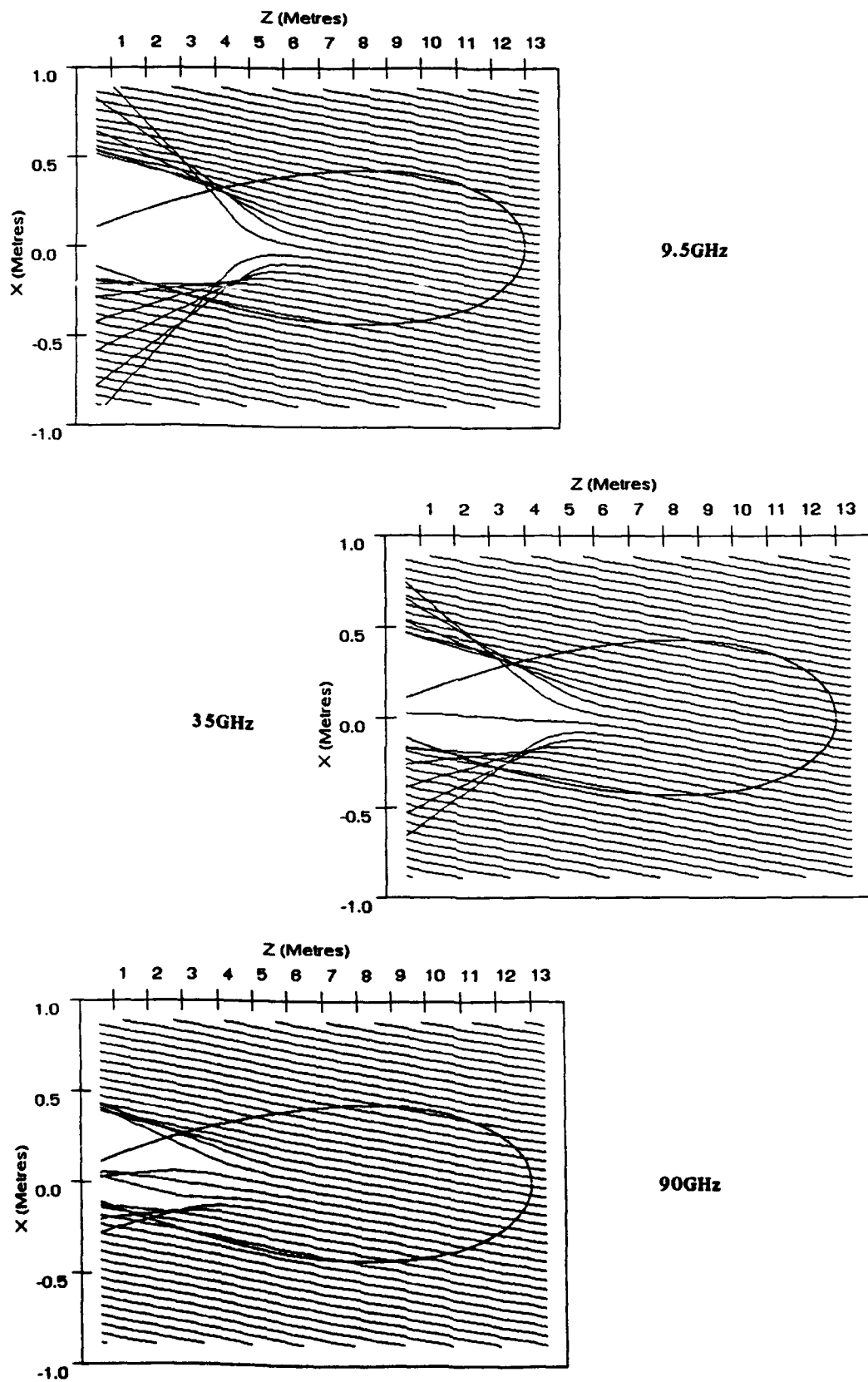
Fig. 14   Ray Progress. Effect of Varying Propagation Frequency
Z = Plume Axis
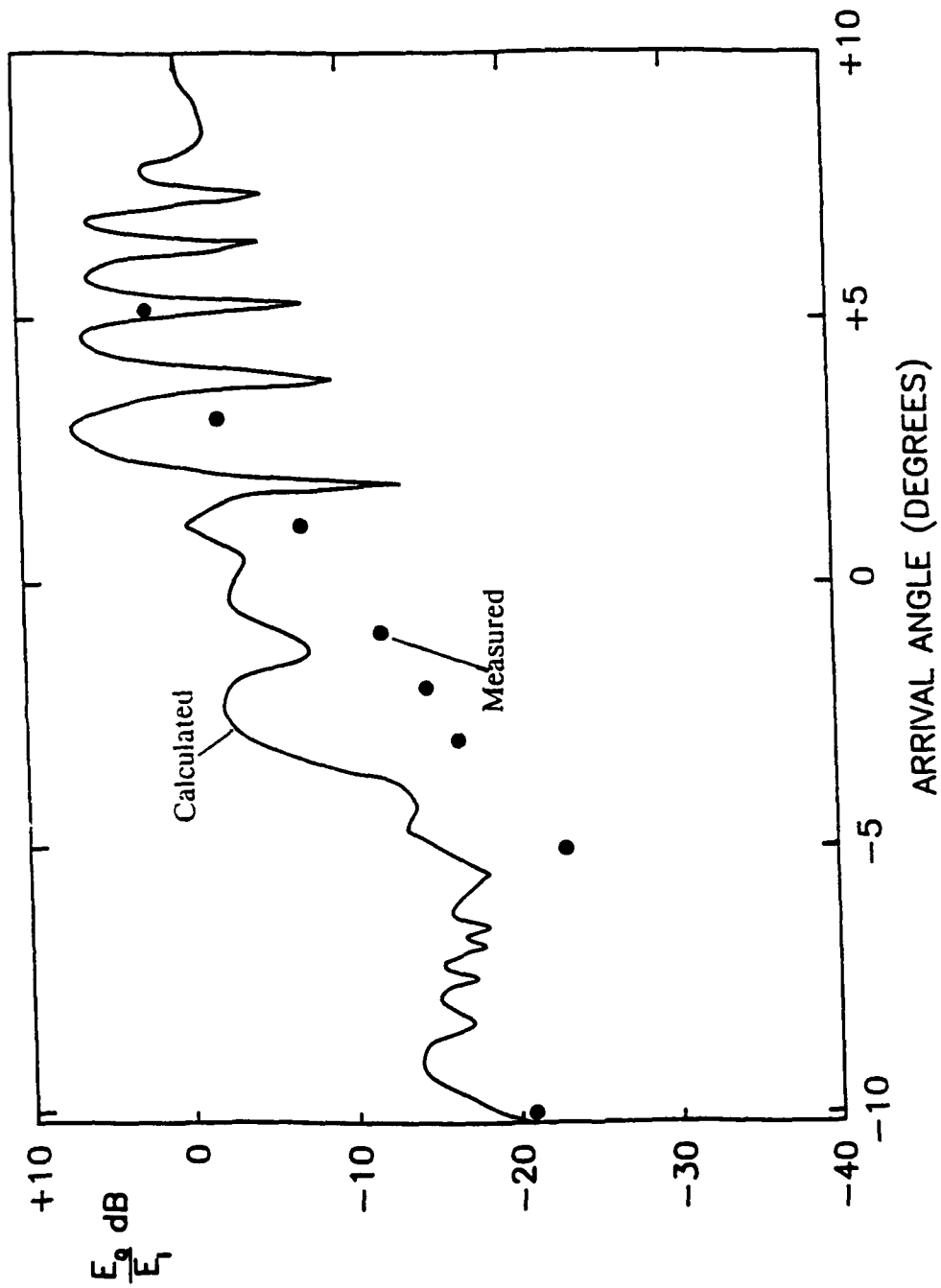
Fig. 15   Comparison between Calculated Diffraction Signal and
Attenuation Measurement.
Double Base Motor, Thrust 30kN. Frequency 10GHz

Doppler, 23.9km, 1890ms^{-1}, 381°

Total Integrated RCS = -7.1 dBsm

Doppler Velocity, 20ms^{-1} per Division

= 176.8 Hz
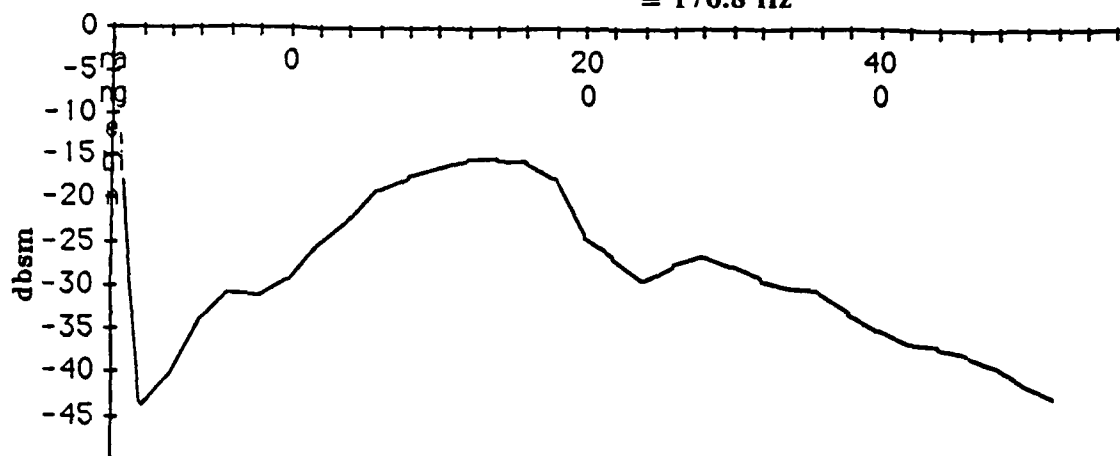
(a)
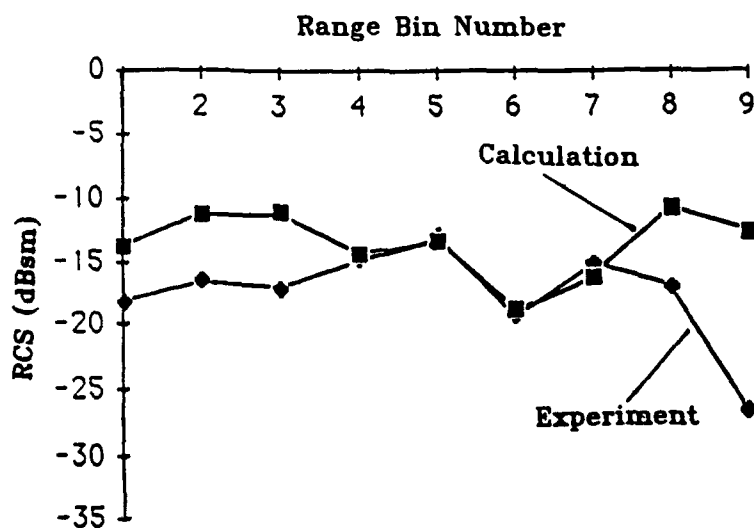
(b)

Fig. 16 **(a)** Total Doppler RCS Spectrum. US Motor (BB).

(b) RCS Spectra. Comparison Between Flight Data and Calculations. US Motor (BB)
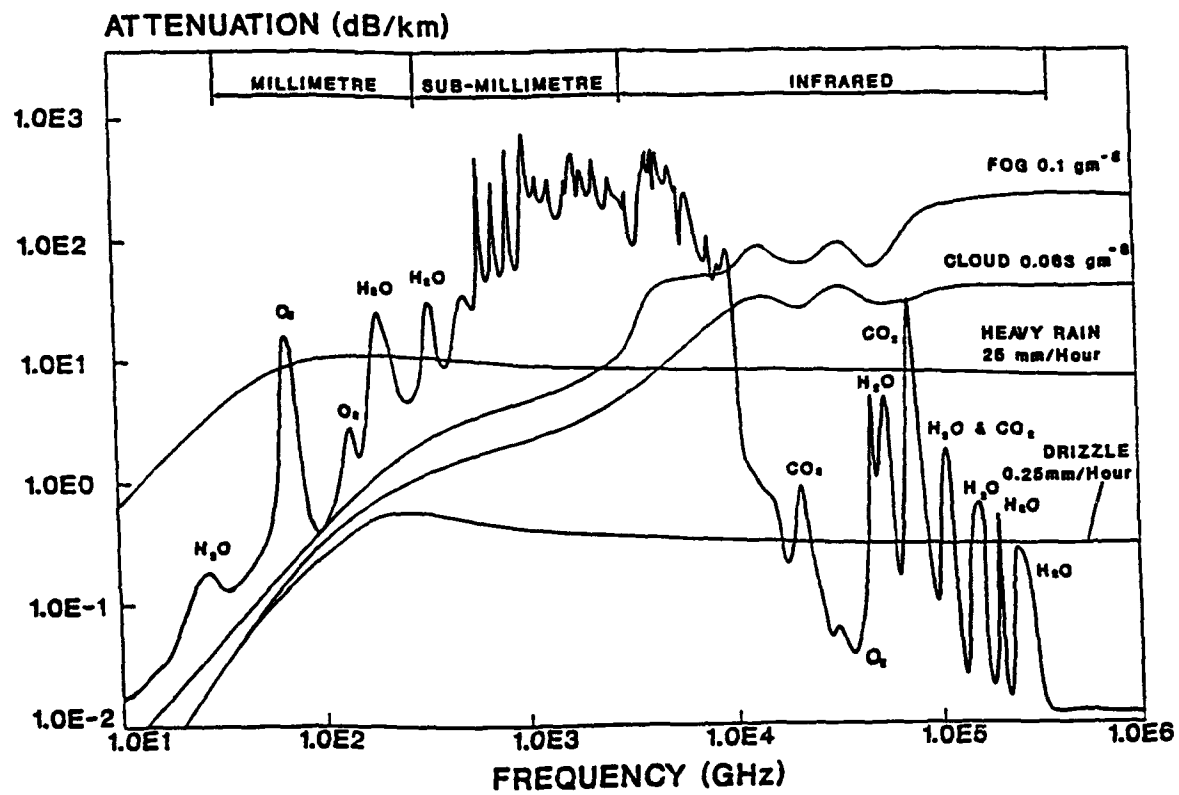
Fig. 17   Atmospheric Attenuation
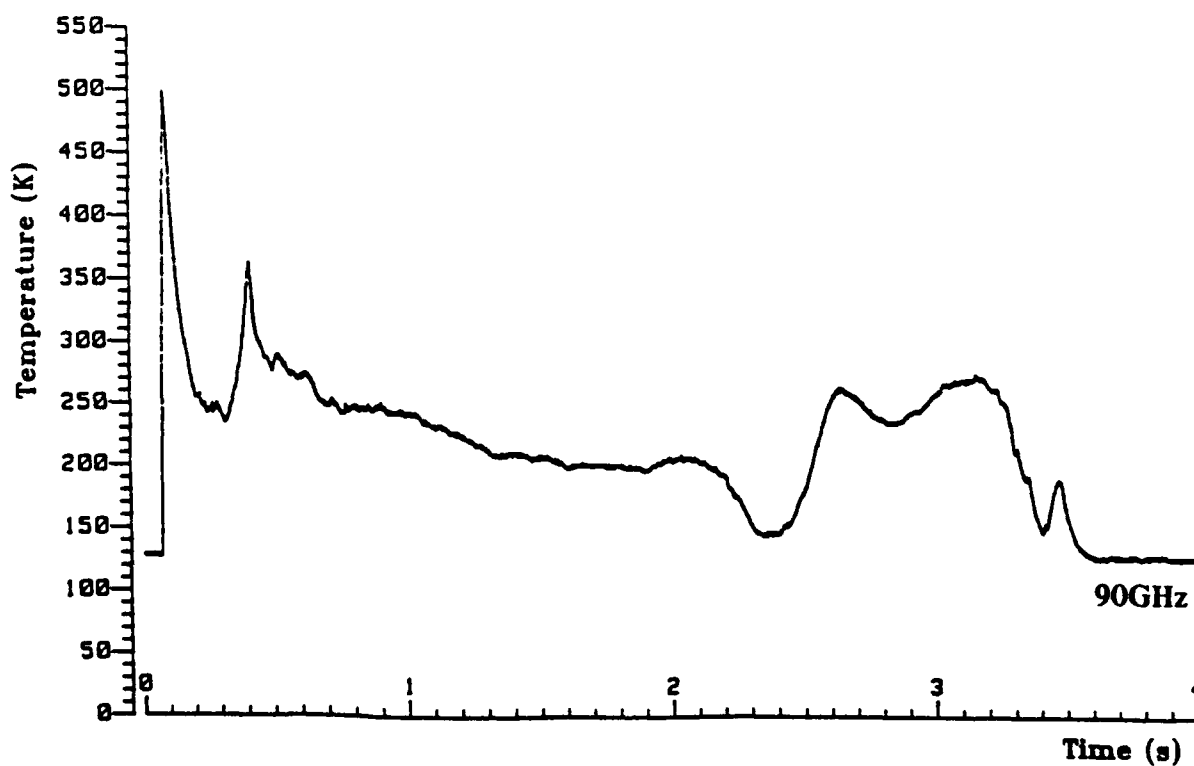
Fig. 18 Emission Apparent Brightness Temperatures for Composite Propellant Motor in Two Wavebands

Vertical Polarisation

Vertical Polarisation
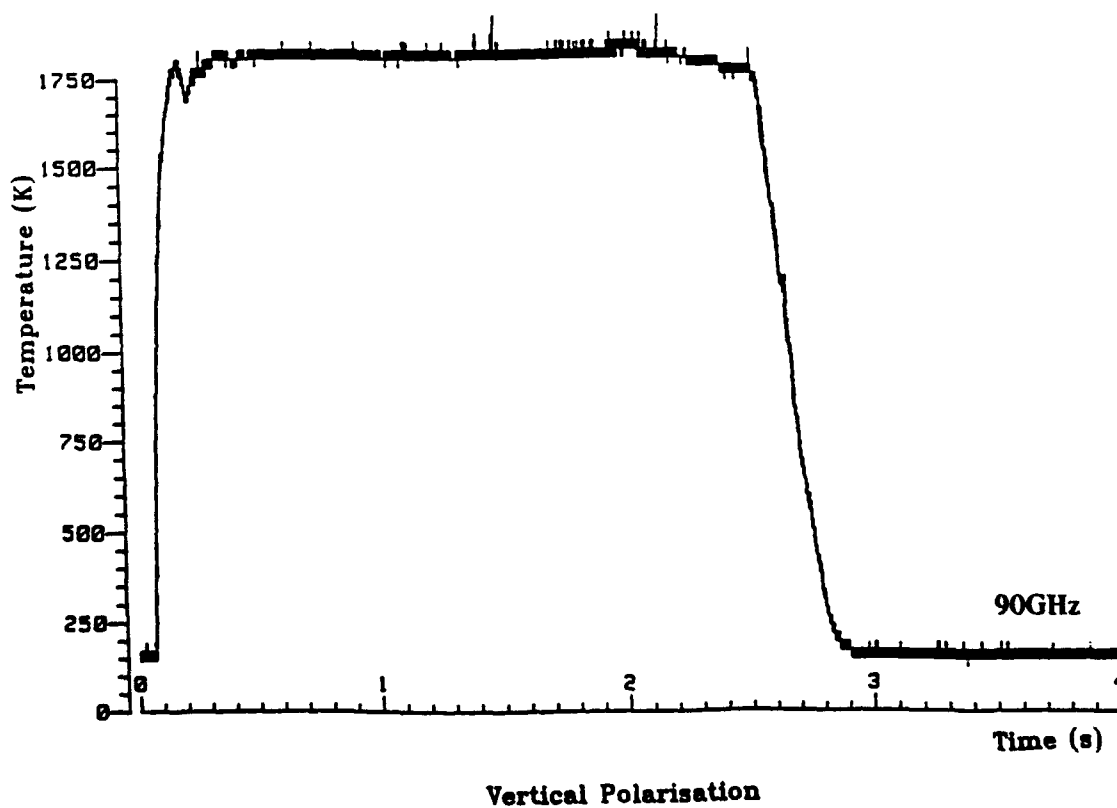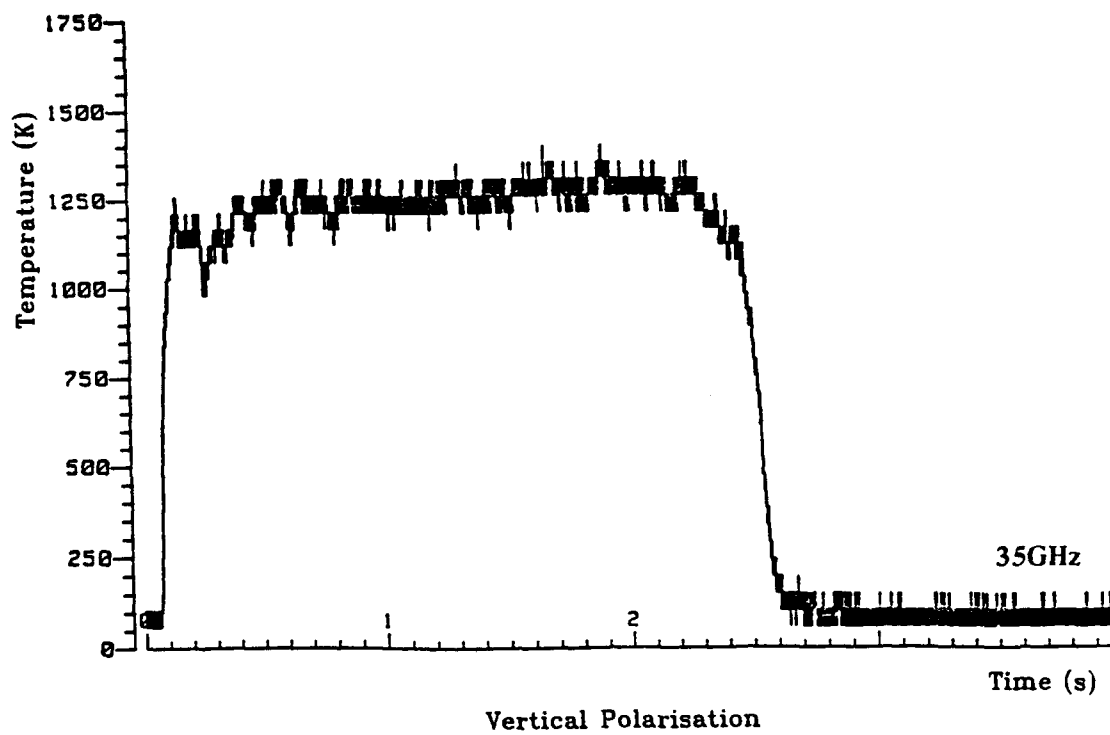
Fig. 19 Emission Apparent Brightness Temperatures for Double Base Propellant Motor in Two Wavebands

Plume Radiation

by
R. Dirscherl
Deutsche Aerospace AG
Dynamics Systems
P. O. Box 801149
D - 8000 München 80
Germany

Summary

The electromagnetic radiation originating from the exhaust plume of tactical missile motors is of outstanding importance for military system designers. Both missile- and countermeasure engineer rely on the knowledge of plume radiation properties, be it for guidance/interference control or for passive detection of adversary missiles. To allow access to plume radiation properties, they are characterised with respect to the radiation producing mechanisms like afterburning, its chemical constituents and reactions as well as particle radiation. A classification of plume spectral emissivity regions is given due to the constraints imposed by available sensor technology and atmospheric propagation windows.

Additionally assessment methods are presented that allow a common and general grouping of rocket motor properties into various categories. These methods describe state of the art experimental evaluation techniques as well as calculation codes that are most commonly used by developers of NATO countries. Dominant aspects influencing plume radiation are discussed and a standardised test technique is proposed for the assessment of plume radiation properties that includes prediction procedures. These recommendations on terminology and assessment methods should be common to all employers of plume radiation. Special emphasis is put on the omnipresent need for self-protection by the passive detection of plume radiation in the ultraviolet (UV) and infrared (IR) spectral band.

1. INTRODUCTION

Due to the change in global balance, NATO strategies are changing also. The future engagement of forces will be more in local conflicts with conventional weapons for quick and internationally guided missions. Of paramount interest in this type of mission is the need of reconnaissance-, surveillance- and warning-sensors and systems

Both ground and air forces are threatened by hostile missiles. 90% of the planes lost in combat during the last years were shot down by missiles with IR seeker heads. The most evident way to counter this threat is by sensing the hostile missile in order to direct countermeasure activities. The radiative emission from the missile's body, or more important its plume signature is used to perform this task.

Despite shrinking military budgets, many government agencies are willing to spend money on weapon system updates including "defensive aid subsystems" (DASS) or "Missile Approach Warning" (MAW) systems to counter that kind of threat, especially for flying platforms. This motivation will direct and steer the future development and research of missile technology - namely its radiative signature, or rather the avoidance or minimisation of signature.

Up to now smoke properties were of prime interest for missile designers, because it is the most striking artefact of a missile being fired. The smoke as seen by the naked eye gives clear evidence of the trajectory, speed and distance of a missile. With the development of "min" smoke or smokeless motors, as described in earlier papers of this lecture series, this most evident signature is controllable. With the

advance of night vision and infrared sensing devices surprise strikes are also performed during night or under adverse weather conditions. This relativates the smoke signature of rocket motors, but emphasises the radiative plume signature of missiles.

At the moment there are two spectral regions most favoured for the passive detection of tactical missileplumes by missile launch and approach warning systems, namely the middle infrared spectral region between 3 -5 μm and the solar blind ultraviolet spectral region below 300 nm.

Another concern of rocket motor plume signature is its interference with missile guiding systems. Laser beam riders or guidance and control systems are disturbed and limited by the infrared signature of the plume.

Rocket designing engineers are working on its performance by changing missile aerodynamics and motor properties. Design of the rocket motor nozzle and missile afterbody geometry can be tailored to reduce IR plume radiation by reducing or eliminating zones of recompression and high temperature thereby moderating or suppressing afterburning. In this way the flight dynamic and accuracy is improved. But by using more energetic propellants burning faster, the radiative signature is also increased. This can be countered to a certain degree by the usage of additives or a different motor design; nevertheless the radiative motor signature is directly related to motor performance and is of outstanding importance.

In cases, where dual stage propulsion is used, the intensity of radiation in the end phase of flight is reduced by a raise of booster mass at the expense of sustainer mass. A modern approach to minimise plume signature is to make the missiles ever faster - so called high velocity missiles - where the speed is increased from Mach 2,5 to Mach 5 and more. The tactical missile is accelerated very fast with the advantage of a short boost phase followed by a long ballistic flight phase after motor burn out. The advantage is a short, yet strong radiation emitting boost phase, with a missing sustainer plume, especially in the critical terminal phase where countermeasure deployment is performed. The approach for minimising overall plume signature is convincing. New problems, like high acceleration, explosion like boost phase, fast initial guidance arise due to changed missile performance.

To address signature problems it is necessary to have a thorough understanding of the mechanisms producing emissions in plumes. The classification of this emitted radiation into spectral regions, the operational role of the system which dictates spectral criteria, and the overall system design help in assessing comparative methods for rocket motor evaluation in terms of plume signature. From a designer's point of view the requirements are system dependent in practically every case and a simple grouping into two or three system based categories might be considered like

- small tactical missiles - short range (low altitude)
- large missiles - long range (low and high flying, booster phase and sustainer phase).

This "AGARD advisory report" can only give guidelines, general rules and basic recommendations for assessment methods such as:

(i) theoretical calculation techniques

(ii) measurement procedures

(iii) presentation of results

(iv) standards

(v) units used

(vi) limitation of measurements and computer codes

The achievable prognostic results of plume radiation depend a lot on available measuring techniques and devices and on the effort and level of understanding that goes into the computation of radiation phenomena. It is a continuous interplay between measured results, plume flow field parameters and radiation calculation models.

2. CHARACTERISATION OF ROCKET MOTOR PLUME RADIATION

2.1 General Description

The hot combustion products of a rocket propulsion system produce a highly turbulent exhaust plume as they expand through the nozzle into the surrounding atmosphere. These products consist of hot gases from the burning process, activated and deactivated molecules promoted by chemical reactions, accelerated particles of incompletely burnt fuel, soot, metal oxide condensates and other solid constituents. The plume is an extremely complicated chemical and thermodynamic entity whose properties very largely depend upon the type of propellant, motor and nozzle design, gas dynamics and flight conditions. This chapter is mainly concerned with radiation from this complicated source which is scattered, re absorbed and quenched during this emission process.

In a typical propulsion system, plume solid particles, the nozzle and other parts which operate at elevated temperatures fall into the thermal emitter category. Thermal emitters produce radiation which can be partially described by Planck's spectral distribution of emissive power. Considerable energy is produced in the infrared. The presence of this source of radiation is of importance in weapon systems where thermal seekers are used. Solid particles are evident in the far field plume region because they produce smoke but in this chapter we are concerned about the near field region, where several types of solid may be excited to emit radiation. Soot is one type of species that is excited to emit radiation. It exists predominately in rocket motors using carbon-hydrogen fuel with a C/H ratio of over 0.5. Metal oxides are formed from metallic additives such as Al, Mg, and Zr where concentrations between 5% and 20% are used in composite-double base propellants. Boroxides are sometimes produced in solid ramjets where Boron is a content of the fuel.

Further flame emission comes from molecular reactions which can be divided into the emission of rotational, vibrational and electronic spectra.

In these normally complicated processes there is rarely complete knowledge of the kinetics of the chemical reactions occurring within the plume. The character of radiation from these sources is not simply described by blackbody radiation and therefore more difficult to treat than that from solid bodies.

2.2 Phenomenology

Rocket exhaust plumes are characterised by turbulent mixing and afterburning in a flow initially dominated by strong wave processes. The under-expanded exhaust equilibrates to ambient pressure via a sequence of expansion and compression waves. Mixing and afterburning processes commence and develop in the shear layer formed between the exhaust plume and ambient external flow.

The overall plume flow field can be subdivided into the three regions as seen in Figure 1, namely:

- the predominantly nearfield inviscid plume where wave strengths are strong and turbulent mixing processes are generally confined to thin layers.

- a transitional region where the mixing layers engulf the entire plume and wave strengths diminish due to turbulent dissipation.

- the farfield fully viscous plume where wave processes have totally diminished and a constant pressure, turbulent mixing environment prevails.

Given this complicated flow field regime, it is a challenging task to understand and predict its radiation properties. The objectives are to define plume signature mechanisms, quantify their temporal, spatial and spectral characteristics for various types of propellant and altitude regimes and list their importance for selected missile flight tasks. To engage this problem one has to secure agreement on key definitions, on the recognition of crucial geophysical constraints and on the way the parameters are described. Such agreement would establish a common, uniform method of information gathering and would likely describe:

(i) the mechanisms that create or produce plume radiation.

(ii) the intensities of electromagnetic radiation produced over a given wavelength band, the spectral distribution of energy within that band and how measured or predicted values relate to the source of emissions

(iii) how these radiation properties are influenced by
   a) motor design (performance optimisation, propellant composition etc.)
   b) conditions independent of motor design e.g. flight regime, atmospheric extinction, plume background.

This type of characterisation forms a parametric study, it allows for an understanding of plume radiation phenomena and the formation of a radiation prediction technique for applications in support of missile detection, guidance and tracking. As rocket flight tests are extremely expensive and plume radiation measurements in flight are difficult to perform it is important to have accurate prediction codes.

In designing passive sensor systems, battle scene simulation codes are a vital aid. They must address all possible scenarios, a wide range of atmospheric conditions, variations in background structure, turbulence, short motor burn times etc. To distinguish a missile operating in such an inconstant environment its exhaust radiation must be characterised, emphasising unique spectral properties for positive identification.

Table 1: PLUME RADIATION MECHANISMS AND MAXIMUM EMISSION RATES

	Mechanism	Approximate Maximum Spectrum-Integrated Energy Supply Rates for an Exhaust With $\dot{W} = 350$ kgs^{-1}(*)		Spectral Region
1	Core Radiation	2.30×10^3	Watts	IR
2	Afterburning Radiation	1.97×10^3	Watts (h $\leq$ 50 km)	IR
3	Collisional Deceleration Radiation	11.8×10^3	Watts (h $\approx$ 0 km)	
		0	Watts (60 $\leq$ h $\leq$ 90 km)	IR/VIS/UV
4	Internal Shock Radiation	32.8×10^3	Watts (h $\geq$ 200 km)**	
5	Atmospheric Pumping Radiation	4×10^7	Watts/km (90 $\leq$ h $\leq$ 130 km)	IR
6	Atomic Oxygen Chemi luminescence			
7	High Altitude Molecular Association/Dissociation Radiation	3.6×10^3	Watts/km (h $\geq$ 130 km)	IR/VIS/UV
8	Airglow from Rocket Vehicle Friction	6.70×10^3	Watts (h $\sim$ 100 km)	IR/VIS/UV
9	Scattering of Chamber Radiation by Plume	6.73×10^3	Watts	IR
10	Solar Radiation Scattered by Solid Particles in Plume	2.2×10^4	Watts/km	VIS
11	Solar Radiation Scattered by Gaseous Species in Plume	0.39	Watts/km	VIS
12	Absorption of Solar UV by Plume Gases and Reemission in UV, VIS and IR	7.48×10^6	Watts/km	IR/VIS/UV
13	Plume-Reflected Earthshine	5.85×10^{-5}	Watts/km	IR

* The ascending rocket is assumed to follow a typical trajectory for near-earth orbit injection: h = altitude. Radiations given in watts/km refer to km of trail length with $V_v \sim$ 3 kms^{-1}.

** This value is for W = 350 kgs^{-1}. Usually at this altitude, a second or third stage is burning and the radiation should be scaled down by a factor of 350/50 = 7.

2.3 Origin of Plume Radiation

Emission spectra are governed by the excitation energy of atoms and molecules throughout the exhaust which, among others, is a function of local energy and thermodynamic conditions. Gas phase radiation species present in the plume are, in major part, determined by the propellant composition and the reaction of its combustion products with the ambient air. In most cases a line-by-line model has to be replaced by a band model to describe the radiation characteristics. Table 1 denotes a number of possible plume radiation mechanisms.

Plume radiation can originate from:

(i) chemical reactions in the burning process

- molecular and electronic excitations and transitions
- chemiluminescence, fluorescence

- exothermal, radiation producing reactions

(ii) thermal emission in the afterburning phase, plume/atmosphere mixing and shock heating in the afterburning region produced by liquid or solid particles.

From the foregoing radiation producing mechanisms we shall consider here in more detail only the chemistry of plumes, afterburning effects on plume radiation and particle radiation in the plume.

2.3.1 Chemistry of Plumes

The variety of emitting species in the complex flow system of a rocket exhaust is a result of the radiation kinetics of collision processes in the gas phase. Contributions to the radiation stem from evaporation and condensation processes, particle-

molecule reactions and reactive and inelastic collisions. A normal radiation producing chemical reaction (chemiluminescence)is written:

$$A + B \rightarrow C + D*$$

or e.g. $\quad CH + O_2 \rightarrow CO + OH*$
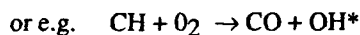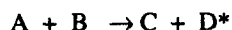
where one of the products of the exothermal reaction is in an excited state (*) which is deactivated by the emission of radiation. The wavelength of this emitted radiation depends on the available energy so that emitted line spectra in the infrared, although broadened by the known effects of collision and Doppler broadening, come from vibrational-rotational transitions, where UV and visible radiation between 100 nm and 800 nm have their origins in the more energetic electronic transition states. A listing, representing classes and examples of plume chemical reaction, is given in Table 2. Classes of reactive and inelastic collision processes are listed as well as their major effect on plume exited-state distribution. The first four reaction classes listed (A through D)

represent bulk chemical rate processes where the reactants and products are assumed to have internal state distributions consistent with "Local Thermodynamic Equilibrium" (LTE), and all the energy consumed or released by the reactions is reflected in the local kinetic temperature.

These four reaction classes, along with condensation, evaporation and heterogeneous reaction processes are sufficient to describe most chemical effects in low-altitude LTE exhaust plumes. If LTE is not guaranteed, the hypothesis involved in developing a radiation model is no longer valid, since the radiation is dependent upon the population of upper and lower states which are no longer related by a Boltzman distribution. Rather, the populations of the states must be calculated by codes that include finite rate kinetic processes along streamlines. This difficult type of calculation has been performed for the UV spectral range and yields values that range above those of the normal "Standard Plume Flowfield" (SPF) species calculations.

To a large extent, emission from molecular bands

Table 2: CLASSES AND EXAMPLES OF PLUME CHEMICAL REACTIONS

Reaction Class	Generalized Formula (ME Arbitrary Collision Partner)	Examples	Major Effect on Excited State Distribution
Reactions that release or Consume Heat			
A Exothermic Bimolecular Reactions	$A + B \rightarrow C + D + heat$	$OH + H_2 \rightarrow H_2O + H$ $CO + OH \rightarrow CO_2 + H$	Raises gas temperature
B Thermolecular Combinations	$A + B + M \rightarrow AB + M$	$H + H + M \rightarrow H_2 + M$ $OH + H + M \rightarrow H_2O + M$	Raises gas temperature
C Endothermic Bimolecular Reactions	$A + B + heat \rightarrow C + D$	$H_2O + O \rightarrow 2OH$ $CO_2 + O \rightarrow CO + O_2$	Lowers gas temperature
D Collisional Dissociations	$AB + M \rightarrow A + B + M$	$O_2 + M \rightarrow 2O + M$ $H_2O + M \rightarrow H + OH + M$	Lowers gas temperature
Reactions That Create, Destroy or Transmute Excited Internal States			
E Chemiluminescent Bimolecular Reactions	$A + B \rightarrow C^{*\dagger\lambda} + D$	$CH + O_2 \rightarrow OH^* + CO$ $C_2O + O \rightarrow CO^* + CO$	Directly creates excited internal state
F Chemiluminescent Combination Reactions	$A + B + (M) \rightarrow AB^{*\dagger\lambda} + (M)$	$CO + O + M \rightarrow CO_2^* + M$ $O + H + M \rightarrow OH^* + M$	Directly creates excited internal state
G Collisional Excitation	$A + B \rightarrow A^{*\dagger\lambda} + B$	$CO_2 + CO_2 \rightarrow CO_2^{\dagger} + CO_2$ $O + H_2O \rightarrow H_2O^{\lambda} + O$	Directly creates excited internal states
H Collisional Quenching	$A^{*\dagger\lambda} + B \rightarrow A + B$	$OH^* + M \rightarrow OH + M$ $CO^{\lambda} + M \rightarrow CO_2 + M$	Directly excited internal state to heat
I Reactive Quenching	$A^{*\dagger\lambda} + B \rightarrow C + D$	$OH^* + O \rightarrow O_2 + H$ $HCl^{\dagger} + O \rightarrow OH + Cl$	Destroys excited internal state
J Excitation Transfer	$A^{*\dagger\lambda} + B \begin{array}{l} \rightarrow A + B^* \\ \rightarrow C + D^* \end{array}$	$NO^* + O \rightarrow N_2 + O^*$ $H_2^{\dagger} + O \rightarrow OH^{\dagger} + H$	Transmutes excited internal state

* Excited electronic state
† Excited vibrational state
λ Excited rotational state

is concentrated in the infrared spectral region, with emitting molecules and band centres being documented in Table 3. When viewing plume radiation over long distances, atmospheric attenuation becomes important and detection is possible only in atmospheric "windows". Dominant IR-emission is that from CO, CO_2, and OH. If Boron is abundant emission from HBO_2 and B_2O_3 can be obtained. Visible radiation originates predominantly from Alkaline metals such as Na (0.585μm), K (0,72μm) or oxides like BO_2 and AlO. Due to chemiluminescence OH-intensities can be higher, as described by Planck's radiation laws. Examples of rate constants and spectra for CO + O chemiluminescent reactions are given in Figures 2a, 2b, 2c. The reader is also directed toward Reference 18. A listing of important electronic chemiluminescent reaction mechanisms is given in Table 4.

entrained air in the so called "Plume Mixing Layer" after leaving the nozzle (Fig. 4). A descriptive term for this secondary combustion is "afterburning". With energetic propellants this oxidation is very similar to the combustion that occurs in turbulent diffuse flames, except that it now occurs in a complex multi-phase expansion accompanied by strong shocks.

As in the case of ordinary combustion, afterburning is a free-radical chain reaction process requiring a moderate density of both oxidiser and fuel species to sustain the chain, a requirement that generally restricts this phenomena to low altitude LTE exhaust plumes. Afterburning can be suppressed at high missile velocities which tend to "blow off" the afterburning plume regions in much the same manner as the flames from a Bunsen burner can be extinguished by increasing the air/fuel flow rate above a critical value.

Table 3: Principal Plume Exhaust Gases Near-Infrared Emission Bands	
Molecule	Band Centres (microns)
CO_2	1.96, 2.01, 2.06, 2.69, 2.77, 4.26, 4.68, 4.78, 4.82, 5.17, 15.0
CO	4.66, 2.34, 1.57
HCl	3.45, 1.76, 1.20
H_2O	0.94, 1.1, 1.38, 1.87, 2.66, 2.73, 3.2, 6.27
NO_2	4.50, 6.17, 15.4
N_2O	2.87, 3.90, 4.06, 4.54, 7.28, 8.57, 16.98
OH	1.00, 1.03, 1.08, 1.14, 1.21, 1.29, 1.38, 1.43, 1.50, 1.58, 1.67, 1.76, 1.87, 1.99
SO_2	4.0, 4.34, 5.34, 7.35, 8.69

2.3.2 Afterburning Effects on Plume Radiation

For applications keyed to missile detection, guidance, etc., the overall plume structure and its radiation is of strong interest with attention generally focused on the far field solution.

For detection purposes in the terminal flight phase the plume geometry and dimensions are of great importance, because "side on" aspect angles change to a direct "head on" situation were the centre part of the plume is shaded by the missile body, as seen from the target (Fig.3).

For such applications, the near field solution serves to provide starting conditions for a farfield, constant pressure mixing/afterburning calculation (14). Both requirements and their interface present a challenge to mathematical modelling. The fuel rich products of combustion inherent in solid rocket motors, often combined with significant amounts of ignition residue, liner and inhibitor, mix and burn with the

The chief impact that afterburning chemistry has on plume radiation signatures comes from the increase in plume temperatures through heat release. Most rocket exhausts produce H_2 and CO as the main gas phase species that fuel afterburning reactions with O_2 from the surrounding atmosphere to produce H_2O and CO_2. The energy transfer in the afterburning region producing exited vibrational, rotational and electronic states is rather complex and we refer here to the extensive available literature.

Predictions of exhaust plume temperature profiles for a typical tactical missile with a highly energetic propellant is exhibited in Figure 5a, 5b. Particulates (16% aluminium in the propellant) were equilibrated with the gas phase in performing these calculations. The afterburning is quite rapid at sea level, with significant quantities of unburned CO and H_2 in the exhaust being depleted within 100 radii of the nozzle exit. Non equilibrium gas/particle calculations for this system would exhibit substantial difference in the flow structure due to the high particle loading.

TABLE 4

EXHAUST PLUME ELECTRONIC CHEMILUMINESCENT REACTION MECHANISMS

Emitting Species	Emitting State	CM^{-1}	$\lambda(\mu m)$	Possible Pumping Reaction
CO	$A'\Pi$	65074.8	0.154	$C_2O + O \rightarrow CO^* + CO$
	$d\,^3\Delta$	61120.1	0.164	
	$e\,^3\Sigma^-$	90973	0.110	$CH\,(^4\Sigma^-) + O \rightarrow CO^* + H$
	$a'^3\Sigma^+$	55901	0.179	
	$a\,^3\pi$	48687	0.205	$CH\,(X^2\Pi) + O \rightarrow CO^* + H$
OH	$A^2\Sigma^*$	32684.1	0.306	$H + OH + OH \rightarrow OH(A) + H_2O$ $CH + O_2 \rightarrow OH(A) + CO$ $OH + N_2(A) \rightarrow OH(A) + N_2$
CH	$C^2\Sigma^+$	31828	0.314	$C_2(^1\Sigma^+,\,^3\Pi_U) + OH \rightarrow CH^* + CO$
	$B^2\Sigma^-$	25949	0.385	
	$A^2\Delta$	23150	0.432	
C_2	$d^3\Pi$	20022.5	0.499	$C_3 + O_2 \begin{array}{l}\rightarrow C^* - CO_2 \\ \rightarrow C_2^* + CO + O\end{array}$
N_2	$(A^3\Sigma^+,\,\text{Metastable})$	50206	0.199	$N_2H_2 + O \rightarrow N_2^* + H_2O$
NH	$A^3\Pi$	29772.5	0.336	$N_2^* (A) + NH \rightarrow NH^* + N_2$
NH_2	$^2A_1$			Unknown
NO.	$A^2\Sigma$	43965.7	0.227	$N_2^* (A) + N \rightarrow NO^* + N_2$
Na	$2p$	16973 or 56	0.589	$N_2^* (A) + Na \rightarrow Na^* + N_2$ $NaO + O \rightarrow Na^* + O_2$
CO_2	continuum $(^1B_2)$		0.28-0.45	$CO + O + M \rightarrow CO_2^* + M$
O_2	$A^3\Sigma^+,\,B\,^3\Sigma^-$	36096 49802	0.277 0.201	$O + O + M \rightarrow O_2^* + M$
NO_2	continuum $(^2B_1,\,^2B_2)$		0.48-0.8	$O + NO + M \rightarrow NO_2^* + M$

In flight, as missile altitude increases, the afterburning rate decreases due to a reduction in ambient pressure. Above 10-15 km and/or for "cooler" double-base propellant systems (i.e., those with exhaust temperatures less than 1000K), the onset of afterburning is partially controlled by the conditions in the missile base region. The role of the base region as a flame holder has been noted during a number of studies and combustion that occurs at the base can induce afterburning in the downstream plume shear layer which would not otherwise be present. This is caused by higher initial temperatures in the plume shear layer and an increase in free radical concentrations.

2.3.3 Particle Radiation in the Plume

In general, particulate matter in the plume may influence the plume radiation signature in at least five ways:

(i) by thermally interacting with plume gases

temperature, and concentration (Figures 6 and 7). For certain applications, such as scattering from laser beams it is also necessary to know the particle shape. Temperature is, in general, dependent upon particle size (i.e. thermal lag), especially for small motors and high altitude plumes. In addition to the preceding flow field particle parameters, the plume signature also depends upon certain optical parameters, specifically the variation of emissivity with particle size, temperature, and wavelength. The variation of emissivity with size can be computed using Mie theory, it provides the scattering and emitting properties of a spherical particle of known size and refractive index. The assumption of spherical shape is probably acceptable for emission, but it can lead to serious errors in certain scattering properties if the particles are actually non-spherical.

For plume calculations such information about particle properties is not generally available other than that for the more common materials of carbon and Al_2O_3. Values for the absorption coefficient of

Table 5: Radiation Mechanisms/Wavelength Regions		
Propellant Type	Radiation Mechanism	Wavelength Region
Aluminised Solid Composites	Al_2O_3 Particle Thermoluminescence	Mid UV-Near UV
	$OH, CO + O$ Chemiluminescence	Near UV
	Al_2O_3, Na D Line Thermoluminescence	Visible
	Al_2O_3, H_2O, CO_2, CO Thermoluminescence	IR
	Al_2O_3, H_2O, CO_2 Thermoluminescence	Far IR

(ii) by chemically reacting with plume gases

(iii) by catalysing physical or chemical changes in plume gases

(iv) by emitting thermal radiation as a result of heating in the rocket combustion chamber or plume afterburning regions

(v) by scattering radiation, such as sunshine, earthshine or combustor radiation (searchlight effect)

It should be noted that measurements of plume radiation in the IR can be influenced by the hot nozzle exit which also emits in the IR.

The presence of hot particles in the exhaust plume generally leads to significant levels of radiation throughout the ultraviolet, visible, and infrared spectral regions. There are also other important particle effects such as the scattering of sunlight and the scattering of emissions from the combustion chamber and other hot parts of the motor. The important particle parameters affecting plume signature are their size distribution,

Aluminium Oxide (leucosapphire) can be three or more orders of magnitude underestimated as experiments with particles in flames have shown. Absorption coefficients and indices of refraction for temperatures up to 2950K are given in Reference 16.

Size of motor and, as indicated in Table 5, propellant formulation are two important factors in the computation of radiation from particles within a plume. The optical depth is the relevant non-dimensional parameter for determining the nature of the radiation transport and is the path integration (absorption + extinction) coefficient, or equivalently the ratio of path length to photon mean free path. If the motor is small and particles are present in small concentrations only as a stabiliser, the situation is one of low optical depth and the particle continuum radiation and gas band radiation may simply be added together linearly. At higher optical depths the two contributions must be combined in a non-linear fashion. For "black" particles such as carbon, this is easy since the effects of scattering can be neglected. In such cases the plume signatures can be calculated using a simple, one-dimensional line of sight integration as used for gaseous emission. when scattering becomes important

the signature calculation is considerably more difficult and must recognise the three-dimensional nature of the radiative transport process.

Common among important particle species in tactical missile plumes are carbon and metal oxides such as Al_2O_3, MgO, ZrO_2 and ZrC. The optical properties of these condensed species are considerably more complex than those of gaseous species such as H_2O and CO_2. Carbon usually occurs as a product of incomplete combustion and it is generally not possible to calculate the soot concentration in a plume a priori. Soot particle sizes tend to be strongly sub micron and under certain conditions there is evidence of agglomeration, the building of smaller particles into longer chains. Carbon is a strong emitter over the entire ultraviolet, visible and infrared region. The optical properties are somewhat variable and depend, among other things, upon the hydrogen content. Al_2O_3 occurs either as a product of aluminised propellant combustion or as a stabiliser where it is added directly to the propellant in small quantities to suppress acoustic oscillations in the motor chamber. The efficiency per gram of a stabiliser material is maximum for particles of micron size without absorbing energy, whereas larger particles have lower surface area per unit mass. Typical radiation mechanisms related to propellants and wavelength region are given in Table 5.

Like the other metal oxides, Al_2O_3 is a large band gap semiconductor in the solid phase. The emissivity is high in the ultraviolet and far infrared but lower in the visible and mid-infrared (transparent regime). To a large extent emissivity in this regime depends upon the semiconductor contamination level. Al_2O_3 is generally liquid in the motor chamber and solidifies in the nozzle and external plume. There have been many attempts to model the formation of Al_2O_3 particles, but progress has been limited by lack of reliable size distribution measurements.

2.4 Classification of Rocket Motor Plume Signatures on Spectral Regions of Emitted Radiation

The design engineer must be aware of the spectral range of plume radiation whether it is his task to provide effective missile detection systems or, in the case of rocket motor design, a stealthy propulsion unit. Equally, he must recognise the spectral discrimination of atmospheric propagation and, in particular, that of the regime under which a given missile operates. Spectral information is important for design purposes since the required techniques for different parts of the electromagnetic spectrum can vary significantly. For instance, it is understood that ultraviolet emission can be dominated by minor constituents of the plume, whereas the infrared signature is generally dominated by the plume species of highest concentration. Theoretical models employ a range of application codes to cover the electromagnetic spectrum.

With a wide available choice of propellants, igniters and materials used for, or in contact with the combustion process it is important to remember that one spectral feature may uniquely identify a missile.

It is possible to classify plume radiation signatures by dividing plume emissions into four principal wavelength regions.

- Ultraviolet: 100 - 400 nm

- Visible: 400 - 700 nm

- Infrared: 700 nm - 14μm

- Microwave: 2 - 300 GHz

The ease with which detection can be achieved within each region will determine its operational importance. Many factors govern the choice such as missile flight, altitude and attitude, type of propellant and motor, ways of sensing, and interactions with local environment and atmospheric propagation.

Until recently the IR-region was the most studied sub-region in plume radiation investigations. Infrared handbooks allow public access to all important facts in this spectral band, be it atmospheric propagation, reflectivities and material properties or even IR sensor technology. Because of problematic background behaviour in the infrared newly developed sensing devices in the UV-region are gaining in importance. Table 6 defines the IR, visible and UV wavelength regions of interest.

2.4.1 Ultraviolet-Radiation

The Ultraviolet (UV) region can be further divided into the vacuum UV (VUV) (0.1μm to 0.2μm), the mid UV (0.2μm to 0.3μm), and the near UV (0.3μm to 0.4μm). At VUV wavelengths atmospheric attenuation limits transmission to extremely short ranges. Test cell measurements can be made by operating in a vacuum and viewing through appropriate window materials. For tactical missiles this region is of no practical interest.

In the mid UV, or "solar blind" region, atmospheric attenuation confines measurements, but the availability of extremely sensitive detectors and the absence of natural radiation sources in this region make the mid UV an attractive region for the detection of

Table 6: Definition of Wavelength Regions of Interest

$\lambda = 100$ nm			$\nu = 3 \cdot 10^{15}$ Hz	$\sigma = 10^4$ mm^{-1}	$Q = 12,4$ eV
Optical Radiation	**UV** / Ultraviolet. Radiation	UV-C	VUV Vacuum-UV / FUV FAR-UV	$\lambda = 200$ nm	$Q = 6,2$ eV
			$\lambda = 280$ nm	$\sigma = 3,6 \cdot 10^3$ mm^{-1}	$Q = 4,4$ eV
		UV-B	MID-UV		
			$\lambda = 315$ nm	$\sigma = 3,2 \cdot 10^3$ mm^{-1}	$Q = 3,9$ eV
		UV-A			

$\lambda = 380$ nm	$\nu = 7,9 \cdot 10^{14}$ Hz	$\sigma = 2,6 \cdot 10^3$ mm^{-1}	$Q = 3,3$ eV

VIS / Visible Radiation:

violet	
	424 nm
blue	
	486 nm
bluegreen	
	517 nm
green	
	527 nm
yellowgreen	
	575 nm
yellow	
	585 nm
orange	
	647 nm
red	

Legend:

$\nu \quad = c/\lambda$ frequency
$\sigma \quad = 1/\lambda$ Wavenumber
$Q \quad = h \cdot \nu$ Photon energie
(h = Planck's; constant
$1 \text{ eV} = 1,602 \cdot 10^{-19}$ Joule)

$\lambda = 780$ nm	$\nu = 3,85 \cdot 10^{14}$ Hz	$\sigma = 1,3 \cdot 10^3$ mm^{-1}	$Q = 1,6$ eV

IR / Infrared Radiation	IR-A	NIR NEAR IR		
	$\lambda = 1,4$ μm		$\sigma = 700$ mm^{-1}	$Q = 0,9$ eV
	IR-B			
	$\lambda = 3,0$ μm		$\sigma = 330$ mm^{-1}	$Q = 0,4$ eV
	IR-C	MIR MID IR / FIR FAR IR	$\lambda = 50$ μm	$\sigma = 20$ mm^{-1}

$\lambda = 1$ mm	$\nu = 3 \cdot 10^{11}$ Hz	$\sigma = 1$ mm^{-1}	$Q = 10^{-3}$ eV

detection of tactical missile plumes. In the near UV atmospheric transmission permits measurements over long ranges, but solar scatter is prominent.

2.4.2 Visible Radiation

Visible radiation is easily detectable by the human eye. Its atmospheric propagation is constrained by water clouds. Very advanced detector technology is available using a range of silicon devices as well as high gain photo multiplier tubes. Principal interests are in the strong sodium (Na) and potassium (K) line emissions (Fig. 8 for Na). The emissivity is strong enough to detect impurities at levels of a few parts per million.

Because of the dominating background clutter from the sun and artificial light sources causing high false alarm rates, the visible spectral band has hardly been employed for automated plume sensing devices.

2.4.3 Infrared Radiation

The IR region is subdivided into the near IR (0.7µm to 2.5µm), the mid IR (2.5µm to 5µm), the far IR (5µm to 14µm), and the extreme IR (14µm to microwave). These regions have atmospheric transmission windows, with significant, naturally occurring background radiation sources (Fig.9).

2.5 Plume Flowfield and Motor Design

The potential use of plume electromagnetic radiation to uniquely describe a missile for whatever purpose requires detailed knowledge of the exhaust flow field properties that generate the chemo-physical emission mechanisms. Development of the flow field is governed initially by conditions inside the combustion chamber starting with the propellant, its formulation and the conditions under which it burns, the acceleration of gases through the nozzle throat and their controlled expansion to meet ambient conditions external to the motor at the nozzle exit. Fuel rich gases exiting the nozzle mix with oxygen from the surrounding air to promote secondary combustion (afterburning) creating an exhaust flow field which is a fiercely burning, highly turbulent gas jet.

From the foregoing it is clear that plume radiation signatures for a given motor can vary widely depending upon the conditions under which measurements are performed, ranging from those of static firings to those of flight tests. Comparison and assessment of missile plume radiation signatures should be made utilising information from a variety of sources, using motor properties, flow field parameters and experimental test results. A listing to indicate the relevant data required would read:

Motor properties promoting the flow field

- Propellant formulation including trace elements which might create non equilibrium phenomena producing highly excited states
- Thrust and mass flow
- Nozzle geometry and exit Mach number
- Presence of flame suppressants
- If a liquid engine, then fuel and oxidant composition and fuel ratio (F/O)

Table 7: Rocket Engine Exit Plane Flowfield Parameter/Chemical Composition

Flowfield Parameters		Chemical Composition (Mole fraction, X_i)	
M	2.2	CO	.164
PS	36.67 kN m^{-2}	CO_2	.2096
V	2036 ms^{-1}	H	.0416
T	2199 K	HO_2	.0000712
MW	26.14 lbm/lbm mole	H_2	.0324
Γ	1.23	H_2O	.2843
		O	.0458
		OH	.0514
		O_2	.1704

An example of a one dimensional kinetic analysis is shown in Table 7 and a calculation of plume radiance using the parameters of Table 7 is given in Figure 10.

Static firing radiation measurements

- Radiometric and spectroscopic measurements
- Motor parameters
- Viewing geometry and range
- Atmospheric conditions

Flight radiation measurements

- Radiometric and spectroscopic measurements
- Time history of flight to relate to measurements
- Atmospheric conditions
- Time history of flight must recognise the missile altitude, velocity, roll rate, attitude, range and geometric relationship between the plume and measuring instrument for any instant during flight

Influences of environment

- Flight trajectory
- Altitude regime
- Constituents of surrounding air and mixing

The detailed plume shock structure of a rocket motor operating at simulated flight velocity of Mach 2 is shown in Figure 11. It is based on photographs and pressure measurements. The motor exhaust flow expands to an altitude static pressure and intersects with the supersonic free-stream airflow. The exhaust gases mix with the gases in the base recirculation zone which, in turn, mix with the free-stream airflow. The flow downstream of each Mach disk (normal shock wave) is subsonic and is reaccelerated to supersonic flow at the sonic line.

3. ASSESSMENT METHODS OF PLUME RADIATION-DETAILED DESCRIPTION

There are no generally accepted standards or methods in use to assess the radiation properties of rocked motor exhausts. If the radiation producing mechanisms are known to a certain degree of confidence then other aspects to be taken into account are:

(i) the opacity or optical depth of the plume with respect to its own emissions to determine the radiation exiting the plume. This will depend on the size and concentrations of particles within the plume and the existence of any quenching molecules.

(ii) the opacity of the plume's immediate environment to the radiation released from the plume which would, for example, include smoke or any other form of local obscuration in the line-of-sight to the observer.

(iii) the complex and multiparametric problems of solar illumination, background radiation and atmospheric transmission where "windows" exist subject to various loss mechanisms such as Rayleigh and Mie scattering, molecular absorption and aerosol attenuation. Fig. 12 shows atmospheric transmission windows.

3.1 Experimental Methods

The majority of experimental methods used to assess plume radiation employ one or more of three types of instruments

- Radiometric devices which measure radiation intensity in a specific, broad band spectral region.

- spectrometric devices which measure the radiated plume intensity as a function of wavelength

- imaging devices which record intensities and radiating plume geometries on a time scale given by the camera type

It is important to note that spectral measurements permit statements to be made about the chemical composition of a plume leading to the possibility of positive missile identification.

3.1.1 Radiation Essentials

As measurements depend to a large extent on "state of the art" instrumentation we shall avoid detailed descriptions of equipment. An outline of how to proceed is given in Figures 13 to 15. Figure 13 is essentially a diagram of the radiative heat transfer equation, in Figure 13 detectors and artificial light sources over a broad spectral range are given. In Figure 15 a calibration procedure for a camera/radiometer is presented in a general graphical form.

3.1.2 Test Techniques

Backed by technical and financial feasibility, rocket motor plume radiation characteristics may be determined using a variety of techniques selected to focus upon the parameter of interest with the desired accuracy for the characterisation.

Plume characterisation may be performed by computations, measurements during static, sea-level tests, simulation chamber tests, or flight tests. In principle, the flight test is superior in that it provides a real environment but the cost and measurement difficulties make it generally prohibitive. Testing under simulated conditions and simple static testing follow in order of reduced expense and complexity. The alternative, that of computer based theoretical modelling, is attractive but demands of confidence and usually make validation by test firings necessary.

3.1.2.1 Static Testing

Open site, ground level, static testing of a solid propellant rocket provides access to the plume by radiometric instrumentation. It is the cheapest and easiest test to conduct. In terms of utility it is the least desirable since the rocket motor does not experience the conditions found in flight, consequently the static plume does not have burning characteristics identical to those in flight. Plume spectral and spatial radiation properties may be measured and used to validate predictive codes for the static condition. Atmospheric interference can affect measurements in this type of test, particularly over long ranges. It is necessary to adequately determine attendant atmospheric conditions to calculate signal losses.

During a static test general motor performance is monitored. Dimensions, propellant formulations, and the like are predetermined but performance parameters such as thrust, chamber pressure, temperature, and body deformation can be measured.

Instrumentation deployment is relatively straightforward with fields of view and ranges stationary and easily determined. Limitations only exist where constraints produced by the test stand and terrain are encountered.

3.1.2.2 Altitude Chambers

Large vacuum chambers exist capable of testing full-scale models and subsystems up to simulated altitudes of 30 km. Near field data (nominally one exit diameter) can be acquired which are useful for start

conditions to code predictions. An example is given in Figure 16.

3.1.2.3 Simulated Flight Facilities

Testing a solid rocket motor under simulated flight conditions provides a more realistic plume than a static firing but often has restricted access to the plume by radiometric instrumentation. Flight simulation is more expensive than the static test although it is far easier and cheaper to conduct than a flight trial. In terms of utility it allows some parameter changes but still may not produce the true characteristics of the flight plume, especially when scaled models are used. Parameters considered for measurement in static tests apply equally to flight simulation and are increased in number by those introduced by simulation. (Fig. 17)

Test cells are available which can simulate flight conditions from sea level to altitudes of some 25 km and from subsonic velocity to over M3.0. The capability exists for full operational speed manoeuvres. Facilities are flexible enough to accommodate the complete propulsion system and during simulated flight tests, conditioned air flows past a stationary model and flight characteristics are measured. The airflow can be distorted to simulate conditions found in actual flight manoeuvres.

The major advantage of testing tactical missiles under controlled simulated flight conditions is the ability to conduct extensive plume flow field and radiometric measurements of a given phenomenon to acquire data to validate flow field and radiative predictive codes. The major disadvantage is the inability to acquire fare field data and perhaps that flight condition which identifies the onset or termination of afterburning.

3.1.2.4 Flight Tests

Flight tests offer true realism but they are expensive and present extreme experimental difficulties. Observations (measurements) may be from fixed or mobile sites. Instrumentation may be ground based with either fixed or tracking mounts, it may be mounted on mobile carriers (such as a tracking aircraft or missile), or it may be mounted on the vehicle. Generally, limited instrumentation is available from observation platforms to assist in the full characterisation of the plume signature.

As with static measurements these tests suffer atmospheric effects which confuse measured quantities, consequently, a need exists to adequately monitor atmospheric conditions. Normally,

atmospheric temperature, pressure, humidity, visibility, composition and wind conditions are determined.

Trajectory and range are also of great importance both from the point of determining atmospheric effects as well as basic interpretation of results and must be adequately addressed.

3.2 Calculation Methods

Any attempt to model plume radiation from rocket motors must rely upon the construction of a theoretical plume in which flow field properties are structured so as to interface with radiation application codes. Many such codes are split into:

(i) a thermodynamic part (with input parameters such as propellant composition, pressure, temperature, expansion ratio etc.),

(ii) a flow field part (with input parameters such as nozzle exit plane data, relevant motor design features, relevant chemical reactions with non-equilibrium chemistry solutions, turbulence model, atmospheric data, altitude and velocity, etc.),

(iii) a radiation part (with input parameters like input from flow field structure, emitting chemical species, molecular band model, gaseous and particle radiation, scattering, quenching, geometry, aspect angle.

3.2.1 Plume Fluid Dynamics of Tactical Missiles

Calculation methods [14] [15] for plume fluid dynamics have been established in various countries like the USA, Great Britain and France. They all have a similar approach to solving problems. Most of the advanced codes are classified. Here, as an example, we describe in more detail the American Standard Plume Flowfield (SPF) model. Further codes for the prediction of ultra-violet plume signatures exist by the names of SPURC and PRUV (21). In Great Britain the code being used is called REP (Rocked Exhaust Plume). French codes exists, like EMIR and AJAX, Canadian ones by the names IPHASE and FREEJET.

A starting point for surveying the status of plume flow field models prior to the year 1964 is Chapter 2 of the Rocket Exhaust Plume Technology Handbook prepared for JANNAF (Joint Army, Navy, NASA and Air Force agencies). At this time, the "standardised" US plume model was the Low Altitude Parabolic Plume LAPP code developed at the AeroChem Corporation. The LAPP code is a balanced pressure farfield plume model that contains a generalised, fully implicit, chemical kinetics package. Its use is restricted to engineering studies geared to predicting plume "observables", and simplistic procedures are used to "globally" represent the influence of the nearfield structure. During the Period 1975-1976, an advanced plume model was developed at General Applied Science Laboratories (GASL) which solved the viscous/inviscid nearfield structure in detail using boundary layer type coupling concepts, and contained

Table 8: Block Schematic Modular Structure of JANNAF SPF

		Executive Driver		
Inviscid/ Shock	Viscous/ Mixing	Overlaid Viscous/ Inviscid	Fully Coupled Viscous/ Inviscid	Principal Modules
	Chemistry		Gas/particle Interaction	Auxiliary Integration Modules
	Mach Disc	External Flow	Turbulence	Speciality Modules
		Data Bank		Data Module
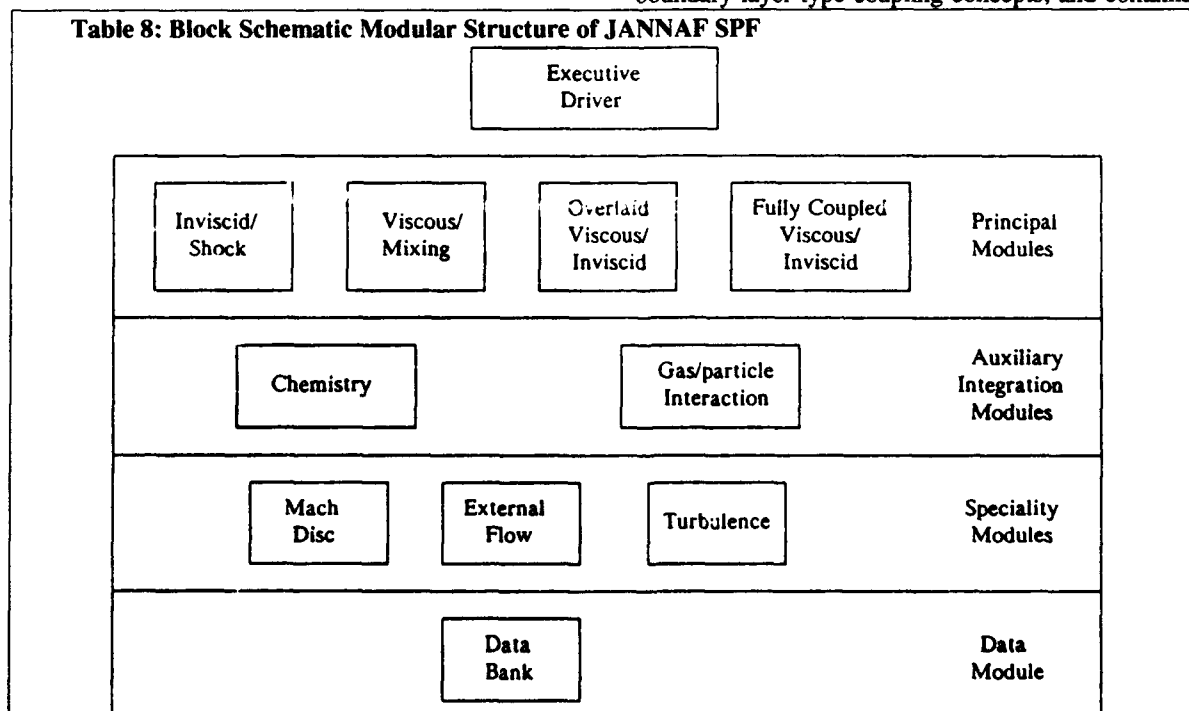
a two-equation, compressibility corrected turbulence model.

Development of plume flow field models is an evolutionary process to include additional physical phenomena and more efficient numerics. Physical processes are added as they are better understood and as dictated to improve the accuracy of the prediction model. Numerics also changed to decrease computer run time when feasible.

A JANNAF program was initiated in 1978 to combine the features of the GASL and LAPP codes which is now know as JANNAF "Standardised Plume Flowfield" (SPF) model. The current version is SPF III. It is the primary tool in the US to analyse tactical missile exhaust plumes. The modular structure and computational techniques used in the basic SPF are given in the following block schematic (See Table 8).

3.2.2 Validation of Plume Radiation Calculations by Experiment

Validation exists for the infrared and visible regions, in many instances with sensible agreement taking into account the limitations of measurement conditions like altitude, range of motor size or simplified propellant constituents. In certain circumstances not enough parameters can be incorporated into the calculation methods to yield global emission characteristics.

The infrared region 1.5μm to 3μm is mainly concerned with water bands, these are strong emitters but radiation suffers from heavy absorption through the atmosphere and detection ranges are short, consequently little interest is shown in this waveband.

Much interest has focused on "CO_2 blue spike" radiation a common feature in rocket exhausts. It occurs in the very narrow spectral band of 4.17μm, has good atmospheric transmission properties and lends itself to easy selection because of its narrow profile. Background and other spectral interference can be minimised by the use of narrow band optical filters. Line-by-line methods for modelling the blue spike have produced absolute spectral radiant intensities that agree to within about 20% of measured values.

Emissions in the 4.2μm to 5μm region come largely from CO_2 symmetric stretch vibrations with contributions from CO and some N_2O. They form what is termed the "red wing". Because a great number of individual rotational lines contribute to the radiation, the theoretical concept is to divide the spectral base into a number of bands each overlaying a number of rational lines. Each molecule in each band

is given parameters describing effective strength and shape and these quantities go to form the emission spectrum. As might be expected, this calculation method is known as a "band model" and can equally be applied to the 1.5μm to 3μm spectral region.

Band model predictions have been compared with experiments made over a wide range of circumstances resulting in a mixture of agreement. It has been argued that the uncertainty in absolute spectral radiant intensity given by predictions is typically a factor of 2 although this varies up or down with the complexity of modelling circumstances.

Propellant metal impurities such as sodium and potassium, catalyst metals, ballistic modifiers and others form a source of atoms from which visible radiation id emitted. Line emissions from the first resonance doublet of sodium and potassium atoms are prominent in afterburning rocket exhausts. For these and other line emissions a line-by-line prediction model is adopted for the calculation of spectral radiant intensities. Lorentz and Doppler broadening occurs and a Voight profile is commonly used to describe line shapes. Although good agreement is sometimes achieved, it is considered that uncertainties in the plume flow field structure and the radiation model, particularly collision broadening parameters, can justify no better uncertainty factor than 3 in absolute radiant intensity.

Theoretical plume flow field models have not been directly validated due to the difficulties in measuring the relevant plume properties, i.e. spatial distributions of temperature, pressure and concentrations of chemical species etc. Laser diagnostic techniques are showing promise in this field of work, particularly since the laser beam does not disturb the medium under investigation. Some examples of validation of theory by experiment are given in Figures 3 and 18.

3.2.3 Limitations of Computer Codes

Limiting factors are:

(i) lack of optical property data to adequately describe particles and radiating gases

(ii) lack of codes to handle base flow and an inadequacy showing the uncertainties of turbulent chemical interaction models

(iii) cessation of afterburning especially at high altitudes

(iv) incomplete treatment of particle multiple scattering

(v) the use of simplified assumptions such a steady state conditions only, simple geometries, no compression zones with perpendicular collisions.

3.3 Discussion of Plume Influencing Aspects

Afterburning is a major plume effect. The nozzle area ration is an important factor in the prevention of afterburning especially when considering radiation in the UV spectral region. Base flow recirculation affects afterburning, in many instances anchoring the flame to the base region. Contributions to plume radiation are strongly affected by propellant formulation, high metallic content produces a high continuum radiation in addition to gaseous emissions. Particle optical properties are very important, especially in areas where there are no molecular spectra. They also influence scattering losses and the "searchlight effect".

Fee-free electron emission (Bremsstrahlung) is probably the dominant mechanism for millimetric emissions.

Flame suppression in the exhaust brings about a marked reduction in infrared emission, for instance, it has been found to reduce the "red wing" (4.4μm to 5.0μm) by more than an order of magnitude.

Conditions favouring flame suppression are:

(i) Low exit plane temperatures

(ii) Low concentrations of plume particulates

(iii) Nozzle imperfections (any step or burr increasing turbulence)

(iv) Choice of propellant and suppressants

Plume suppression can be assisted by the introduction of additives into certain propellants to accelerate removal of flame radicals H and OH. Examples of the effect of plume suppression are given for a double base propellant in Figures 19 and 20 where the main sources of IR radiation are molecular band radiation such as CO_2 and H_2.

4. RECOMMENDATIONS

4.1 General

Knowledge of rocket plume radiation properties is important in the context of guidance, tracking and detection. It is expensive and often difficult to measure these radiation properties and to determine their dependence on operational parameters like missile forward velocity, range, altitude and aspect angle. It is even more difficult to acquire this information about rocket motors of an adversary. To ensure guidance system integrity, to avoid interference with friendly opportunities, the rocket plume and its properties must be regarded as an integral part of the missile system and, where possible, "tailored" to meet operational needs.

The following recommendations comprise a procedure for assessing rocket plume radiation that will enable uniform application of technology to:

(i) set quantitative technical requirements on rocket motor signature

(ii) compare rocket motors

(iii) recommend a terminology related to plume radiation based on quantitative criteria.

4.2 Recommended Test - Prediction Procedure

In trying to propose a standardised test technique for the assessment of plume radiation properties a general outline is given here. Its feasibility depends to a large extent on the availability of necessary measuring devices and instrumentation, rocket motors and prediction codes. The logic behind the assessment process is as follows:

(i) Define the objective(s) and requirements.

(ii) Define the needed data base and the experimental approach to ensure that objectives are accomplished.

(iii) Set up and calibrate equipment.

(iv) Run most appropriate test to acquire data base.

(v) Run necessary(available plume and radiation codes to match acquired data base.

(vi) Use measured results for theoretical model validation.

(vii) Use validates plume and radiation codes to predict plume properties at conditions appropriate to the defined objective.

(viii) Present results, stating all assumptions and code modifications and using standard terminology and units.

The following eight steps enlarge on these concepts:

Step 1:

Clear definition of objective and the requirements to meet those objectives may be the most difficult part of a program to conduct successfully. The objectives might read:

• detect, identify, track and destroy a target

• detect, identify a missile threat and counter with evasive action

• assess the feasibility of guidance and tracking methods

• develop a threat countermeasure

• acquire phenomenology data for code validation

• influence motor design with signature control proposal

At this stage it is important to define the system and the spectral regions in which it is to function. If, for instance, a detection system is called for, then specific details of sensor wavelength, bandwidth, resolution, limiting noise level and environmental details that affect signal transmission and distortion must be considered. There should be no compromise at this step, it is the least expensive to perform and study topics overlooked at this point may remain overlooked to the detriment of the system or be costly to be introduced later in the program. It is better and more cost effective to include tasks of potential value in the definition stage even if, for whatever reason, they subsequently become redundant.

Step 2:

Defining the information needed for a project data base and the measurements required to obtain that information usually calls for a compromise dictated by available funding. Within financial constraints the objectives in Step 1 are assessed and the requirements and limits set. One obvious compromise is in the choice between flight tests and those undertaken in dedicated ground facilities where it is possible to use scaled, heavyweight test motors with reusable hardware. Use of the wind tunnel, altitude chamber or static test site combined with standard measuring instrumentation will often satisfy most, if not all, of the data base requirements.

Rocket motor experiments involve many technical staff and it is vital that test procedures are thoroughly documented and the staff cognisant of the data gathering process. The prospect of meeting an objective is advanced by the prudent use of theoretical predictions and experiment. Theoretical studies may play a part in planning the course of an experimental program. Before embarking on such a program several questions are posed, not least among them is whether an experiment can be mounted that will directly or indirectly provide the data to satisfy the objective. The answer will depend upon the existence of test vehicles, test facilities and the correct diagnostic instrumentation. Test vehicles are generally available for ground or flight tests. However, should the missile of an adversary be under investigation then the supply of a test vehicle is improbable. In such a case calculations are made using whatever data is available and rare experimental firings would only be those to study the phenomena for prediction validation purposes. The choice of test facility, whether it be static, sea-level, an altitude chamber or wind tunnel depends upon the simulation desired.

The selection of diagnostic instrumentation is governed by the radiation properties to be measured, focusing on spectral wavelength range, radiance level, spectral, spatial and temporal resolution and sensor sensitivity and speed. Flow charts are presented as guidelines in Figures 21 to 23. Types of optical detectors are shown in Figure 21. Radiometric measurements are presented in Figure 22 followed by a typical radiometric measurement system in Figure 23. To avoid later problems it is important to ensure that the instrumentation selected is well able to meet all the measurement demands and that it is backed by a full data analysis capability.

Step 3:

The importance of accurate calibration, as indicated by Figure 24, cannot be overemphasised. Measurements can be complicated or invalidated by atmospheric absorption or extinction, obscuration by smoke, impractical or impossible sensor positioning and carelessness in ignoring background signature effects. It is a valuable exercise to rehearse the entire test procedure to identify and eliminate any interference between instruments or power circuits that might cause a later test failure.

Step 4:

The way in which the experiments is conducted (Section 3.1) is a critical factor in the acquisition of good data. Details of motor performance, its environmental test conditions such as Mach number, altitude and trajectory; the deployment of instrumentation giving aspect angles, atmospheric transmission path, fields of view and the like, all contribute essential information for analysis and project assessment. Radiometric requirement were discussed in Section 3.1.1. Where similar instruments are used they should show a consistency of measurement and all instruments should have a specified accuracy. Error limits should be assigned to all data sets recorded and assumptions, where made, documented. If the preceding steps have been properly observed the measurement programs should be successful. To mitigate the effects of any equipment failure during a test firing it may be possible to duplicate some essential measurements. Instruments should be sited to guard against acoustic and ground-borne vibration, equally they should be protected from the possibility of rocket motor failure.

Step 5:

The purpose of this step is to formulate techniques for calculating plume radiation signatures against test data obtained from the foregoing steps. To compare calculated levels of plume radiation which measured test results, the parameters pertaining to the test conditions must be used as input data for calculations. The measure of agreement coming from these comparisons will determine the confidence placed on the calculations for use, where measurements are not possible.

A plume flow field should be calculated for the conditions under which the actual test took place, observing the precise propellant composition with trace metal impurities and motor design features affecting gas flow. Radiation codes should reflect sensor wavelengths together with their deployment position and plume viewing aspect angles, the spatial and temporal nature of the radiation and the atmospheric signal attenuation. If measurements are made in a wind tunnel or on a missile plume in flight, the appropriate free-stream flow conditions must be known.

Prediction of rocket exhaust properties generally follow the stages indicated in Figure 25. First an equilibrium chemistry code is used to calculate chamber conditions and the temperature, pressure and equilibrium chemical species concentrations at the nozzle throat. Nozzle expansion flow calculations may

be made in a number of ways ranging from one-dimensional chemical equilibrium, to three-dimensional multi-phase flow with chemical kinetics. The exhaust structure for static motor firings can usually well be simulated by a program (such as REP or SPF) which gives spatial distributions of non-equilibrium chemical species, temperature, velocity, pressure, and turbulent mixing based on limited assumption. For wind tunnel and flight plumes, base recirculation or separated flow effect with non-equilibrium chemistry may have to be included to obtain more accurate calculations of plume structure. The appropriate applications code(s) are then applied to the calculated flow field using the test geometry and applicable transmission path effects to obtain the results that may be compared with the measured data base.

Step 6:

Comparison between calculated and measured values often yields discrepancies. In this step appropriate, judicious adjustments to the calculations are made within underlying scientific bounds to give closer agreement with measured values. For instance, if the near field radiation values includes a searchlight effect, the measured plume continuum radiation will be larger than that predicted by a code ignoring such effects. The demands of prediction accuracy may require modification of the code to accommodate this feature. Alternatively, disagreement between data and prediction may be caused by different phenomena. An impurity in the propellant, such as sodium, may produce strong emissions in the visible spectrum that are not predicted by the code. This may be the result of excluding sodium reactions from the plume flow field calculations or an inability of the radiation code to predict these line emissions.

A prediction technique is strengthened if it can be confirmed against a range of conditions including flight. Although these conditions may not completely match those for the systems of interest (e.g. a different motor) the validation process increases confidence in the calculation putting it on a much broader base.

Step 7:

This is the step where plume flow field and application codes are run for the operational conditions of interest. Predicted values of plume signature and other effects yield information from which decisions about system design, tactics and other system-level parameters may be made. Depending upon the codes used for the specific test and operational conditions, improvements can be achieves when:

i. allowance is made for radial pressure gradients

ii. non-equilibrium two-phase flow (thermal and velocity lags of condensed particles) is included.

iii. "base flow effects" are included, i.e. when a flight missile has a base diameter significantly greater than the nozzle exit diameter.

iv. shock structure effects are treated

If, for instance, the missile has a large base diameter which could induce base flow recirculation and afterburning, a code without a base flow model would not be applicable, equally, inappropriate choice of chemical mechanisms can produce false plume properties resulting in incorrect emission data. It is essential that the thermodynamic, chemical and physical attributes of the plume modelled by the code, the model limitations and the necessity for enlightened use of input data should be thoroughly understood if accurate analytical assessment is to be performed. After proper validation the code can be applied to meet the overall system objectives.

Step 8:

With the continued advance of computer use in experiments and modelling the analysis of results becomes more "machine dependent" and the user faces the problems of incompatibility of operating systems for information exchange and languages used to describe the information.

Suggested data to characterise a plume signature are:

- Spectral radiance vs wavelength (spectrometers) and vs time

- In-band radiance vs time (radiometers)

- Radiant intensity vs time

- Other types of data presentation helpful in evaluating the signature are:

- Video tapes from imaging sensors which provide a "false colour" image of in-band radiance versus position. Their use is for subsequent analysis of spatial fluctuations, spectral irradiance, shape and geometry of the radiating plume (isoradiance contours). In-band radiance plume radial and/or axial profiles within the image field allow the

assessment of radial symmetry, axial decay etc. A properly calibrated video tape can be examined pixel by pixel to obtain information about the temporal and spatial distribution of "in-band" radiance from the plume.

- Power spectral density plots which may be performed on the radiometric data to determine plume frequencies.

- Radiant intensity vs time for variations in Mach numbers, altitude etc.

An experienced approach to data reduction is necessary to ensure that proper interpretations are made for code validation and the provision of sufficient information for their modification. Of primary importance is the correct data for atmospheric absorption as discussed in Section 3.

Documentation of records should be comprehensive such that there will be no need to repeat the work should future interest arise. Terminology should follow the accepted standards given in this report and universal SI-units, as defined in Table 9, should be used.

Table 9: Terminology of Spectrometry and Radiometry

Symbol	Term		Units
Φ	radiant power power	rate of transfer of radiant energy	W
$\Phi(\lambda)$	spectral radiant power	rate of transfer of radiant energy per unit wavelength interval centred at wavelength λ	$W\,\mu m^{-1}$
I	radiant intensity	radiant power emitted by a source into a unit solid angle	Wsr^{-1}
$I(\lambda)$	spectral radiant intensity	radiant intensity per unit wavelength interval centred at wavelength λ	$Wsr^{-1}\,\mu m^{-1}$
L	radiance	radiant power emitted by unit area of a source into a unit solid angle	$Wm^{-2}sr^{-1}$
$L(\lambda)$	spectral radiance	radiance per unit wavelength interval centred at wavelength λ	$Wm^{-2}sr^{-1}\mu m^{-1}$
E	irradiance	radiant power incident upon unit area of a	Wm^{-2}
$E(\lambda)$	spectral irradiance	irradiance per unit wavelength interval centred at wavelength λ	$Wm^{-2}\mu m^{-1}$
R_p	radiant power responsivity	the output of an instrument for unit radiant power input	instrument units W^{-1}
$R_p(\lambda)$	spectral radiant power responsivity	radiant power responsivity per unit interval centred at wavelength λ	instrument units $W^{-1}\mu m^{-1}$

Notes 1   The output signal of radiometers and spectrometers is the output voltage of the instrument detector/pre-amplifier combination modified by subsequent electronic and mathematical signal conditioning. When used in evaluating R_p and $R_p(\lambda)$ it is usually referred to as a standard gain configuration of any variable gain amplifiers.

5.0 SYSTEM ASPECTS AND OPERATIONAL CONSIDERATIONS

So far, the whole chapter on plume radiation dealt with the origin of exhaust radiation, its classification into useful spectral bands and ways to address assessment and description of plume radiation properties in a generalised manner.

All this is quite academic and needs a connection to real applications, because world-wide the money on plume research and development is not spent to know more about it, but to apply it to ones own benefit. This last section shall go more into the details of applications as of today and shall show the te relencies for future plume signature avoidance or application.

A missile is either hostile and wants to harm you - or it is your own one and you want to employ and target it to the best of your own ability. In both cases missile signature is an existing fact and designers want to minimise its magnitude as much as allowed by overall system restrictions.

From a users point of view the performance requirements of a tactical missile are:

- a stealthy body
- a no- or minimum-smoke plume
- plume radiation emission as small as possible
- a high enough propellant burning rate and temperature to supply the necessary thrust
- the usual requirements on weight, size, price and ease to use.

It depends a lot on the designers skills to produce a high performance missile with minimised signature.

From a defender's point of view one is faced with the signature of existing missiles and has to make the best use of it.
The limitations are:

- the cross section for radar reflection of a missile body depends a lot on material properties, whereas the diameter and length are dictated by the volumes of warhead, seeker head and motor

- minimum smoke motors are available with limitations imposed by thrust and other performance degradation

- minimising plume radiation signature is the challenge of the future in competition with ever more sensitive sensors to detect radiation levels down to single photon events

- burning rate and burning temperature are closely related to thrust and mass flow, but also to radiation signature. Performance improvement in many cases goes hand in hand with a raise in radiation signature.

5.1 GUIDANCE AND CONTROL PROPERTIES

In this lecture series we are concerned only about tactical missiles. Their range is limited to a few hundred kilometres. But the majority of tactical missiles have medium (-50 km) and short (-10 km) ranges with accordingly shorter and smaller signatures. The very short range, men portable, shoulder fired SAM's (Redeye, Stinger, SA-14 type) pose a world-wide threat to ground and air targets, because they are available to, and usable by unskilled personnel (also terrorists) and are employed in all kinds of conflicts.

The long and medium range missiles are in many cases radar guided, possibly with an optical- or semi active radar- seeker head for the terminal phase. The majority of short range missiles have passive IR homing or wire guidance. After acquisition within the necessary field of view (FOV) they fly autonomous and are guided in almost all cases by IR or dual waveband seeker heads. Many of the antitank missiles have a wire or fibre link to the gunner. The guidance is performed by goniometer or line of sight tracking with the aid of an artificial IR spot on the tail of the missile or by a TV seeker head.

IR sensors, goniometers, guidance fibres and radar interferes with the missile and its exhaust plume in a manifold way.

A typical time scale of a rocket motor functioning is shown in Figure 26. If radiation sensors are used for guidance and control they have to be sensitive enough in order to distinguish rocket and target signatures at target distance. Propagation of optical radiation is governed by the attenuation law

$$A = I/R^2 \cdot \exp(-\sigma R)$$

with:

A - attenuation in $[W/km^2 \, sr \, \mu m]$
I - source signal strength in $[W/sr \, \mu m]$
R - Range in km
σ - extinction coefficient in $[1/km]$

σ is usually broken up into

$$\sigma = \sigma_{Rayleigh} + \sigma_{Aerosol} + \sigma_{Molecule}$$

With given values for R, I and σ the irradiance of the optical guidance sensor can be calculated. Its signal to noise ratio (S/N) under battlefield atmospheric conditions has to be large enough to discriminate target and missile (see Figure 27).

Problems arise due to the limited dynamic range of sensing devices. During boost phase the rocket motor exhaust signature is largest and plume - sensor distance is smallest. After ignition the strong optical (UV-VIS-IR) signature (up to kW power ranges) irradiates the sensing device and fully saturates the sensor to the limits of destruction. If fired from a launcher or flying platform containing the guiding instrumentation (mainly in the IR-spectral band), the exhaust gases heat up the IR entrance optics and the atmosphere within the FOV and makes the sensor useless. A temporary shutter in front of the sensor or a local separation of rocket and sensor can circumvent this problem with the disadvantage of temporal blindness of the sensor and the possible loss of target or missile during the boost phase.

Smoke and change of refractive index of the atmosphere in the line of sight can cause problems with neighbouring missiles being fired. Other problems from a close-by firing of a booster, like particle impingement, fogging of windows, pressure, temperature and acoustic induced harm to the launch vehicle environment and persons shall not be treated here.

A general approach to master these problems is by:

- splitting the guidance in near field and far field regimes with different guiding principles
- narrowing down the used spectral band
- employing multicolour sensors, e.g. two or more narrow spectral peaks within the 3μm - 5μm sensitivity band of the sensor
- shifting the guidance to a separate wavelength band with the aid of artificial, coded light source on the tail of the missile irradiating the guiding sensor.

This is, combined with phase sensitive signal processing algorithms and appropriate mathematical signal handling techniques, like difference and ratio relationships of signal and background treatment, a general approach to track the signal with a large enough S/N - ratio.

5.2 Detection and tracking of adversary missiles

Sole its signature makes an adversary missile detectable. The possibility of detection starts right from launch. Principally the detection of missiles can be split into two groups.

(i) the detection by **active** radiation

(ii) the detection by **passive** radiation.

In the first case the missile is illuminated for detection by laser or radar beams. The reflected radiation is detected and analysed with respect to velocity and distance by the principles of Doppler shift. Up to now mm-wave radar is the most practised method for Missile Approach Warning (**MAW**) detectors.

The information gained by pulse-Doppler-radar should allow the accurate calculation of the time to impact. Range is of outstanding importance. It is in all applications a matter of signal to noise ratio and the ability of the sensor to pick up and identify the target within the background clutter of the scenario. The range to detect attacking missiles is in this case determined by the radar beam, its power and beam divergence, the propagation through the atmosphere and the radar cross section of the missile and its plume. In most cases the plume radar cross section can be neglected.

Major disadvantages of missile approach warning by Doppler radar are its limited range despite high power radar and the self exposure by the radar beam itself. It can be picked up easily over long distances and can be used as homing source for counter attack.

The second group of missile detection is a passive one. Radiation emitted by the missile itself is detected and used for threat analysis. The easiest way is to see the trail of primary or secondary smoke which marks the flight trajectory of the missile
Because the time scale for reaction is very short, one tries to avoid the human within the chain of actions as much as possible. Sensors in the visible spectral range have the disadvantage of strong background clutter and it is hard to circumvent this fact.

A new way of establishing Missile Launch Detectors (MLD) and MAW systems is by passively picking up the plume signature in the infrared or ultraviolet spectral bands. In both cases the plume radiation is sensed, analysed and processed by optical sensors which belong to categories like

- non-imaging or

- imaging sensors.

The imaging sensors again can be grouped into

— scanning point- or linear array sensors
— focal plane array sensors.

Non-imaging sensors have the advantage of simplicity and low cost. They give, within a quadrant FOV, a threat warning indication, listing priority and crude time to impact.

Imaging systems, although more elaborate and expensive, give much more information about the target like

- high spatial determination of target location in real time
- dynamics of flight path
- threat priority of many targets simultaneously.

In all cases a certain portion of the broad band optical exhaust plume signature is imaged with an entrance optic onto the sensor. The signal is analysed according to

- be a true missile signal
- be a real threat
- fulfil certain missile specific behaviours
- time frame for impact
- angle of arrival
- threat priority

Common systems can process from about 10 up to 50 threats simultaneously.

The design of passive missile launch detectors is dictated by the

- emissivity of the plume
- the existence of atmospheric windows at the strongest emissivity bands
- appearance of typical attack scenarios in the same wavelength band
- availability of appropriate sensor systems

Up to now the two most favoured spectral bands for missile plume detection are the mid infrared between 3μm and 5μm and the ultraviolet spectral band below 300 nm. This is the so called solar blind region, because solar UV radiation is absorbed by the Ozone layer between 15 and 35 km altitude. The sun as the only natural UV light source is absent. Therefore sensors working in the solar blind regime have the big advantage of a low background with a largely

improved S/N ratio in this spectral band and the adherent improved false alarm rate.

The choice and preference of a certain system depends on many aspects like, price, range, false alarm rate, angular resolution, time needed for target identification, field of view in azimuth and elevation and reliability.

Here only the plume relevant aspects shall be pointed out. From Fig. 27 and 28 the distribution of plume radiation strength can be seen. It is strongest in the 3 -5 μm band with emitted power ranges up to the kW range for tactical missiles. Signature emissivity originates as mentioned above, to a large extent from plume afterburning. Although plume temperatures up to 2500 K exist in the inner zones, the radiating envelope propagating most of the radiation for detection has cooled down to 500 - 1000 K. Its Planck curve peaks in the 3-5μm range. A further cooling of the plume exhaust down to 300 K would favour the detection at the long IR wavelength band between 8 - 12μm. Due to high background levels at low signal levels in this spectral band it is omitted in favour of the 3-5μm band.

Both IR spectral bands have good atmospheric transmission (see Fig. 12). A further advantage is the good documentation of almost every aspect of infrared optical radiation (see Ref. 3), be it sensors, atmospheric propagation, material properties, reflectivities, optical materials and filtering or natural and artificial light sources.

The principal sensors used in the mid IR are scanning line array sensors or staring matrix sensors, both of them being imaging sensors. Sensor materials are e.g. Platinum Silicide (PtSi), InSb or Mercury Cadmium Telluride (MCT). They usually are cooled down to 80 K for optimum performance. Scanning line array systems employ polygon scanners to scan the FOV in order to generate an image of the scene. Scanning systems have the advantage of large angular coverage (up to 180 degrees) at least in one dimension with the disadvantage of a short dwell time of the sensor footprint on the target. Staring array matrix sensors continuously image the whole FOV. State of the art sensors employ a temperature resolution of below 0,1 degree with a matrix of 512 by 512 pixels and more.

The plume signal of imaging IR missile approach warners is analysed by image processing computers. Because of the highly resolved and structured background in the IR band, the workload and storage capacity for the image processing computers is enormous and can be mastered only by very advanced hard and software.

Because of all these problems a different type of sensor is considered for missile approach warning. It works in the ultraviolet spectral band either as an imaging or nonimaging sensor. The UV plume signal strength is weak compared to the IR and the useful atmospheric propagation is limited to wavelengths between 240 and 300 nm. Nevertheless there are still advantages that make the UV spectral range a promising candidate for missile detection. As mentioned earlier, major contributions to UV plume radiation mechanisms originate

- from the afterburning effects
- hot plume particle radiation
- deactivation of exited molecular states which mostly happen in the outer plume envelope and therefore emit UV radiation very similar to visible radiation

An example of the spatial- and intensity profiles of a tactical rocket motor plume is shown in Figure 29. The measurement was performed simultaneously with 3 imaging sensors in different wavelength bands. The spatial extension in the UV and visible spectral range is quite similar, as should be expected by the similarity of radiation producing mechanisms. The cameras were partly set to yield grey scale values in order to allow radiometric parameter evaluation.

State of the art sensors used in the "solar blind" UV are either non imaging point sensors or imaging focal plane array sensors with a resolution of 512 by 512 pixels. In both cases the photosensitive detector materials are photocathodes with sensitivity peaking in the mid UV, as shown in Figure 14 and Table 6. UV sensors have the advantages to be compact, low power consuming with no cooling and moving parts required. With the use of adequate antiblooming and threshold settings of the UV sensor the dynamic range is high enough not to be blinded by plumes of own rockets being fired. The geometric extensions of entrance optic and sensor are smaller than comparable IR systems due to the shorter wavelength.

The most convincing advantage of imaging UV sensors is the low signal to noise ratio which originates from the low background level of solar radiation and the use of image intensifiers. The prime function of image intensifiers is to raise the image intensity well above the noise level of the read out device which enables to detect essentially single photon events. Signal gains of up to 6 orders of magnitude are possible.

The workload for image processing equipment is comparatively low because of the missing background clutter although the signal strength is much less than in the IR. It is quite difficult to produce artificial UV light sources for deceiving purposes which, apart from missing scene structure, considerably lowers the false alarm rate of UV missile detection systems.

Improvement of the design of passive missile plume detection system is being worked on to fulfil the requirement of the end-user. On the other hand missile motor designers are improving to cut down on plume signature emission and it will be a continuos interplay between both efforts to gain advantages over the other side.

6. REFERENCES

1)   JANNAF Handbook
     Rocket Exhaust Plume Technology, Chapter 3, Rocket Exhaust Plume Radiation

2)   Eerkens, J. W. et al,
     Rocket Radiation Handbook:

     Volume I: Rocket Radiation Phenomenology and Theory (1974)
     Volume II: Model Equations for Photo Emission Rates and Absorption Cross-Sections (1973)
     Volume III: Fundamentals of Photonics
     Volume IV: Gas Dynamics and Flow-Field of Rocket Exhausts
     Volume V: Atmospheric Properties and Optical Transmission
     Volume VI: Radiation Sensing Systems Theory

     US Department of Commerce, National Technical Information Service

3)   Wolfe W. L., Zissis G. J. ed., The Infrared Handbook, Office of Naval Research, Dept. of the Navy,
     Washington DC (1978)

4)   Gaydon, A. G., The Spectroscopy of Flames, John Wiley & Sons Inc., New York (1957)

5)   Gaydon, A. G. and Wolfhard, H. G., Flames: Their Structure, Radiation and Temperature, Chapman and
     Hall Ltd, London (1970

6)   Ludwig, C. B., et al, Handbook of Infrared Radiation from Combustion Gases, NASA SP-3080 (1973)

7)   Lyons, R. B., Wormhoudt, J. and Kolb, C. E., Calculation of Visible Radiation from Missile Plumes,
     AIAA-81-1111 (1981)

8)   Kolb, C. E., Ryali, S. B. and Wormhoudt, The Chemical Physics of UV Rocket Plume SignaturesJ. C.,
     Proceedings of SPIE, Vol 932, 2. April (1988)

9)   Rothschild, W. J. and Martin, C. W.,
     Experimental Results for Hydrocarbon Exhaust Infrared Model Verification
     Air Force Armament Laboratory: AFATL-76-74 (1976)

10) Sukanek, P. C., Davis, L. P., An Assessment of the NASA Band Model Formulation for Calculating the
     Radiance and Transmission of Hot and Cool Gases Air Force Rocket Propulsion Laboratory, AFRPL-76-
     9 (1976)

11) Jeffrew, W., et al, Rocket Engine Exhaust Plume Temperature Profile by Line Reversal Technique, Air
     Force Armament Laboratory: AFATL-TR-77-50 (1977)

12) Stephen, J. Young, Inversion of Plume Radiance and Absorptance Data for Temperature and
     Concentration, Air Force Rocket Propulsion Laboratory AFRPL-TR-78-60 (1978)

13) Dennis, R., et al, Photographic Spectroscopic Measurement of Ultraviolet Solid Rocket Motor Plumes,
     The University of Tennessee Space Institute, Tullahoma, Tennessee (1980)

14) Dash, S. M., Analysis of Exhaust Plumes and their Interaction with Missile Airframes, from Tactical
     Missile Aerodynamics, ed. Hemsch, M. J., Vol 104, AIAA, New York (1986)

15) Dash, S. M., Wolf, D. E., Beddini, R. A. and Pergamont, H. S., Analysis of Two-Phase Flow Processes
     in Rocket Exhaust Plumes, J. Spacecraft, Vol 22, No 3 (1985)

16) Linghard Yu., K. Petrov, V. A. and Tikkonova, N. A., Optical Properties of Leucosapphire at High Temperatures, Institute of High Temperatures, Academy of Sciences of the USSR, Translated from Toplofizka Vysokikh Temperature, Vol 20, No 6, pp 1085-1092, Nov.-Dec. (1982)

17) Dash, S. M., Analysis of Tactical Missile External Plume Interaction Flow-fields, AGARD Symposium on Missile Aerodynamics, Friedrichshafen, FRG, April 23-26 (1990)

18) Slack, M. and Gillow, A., High Temperature Rate Coefficient Measurement of CO + O Chemiluminescence, Combustion and Flame, Vol 59, pp 186-196 (1985)

19) Evans, G. I. and Smith P. K., The Reduction of Exhaust Signature in Solid Propellant Rocket Motors, AGARD-CPP-391, 16, (1985)

20) Jensen, D. E. and Jones G. A., Theoretical Aspects of Secondary Combustion of Rocket Exhausts, Combustion and Flame, Vol 41, pp 71-85, (1981)

21) O'Donnel, R. M., and Sauer, L. W., Development of Ultra-Violet Plume Signature Prediction Code (PRUV), Proc. IRIS Targets, Backgrounds and Discrimination, Vol. II, pp 113-124,(1991)
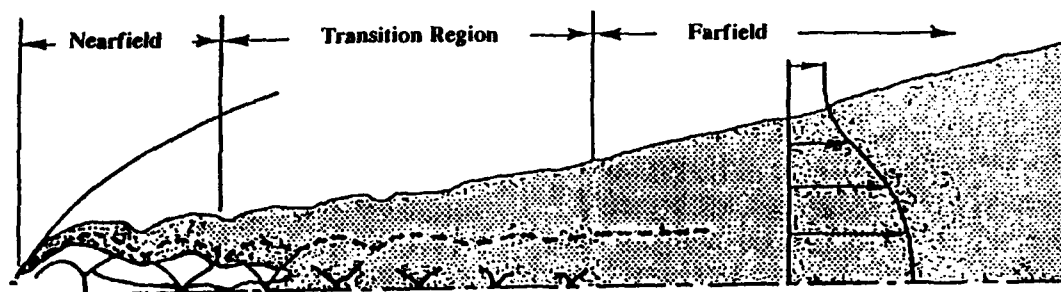
Fig.1   Regional Division of a Typical Plume
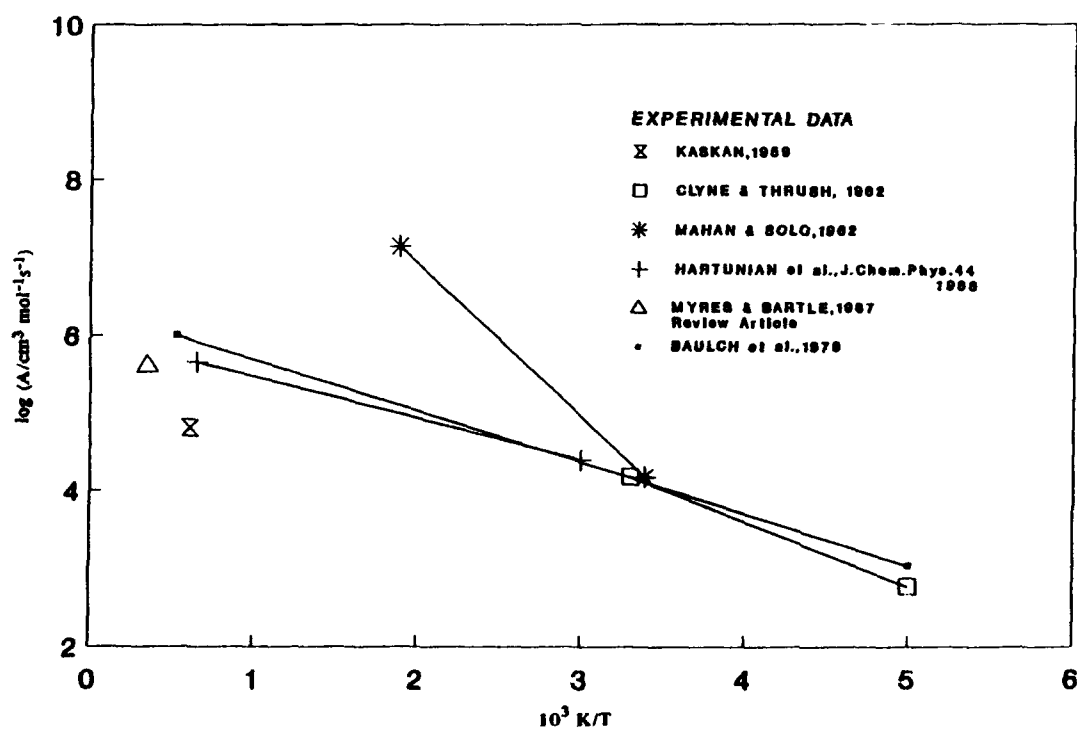
Fig. 2a   CO + O Chemiluminescence Rate Constant Data
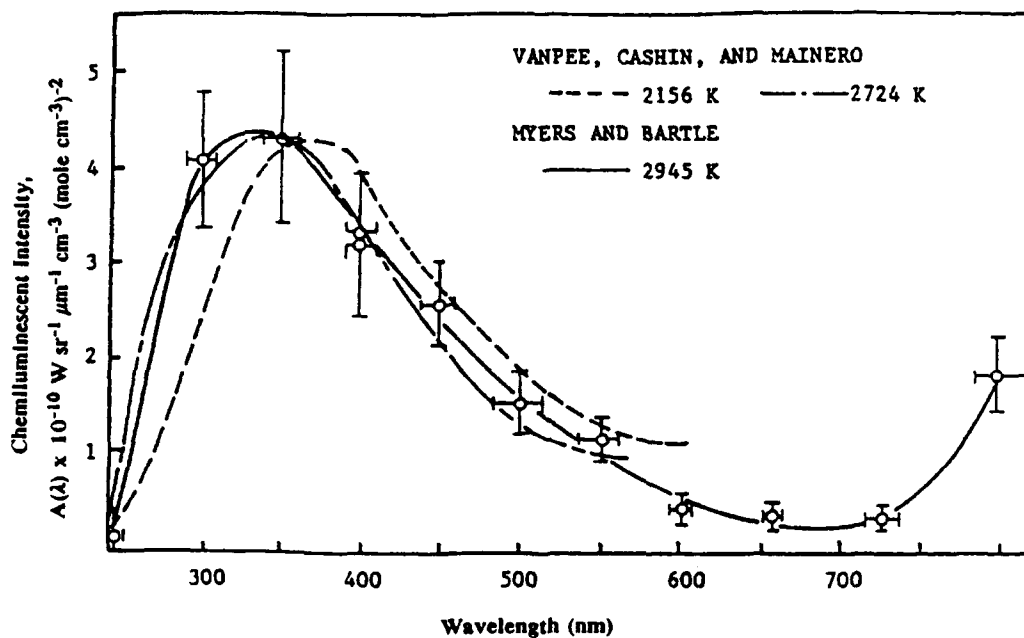
Fig. 2b CO + O Chemiluminescence Intensity Spectra

The points with indicated error bars as well as the solid line are the absolute intensity measurements of Myers and Bartle. The other two curves were normalized to the peak intensity of the Myers and Bartle curve.
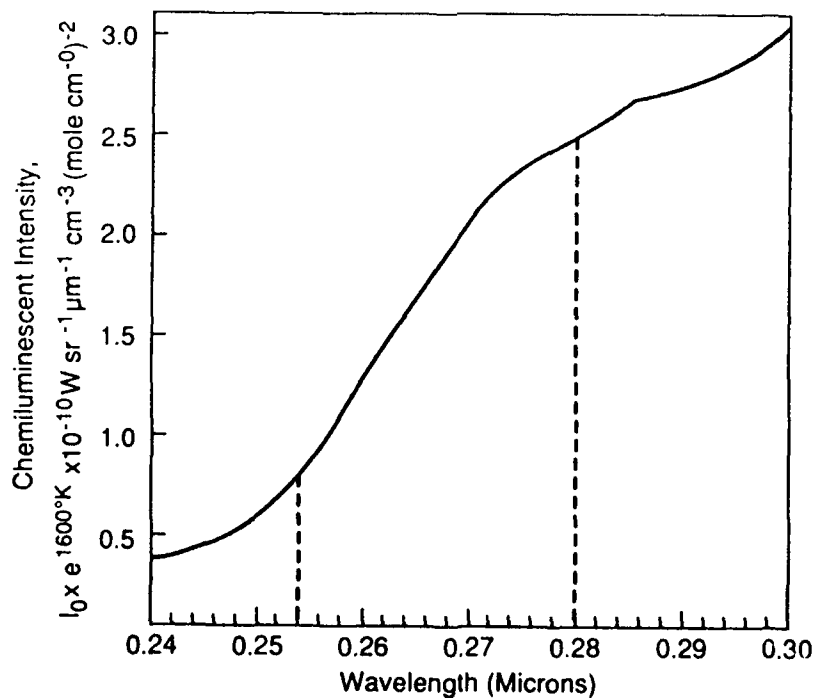
Fig. 2c Ultraviolet Portion:CO + O ChemiluminescenceIntensity Spectrum
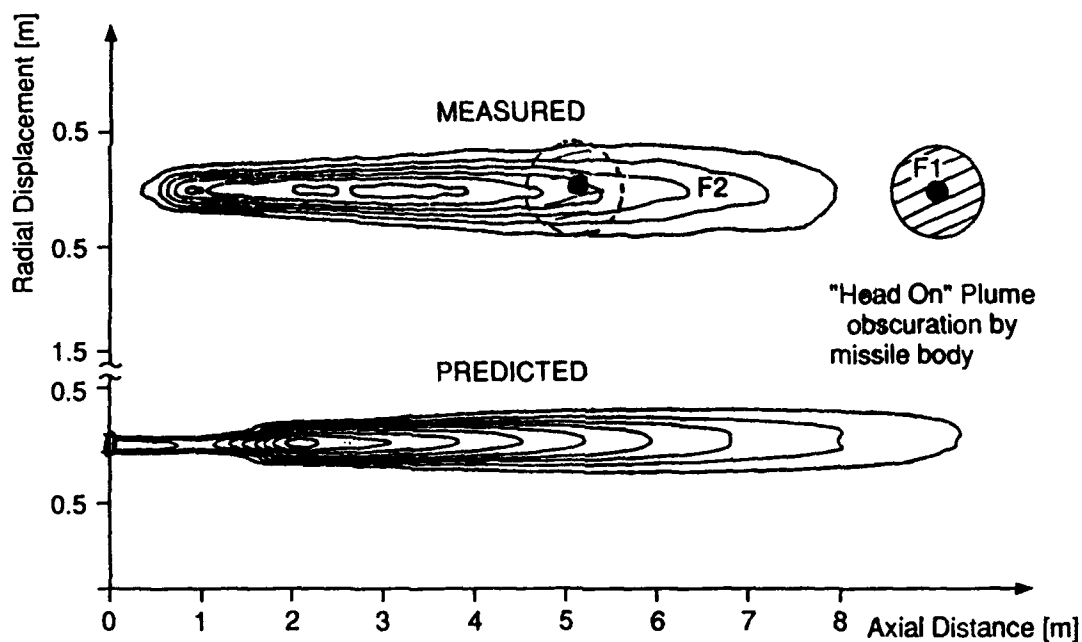
Fig. 3 ISO-radiance Contours for a Composite Propellant Rocket Motor Exhaust (IR)
with "Head On" Obscuration
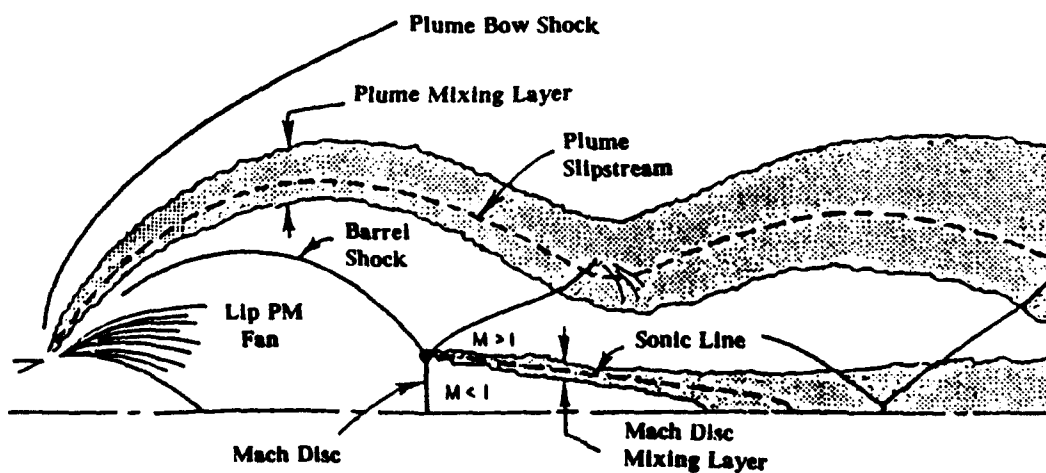
Fig. 4 Nearfield Viscous Inviscid Structure of Under Expanded Plume at
Supersonic Flight Conditions
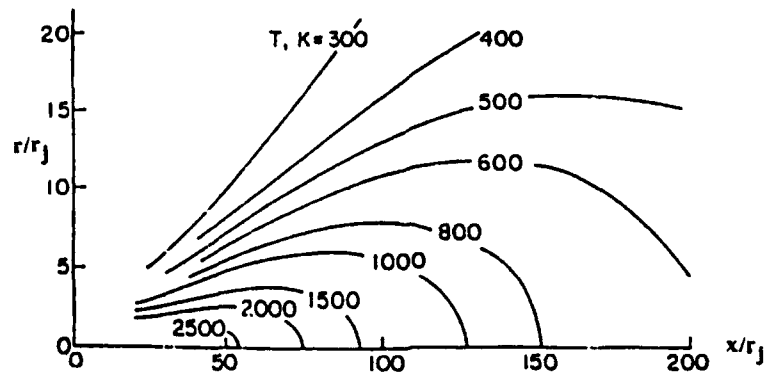
Fig 5a   Temperature Contours in Farfield of Energetic Tactical Missile Exhaust Plume
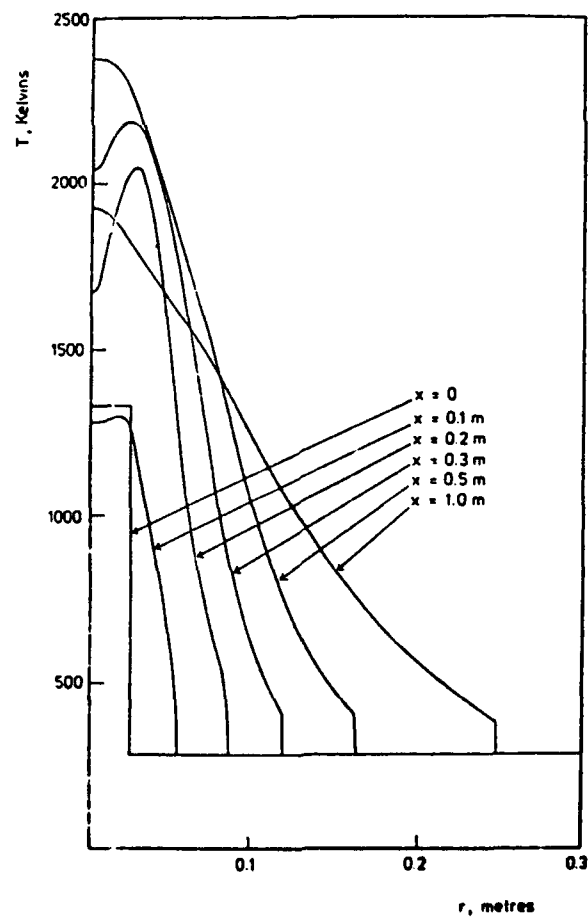
Fig. 5b   Radial Temperature Profiles of a Doublebase Solid Propellant
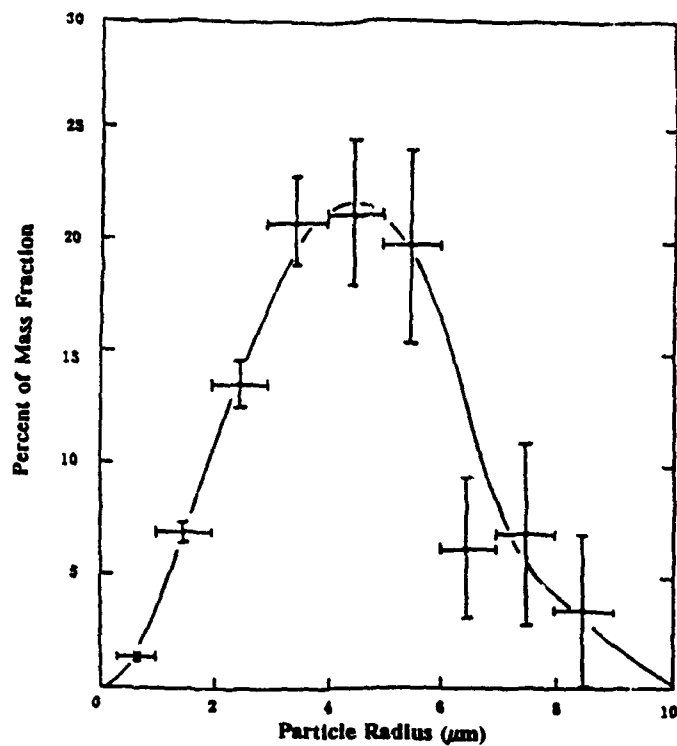
Fig. 6 Typical Measured Particle-Size Distribution
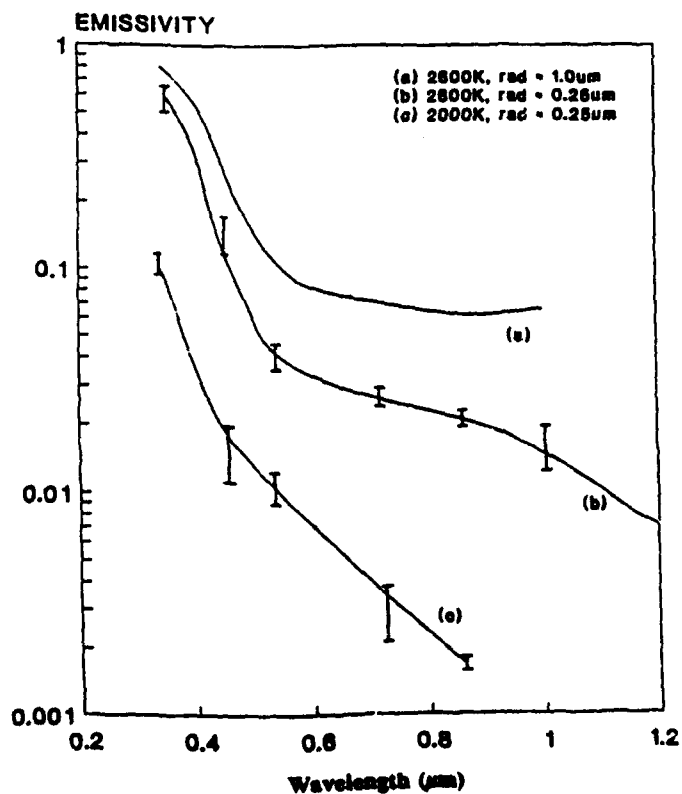
Fig. 7 Emissivity of Alumina Particles as a Function of Wavelength for Selected Values of Particle Radius and Temperature. Error Bars are for the Pure Alumina Measurements
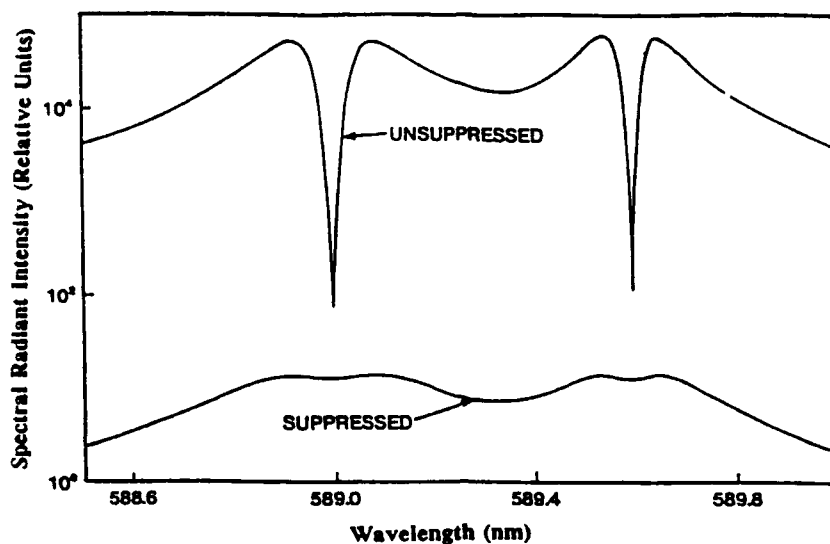
Fig. 8   Wavelength Distributions of Sodium Resonance-Line Emission Intensities for Unsuppressed and Suppressed Secondary Combustion Conditions
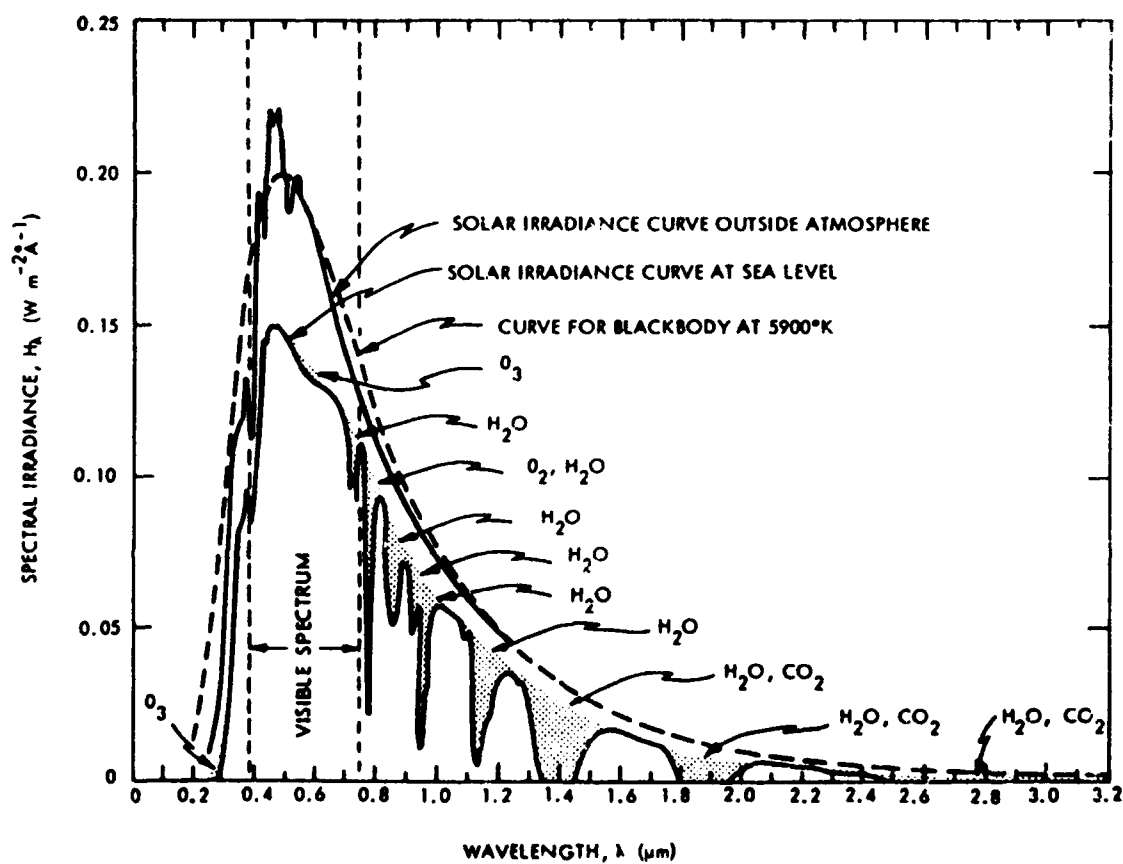
Fig. 9   Spectral Irradiance Hλ of the Sun at Mean Earth Separation. Shaded Areas Indicate Absorbtion at Sea Level Due to Atmospheric Constituents
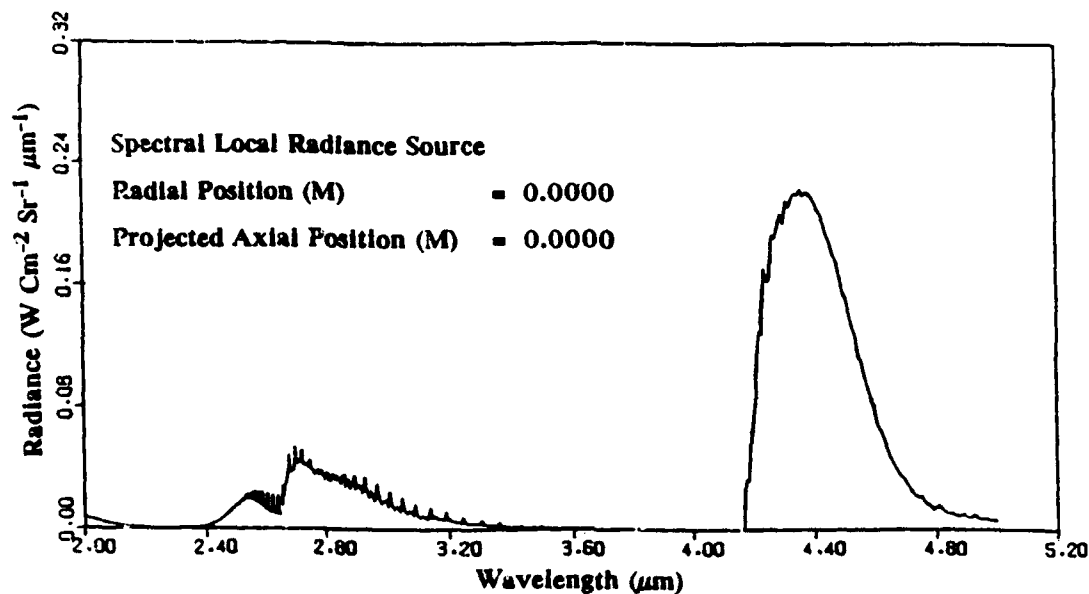
Fig. 10 Plume Radiance Calculation Performed with Parameters of Table 7
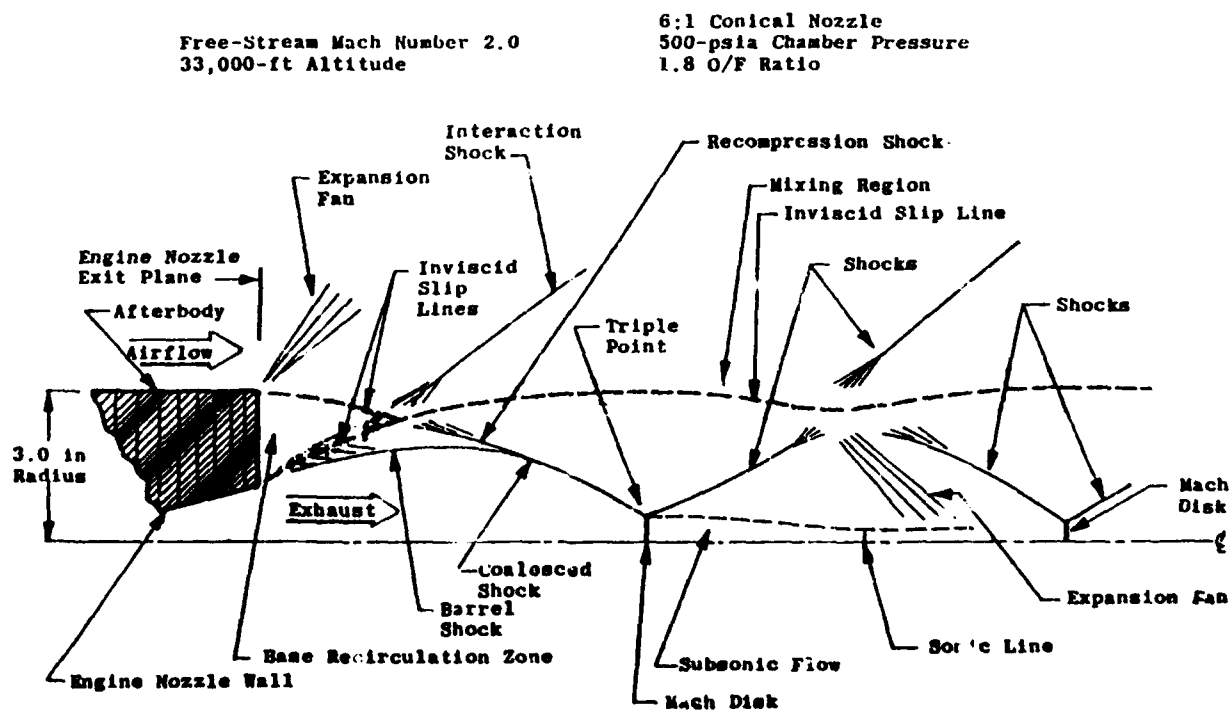
Fig. 11 Sketch of Plume Flowfield Shock Structure
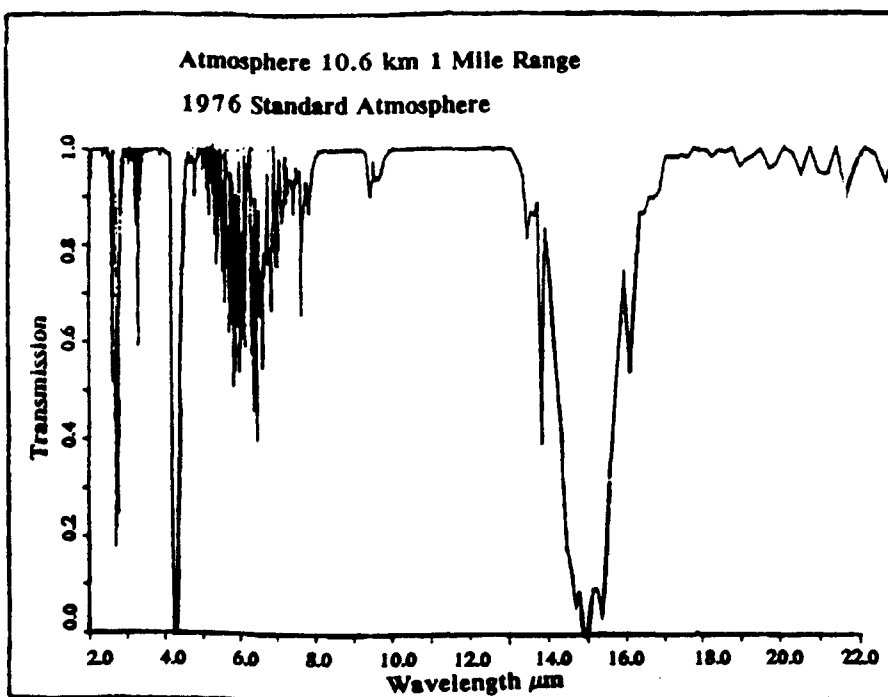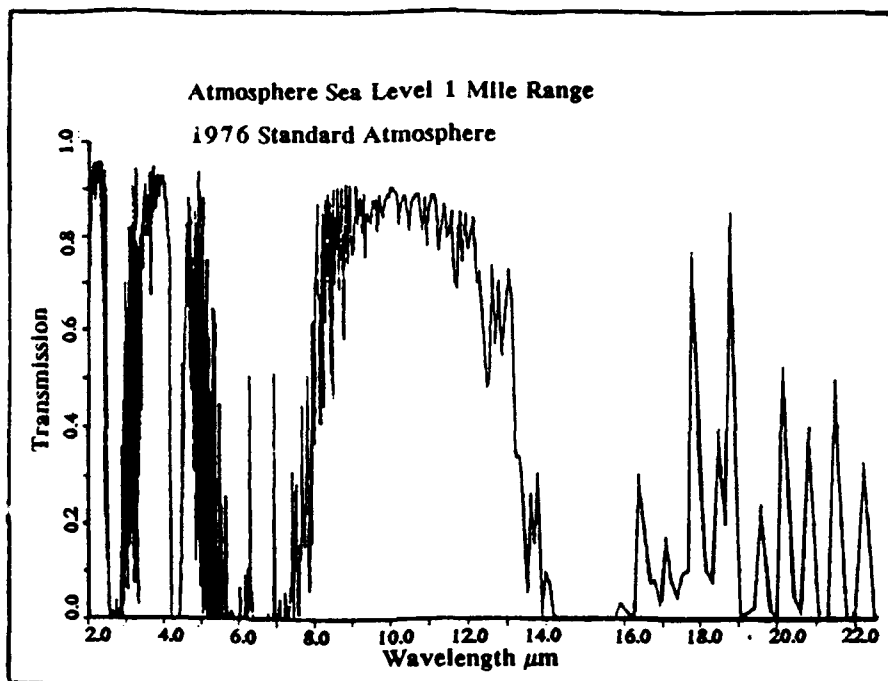
Fig. 12 Atmospheric Transmission (between 2.0μm and 22.0μm) at Sea Level and High Altitude

Fig. 13 Radiometric Essentials

$S(\lambda)$ Detected = {Object Radiation (Sa) + Reflected Radiation (Sc') + Transmitted Radiation (Sb') + Atmospheric Radiation (Sd)} x {Atmospheric Absorption}

Sd includes the emitted and scattered term

Fig. 14 Spectral Ranges of Applicability

$$L = \frac{\epsilon C_1}{\pi \lambda^5 \left(e^{\frac{C_2}{\lambda T}} - 1\right)}$$

Calculate radiances of calibration sources use at least two sources.(e.g. different temperatures)

Find the transmission of filters being used. Include windows,etc.

$\tau_F(\lambda)$
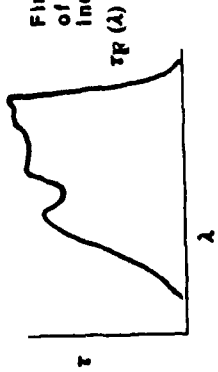
Find the spectral response of the camera/radiometer

Find the normalized product of the spectral transmission of the filters,windows, mirrors,detectors,etc.

$\overline{\tau_F(\lambda) S_c(\lambda)}$

$\tau_t(\lambda)$

Find the product of source radiance and normalized transmission term

$L_C \tau_t$

$L_B \tau_t$

$L_A \tau_t$

Calculate the instrument response

$R = \frac{c-a}{V_C - V_a}$

Valid for narrow bandpasses and greybody sources.
No atmospheric effects have been considered

$\Sigma L_A \tau_t \, d\lambda = A \, (w/(Sr \, cm^2)) \Rightarrow V_A$

$\Sigma L_B \tau_t \, d\lambda = B \, (w/(Sr \, cm^2)) \Rightarrow V_B$

$\Sigma L_C \tau_t \, d\lambda = C \, (w/(Sr \, cm^2)) \Rightarrow V_C$

Integrate the calculated spectral radiance/transmission product and measure the corresponding camera/radiometer voltage (with overfilled FOV)

$W \, sr^{-1} \, cm^{-2}$

Fig. 15 Inband Radiance Calibration of Camera/Radiometer
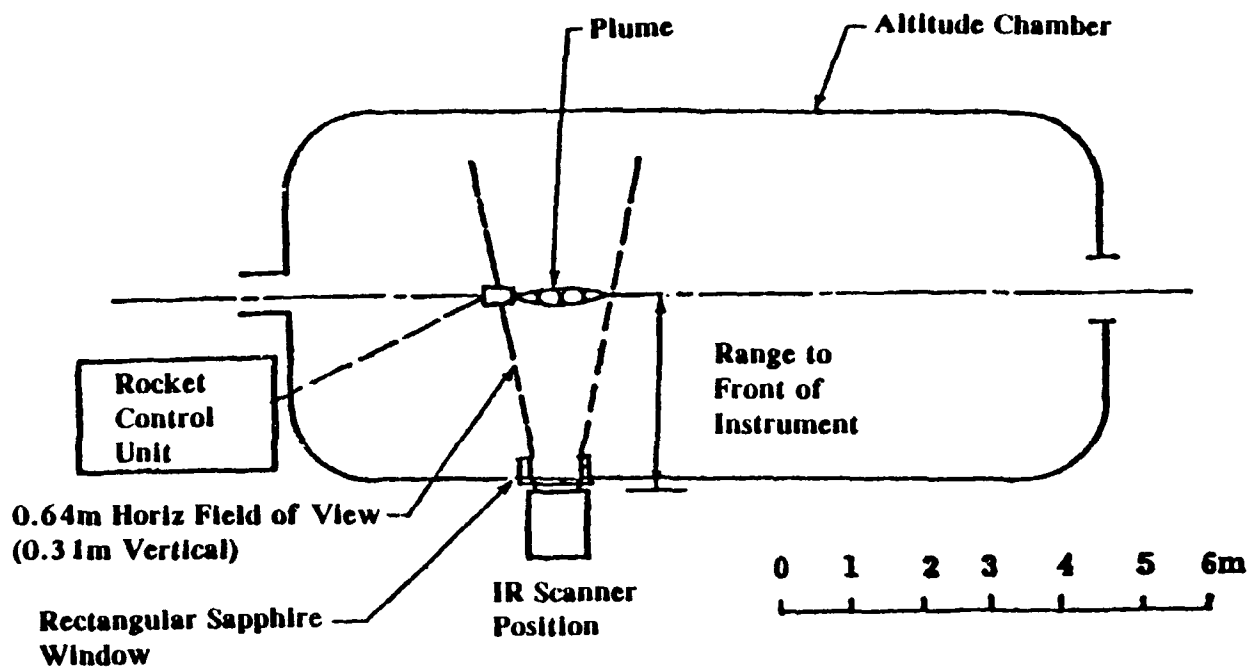
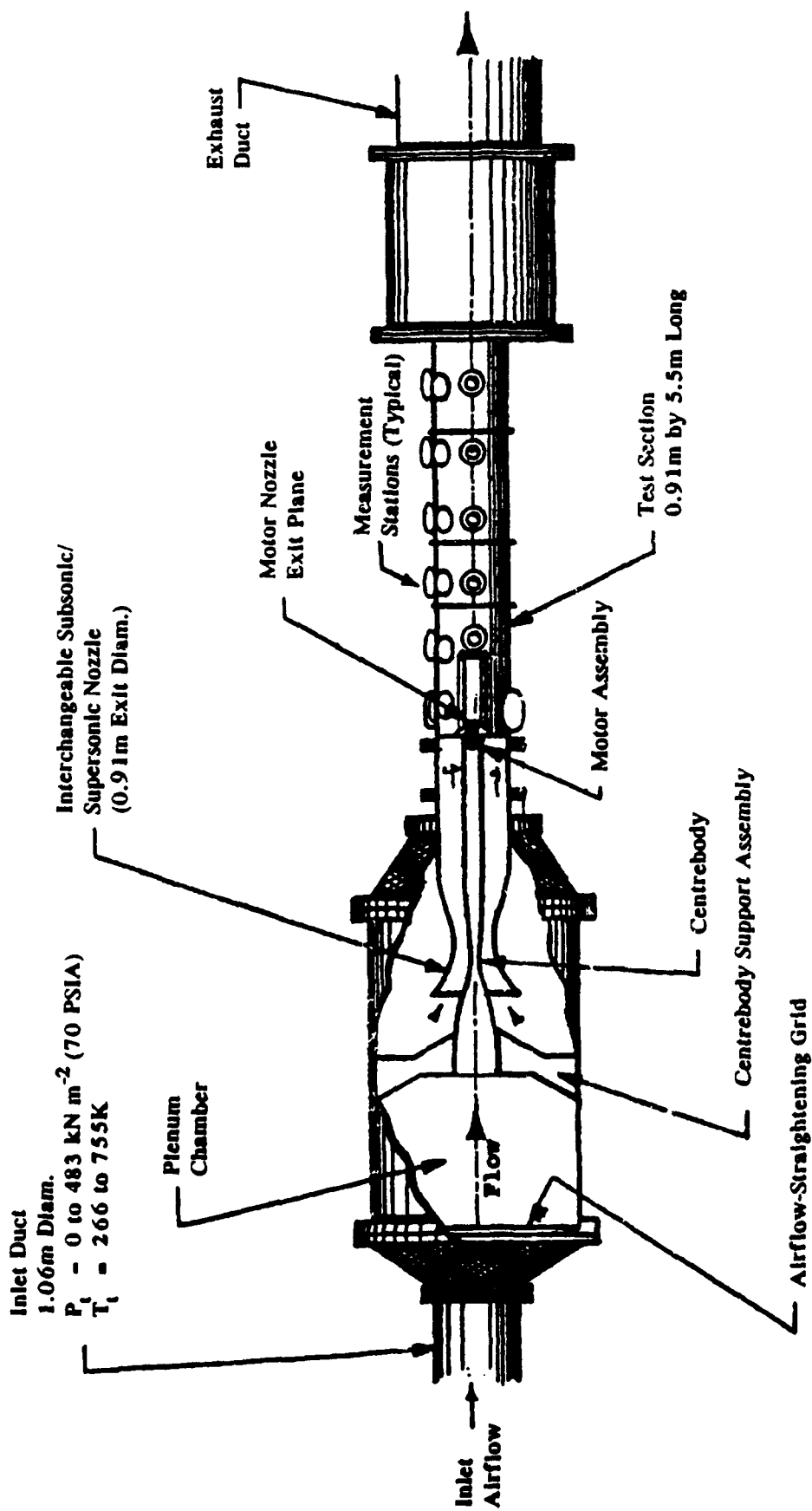**Fig. 16 Experimental Geometry for Infrared Scanner Plume Measurements**

6-38

Inlet Duct
1.06m Diam.
$P_t = 0$ to 483 kN m^{-2} (70 PSIA)
$T_t = 266$ to 755K

Plenum Chamber

Interchangeable Subsonic/Supersonic Nozzle
(0.91m Exit Diam.)

Motor Nozzle Exit Plane

Measurement Stations (Typical)

Test Section 0.91m by 5.5m Long

Motor Assembly

Centrebody

Centrebody Support Assembly

Airflow-Straightening Grid

Exhaust Duct

Inlet Airflow

Flow

Fig. 17 Simulated Flight Test Facility Schematic
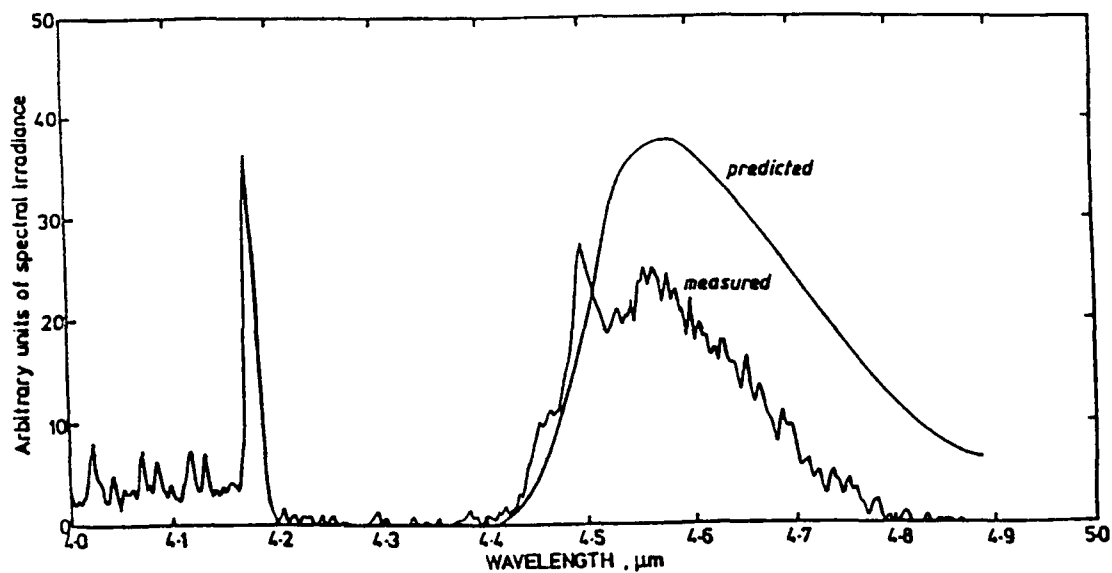
Fig. 18   Spectral Irradiance at 700m Range, 25° Aspect for a Composite
Propellant Rocket Motor Exhaust
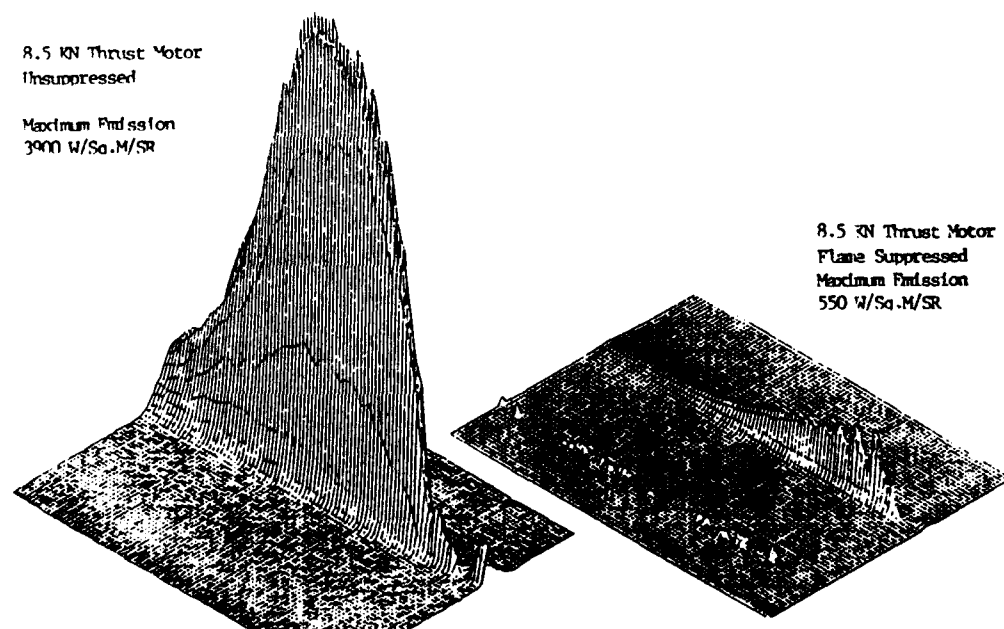
Fig. 19   Effect on Flame Suppression on Infrared Emission (4,1 - 5,0 μm)
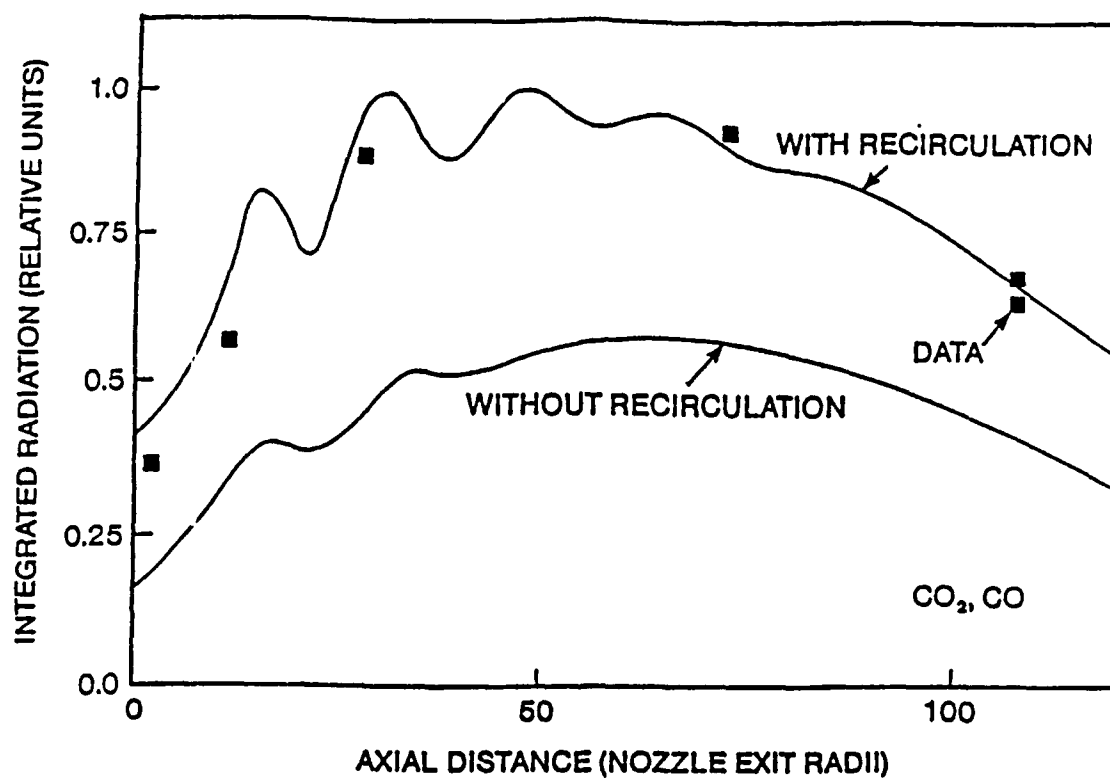
Fig. 20 Infrared Station Radiation Distributions from CO_2 and CO in the Waveband 4.3μm to 4.7μm
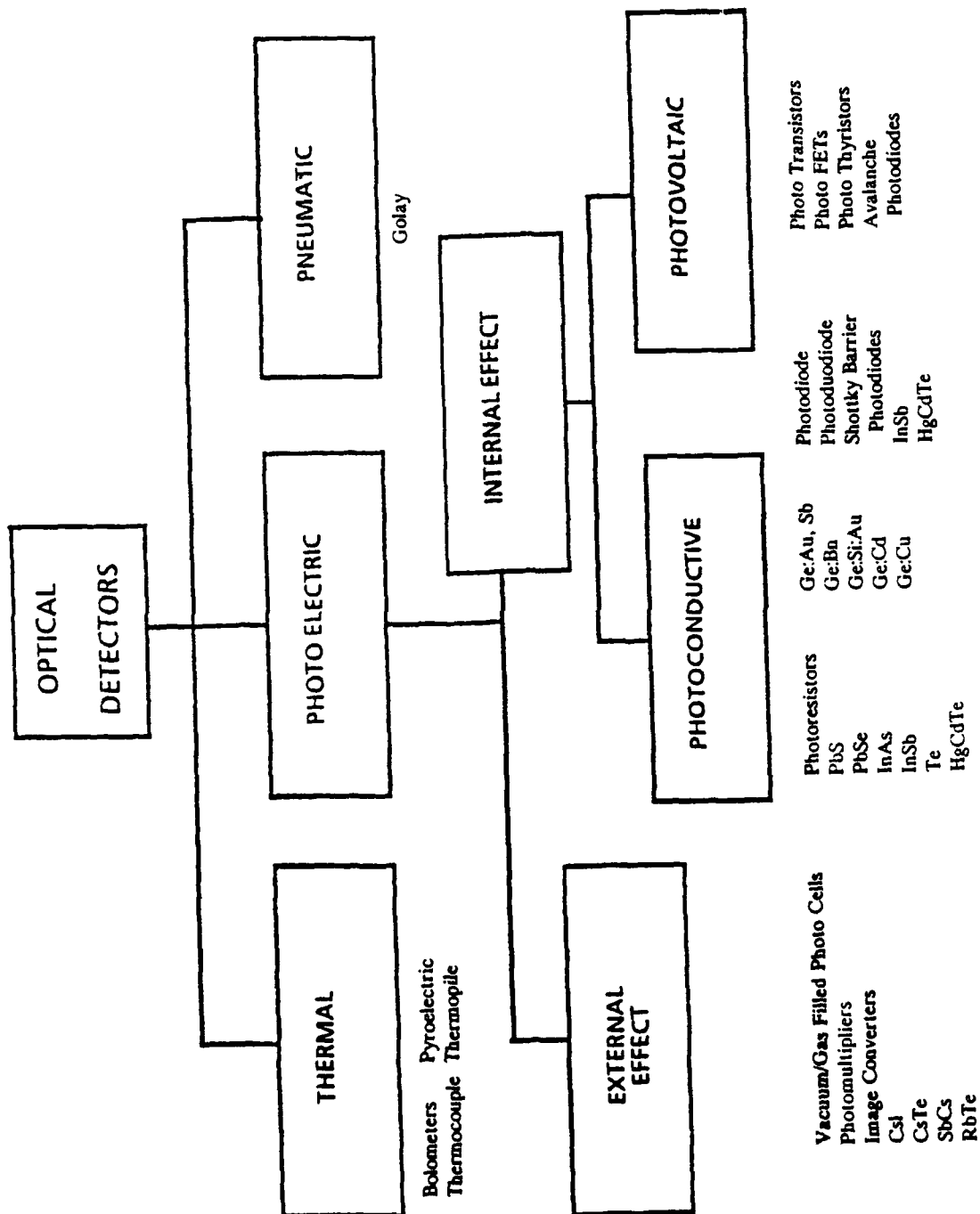Comparisons between Predictions (with and without Recirculation included in Calculations) and Data
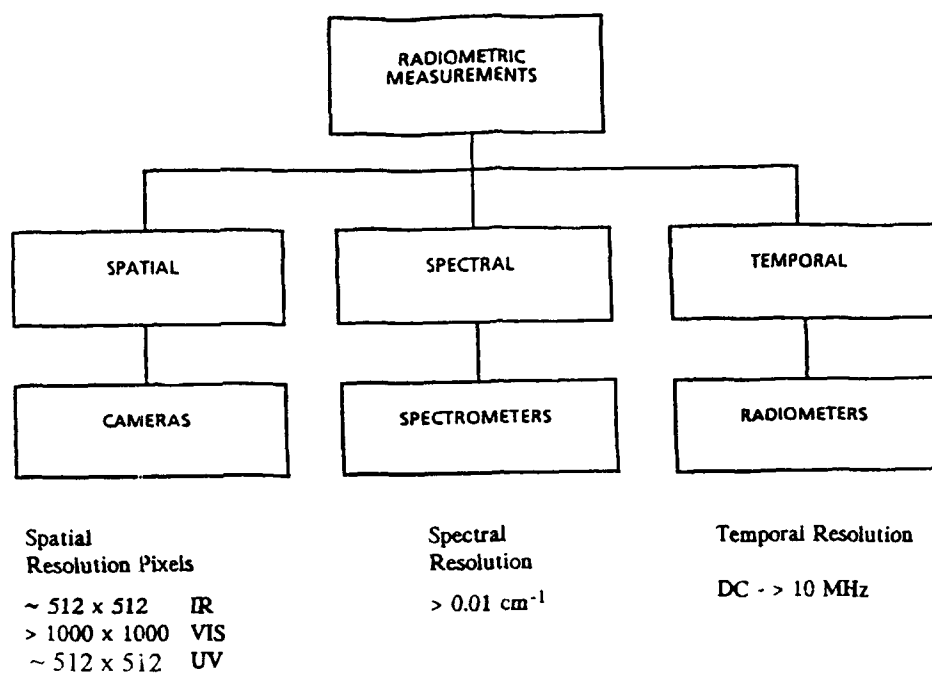
Fig.21   Selection Guide for Optical Detectors

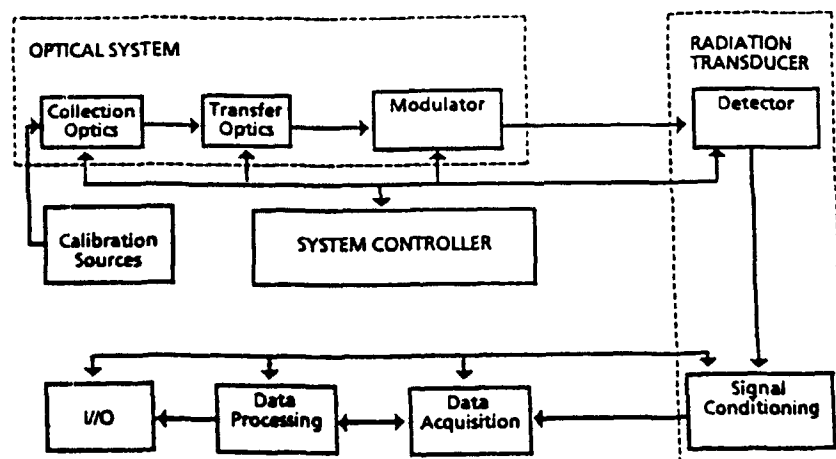Fig. 22 Ways to Perform Radiometric Measurements

Fig. 23 Schematic Diagram for a Radiometric System
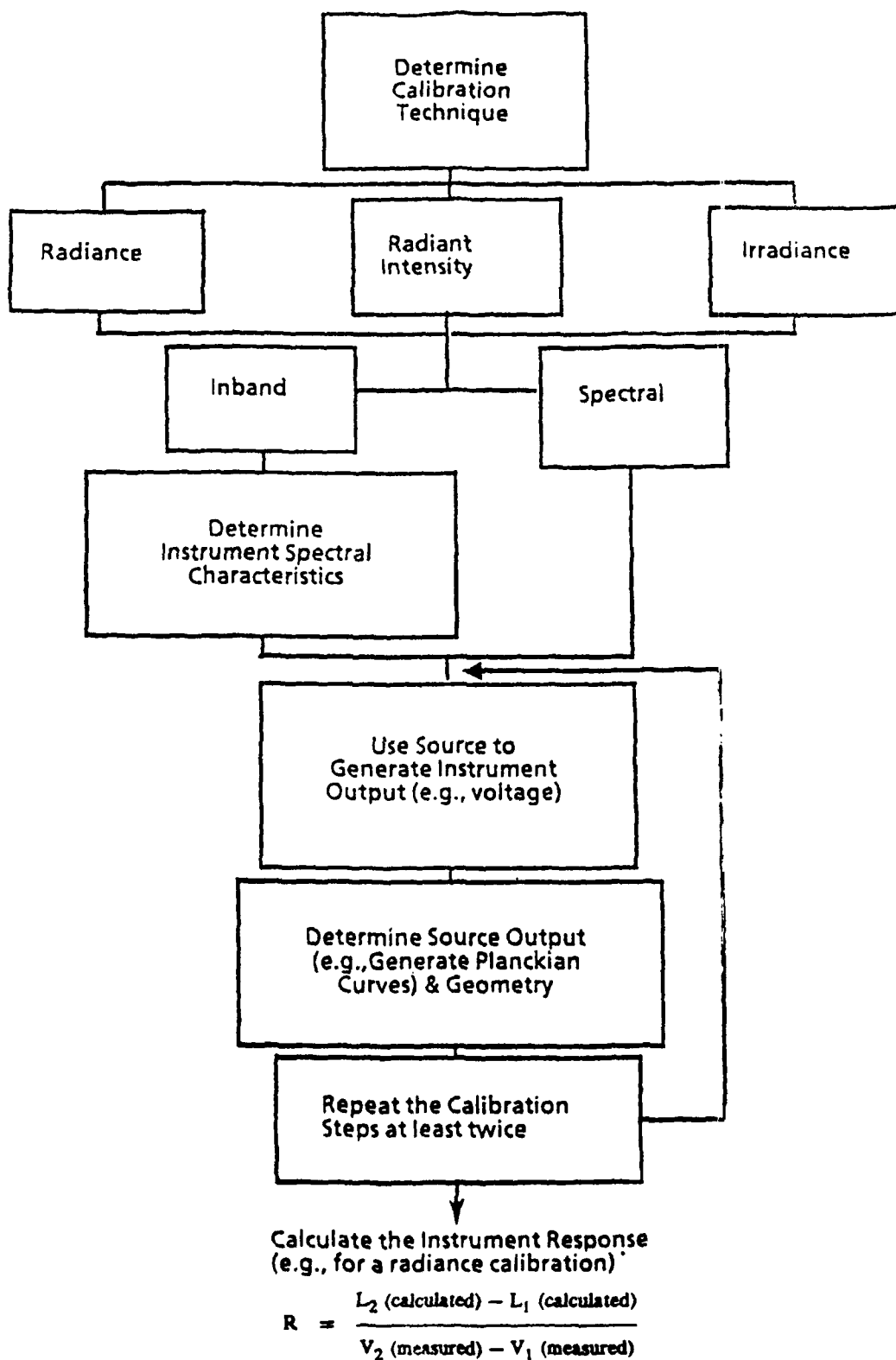
Fig. 24   Proposed Calibration Procedure

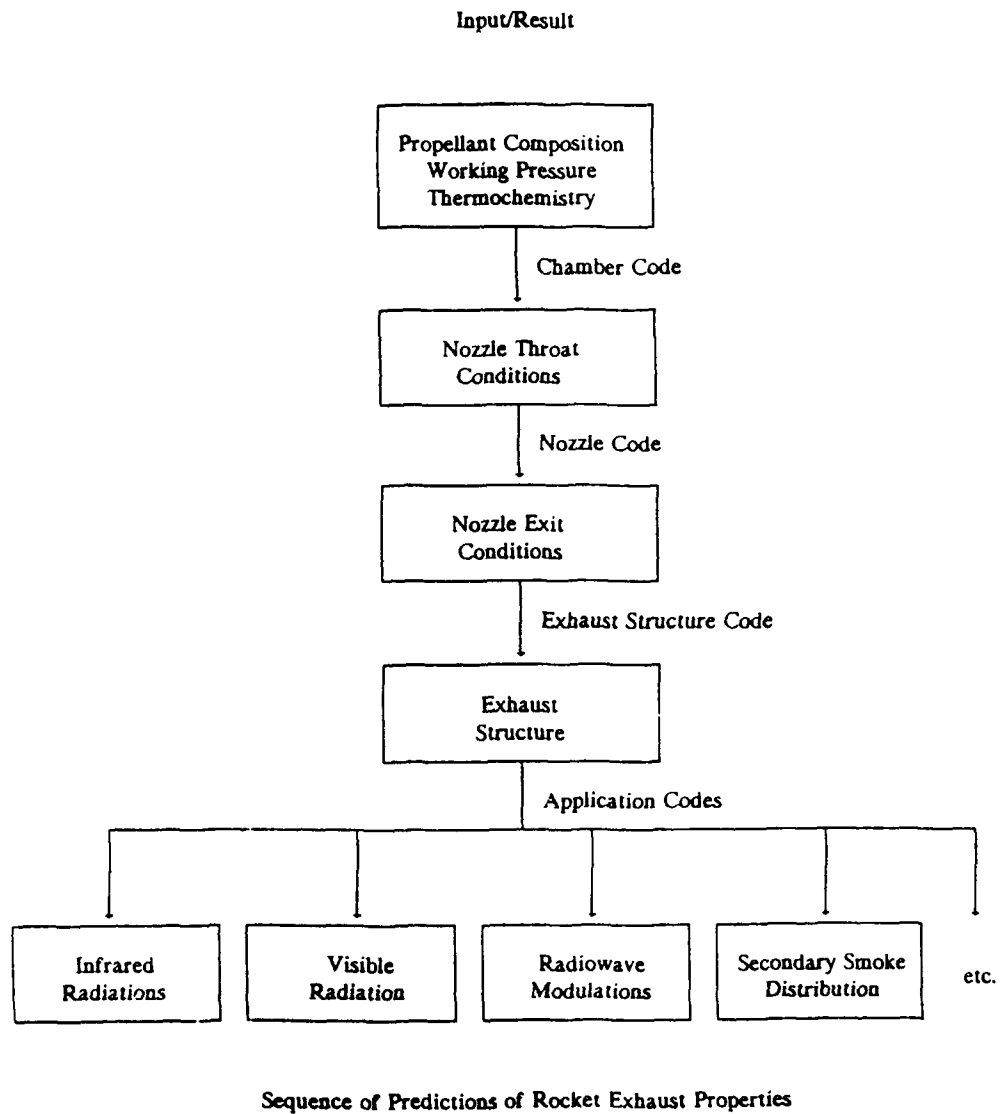Input/Result

Propellant Composition
Working Pressure
Thermochemistry

Chamber Code

Nozzle Throat
Conditions

Nozzle Code

Nozzle Exit
Conditions

Exhaust Structure Code

Exhaust
Structure

Application Codes

| Infrared Radiations | Visible Radiation | Radiowave Modulations | Secondary Smoke Distribution | etc. |

Sequence of Predictions of Rocket Exhaust Properties

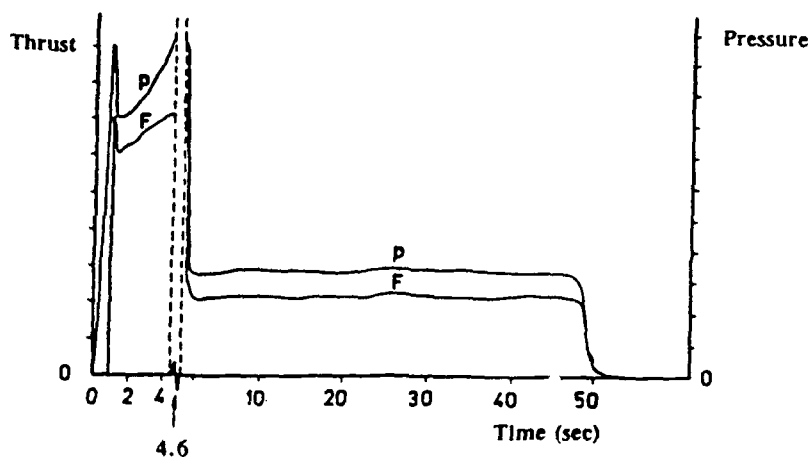Fig. 25   Typical Prediction Procedure

Fig. 26 Typical Thrust-Time and Pressure Curves for a
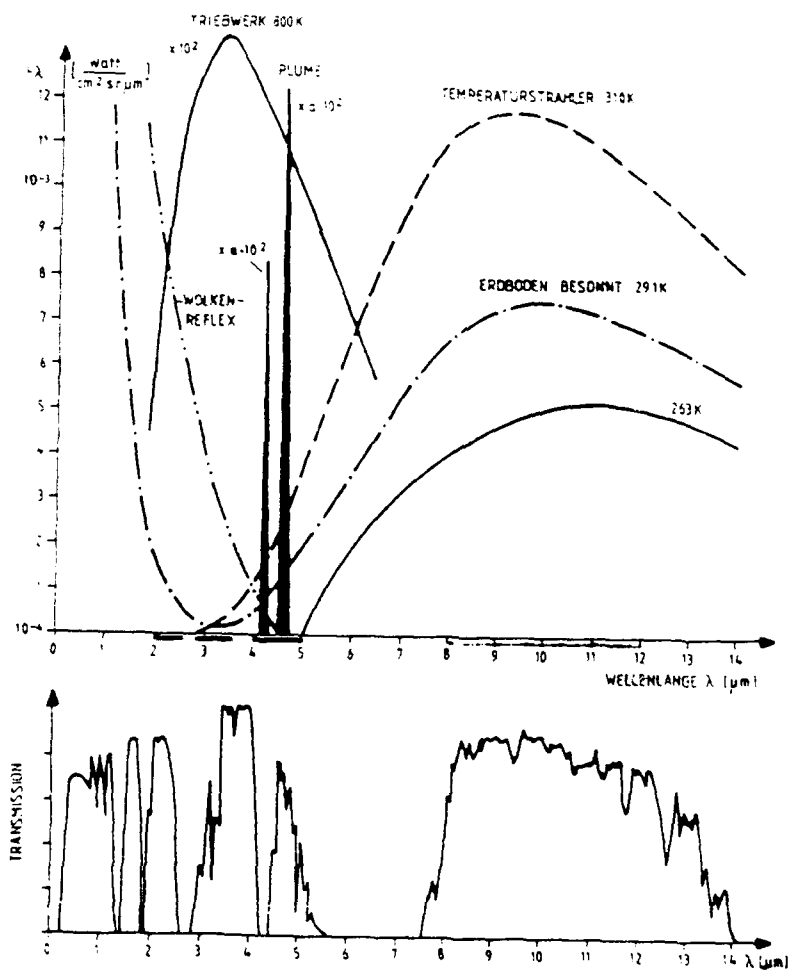Boost-Sustain Rocket Motor (see also Chapter 1)

Fig. 27 Spectral Characteristics of Typical Targets, Background and
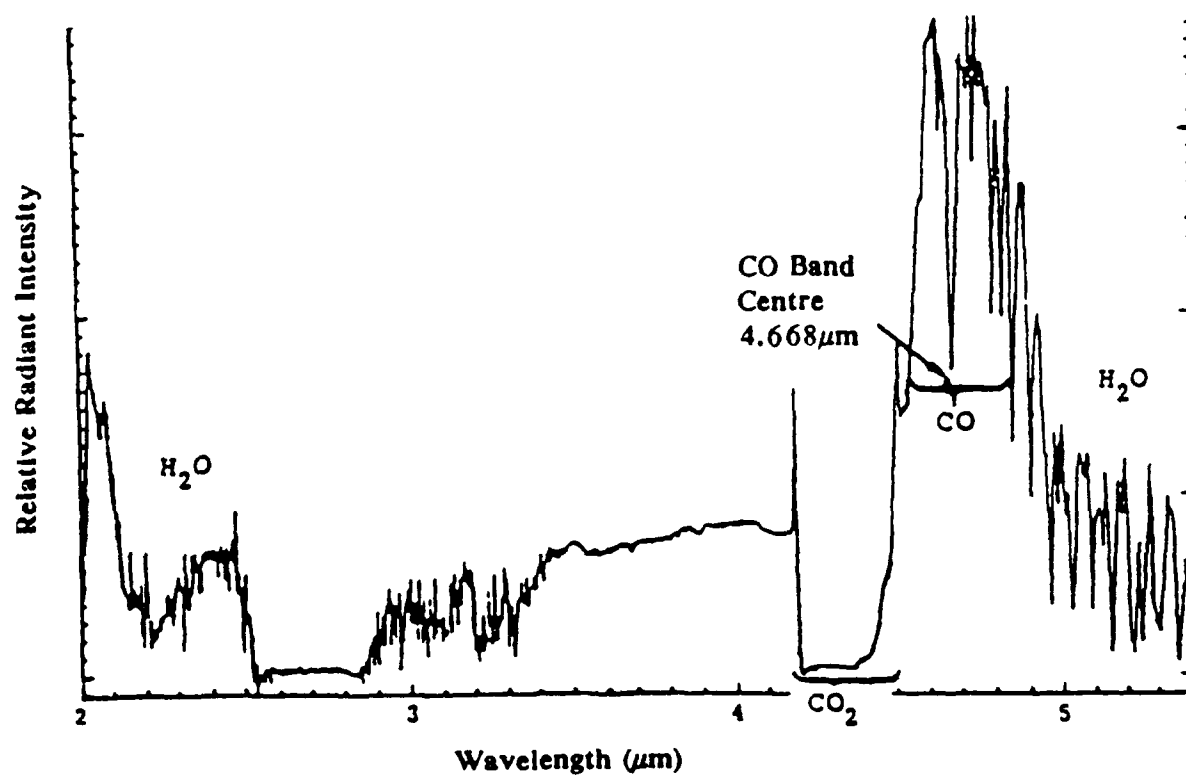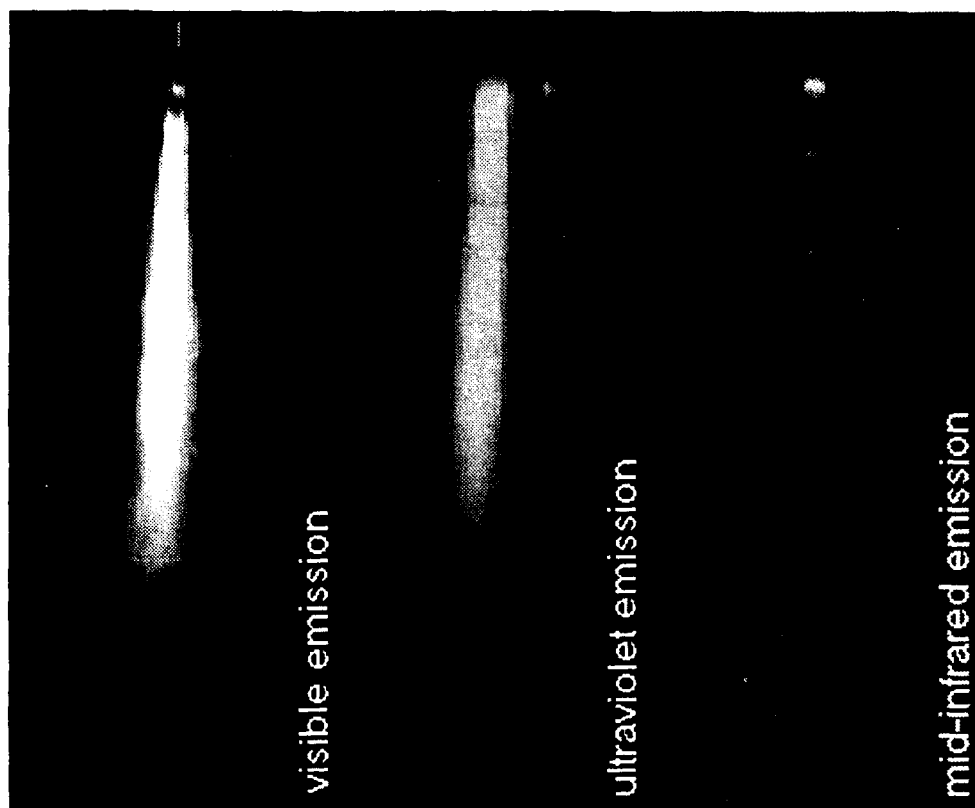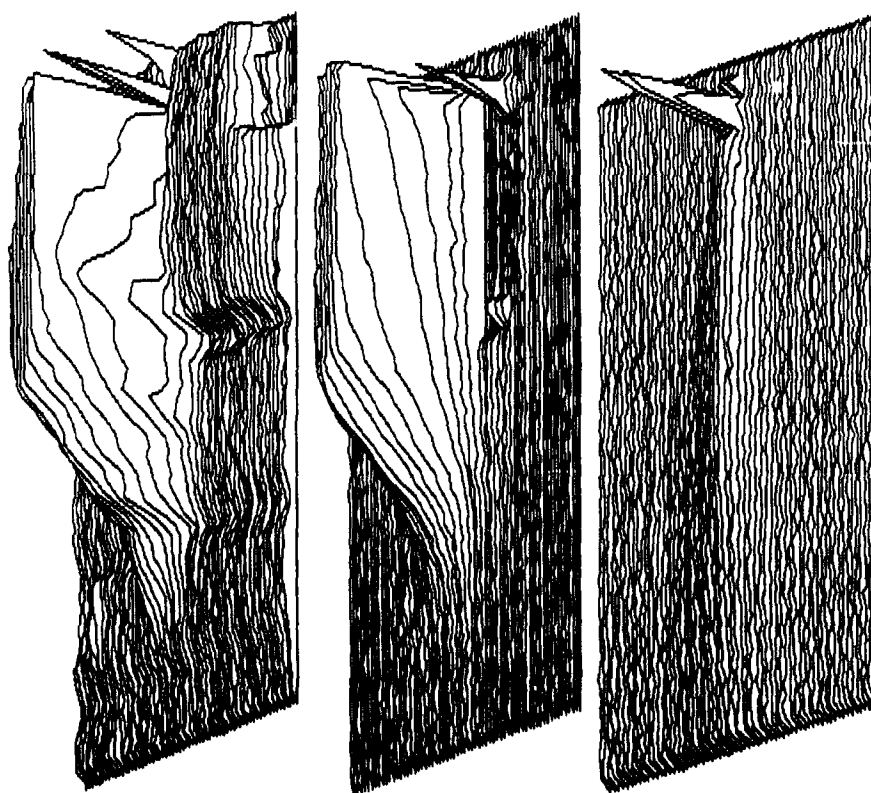Atmospheric Transmission

Fig. 28 Infrared Emission from a Plume

visible emission

ultraviolet emission

mid-infrared emission

Plume Images as Seen by Cameras in Different Spectral Bands

3-Dimensional Intensity Profiles

Fig. 29 Images of a Rocket Motor Exhaust in Various Spectral Bands

REPORT DOCUMENTATION PAGE

1. Recipient's Reference	2. Originator's Reference	3. Further Reference	4. Security Classification of Document
	AGARD-LS-188	ISBN 92-835-0713-4	UNCLASSIFIED/ UNLIMITED

5. Originator	Advisory Group for Aerospace Research and Development North Atlantic Treaty Organization 7 rue Ancelle, 92200 Neuilly sur Seine, France

6. Title	ROCKET MOTOR PLUME TECHNOLOGY

7. Presented on	7th--8th June 1993 in Neubiberg, Germany, 10th—11th June 1993 in Ankara, Turkey.

8. Author(s)/Editor(s)	9. Date
Various	June 1993

10. Author's/Editor's Address	11. Pages
Various	194

12. Distribution Statement	There are no restrictions on the distribution of this document. Information about the availability of this and other AGARD unclassified publications is given on the back cover.

13. Keywords/Descriptors

Rocket exhaust	Infrared signatures
Missile plumes	Signature reduction
Plume detection	Microwave frequencies
Combustion products	Stealth — signature reduction

14. Abstract

Requirements for missile guidance and stealth properties are changing and becoming more stringent. There is no up-to-date synthesis relating rocket motor plume properties to these new requirements. The work performed and recently finished within PEP WG 21 has formed the basis for this Lecture Series.

The scope of the Lecture Series will be rocket motor exhaust products and plumes in all their aspects. Plume properties will be addressed and methods of numerical simultation and experimental assessment described.

Specifically, plume structure, after-burning phenomena, primary and secondary smoke, plume radiation signatures and plume microwave interactions will be described in detail.

Operational aspects linked to these topics will discuss how rocket plumes influence missile detection, guidance and tracking. Ways in which plumes may be modified to reduce or eliminate this influence will be suggested.

This Lecture Series was sponsored by the Propulsion and Energetics Panel and the Consultant and Exchange Programme of AGARD.

AGARD-LS-188

Rocket exhaust
Missile plumes
Plume detection
Combustion products
Infrared signatures
Signature reduction
Microwave frequencies
Stealth — signature reduction

AGARD Lecture Series 188
Advisory Group for Aerospace Research and
Development, NATO
ROCKET MOTOR PLUME TECHNOLOGY
Published June 1993
194 pages

Requirements for missile guidance and stealth properties
are changing and becoming more stringent. There is no up-
to-date synthesis relating rocket motor plume properties to
these new requirements. The work performed and recently
finished within PEP WG 21 has formed the basis for this
Lecture Series.

The scope of the Lecture Series will be rocket motor
exhaust products and plumes in all their aspects. Plume
properties will be addressed and methods of numerical
simulation and experimental assessment described.

P.T.O.

AGARD-LS-188

Rocket exhaust
Missile plumes
Plume detection
Combustion products
Infrared signatures
Signature reduction
Microwave frequencies
Stealth — signature reduction

AGARD Lecture Series 188
Advisory Group for Aerospace Research and
Development, NATO
ROCKET MOTOR PLUME TECHNOLOGY
Published June 1993
194 pages

Requirements for missile guidance and stealth properties
are changing and becoming more stringent. There is no up-
to-date synthesis relating rocket motor plume properties to
these new requirements. The work performed and recently
finished within PEP WG 21 has formed the basis for this
Lecture Series.

The scope of the Lecture Series will be rocket motor
exhaust products and plumes in all their aspects. Plume
properties will be addressed and methods of numerical
simulation and experimental assessment described.

P.T.O.

AGARD-LS-188

Rocket exhaust
Missile plumes
Plume detection
Combustion products
Infrared signatures
Signature reduction
Microwave frequencies
Stealth — signature reduction

AGARD Lecture Series 188
Advisory Group for Aerospace Research and
Development, NATO
ROCKET MOTOR PLUME TECHNOLOGY
Published June 1993
194 pages

Requirements for missile guidance and stealth properties
are changing and becoming more stringent. There is no up-
to-date synthesis relating rocket motor plume properties to
these new requirements. The work performed and recently
finished within PEP WG 21 has formed the basis for this
Lecture Series.

The scope of the Lecture Series will be rocket motor
exhaust products and plumes in all their aspects. Plume
properties will be addressed and methods of numerical
simulation and experimental assessment described.

P.T.O.

AGARD-LS-188

Rocket exhaust
Missile plumes
Plume detection
Combustion products
Infrared signatures
Signature reduction
Microwave frequencies
Stealth — signature reduction

AGARD Lecture Series 188
Advisory Group for Aerospace Research and
Development, NATO
ROCKET MOTOR PLUME TECHNOLOGY
Published June 1993
194 pages

Requirements for missile guidance and stealth properties
are changing and becoming more stringent. There is no up-
to-date synthesis relating rocket motor plume properties to
these new requirements. The work performed and recently
finished within PEP WG 21 has formed the basis for this
Lecture Series.

The scope of the Lecture Series will be rocket motor
exhaust products and plumes in all their aspects. Plume
properties will be addressed and methods of numerical
simulation and experimental assessment described.

P.T.O.

Specifically, plume structure, after-burning phenomena, primary and secondary smoke, plume radiation signatures and plume microwave interactions will be described in detail.

Operational aspects linked to these topics will discuss how rocket plumes influence missile detection, guidance and tracking. Ways in which plumes may be modified to reduce or eliminate this influence will be suggested.

The material in this publication was assembled to support a Lecture Series under the sponsorship of the Propulsion and Energetics Panel and the Consultant and Exchange Programme of AGARD presented on 7th—8th June 1993 in Neubiberg, Germany, 10th—11th June 1993 in Ankara, Turkey.

Specifically, plume structure, after-burning phenomena, primary and secondary smoke, plume radiation signatures and plume microwave interactions will be described in detail.

Operational aspects linked to these topics will discuss how rocket plumes influence missile detection, guidance and tracking. Ways in which plumes may be modified to reduce or eliminate this influence will be suggested.

The material in this publication was assembled to support a Lecture Series under the sponsorship of the Propulsion and Energetics Panel and the Consultant and Exchange Programme of AGARD presented on 7th—8th June 1993 in Neubiberg, Germany, 10th—11th June 1993 in Ankara, Turkey.

Specifically, plume structure, after-burning phenomena, primary and secondary smoke, plume radiation signatures and plume microwave interactions will be described in detail.

Operational aspects linked to these topics will discuss how rocket plumes influence missile detection, guidance and tracking. Ways in which plumes may be modified to reduce or eliminate this influence will be suggested.

The material in this publication was assembled to support a Lecture Series under the sponsorship of the Propulsion and Energetics Panel and the Consultant and Exchange Programme of AGARD presented on 7th—8th June 1993 in Neubiberg, Germany, 10th—11th June 1993 in Ankara, Turkey.

Specifically, plume structure, after-burning phenomena, primary and secondary smoke, plume radiation signatures and plume microwave interactions will be described in detail.

Operational aspects linked to these topics will discuss how rocket plumes influence missile detection, guidance and tracking. Ways in which plumes may be modified to reduce or eliminate this influence will be suggested.

The material in this publication was assembled to support a Lecture Series under the sponsorship of the Propulsion and Energetics Panel and the Consultant and Exchange Programme of AGARD presented on 7th—8th June 1993 in Neubiberg, Germany, 10th—11th June 1993 in Ankara, Turkey.